Universidad Pública de Navarra
Nafarroako Unibertsitate Publikoa

UNIVERSIDAD PÚBLICA DE NAVARRA
Departamento de Ingeniería Eléctrica, Electrónica y de Comunicación
PUBLIC UNIVERSITY OF NAVARRE
Electrical, Electronic and Communications Engineering Department

SYNTHESIS OF HIGH-PERFORMANCE SMOOTH-PROFILED TAPERS AND FILTERS IN MICROSTRIP AND RECTANGULAR WAVEGUIDE TECHNOLOGIES

SÍNTESIS DE TAPERS Y FILTROS DE PERFIL SUAVE DE ALTAS PRESTACIONES EN TECNOLOGÍAS MICROSTRIP Y DE GUÍA DE ONDA RECTANGULAR

Doctoral Thesis by / Tesis Doctoral realizada por
Jon Mikel Percaz Ciriza

Supervised by / Dirigida por
Israel Arnedo Gil
José María Lopetegi Beregaña

Pamplona, 2020

upna
Universidad Pública de Navarra
Nafarroako Unibertsitate Publikoa

upna

Universidad Pública de Navarra
Nafarroako Unibertsitate Publikoa

upna

Universidad Pública de Navarra
Nafarroako Unibertsitate Publikoa

upna

Universidad Pública de Navarra
Nafarroako Unibertsitate Publikoa

Dedicada a Merche, mis padres, Josu y Mikel

upna
Universidad Pública de Navarra
Nafarroako Unibertsitate Publikoa

upna

Universidad Pública de Navarra
Nafarroako Unibertsitate Publikoa

AGRADECIMIENTOS

Ahora que la realización de esta tesis está llegando a su fin, me gustaría mostrar mi más profunda gratitud y admiración a mis directores de tesis, Israel Arnedo y Txema Lopetegi, por su dedicación y orientación constantes, así como por todo lo que me han enseñado y la paciencia con la que lo han hecho.

También agradezco profundamente a Mikel Gómez Laso su incansable búsqueda de ideas, recursos y su agradable compañía durante muchos viajes. La ayuda desinteresada y los buenos consejos de Iván Arregui a la hora de afrontar las cuestiones más prácticas de la tesis merecen así mismo, mi más sincero agradecimiento.

Quiero destacar y agradecer a Fernando Teberio su amistad durante estos años, su perpetua e inalterable predisposición a ayudar y su actitud positiva.

Igualmente, me gustaría mostrar mi gratitud a todas las personas que están o han pasado por el MCG (David Benito, Magdalena Chudzik, Petronilo Martín Iglesias, Luis Miranda, David Santiago, Abdul Sami, Jabir Hussein, Jamil Ahmad, Germán Álvarez, Cristian Martínez de Morentin, Ibai Calero, Celia Gómez, Adrián Gómez, Esteban Menargues, …) y con los que he siempre he podido contar.

No me olvido de todos los proyectistas y compañeros con los que he tenido el placer de compartir tiempo y de los que tanto he aprendido.

Agradezco así mismo la ayuda prestada en numerosas ocasiones por Jorge Teniente, así como por el resto de personal del Departamento de Ingeniería Eléctrica, Electrónica y de Comunicación, con una mención especial para Santiago de Miguel y Pablo Etxeberria.

Muchísimas gracias a Leni, una de las grandes amistades que me llevo de todos estos años y experto en el dificilísimo arte de provocar una sonrisa los días que más cuesta todo.

Quisiera mostrar mi más profundo y sincero agradecimiento a mi familia y amigos por todo lo que han perseverado y ayudado para que llegue este momento. Si nos lo llegan a decir hace diez años…

Por último, me gustaría otorgar mi más afectuoso agradecimiento a mi pareja, Merche, quien debería figurar como coautora de esta tesis, dado que nada de esta hubiera sido posible sin su apoyo, esfuerzo, paciencia, ánimo y ayuda incondicionales y continuados durante estos últimos cinco años.

Muchas gracias a tod@s!

Jon Mikel Percaz Ciriza

ABSTRACT

In this thesis, the theoretical foundations and the formulation of the Coupled-Mode Theory for the electromagnetic analysis and modeling of non-uniform waveguides are employed to develop different techniques for the synthesis of microwave and millimeter wave devices that are completely automatic and independent from the physical technology of implementation.

Firstly, the technique for synthesizing optimal electromagnetic bandgap (EBG) structures is described and thoroughly reviewed. Subsequently, the general and exact one-dimensional Inverse Scattering techniques of Gel'fand, Levitan, Marchenko (GLM), Continuous Layer Peeling (CLP) and Integral Layer Peeling (ILP) are presented in detail. These Inverse Scattering techniques allow the calculation of the coupling coefficient for any single-mode targeted response in reflection that fulfills the physical principles of stability, causality and passivity.

Novel design techniques inspired in the use of these synthesis methods are proposed for different microwave components such as multiplexers and tapers. In addition, a design method for low-pass and band-pass filters without spurious rejection bands is proposed. The application of this technique for the design of filters with high rejection levels in rectangular waveguide technology leads to structures that are very suitable to be fabricated with the novel additive manufacturing (AM) techniques in metal.

The proposed design techniques are validated through the realization of practical design examples in the microwave range, where a high degree of agreement is achieved between the targeted, simulated and measured responses.

Resumen

En esta tesis, los fundamentos teóricos y la formulación de la Teoría de Acoplo de Modos para el análisis y el modelado electromagnético de guías de onda no uniformes son utilizadas para desarrollar diferentes técnicas de síntesis de dispositivos de microondas y de milimétricas que son automáticas e independientes de la tecnología concreta de implementación.

En primer lugar, la técnica para sintetizar estructuras EBG óptimas es descrita y revisada en profundidad. Posteriormente, las técnicas generales y exactas de Inverse Scattering de Gel'fand, Levitan, Marchenko (GLM), Continuous Layer Peeling (CLP) e Integral Layer Peeling (ILP) son presentadas en detalle. Estas técnicas de Inverse Scattering, permiten calcular el coeficiente de acoplo para cualquier respuesta monomodo en reflexión objetivo que cumpla con los principios físicos de estabilidad, causalidad y pasividad.

Inspirados en estos métodos de síntesis, se proponen novedosas técnicas de diseño de diferentes componentes de microondas como tapers y multiplexores. Además, se propone un método de diseño de filtros paso bajo y paso banda de perfil suave que no presentan bandas de rechazo espurias. La aplicación de esta técnica para el diseño de filtros de alto rechazo en guía de onda rectangular da lugar a estructuras que resultan sumamente apropiadas para ser fabricadas con las novedosas técnicas de fabricación aditiva (AM) en metales.

Las diferentes técnicas de diseño propuestas son validadas mediante la realización de varios ejemplos de prácticos de diseño en el rango de microondas en los que se logra alto grado de concordancia entre las respuestas objetivo, simuladas y medidas.

CONTENTS

CHAPTER 1. INTRODUCTION

Microwave engineering can be defined as the study and design of components and technologies employed for processing electromagnetic signals with frequency components that approximately belong to the range located between 300 MHz and 300 GHz, see Fig. 1.1. However, this delimitation should be interpreted as a rule of thumb, since the borders of the microwave term can be easily expanded in both, lower and upper limits, depending on the particular situation to be considered. The field of application of microwave engineering specifically starts when dealing with structures able to propagate electromagnetic waves that feature a wavelength comparable to the physical dimensions of the device under study [1]. In this situation, the classic circuit theory begins to fail due to the excessive size of its characteristic discrete elements (resistors, capacitors, inductors, …) when they are compared with the wavelength of the signals that are being processed. Indeed, it can be actually stated that circuit theory is an approximation of the microwave theory for those devices that feature very small sizes with respect to the concerning wavelengths. In contrast to the discrete elements of the standard circuit theory, microwave components are considered as distributed elements since the properties of the electromagnetic waves change significantly over the physical dimensions of the device. On the other hand, i.e. if the wavelength is much smaller than the structure, the geometrical optics approach will be employed for the modelling of the situation. From a general point of view, the general laws that govern the electromagnetic waves and their interaction with matter are gathered in the Maxwell's equations.

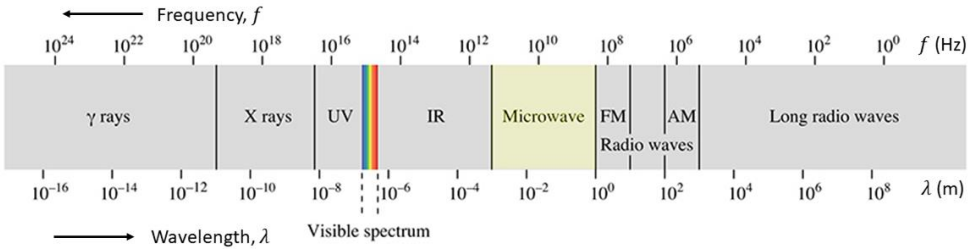

Fig. 1.1. Location of the microwave range in the electromagnetic spectrum.

The challenge that implies the analysis and design of components for microwave signal processing with their short wavelengths also becomes one of its most important advantages and fruitful source of opportunities, since the large amount of data managed by practically any current application devoted to provide information can be processed with small-sized components, thanks to microwave technologies. Regarding this aspect, one of the most frequent questions that non-initiated people ask me concerns the daily uses of the microwave technologies and it can be summarized as: What are the microwaves used for?

In the recent years, the improvement of the data rate capabilities that has been achieved by some devices like smartphones has suffered an exponential growth linked to the continuous evolution of the different communication standards. Each new telecommunication standard required even more miniaturized microwave components that supported the necessary requirements of operational bandwidths and transmission velocities, and the research in the design and synthesis of microwave components and subsystems was accordingly essential. In fact, this innovation is still fundamental for the current deployment of the new 5G standard [2]-[4], and it will continue being essential for the future standard releases.

Moreover, private and broadcasting voice, video, and data services are based on modern satellite communications [5], [6], without forgetting the global positioning functions provided by the GPS, Galileo and GLONASS systems. In this case, the reduced space for the payload and the tight energy availability in the satellite lead to stringent requirements in terms of low losses, maximum power capabilities and reduced footprint and weight for the microwave components. Therefore, the research on high performance microwave components, especially filters, is being continuously addressed. Moreover, the benefits that can be added by the novel Additive Manufacturing techniques [7] are being presently explored so as to integrate different elements of the communication chain in a single piece and for the fabrication of many components at the same time in the context of large satellite platforms [8].

Different areas as radar, biomedical testing, wireless networking, security, and environmental remote sensing systems, among many others, are also benefited in a lesser or

greater degree from the application of microwave technology and the use of microwave components [1].

Since the fields that directly or indirectly make use of the microwave technology are so broad and varied, the associated research covers a lot of different topics. The contents gathered in this thesis conform my humble contribution to this research.

1.1. MOTIVATION

A wide variety of techniques have been proposed in order to design each of the components that can be employed in a microwave system. Additionally, specific design techniques depend frequently on the particular technology that is considered for the physical implementation of the component. Thus, the design technique that has been developed for a certain technology may not be easily translated to another, something that is simply impossible in many cases.

Moreover, the design technique commonly starts from a first theoretical approach for calculating the initial values of the dimensions of the waveguide elements that compose the device. However, a subsequent design stage based on time-consuming optimization procedures is almost always needed in order to adjust the final dimensions of the different elements that conform the device so as to achieve the desired behavior.

A good example of this design philosophy is applied to one of the most attractive topics in the microwave literature: the filters [9]-[17]. Microwave filters can be defined as two-port networks employed for controlling the frequency response at a certain point of the microwave system. The frequency response of the filter provides a transmission feature for a frequency range of interest that conforms the so-called passband, while a characteristic of attenuation is applied to the frequencies that are not desired in the following stages of the microwave system, i.e. the stopband. Depending on the selectivity characteristics of the frequency response of the filter, it can be classified into four categories: low-pass, high-pass, band-pass, and reject-band.

Several classical filter design techniques rely on the insertion-loss method that comes from the classical network synthesis theory [12], which was originally developed for lower frequencies, where discrete elements are employed in order to satisfy a desired rational transfer function such as Butterworth, Chebyshev or Cauer. As it has been already mentioned, the discrete elements like resistors, capacitors, inductors, etc., are not valid for high frequencies, and then, the dimensions of transmission line sections are selected so as to act as a desired discrete element for the bandwidth of interest. An additional optimization step is always needed so as to adjust the frequency response of the filter. However, since the frequency response of the transmission line sections is variable, the frequency response of the filter gets rapidly degraded with respect to the one expected from the insertion-loss starting model when the frequency considered is far from the one employed for the design. This inaccuracy typically results in a loss of steepness between the passband and the stopband. Furthermore, this design methods are characterized by a complete lack of control for the frequency response out of the bandwidth of interest, where spurious rejection/transmission bands appear as a result of the inherent periodic behavior of the

distributed elements and the influence of higher-order modes. The sum of these problems may not affect the narrow band applications, but it becomes undoubtedly much more troublesome when wider band applications are considered.

In contrast to the aforementioned limitations of generality and control over the entire frequency response that are characteristic from other techniques, in this thesis the direct synthesis procedure that was initially proposed by Israel Arnedo and the members of the Microwave Components Group of the Public University of Navarre will be followed [18]. The main characteristics of this method are:

a) It is direct, due to the fact that it is not necessary to use lumped-element circuit models.
b) It is exact for all the bandwidth required since neither degradation of the frequency response nor spurious bands are allowed.
c) It is flexible since it is valid for any frequency response that fulfills the physical requirements of causality, stability and passivity.
d) It is general because neither the implementation technology, nor the operation frequency band, is an intrinsic limitation of the method.

As it can be seen in Fig. 1.2, the synthesis procedure starts from the definition of a target frequency response in reflection, $S_{11}(\beta)$, that can be also specified in terms of its corresponding impulse response in reflection, $F(\tau)$, due to the Fourier transform relationship [19], i.e. $S_{11}(\beta) = FT\{F(\tau)\}$. Then, different synthesis techniques can be employed to calculate the coupling coefficient, $K(z)$, of the structure that satisfies that response. The study of the Coupled-Mode Theory [20], which is devoted to the analysis of nonuniform waveguides, clearly shows

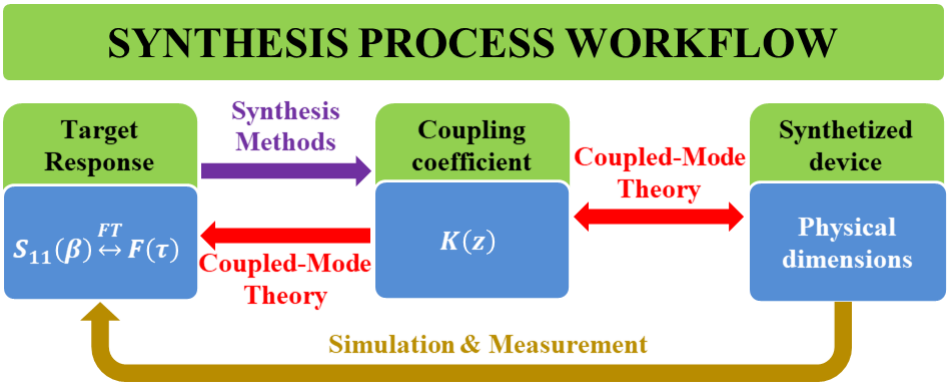

Fig. 1.2. Scheme of the general synthesis workflow that is going to be followed within the thesis.

that the coupling coefficient determines the frequency response of the structure. However, another key conclusion that can be extracted from the study of the Coupled-Mode Theory is that the coupling coefficient is also related with the physical dimension of the nonuniform waveguide device [20]. Thus, if the coupling coefficient can be deduced from the $S_{11}(\beta)$ by means of the synthesis techniques, the Coupled-Mode Theory will allow us to calculate the physical dimensions of the structure that features the sought $S_{11}(\beta)$. Moreover, the frequency response of a certain device can be deduced just from its coupling coefficient. The synthetized device is finally tested by means of electromagnetic simulations, while proper measurements are performed when the prototype is fabricated.

The synthesis techniques that are employed for the determination of the coupling coefficient into the design workflow of Fig. 1.2 can be classified into two large categories [18]. The first one is formed by the synthesis techniques for one dimensional electromagnetic bandgap (EBG) structures [21], [22], which can be considered as a special and analytical solution of the synthesis problem under the formulation of single-mode approximation of the Coupled-Mode Theory [23]. Since the EBGs are a particular solution of the synthesis problem, they can only satisfy a specific kind of frequency response characterized by a controllable passband and/or stopband feature.

On the other hand, the second group of synthesis methods can be encompassed in the realm of the one-dimensional Inverse Scattering techniques. These methods are employed in other ranges like optics and even, in (a priori) very far sciences like quantum mechanics, geophysics or acoustics, among others [24], [25]. Indeed, the one dimensional is only a part of the inverse scattering framework, which is devoted to the most general task of calculating the dimensions of a certain space by means of measurements carried out at a distant position. One-dimensional inverse scattering techniques originally began in the field of quantum mechanics [26], [27] for determining the scattering potential in the time-independent Schrödinger equation. It was in 1967 when the inverse scattering techniques were firstly studied from the point of view of the microwave research [28] that was afterwards emphasized with the special issue on Inverse Methods in Electromagnetics that was published by the *IEEE Transactions on Antennas and Propagation* [29]. The aim of these methods in the microwave and millimeter wave range is to deduce the unknown physical dimensions of a waveguide structure just from the response in reflection that it features. Unlike the EBG approach, the solution of the Inverse Scattering techniques can be considered as completely general, since it can be employed to synthetize any target response in reflection only limited by the physical constraints of stability, causality and passivity.

A common aspect of both EBG and Inverse Scattering methods is the fact that their resulting structures exhibit a smooth variation (without abrupt discontinuities) of their physical

dimensions along the propagation direction. Some of the advantages of these smooth-profiled structures are the flexibility in the design [30], robustness in the implementation [31], spurious-multimode-excitation avoidance [31], and a high-power handling capability [32].

Therefore, the initial aims of this thesis will be to review the study of the Coupled-Mode Theory performed in [33] and the synthesis methods that were summarized in [18], paying special attention to the spurious-free EBG synthesis method [34], the exact series solution of the one-dimensional Inverse Scattering problem (also known as the Gel'fand, Levitan, Marchenko (GLM) synthesis method [35]) and the Continuous Layer Peeling (CLP) technique [33], [36]. However, the main aim will be to develop, and study the practical implementation, of a new synthesis technique that will surpass the performance of the previous ones in terms of the rejection levels that can be achieved. As a result of the study and development of those synthesis techniques as well as of the Coupled-Mode Theory, different target applications for the design of the most employed microwave components should be proposed.

As it has been previously mentioned, filters are one of the most employed components in microwave engineering. Thus, it will be of particular interest to develop a design method for smooth-profiled low-pass and band-pass rectangular waveguide filters where the final length and extreme dimensions of the cross-section of the structure will be under tight control. This design method will be linked with the improvement and development of the synthesis techniques, since they cannot provide an accurate coupling coefficient for the high-reflectivity (high-rejection) responses that are typical from rectangular waveguide filters. However, the development of this method will be of great importance for the new metal Additive Manufacturing (AM) [37] technique of Selective Laser Melting (SLM), which is also known as Direct Laser Metal Sintering (DMLS).

The fabrication of a piece by means of the DMLS technique consists of several steps. The first one requires the slicing of the 3D computer-aided design (CAD) file data of the structure to be fabricated into layers, leading to a 2D image of each layer. The collection of 2D data is exported to the sintering system and the building process depicted in Fig. 1.3 starts. A thin layer of metal powder is uniformly deposited by a roller over the working platform, which is placed in the building chamber. Then, a high-energy density laser is employed to melt the desired surfaces according to the first 2D layer. Once the layer is fused, the building platform is lowered and a new layer of metal powder is deposited, allowing the melting of the next 2D layer just above of the previous one. Proceeding in an iterative manner, the laser scanning will come to its end when the last 2D layer will be fused, giving rise to the whole desired metal piece.

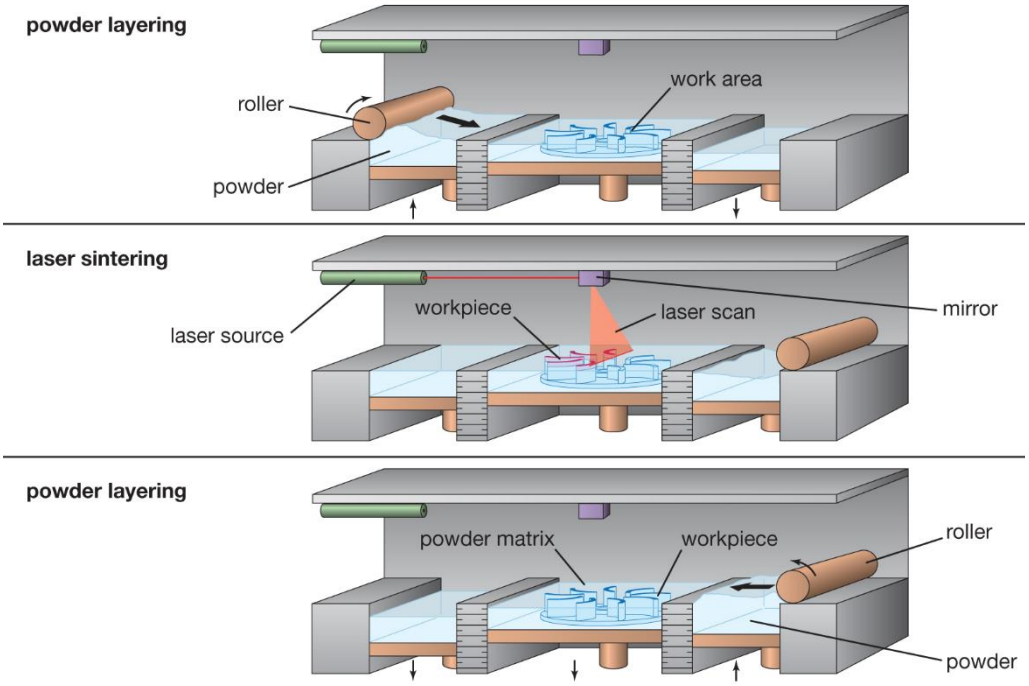

Fig. 1.3. Sketch of the DMLS fabrication procedure.

The DMLS technique allows the fabrication of complex structures as well as the manufacturing of objects that are already assembled, without the need of junctions [37]. Moreover, it has a great potential for reducing the weight and volume of metallic parts that are currently fabricated with classical techniques like Numerical Controlled (CNC) Milling, among others. Nevertheless, one of the most critical drawbacks of DMLS is the impossibility of fabricating overhanging surfaces, because they would eventually warp or even fall off during the melting process. Unfortunately, if we try to print a waveguide component designed by classical techniques, following the propagation direction, we will typically find plenty of problematic overhanging walls as it is shown in Fig. 1.4a. Since it is commonly impossible to use inner auxiliary supports in a waveguide structure, the only available option is to print the piece in a different orientation with the help of external auxiliary supports that must be designed ad-hoc for each different waveguide structure (see Fig. 1.4b).

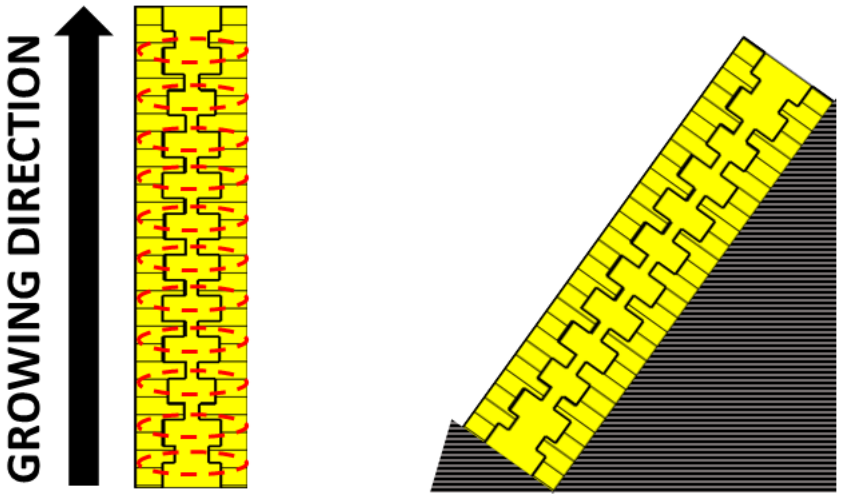

(a) (b)

Fig. 1.4. (a) Detail of the problematic overhanging surfaces that are found when a classical corrugated waveguide filter is going to be fabricated with Additive Manufacturing in metal. (b) The only possibility is to modify the orientation of the piece by means of auxiliary supports.

However, large overhanging surfaces are avoided when considering a structure that changes its dimensions in a smooth fashion along the propagation direction. Accordingly, the auxiliary supports would not be needed in a fabrication of a smooth-profiled rectangular waveguide filter, leading to a reduction of the auxiliary costs. Therefore, the last main objective of this thesis will be to verify the suitability of the smooth profiled rectangular waveguide filters that result from the synthesis methods for a later fabrication with DMLS technique.

1.2. OVERVIEW OF THE THESIS

The thesis is divided into eight chapters, where the present Introduction conforms the first of them.

The foundations of the Coupled-Mode Theory will be rigorously presented for the case of general non-uniform waveguide structures in CHAPTER 2. The cross-section method will be employed to achieve the so-called coupled mode equations, where the coupling coefficients will be presented as the key parameters. The Coupled-Mode Theory will be thoroughly applied to the case of rectangular waveguide technology. Moreover, the single-mode operation approximation that is needed for solving the synthesis problem will be formulated using this theory. As a result, closed-form expressions will be attained so as to relate the coupling coefficient with the physical dimensions of the rectangular waveguide. A similar relationship will be studied between the coupling coefficient and the characteristic impedance for the case of transmission lines that will be developed in depth for the case of single and coupled microstrip lines. The necessary theoretical tools will be completed with several models developed to assimilate the variation of the phase constant along the propagation direction, as well as the effects caused by the higher-order modes into the single-mode approximation of the Coupled-Mode Theory.

In CHAPTER 3, the synthesis solution for spurious-free electromagnetic bandgap (EBG) structures will be described in detail. Using this EBG concept, a method for the design of multiplexers based on simultaneous forward and backward coupling in microstrip coupled lines will be presented.

CHAPTER 4 will cover the exact series solution of the one-dimensional Inverse Scattering problem, which is also known as the Gel'fand, Levitan and Marchenko (GLM) synthesis method. Since the reflectivity that can be achieved by means of this method is limited, the GLM solution will be employed in a novel procedure for the design of tapered matching sections in general waveguide technology, where the rejection of the required response is typically low. This novel procedure will apply the GLM method for the synthesis of tapers. Classical and novel tapering responses will be presented, and several design examples will be provided in rectangular waveguide technology as a result.

In CHAPTER 5, the performance of the synthesis methods will be improved through the Continuous Layer Peeling (CLP) technique. The technique will be rigorously presented from a mathematical point of view, and practical considerations of its numerical implementation will be addressed. Taking advantage of the increase of the rejection levels of the responses that can be synthetized with CLP, a method for the design of low-pass and band-pass filters without spurious

rejection bands will be detailed. A successful design example will be provided in microstrip technology.

CHAPTER 6 introduces the most accurate synthesis technique developed in this thesis, the Integral Layer Peeling (ILP) method. As in previous cases, it will be formulated in depth, and its practical implementation features will be pointed out and compared with the ones of CLP. The ILP technique will be employed to synthetize rectangular waveguide filters with challenging specifications that cannot be correctly synthetized with CLP. Several design examples will be provided where the methods proposed in CHAPTER 2 for the compensation of the effects of higher-order modes will be successfully applied and demonstrated. Some of the synthetized filters will be fabricated using a technique of Additive Manufacturing in metal. Finally, a complete assessment of the critical parameters for the synthesis with the ILP technique will be provided.

In CHAPTER 7, the most important conclusions of this thesis will be given.

Finally, in CHAPTER 8, the most interesting open research lines for the future will be listed.

REFERENCES

[1] David M. Pozar, Microwave Engineering, Fourth Edition, New York, USA. John Wiley & Sons, 2001.

[2] T. S. Rappaport *et al*., "Millimeter Wave Mobile Communications for 5G Cellular: It Will Work!," *IEEE Access*, vol. 1, pp. 335-349, 2013.

[3] J. G. Andrews *et al*., "What Will 5G Be?," *IEEE J. Sel. Areas Commun.*, vol. 32, no. 6, pp. 1065-1082, June 2014.

[4] R. Waterhouse, and D. Novack, "Realizing 5G: Microwave Photonics for 5G Mobile Wireless Systems," in *IEEE Microwave Magazine*, vol. 16, no. 8, pp. 84-92, Sept. 2015.

[5] G. Maral, and M. Bousqued, Satellite Communications Systems: Systems, Techniques, and Technology, Fifth Edition, Techniques and Technology. John Wiley & Sons, 2002.

[6] B. G. Evans, Satellite Communication Systems, Third Edition. Institution of Engineering and Technology. 1999.

[7] R. Sorrentino, and O. A. Peverini, "Additive manufacturing: a key enabling technology for next-generation microwave and millimeter-wave systems," *Proc. IEEE*, vol. 104, no. 7, pp. 1362-1366, July 2016.

[8] D. E. Koelle, "Cost reduction trends in space communications by larger satellites/platforms," Acta Astronautica, vol 11, no 12, pp. 785-794. 1984.

[9] R. Levy and S. B. Cohn, "A history of microwave filter research, design, and development," *IEEE Trans. Microwave Theory Tech.*, vol. 32, no. 9, pp. 1055- 1067, Sept. 1984.

[10] R. Levy, R. V. Snyder, and G. Matthaei, "Design of Microwave Filters," *IEEE Trans. Microwave Theory Tech.*, vol. 50, no. 3, pp. 783-793, Mar. 2002.

[11] I. C. Hunter, L. Billonet, B. Jarry, and P. Guillon, "Microwave Filters – Applications and Technology," *IEEE Trans. Microwave Theory Tech.*, vol. 50, no. 3, pp. 794-805, Mar. 2002.

[12] G. Matthaei, L. Young, E. M. T. Jones, Microwave filters, impedance-matching networks, and coupling structures, Artech House, Inc., 1980.

[13] I. C. Hunter, Theory and Design of Microwave Filters, Electromagnetic wave series 48, London, The Institution of Electrical Engineers, 2001

[14] R. J. Cameron, C. M. Kudsia, R. R. Mansour, "Microwave filters for communication systems: fundamentals, design and applications", Hoboken, NJ: John Wiley & Sons, 2007.

[15] J. S. Hong and M. J. Lancaster, "Microstrip Filters for RF/Microwave Applications", New York, NY: John Wiley & Sons, 2001.

[16] J. A. G. Malherbe, "Microwave Transmission Line Filters", Dedham, MA: Artech House, 1979.

[17] R. W. Rhea, “HF Filter Design and Computer Simulation”, Tucker, GA: Noble Publishing, 1994.

[18] I. Arnedo *et al*., "Direct and Exact Synthesis: Controlling the Microwaves by Means of Synthesized Passive Components with Smooth Profiles," *IEEE Microw. Mag.*, vol. 16, no. 4, pp. 114-128, May 2015.

[19] A. Papoulis, The Fourier Integral and its Applications (Electronic Science Series). New York, NY, USA: McGraw-Hill, 1962.

[20] B. Z. Katsenelenbaum, L. Mercader, M. Pereyaslavets, M. Sorolla, and M. Thumm, Theory of nonuniform waveguides – the cross-section method, London, UK: IEE Electromagnetic Waves Series, 44, 1998.

[21] Charles Elachi, “Waves in Active and Passive Periodic Structures: A Review,” *Proc. IEEE*, vol. 64, no. 12, pp. 1666-1698, Dec. 1976.

[22] Y. Rahmat-Samii and H. Mosallaei, “Electromagnetic band-gap structures: Classification, characterization and applications”, *Proc. Inst. Elect. Eng.-ICAP Symp.*, pp. 560-564, 2001.

[23] T. Lopetegi, M. A. G. Laso, M. J. Erro, M. Sorolla, and M. Thumm, “Analysis and design of periodic structures for microstrip lines by using the coupled mode theory,” *IEEE Microw. Wireless Compon. Lett.*, vol. 12, no. 11, pp. 441-443, Nov. 2002.

[24] A. M. Bruckstein, B. C. Levy and T. Kailath, “Differential methods in Inverse Scattering,” Information Systems Laboratory Technical Report, LIDS-P-1313, June, 1983.

[25] R. Pike and P. Sabatier, “Scattering – Scattering and Inverse Scattering in Pure and Applied Science”, San Diego, Academic Press, 2002.

[26] I. M. Gel’fand and B. M. Levitan, “On the determination of a differential equation by its spectral function,” *Am. Math. SOC. Transl.*, vol. 1, pp. 253-304, 1955.

[27] V. A. Marchenko, “Reconstruction of the potential energy from the phase of scattered waves,” *Dokl. Akad. Nauk. SSR*, vol. 104, pp. 635-698, 1955.

[28] D. S. Heim and C. B. Sharpe, “The synthesis of nonuniform lines of finite length- Part I,” *IEEE Trans. Circuit Theory*, vol. CT-14, pp. 393403, 1967.

[29] Special Issue on Inverse Methods in Electromagnetics, *IEEE Transactions on Antennas and Propagation*, vol. AP-29, no. 2, March, 1981.

[30] D. C. Youla, “Analysis and synthesis of arbitrarily terminated lossless nonuniform lines,” *IEEE Trans. Circuit Theory*, vol. 11, pp. 363–372, Sept. 1964.

[31] R. P. Hecken, “A Near Optimum Matching Section without Discontinuities,“ *IEEE Trans. Microw. Theory Techn.*, vol. MTT-20, pp. 734–739, Nov. 1972.M. D. Abouzahra and L. Lewin, “Radiation from microstrip discontinuities,” *IEEE Trans. Microwave Theory Tech.*, vol. 27, pp. 722–723, Aug. 1979.

[32] V. E. Semenov, J. Rasch, E. Rakova, and J. F. Johansson, “General study of multipactor between curved metal surfaces,” *IEEE Trans. Plasma Sci.*, vol. 42, no. 3, pp. 721–728, Mar. 2014.

[33] Israel Arnedo, “New Methods for the Synthesis of Microwave Devices Based on the Coupled-Mode Theory,” Doctoral Thesis, Universidad Pública de Navarra, España, 2009.

[34] I. Arnedo et al., "Analytical solution for the design of planar EBG structures with spurious-free frequency response," *2009 European Microwave Conference (EuMC)*, Rome, 2009, pp. 1299-1302.

[35] I. Arnedo, M. A. G. Laso, F. Falcone, D. Benito, T. Lopetegi, “A Series Solution for the Single-Mode Synthesis Problem Based on the Coupled-Mode Theory," *IEEE Trans. Microw. Theory Tech.*, vol. 56, no. 2, pp.457-466, Feb. 2008.

[36] Magdalena Chudzik, “Synthesis Techniques for Novel Devices Based on Smooth Profiles with Application from the Microwave to the Terahertz Regions,” Doctoral Thesis, Universidad Pública de Navarra, España, 2013.

[37] F. Calignano *et al.*, "Overview on Additive Manufacturing Technologies," in *Proc. IEEE*, vol. 105, no. 4, pp. 593-612, April 2017.

CHAPTER 2. ELECTROMAGNETIC MODELLING AND ANALYSIS OF NON-UNIFORM WAVEGUIDES

The study of the electromagnetic properties of nonuniform waveguides is a topic that was frequently addressed during the past century in the microwave [1]-[9] and optics [10] engineering realms, although it is still ongoing by providing new solutions and applications [11], [12]. One of the most fruitful strategies to deal with this kind of structures is the so-called Coupled-Mode Theory [13]-[23]. The knowledge that has been achieved to the date constitutes the necessary theoretical basis that will be employed in subsequent chapters to relate the frequency response of a waveguide device with its physical dimensions through a single parameter: the coupling coefficient.

As it will be detailed during this chapter, the coupling coefficients between the different modes govern the complex amplitudes of the waves associated with those modes through the coupled-mode equation system and hence, they determine the frequency response. Therefore, a general study of that coupling coefficient will be of primary importance for a coherent development of this thesis and specific solutions for it will be obtained by applying the cross-section method to particular kinds of waveguides of interest in the microwave and millimeter wave range. In this thesis, the case of close-boundary waveguides will be analyzed by paying special attention to one of the most employed technologies: the rectangular waveguide, which was considered before in [19], [21]. Moreover, the results previously found in [18]-[20] for

waveguides or transmission lines that support pure transversal electromagnetic (TEM) or quasi-transversal electromagnetic (QTEM) modes such as microstrip will be also included in this chapter. In both cases, an exact assessment in terms of the Coupled-Mode Theory will be performed, showing an implicit relationship between the coupling coefficient and the frequency response. A more explicit relationship with the physical dimensions of the waveguide will be also achieved.

However, in order to deal with the synthesis problem, the general Coupled-Mode Theory can be greatly simplified by taking a set of reasonable approximations that will lead to the single-mode operation assumption, and accordingly, to a single coupling coefficient. In addition to allowing the solution of the synthesis problem, one of the most important consequences of this assumption is the closed-form relationship that will be found between the coupling coefficient and the physical dimensions of certain waveguide structures. Indeed, the width and height dimensions for the case of rectangular waveguide will be related univocally with the coupling coefficient under the single-mode assumption. A similar relationship will be attained but with the characteristic impedance for the general case of transmission lines that support TEM or QTEM modes. The final dimensions of these transmission lines will be calculated in a subsequent step by using the related literature. Since the waveguide geometry will be linked with the coupling coefficient under the single-mode operation assumption, the determination of the former will correspond univocally with the latter.

Furthermore, as it will be detailed in CHAPTER 4, the solution of the synthesis problem requires from at least one critical initial assumption apart from the single-mode operation: the phase constant of that mode must not vary along the propagation direction. However, when dimensional changes are performed over the physical dimensions of many waveguide technologies, the variability of the phase constant becomes unavoidable. In order to overcome these troublesome cases, a method based on the use of a normalized propagation axis where a reference phase constant is assumed to be fixed will be presented in this chapter.

Since the possible parasitic contributions of cut-off modes are deliberately neglected for the synthesis, the actual frequency response obtained in certain scenarios may differ from the one that is expected from the single-mode approximation. This inherent inaccuracy of the single-mode approximation of the Coupled-Mode Theory may result particularly troublesome in those cases where the coupling between the fundamental and higher-order modes is not weak enough. Fortunately, as it will be studied in the last part of the chapter, the effects of cut-off modes in closed-boundary waveguides can be modelled, following the Coupled-Mode formulation, as a variation of the phase constant of the fundamental mode, and two different methods to assimilate them in the single-mode coupled-mode equations will be described.

2.1. FORMULATION OF THE COUPLED-MODE THEORY THROUGH THE CROSS-SECTION METHOD

The Coupled-Mode Theory will be accurately formulated for microwave devices making use of the cross-section method. The basic principle of this method is that the electromagnetic fields that are present at any cross section of an arbitrary nonuniform waveguide can be expanded in a set of orthogonal modes (with their corresponding forward and backward travelling waves) that would be found in an auxiliary uniform waveguide if the latter featured the same cross section and identical distributions of electrical permittivity, ε, and magnetic permeability, μ, to the ones of the former [18], [21], [23]. Moreover, if steady-state sinusoidal time dependence of the fields is assumed, and discrete and continuous spectrum modes are considered as well, a complete orthogonal mode system for general open waveguides will be achieved [18], [22], [24]. Therefore, the total electric, $\hat{\vec{E}}$, and magnetic, $\hat{\vec{H}}$, fields at each cross section of interest can be expressed as in (2.1) and (2.2), respectively.:

$$\hat{\vec{E}}(x,y,z) = \sum_i a_i(z) \cdot \vec{E}^i(x,y,z) + \sum_i \int_0^\infty a_i^c(k_t,z) \cdot \vec{E}^i(x,y,k_t,z) \cdot dk_t \tag{2.1}$$

$$\hat{\vec{H}}(x,y,z) = \sum_i a_i(z) \cdot \vec{H}^i(x,y,z) + \sum_i \int_0^\infty a_i^c(k_t,z) \cdot \vec{H}^i(x,y,k_t,z) \cdot dk_t \tag{2.2}$$

where z stands for the propagation direction; x and y for the coordinate axis system of the cross section; and $\vec{E}^i$, $\vec{H}^i$ for the respective electric and magnetic vector mode patterns of the i mode of the auxiliary uniform waveguide associated with the cross section of interest. It must be pointed out that the vector mode pattern exhibits a variation in z direction since the dimensions of the cross section of the nonuniform waveguide also depend on z. Moreover, $a_i(z)$ is the complex amplitude of the i discrete spectrum mode along the waveguide propagation direction, while $a_i^c(k_t,z)$ represents the complex amplitude of the continuous spectrum i mode along z, being k_t the continuous variable that determines the vector mode pattern, and the field contribution of this mode is given by an integral in k_t [18], [22], [24].

2.1.1. Relationship between the Coupling Coefficient and the Frequency Response of General Waveguide Structures

If the field decomposition of (2.1) and (2.2) is introduced into the Maxwell's equations [18], [21]-[23], the so-called coupled-mode equations will be obtained after performing several mathematical manipulations that are fully described in [18]:

$$\frac{da_m}{dz} + j \cdot \beta_m \cdot a_m = \sum_i a_i \cdot C_{mi} + \sum_i \int_0^\infty a_i^c(k_t) \cdot C_{mi}^c(k_t) \cdot dk_t \tag{2.3}$$

$$\frac{da_n^c(\widetilde{k_t})}{dz} + j \cdot \beta_n^c(\widetilde{k_t}) \cdot a_n^c(\widetilde{k_t}) = \sum_i a_i \cdot C_{ni}^c(\widetilde{k_t}) + \sum_i \int_0^\infty a_i^c(k_t) \cdot C_{ni}^{cc}(\widetilde{k_t}, k_t) \cdot dk_t \tag{2.4}$$

being β_m and β_n^c the phase constants of the discrete m and continuous spectrum n mode, respectively, in the auxiliary uniform waveguide associated with the cross section of interest. It must be noticed that these phase constants may not be uniform in z as the dimensions of the cross section in that direction may not remain likewise invariable. Equation (2.3) is valid for any m discrete spectrum mode and thus, C_{mi} and C_{mi}^c are the coupling coefficients between that m mode and the i discrete or continuous spectrum mode, respectively. On the other hand, (2.4) is valid for any n continuous spectrum mode with $\widetilde{k_t}$, and thereby, C_{ni}^c and C_{ni}^{cc} represent accordingly the coupling coefficients of this n mode with the i mode that may belong either to the discrete or the continuous spectrum category. Those coupling coefficients relate the contribution of each mode amplitude in comparison with the variation of amplitude for other modes and then, (2.3) and (2.4) conform a first order integro-differential equation in a_m and $a_n^c(\widetilde{k_t})$ (i.e., for the discrete m and the continuous spectrum n modes) for general open waveguides, which is reduced to a first order differential equation when dealing with closed waveguides since continuous spectrum modes are not supported. The exact expressions to calculate the coupling coefficient depend on the kind of perturbation featured by the nonuniform waveguide [21], [23]. For the most interesting case in microwave technologies, where the waveguide includes conductors with variable cross sections, the coupling coefficient can be exactly determined by means of [18]:

$$C_{mi} = -\frac{1}{2 \cdot N_m} \cdot \iint_{\check{S}} \left(\vec{E}^m \times \frac{\partial \vec{H}^i}{\partial z} + \frac{\partial \vec{H}^m}{\partial z} \times \vec{E}^i \right) \cdot \hat{z} \cdot d\check{S} - \left(\delta_{i,m} + \delta_{i,-m}\right) \cdot \frac{1}{2 \cdot N_m} \cdot \frac{dN_i}{dz} \tag{2.5}$$

$$C^c_{mi}(k_t) = -\frac{1}{2 \cdot N_m} \cdot \iint_{\check{S}} \left[\vec{E}^m \times \frac{\partial \vec{H}^i(k_t)}{\partial z} + \frac{\partial \vec{H}^m}{\partial z} \times \vec{E}^i(k_t) \right] \cdot \hat{z} \cdot d\check{S} + - \left(\delta_{i,m} + \delta_{i,-m}\right) \cdot \frac{1}{2 \cdot N_m} \cdot \frac{dN_i(k_t)}{dz} \tag{2.6}$$

$$C^c_{ni}(\tilde{k}_t) = -\frac{1}{2 \cdot N^c_n(\tilde{k}_t)} \cdot \iint_{\check{S}} \left[\vec{E}^n(\tilde{k}_t) \times \frac{\partial \vec{H}^i}{\partial z} + \frac{\partial \vec{H}^n(\tilde{k}_t)}{\partial z} \times \vec{E}^i \right] \cdot \hat{z} \cdot d\check{S} + - \left(\delta_{i,n} + \delta_{i,-n}\right) \cdot \frac{1}{2 \cdot N^c_n(\tilde{k}_t)} \cdot \frac{dN_i}{dz} \tag{2.7}$$

$$C^{cc}_{mi}(\tilde{k}_t, k_t) = -\frac{1}{2 \cdot N^c_n(\tilde{k}_t)} \cdot \iint_{\check{S}} \left[\vec{E}^n(\tilde{k}_t) \times \frac{\partial \vec{H}^i(k_t)}{\partial z} + \frac{\partial \vec{H}^n(\tilde{k}_t)}{\partial z} \times \vec{E}^i(k_t) \right] \cdot \hat{z} \cdot d\check{S} + - \left(\delta_{i,n} + \delta_{i,-n}\right) \cdot \frac{1}{2 \cdot N^c_n(\tilde{k}_t)} \cdot \frac{dN^c_i(k_t)}{dz} \cdot \delta\left(k_t - \tilde{k}_t\right) \tag{2.8}$$

where $\check{S}$ is the surface of the cross section, excluding the conductors; $\hat{z}$ is the unitary vector in the propagation direction, z; $\delta_{i,m}$ and $\delta_{i,n}$ are Kronecker deltas; and N_i and N^c_i are the normalization factors of the i mode defined as:

$$N_i = \iint_{\check{S}} \left(\vec{E}^i \times \vec{H}^i \right) \cdot \hat{z} \cdot d\check{S} \tag{2.9}$$

$$N^c_i(k_t) \cdot \delta\left(k_t - \tilde{k}_t\right) = \iint_{\check{S}} \left[\vec{E}^i(k_t) \times \vec{H}^i(\tilde{k}_t) \right] \cdot \hat{z} \cdot d\check{S} \tag{2.10}$$

Furthermore, the following relationships are satisfied between the forward ($i > 0$) and backward ($i < 0$) travelling waves of the same i mode [18]:

$$N_i = -N_{-i} \tag{2.11}$$

$$N_i^c(k_t) = -N_{-i}^c(k_t) \tag{2.12}$$

$$\beta_i = -\beta_{-i} \tag{2.13}$$

$$\beta_i^c(\tilde{k_t}) = -\beta_{-i}^c(\tilde{k_t}) \tag{2.14}$$

Regarding the x, y, z components of the fields of both travelling waves of the same i mode, the sign convention of [23] is followed:

$$E_x^{-i} = E_x^i \tag{2.15}$$

$$E_y^{-i} = E_y^i \tag{2.16}$$

$$E_z^{-i} = -E_z^i \tag{2.17}$$

$$H_x^{-i} = -H_x^i \tag{2.18}$$

$$H_y^{-i} = -H_y^i \tag{2.19}$$

$$H_z^{-i} = H_z^i \tag{2.20}$$

When dealing with lossless waveguides and modes that are propagating it is always possible to choose the vector mode patterns, $\vec{E}^i$ and $\vec{H}^i$, in such a way that the transversal components to the propagation direction E_x^i, E_y^i, H_x^i, and H_y^i are real, while the tangential components to that direction, E_z^i and H_z^i, become purely imaginary. Therefore, it can be easily demonstrated that the coupling coefficient between two propagating modes must be real. Additionally, the average power, P, carried by the propagating modes in the increasing z direction can be calculated as the time-averaged Poynting vector integrated over the cross section, i.e.:

$$P = \frac{1}{2} \cdot Re\left\{ \iint_{\check{S}} \left(\hat{\vec{E}} \times \hat{\vec{H}}^* \right) \cdot \hat{z} \cdot d\check{S} \right\} \tag{2.21}$$

Then, by applying in (2.21) the orthogonal mode decomposition of (2.1) and (2.2) with the definition of the normalization factor of (2.9) and (2.10), it is obtained that:

$$P = \sum_{i=-M}^{M} \frac{1}{2} \cdot |a_i|^2 \cdot N_i + \sum_{i=-Q}^{Q} \int_0^{k_0} \frac{1}{2} \cdot |a_i(k_t)|^2 \cdot N_i(k_t) \cdot dk_t = \sum_{i=-M}^{M} P_i + P_{rad} \tag{2.22}$$

where the summation is performed for all the propagating modes, i.e. the M discrete spectrum (or bounded) modes and the Q continuous spectrum modes, by taking into account their corresponding forward and backward travelling waves. In order to calculate the power flow in (2.22), the integral is calculated in the range $0 < k_t < k_0$, which determines the propagating continuous spectrum modes, because the values within $k_0 < k_t < \infty$ correspond to attenuating or evanescent modes that do not propagate power. Consequently, the total power carried by the waveguide in the increasing z direction is the result of the sum of the power of all forward travelling waves and the subtraction of the power carried by the backward travelling ones. It must be stressed that the normalization factors of (2.9), (2.10) satisfy the relationships (2.11), (2.12), and thus the power that flows in the decreasing z direction (corresponding to all the backward travelling waves) will be negative, something that means an opposite propagation direction from a physical point of view.

Therefore, the power carried by each i discrete spectrum mode can be calculated as:

$$P_i = \frac{1}{2} \cdot |a_i|^2 \cdot N_i \tag{2.23}$$

Although a single radiation mode does not have physical meaning, it can be understood as a mathematical tool that describes the radiation phenomenon in general open waveguides, being also a necessary part for the completeness and coherence of the Coupled-Mode Theory in open waveguides. The total radiated power is obtained as a summation of all the radiation modes that carry energy in the same direction of the open waveguide propagation axis [18]:

$$P_{rad} = \sum_{i=-Q}^{Q} \int_0^{k_0} \frac{1}{2} \cdot |a_i(k_t)|^2 \cdot N_i(k_t) \cdot dk_t \tag{2.24}$$

Due to the interference between the fields of different radiated modes, the continuity of modes represented by the integral (2.24) satisfies the expected behavior for the total radiated field.

In addition to the power, other quantities can be directly measured like the amplitude and phase of the waves at certain points of special interest also known as ports. In fact, these physical

magnitudes determine the so-called scattering parameters [25], [26] which are widely employed in microwave engineering to characterize the frequency response of a general waveguide component. These scattering, $S-$, parameters properly ordered conform the scattering matrix [29], which is defined for the case of a structure with X ports as in (2.25), where all m and i modes are considered.

$$[b_{l,m}(f)] = [S_{lk,mi}(f)] \cdot [a_{k,i}(f)] \tag{2.25}$$

where f is the frequency and the l, k variables stand for the port numeration from 1 to X. Considering that nomenclature, $b_{l,m}$ is defined as the amplitude of the m mode wave that flows outwards the waveguide structure at the l port, while $a_{k,i}$ is the corresponding amplitude of the i mode wave that flows towards the waveguide structure at the k port. Regarding the scattering parameters, $S_{lk,mi}$, they can be understood as the amplitude of the m mode wave that flows outwards the l port when the waveguide is excited by means of the i mode wave that flows into the structure at the k port, while other incoming waves from different ports or modes are forbidden. This last condition implies that all ports different to k are terminated with a matched load for all modes, and that the k port is assumed to be matched for modes different to i, something that can be mathematically written as follows:

$$S_{lk,mi} = \left.\frac{b_{l,m}}{a_{k,i}}\right|_{a_{r,s}=0\ \forall\, r\neq k, \forall s\neq i} \tag{2.26}$$

It is worth noting that in (2.25), the amplitudes $b_{l,m}$ and $a_{k,i}$ actually depend on the frequency, f, and hence, the scattering parameters $S_{lk,mi}$ are also a function of f.

Then, for the specific case of a two-port waveguide structure ($X = 2$) that is under study in this chapter, the corresponding scattering matrix is:

$$\begin{bmatrix} b_{1,1} \\ b_{1,2} \\ \cdots \\ b_{1,m} \\ \cdots \\ b_{2,1} \\ b_{2,2} \\ \cdots \\ b_{2,m} \\ \cdots \end{bmatrix} = \begin{bmatrix} S_{11,11} & S_{11,12} & \cdots & S_{11,1i} & \cdots & S_{12,11} & S_{12,12} & \cdots & S_{11,1i} & \cdots \\ S_{11,21} & S_{11,22} & \cdots & S_{11,2i} & \cdots & S_{12,21} & S_{12,22} & \cdots & S_{12,2i} & \cdots \\ \cdots & \cdots & \cdots & \cdots & \cdots & \cdots & \cdots & \cdots & \cdots & \cdots \\ S_{11,m1} & S_{11,m2} & \cdots & S_{11,mi} & \cdots & S_{12,m1} & S_{12,m2} & \cdots & S_{12,mi} & \cdots \\ \cdots & \cdots & \cdots & \cdots & \cdots & \cdots & \cdots & \cdots & \cdots & \cdots \\ S_{21,11} & S_{21,12} & \cdots & S_{21,1i} & \cdots & S_{22,11} & S_{22,12} & \cdots & S_{22,1i} & \cdots \\ S_{21,21} & S_{21,22} & \cdots & S_{21,2i} & \cdots & S_{22,21} & S_{22,22} & \cdots & S_{22,2i} & \cdots \\ \cdots & \cdots & \cdots & \cdots & \cdots & \cdots & \cdots & \cdots & \cdots & \cdots \\ S_{21,m1} & S_{21,m2} & \cdots & S_{21,mi} & \cdots & S_{22,m1} & S_{22,m2} & \cdots & S_{22,mi} & \cdots \\ \cdots & \cdots & \cdots & \cdots & \cdots & \cdots & \cdots & \cdots & \cdots & \cdots \end{bmatrix} \cdot \begin{bmatrix} a_{1,1} \\ a_{1,2} \\ \cdots \\ a_{1,i} \\ \cdots \\ a_{2,1} \\ a_{2,2} \\ \cdots \\ a_{2,i} \\ \cdots \end{bmatrix} \tag{2.27}$$

In view of (2.27), and considering the definitions of the complex amplitude of a mode of (2.1), (2.2), as well as the normalization factor of (2.9) and (2.10), the definition of the scattering parameters of (2.26) can be alternatively written as:

$$S_{11,mi}(f) = \left.\frac{b_{1,m}(f)}{a_{1,i}(f)}\right|_{a_{r,s}=0,\forall\, r=2,\forall s\neq i} = \left.\frac{\sqrt{N_{|m|}(z=0)}\cdot a_m^-(z=0,f)}{\sqrt{N_{|i|}(z=0)}\cdot a_i^+(z=0,f)}\right|_{\substack{a_s^+(z=0,f)=0,\forall\, s\neq i,\\ a_w^-(z=L,f)=0,\forall\, w}} \tag{2.28}$$

$$S_{21,mi}(f) = \left.\frac{b_{2,m}(f)}{a_{1,i}(f)}\right|_{a_{r,s}=0,\forall\, r\neq 2,\forall s\neq i} = \left.\frac{\sqrt{N_{|m|}(z=L)}\cdot a_m^+(z=L,f)}{\sqrt{N_{|i|}(z=0)}\cdot a_i^+(z=0,f)}\right|_{\substack{a_s^+(z=0,f)=0,\forall\, s\neq i,\\ a_w^-(z=L,f)=0,\forall\, w}} \tag{2.29}$$

$$S_{12,mi}(f) = \left.\frac{b_{1,m}(f)}{a_{2,i}(f)}\right|_{a_{r,s}=0,\forall\, r=1,\forall s\neq i} = \left.\frac{\sqrt{N_{|m|}(z=0)}\cdot a_m^-(z=0,f)}{\sqrt{N_{|i|}(z=L)}\cdot a_i^-(z=L,f)}\right|_{\substack{a_s^-(z=L,f)=0,\forall\, s\neq i,\\ a_w^+(z=0,f)=0,\forall\, w}} \tag{2.30}$$

$$S_{22,mi}(f) = \left.\frac{b_{2,m}(f)}{a_{2,i}(f)}\right|_{a_{r,s}=0,\forall\, r=1,\forall s\neq i} = \left.\frac{\sqrt{N_{m}(z=L)}\cdot a_m^+(z=L,f)}{\sqrt{N_{|i|}(z=L)}\cdot a_i^-(z=L,f)}\right|_{\substack{a_s^-(z=L,f)=0,\forall\, s\neq i,\\ a_w^+(z=0,f)=0,\forall\, w}} \tag{2.31}$$

being a_m^-, the complex amplitude of a wave that propagates in the decreasing z direction, i.e. a_m with $m<0$; and a_m^+, that amplitude but for the case of a wave that propagates in the increasing z direction, or in other words, a_m with $m>0$. Furthermore, port 1 is assumed to be placed at the beginning of the waveguide structure ($z=0$), while port 2 is located at its end, i.e. at $z=L$, being L the length of the structure.

It must be stressed that the scattering parameters of (2.27) and (2.28)-(2.31) allow us to obtain the total amplitude of a specific wave that leaves the waveguide structure from a particular port as a sum of the contributions that come from both ports and each mode:

$$b_{1,m} = \sum_i \sum_k S_{1k,mi}\cdot a_{k,i} \tag{2.32}$$

$$b_{2,m} = \sum_i \sum_k S_{2k,mi}\cdot a_{k,i} \tag{2.33}$$

Finally, the key conclusion of this subsection is the implicit relationship that has been shown between the coupling coefficients and the frequency response of the waveguide structure, which is mathematically represented by means of the scattering parameters. The coupling coefficients of (2.5)-(2.8), C_{mi}, $C_{mi}^{c}(k_t)$, $C_{ni}^{c}(\widetilde{k}_t)$ and $C_{mi}^{cc}(\widetilde{k}_t,k_t)$, determine the complex

amplitudes of each mode along the whole nonuniform waveguide structure through the coupled mode equations of (2.3) and (2.4), being the scattering parameters defined in (2.28)-(2.31) special quotients between those wave amplitudes at specific points of the z axis. This important relationship will be greatly simplified and mathematically specified just by introducing several reasonable approximations that will lead to single-mode operation. Moreover, as it will be thoroughly detailed in CHAPTER 4, if additional assumptions are taken, it will be possible to calculate the coupling coefficient from a single scattering parameter, which is the aim of the inverse scattering synthesis techniques.

2.1.2. Relationship between the Coupling Coefficient and the Physical Dimensions of the Waveguide

Once an interesting relationship has been found between the coupling coefficients and the frequency response of a general nonuniform waveguide, some of the expressions previously provided will be employed to relate the coupling coefficient with the physical dimensions of the structure. For doing so, the procedure fully detailed in [18] is followed, and the expressions (2.5)-(2.8) valid for waveguides that include conductors with variable cross section are rewritten as:

$$C_{mi} = \frac{-\pi \cdot f \cdot \oint \nu \cdot \left[\mu_0 \cdot \left(H_z^m \cdot H_z^i - H_t^m \cdot H_t^i\right) + \varepsilon \cdot E_n^m \cdot E_n^i\right] \cdot dt}{N_m \cdot (\beta_m - \beta_i)} \tag{2.34}$$

$$C_{mi}^c(k_t) = \frac{-\pi \cdot f \cdot \oint \nu \cdot \left\{\mu_0 \cdot \left[H_z^m \cdot H_z^i(k_t) - H_t^m \cdot H_t^i(k_t)\right] + \varepsilon \cdot E_n^m \cdot E_n^i(k_t)\right\} \cdot dt}{N_m \cdot [\beta_m - \beta_i(k_t)]} \tag{2.35}$$

$$C_{ni}^c(\widetilde{k_t}) = \frac{-\pi \cdot f \cdot \oint \nu \cdot \left\{\mu_0 \cdot \left[H_z^n(\widetilde{k_t}) \cdot H_z^i - H_t^n(\widetilde{k_t}) \cdot H_t^i\right] + \varepsilon \cdot E_n^n(\widetilde{k_t}) \cdot E_n^i\right\} \cdot dt}{N_n^c \cdot \left[\beta_n^c(\widetilde{k_t}) - \beta_i\right]} \tag{2.36}$$

$$C_{ni}^c(\widetilde{k_t}, k_t) = \frac{-\pi \cdot f}{N_n^c \cdot \left[\beta_n^c(\widetilde{k_t}) - \beta_i^c(k_t)\right]} \cdot \cdot \frac{\oint \nu \cdot \left\{\mu_0 \cdot \left[H_z^n(\widetilde{k_t}) \cdot H_z^i(k_t) - H_t^n(\widetilde{k_t}) \cdot H_t^i(k_t)\right] + \varepsilon \cdot E_n^n(\widetilde{k_t}) \cdot E_n^i(k_t)\right\} \cdot dt}{N_n^c \cdot \left[\beta_n^c(\widetilde{k_t}) - \beta_i^c(k_t)\right]} \tag{2.37}$$

where the t, n, z subscripts of E and H stand for the electric and magnetic field components that follow those directions; being t, the tangential direction to the conducting contour in the cross section and n, the normal direction to that contour in the same cross section. In fact, the edge of the conducting wall that defines the cross section conforms the path where the closed-curve integrals of (2.34)-(2.37) must be performed. It must be noted that the t, n, z directions make up an orthogonal coordinate system as it is represented in Fig. 2.1 for the sake of clarity. The unitary vectors $\hat{z}, \hat{t}, \hat{n}$ that correspond to the z, t, n, directions respectively are defined in the following manner: $\hat{z}$ is parallel to the propagation direction, z, and follows the direction of the forward travelling waves; $\hat{t}$ is the unitary vector of t and follows the direction contained in the cross section that is tangential to the interface between dielectric and metal; $\hat{n}$ is the unitary vector of n and follows the direction contained in the cross section, which is orthogonal to that interface, directed from the dielectric to the metal. These unitary vectors must satisfy $\hat{z} = \hat{n} \times \hat{t}$. Finally, $\nu = \tan(\alpha)$, with α being the angle defined from $\hat{z}$ to the line tangential to the metal-dielectric interface and orthogonal to the cross section metal-dielectric interface, as depicted in Fig. 2.1c.

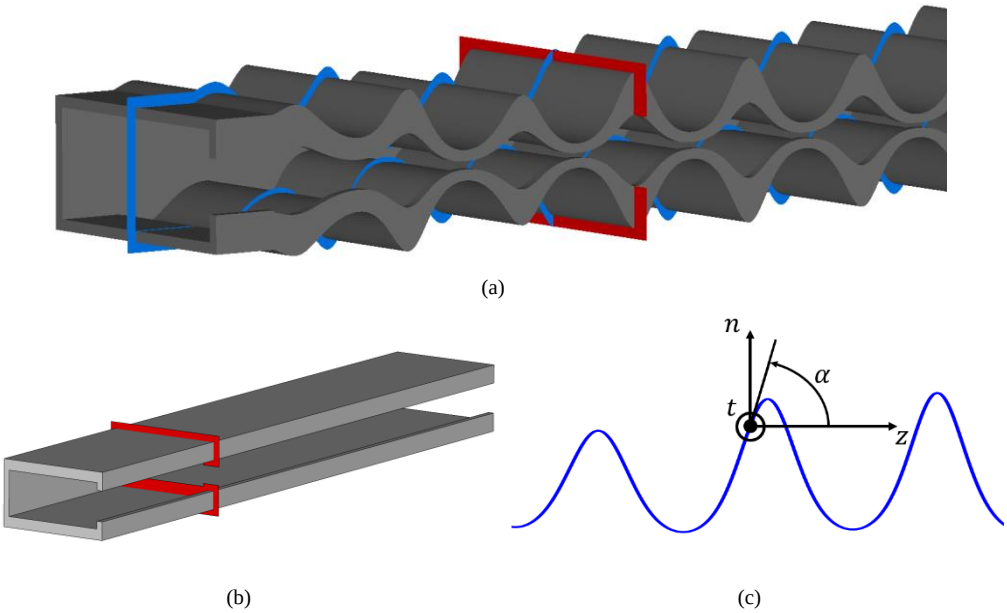

(a)

(b) (c)

Fig. 2.1. Sketch of a general nonuniform waveguide. An arbitrary cross section (red trace) is selected and the line tangential to the metal-dielectric interface is highlighted (blue trace) for the case of the upper and lower interfaces. (b) Auxiliary uniform waveguide associated to the cross-section selected. (c) The local z, t, n coordinate system is given for the upper metal-dielectric interface of (a) and a scheme of the angle α defined in that case between the z-axis and the line tangential to that interface (blue line) is provided as well.

Moreover, the coupling coefficients of (2.34)-(2.37) satisfy the set of properties (2.38)-(2.41) that were demonstrated in [18]:

$$C_{mm} = \frac{-1}{2 \cdot N_m} \cdot \frac{dN_m}{dz} \tag{2.38}$$

$$C_{mm}^{cc}(\tilde{k}_t, \tilde{k}_t) = \frac{-1}{2 \cdot N_m(\tilde{k}_t)} \cdot \frac{dN_m(\tilde{k}_t)}{dz} \cdot \delta(0) \tag{2.39}$$

$$C_{mi} \cdot N_m = -C_{im} \cdot N_i \quad ; \quad m \neq i \tag{2.40}$$

$$C_{mi} = C_{-m,-i} \tag{2.41}$$

Lastly, it is important to stress that the expressions (2.34)-(2.37) relate the coupling coefficient and the physical dimensions of the waveguide, since the different E and H field components are inherent to the modes that may propagate in the auxiliary uniform waveguide. Indeed, the geometrical shape and the dimensions of the nonuniform waveguide may vary in the z direction and the auxiliary uniform waveguide to be studied would be different, leading to different relevant modes in z as well. Hence, the equations (2.34)-(2.37) can be applied to a wide variety of waveguide technologies, from the ones that feature closed metallic boundaries, like the rectangular and circular waveguides, to planar transmission lines such as stripline or microstrip, among others. Indeed, specific expressions for rectangular waveguide technology will be developed in the following subsection, while a closed-form relationship between the coupling coefficient and the characteristic impedance will be provided in subsection 2.2.1.2 for the case of TEM and QTEM transmission lines when single-mode operation is assumed. In this last case, the final physical parameters will depend on the particular relationship between the characteristic impedance and the physical dimensions of the line for each technology. However, straightforward expressions that will not be covered in this thesis can be found for other waveguides [18]-[21].

2.1.2.1. Explicit Expressions for the Coupling Coefficients in Rectangular Waveguide

The rectangular waveguide is one of the most popular waveguide technologies since it features high power handling capability and low dissipative losses when it is compared to other

technologies like the planar ones [29]. These aspects are particularly relevant for satellite communications and they make the rectangular waveguide one of the most employed technologies in the aerospace communications sector. Moreover, its electromagnetic behavior has been thoroughly studied in the classical literature as it is one of earliest technologies employed to carry and process microwave and millimeter wave signals [27]-[31].

The geometry of the rectangular waveguide is quite simple since it can be considered just as a hollow metallic pipe that features a rectangular cross section, which is defined by a width, a, and a height, b. Due to the fact that a nonuniform waveguide is being considered, the width and the height will be consequently z-dependent, i.e. $a(z)$ and $b(z)$, respectively. A sketch of a nonuniform rectangular waveguide is provided in Fig 2.2, where the classical x, y, z spatial coordinate system is also provided.

In order to obtain closed-form expressions for the coupling coefficients of a nonuniform rectangular waveguide as a function of its physical parameters, a first reasonable assumption is going to be made by considering the most common case of a homogeneous and isotropic dielectric inner medium. Thus, the dielectric will be characterized by an electrical permittivity, $\varepsilon = \varepsilon_0 \cdot \varepsilon_r$, and a magnetic permeability, $\mu = \mu_0$, where: $\varepsilon_0 = 8.854 \cdot 10^{-12}$ F/m, is the electrical permittivity of vacuum; ε_r, stands for the relative electrical permittivity of the dielectric; and $\mu_0 = 4 \cdot \pi \cdot 10^{-7}$ H/m expresses the magnetic permeability of vacuum.

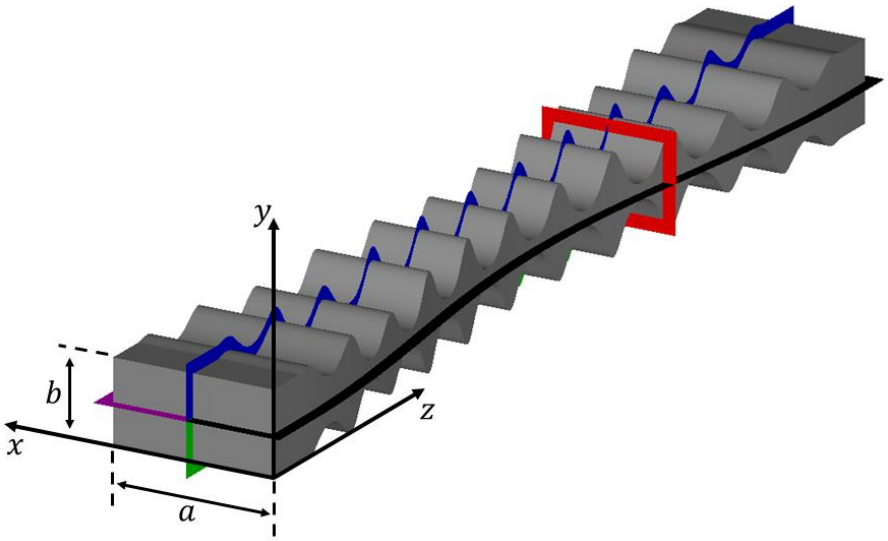

Fig. 2.2. Sketch of a general nonuniform rectangular waveguide. An arbitrary cross section (red shape) is selected and the lines tangential to the metal-dielectric interfaces are highlighted in blue, green, black and magenta for each of the four metallic walls.

Moreover, it must be stressed that a metallic closed-boundary waveguide is under study and only discrete spectrum modes must be taken into account as a result, because the continuous (or radiated) ones are forbidden. By doing so, the mode decomposition of (2.1), (2.2) can be reduced to:

$$\hat{\vec{E}}(x,y,z) = \sum_i a_i(z) \cdot \vec{E}^i(x,y,z) \tag{2.42}$$

$$\hat{\vec{H}}(x,y,z) = \sum_i a_i(z) \cdot \vec{H}^i(x,y,z) \tag{2.43}$$

As it is well known, the modes able to propagate in a rectangular waveguide are classified into two categories [27]-[31]: the so-called transverse electric (TE) modes, that satisfy a null component of the electric field in the propagation direction, $E_z = 0$; and the transverse magnetic (TM) modes that fulfill that null component but for the magnetic field, $H_z = 0$.

Therefore, the system of coupled-mode equations (2.3), (2.4) can be rewritten by only considering the discrete spectrum modes:

$$\frac{da_m}{dz} + j \cdot \beta_m \cdot a_m = \sum_i a_i \cdot C_{mi} \tag{2.44}$$

where β_m is the phase constant of the m mode in the auxiliary uniform waveguide associated with the cross section of interest, which can be determined as follows:

$$\beta_m = -\beta_{-m} = \sqrt{k^2 - k_{cm}^2} \tag{2.45}$$

being k, the plane-wave wavenumber [27]-[31] that can be obtained by means of:

$$k = \frac{2 \cdot \pi \cdot f}{c_0} \cdot \sqrt{\varepsilon_r} = \frac{2 \cdot \pi \cdot f}{c} \tag{2.46}$$

where c_0 stands for the speed of light in vacuum that can be expressed as function of the electric permittivity and the magnetic permeability of vacuum:

$$c_0 = \frac{1}{\sqrt{\mu_0 \cdot \varepsilon_0}} = 299792458 \frac{m}{s} \tag{2.47}$$

Consequently, the speed of light in a medium with relative electric permittivity, ε_r, which is alternatively employed in (2.46) is going to be denoted by c, and calculated as:

$$c = \frac{c_0}{\sqrt{\varepsilon_r}} \tag{2.48}$$

Regarding the variable k_{cm} that can be found in the phase constant expression of (2.45), it is known as the cut-off wavenumber of the m mode [29], and it depends on the width, a, and height, b, of the cross section of interest in the following manner:

$$k_{cm} = \sqrt{\left(\frac{\pi \cdot p_m}{a}\right)^2 + \left(\frac{\pi \cdot q_m}{b}\right)^2} \tag{2.49}$$

where p_m and q_m are the modal indexes ($TE_{p_m q_m}$, $TM_{p_m q_m}$). For TE modes the values of these modal indexes may be $p_m = 0,1,2,\ldots$; and $q_m = 0,1,2,\ldots$, although the simultaneous combination $p_m = q_m = 0$ is forbidden; while $p_m = 1,2,3,\ldots$ and $q_m = 1,2,3,\ldots$ are allowed for the TM case. The cut-off wavenumber allows to determine the cut-off frequency of the m mode, f_{cm}, which is the frequency from which the wave can propagate into the auxiliary uniform waveguide associated with the cross section under study. It is important to note that if the operation frequency of the m mode is below that cut-off frequency, the wave will be under the cut-off regime and will not propagate. The calculation of f_{cm} can be performed by means of [27]-[31]:

$$f_{cm} = \frac{c}{2} \cdot \sqrt{\left(\frac{p_m}{a}\right)^2 + \left(\frac{q_m}{b}\right)^2} \tag{2.50}$$

The expressions for the x, y, z components of the electric and magnetic fields for both TE and TM modes in a uniform rectangular waveguide is a topic that has been widely covered in the microwave engineering literature [27]-[31]. Nonetheless, in order to work with normalized fields, a modified version of the expressions available in reference [32] will be employed. The x, y, z components of $\vec{E}^{\pm m}$ and $\vec{H}^{\pm m}$ for the case of the m TE mode ($TE_{p_m q_m}$) are provided below in (2.51)-(2.56), with $m > 0$; where the choice of the upper sign (+) in the superscripts stands for the forward travelling wave, while the lower (-) describes the backward travelling wave.

$$E_x^{\pm m} = \frac{-\pi \cdot r_m \cdot q_m \cdot \sqrt{2 \cdot \pi \cdot f \cdot \mu_0 \cdot N_m}}{b \cdot k_{cm} \cdot \sqrt{a \cdot b \cdot \beta_m}} \cdot \cos\left(\frac{p_m \cdot \pi}{a} \cdot x\right) \cdot \sin\left(\frac{q_m \cdot \pi}{b} \cdot y\right) \tag{2.51}$$

$$E_y^{\pm m} = \frac{\pi \cdot r_m \cdot p_m \cdot \sqrt{2 \cdot \pi \cdot f \cdot \mu_0 \cdot N_m}}{a \cdot k_{cm} \cdot \sqrt{a \cdot b \cdot \beta_m}} \cdot \sin\left(\frac{p_m \cdot \pi}{a} \cdot x\right) \cdot \cos\left(\frac{q_m \cdot \pi}{b} \cdot y\right) \tag{2.52}$$

$$E_z^{\pm m} = 0 \tag{2.53}$$

$$H_x^{\pm m} = \frac{\mp r_m \cdot p_m \cdot \sqrt{\pi \cdot \beta_m \cdot N_m}}{a \cdot k_{cm} \cdot \sqrt{2 \cdot f \cdot a \cdot b \cdot \mu_0}} \cdot \sin\left(\frac{p_m \cdot \pi}{a} \cdot x\right) \cdot \cos\left(\frac{q_m \cdot \pi}{b} \cdot y\right) \tag{2.54}$$

$$H_y^{\pm m} = \frac{\mp r_m \cdot q_m \cdot \sqrt{\pi \cdot \beta_m \cdot N_m}}{b \cdot k_{cm} \cdot \sqrt{2 \cdot f \cdot a \cdot b \cdot \mu_0}} \cdot \cos\left(\frac{p_m \cdot \pi}{a} \cdot x\right) \cdot \sin\left(\frac{q_m \cdot \pi}{b} \cdot y\right) \tag{2.55}$$

$$H_z^{\pm m} = \frac{j \cdot r_m \cdot k_{cm} \cdot \sqrt{N_m}}{\sqrt{2 \cdot \pi \cdot f \cdot a \cdot b \cdot \beta_m \cdot \mu_0}} \cdot \cos\left(\frac{p_m \cdot \pi \cdot x}{a}\right) \cdot \cos\left(\frac{q_m \cdot \pi \cdot y}{b}\right) \tag{2.56}$$

The normalization factor, N_m, in (2.51)-(2.56) is calculated using (2.9) over the surface $\check{S}$ highlighted in Fig. 2.3a, whereas the value of the parameter r_m depends on the modal indexes as follows:

$$r_m = \begin{cases} \sqrt{2} & \text{for } p_m = 0 \text{ or } q_m = 0 \\ 2 & \text{otherwise} \end{cases} \tag{2.57}$$

Regarding the x, y, z components of $\vec{E}^{\pm m}$ and $\vec{H}^{\pm m}$ for the m TM mode ($TM_{p_m q_m}$), their respective expressions are provided below in (2.58)-(2.63).

$$E_x^{\pm m} = \frac{p_m \cdot \sqrt{2 \cdot \pi \cdot \beta_m \cdot N_m}}{a \cdot k_{cm} \cdot \sqrt{f \cdot a \cdot b \cdot \varepsilon}} \cdot \cos\left(\frac{p_m \cdot \pi}{a} \cdot x\right) \cdot \sin\left(\frac{q_m \cdot \pi}{b} \cdot y\right) \tag{2.58}$$

$$E_y^{\pm m} = \frac{q_m \cdot \sqrt{2 \cdot \pi \cdot \beta_m \cdot N_m}}{b \cdot k_{cm} \cdot \sqrt{f \cdot a \cdot b \cdot \varepsilon}} \cdot \sin\left(\frac{p_m \cdot \pi}{a} \cdot x\right) \cdot \cos\left(\frac{q_m \cdot \pi}{b} \cdot y\right) \tag{2.59}$$

$$E_z^{\pm m} = \frac{\pm j \cdot k_{cm} \cdot \sqrt{2 \cdot N_m}}{\sqrt{\pi \cdot f \cdot a \cdot b \cdot \beta_m \cdot \varepsilon}} \cdot \sin\left(\frac{p_m \cdot \pi}{a} \cdot x\right) \cdot \sin\left(\frac{q_m \cdot \pi}{b} \cdot y\right) \tag{2.60}$$

$$H_x^{\pm m} = \frac{\mp 2 \cdot \pi \cdot q_m \cdot \sqrt{2 \cdot \pi \cdot f \cdot \varepsilon \cdot N_m}}{b \cdot k_{cm} \cdot \sqrt{a \cdot b \cdot \beta_m}} \cdot \sin\left(\frac{p_m \cdot \pi}{a} \cdot x\right) \cdot \cos\left(\frac{q_m \cdot \pi}{b} \cdot y\right) \tag{2.61}$$

$$H_y^{\pm m} = \frac{\pm 2 \cdot \pi \cdot p_m \cdot \sqrt{2 \cdot \pi \cdot f \cdot \varepsilon \cdot N_m}}{a \cdot k_{cm} \cdot \sqrt{a \cdot b \cdot \beta_m}} \cdot \cos\left(\frac{p_m \cdot \pi}{a} \cdot x\right) \cdot \sin\left(\frac{q_m \cdot \pi}{b} \cdot y\right) \tag{2.62}$$

$$H_z^{\pm m} = 0 \tag{2.63}$$

It is important to realize that different signs can be selected in equations (2.54), (2.55), (2.60), (2.61), and (2.62). In these cases the upper sign stands for the upper field component superscript, i.e. $+m$ with $m > 0$ (forward travelling wave of the m mode), while the lower sign must be chosen for the lower field component superscript, corresponding to the backward travelling wave of the m mode, which is denoted by $-m$ with $m > 0$. It is worth noting that the field components given in (2.51)-(2.56) and (2.58)-(2.63) satisfy the general component sign convention for electric and magnetic fields that was already mentioned in (2.15)-(2.20).

Since the components of the electric and magnetic fields for the modes of the rectangular waveguide have been previously presented, the closed-form relationship between the coupling coefficient and the physical dimensions of the waveguide can be determined. For doing so, it must be reminded that only discrete spectrum modes are allowed for this kind of waveguide, so the general expression valid for the case under study that was given in (2.34) is going to employed as a starting point. This equation is provided again below for the sake of clarity:

$$C_{mi} = \frac{-\pi \cdot f \cdot \oint \nu \cdot \left[\mu_0 \cdot \left(H_z^m \cdot H_z^i - H_t^m \cdot H_t^i\right) + \varepsilon \cdot E_n^m \cdot E_n^i\right] \cdot dt}{N_m \cdot (\beta_m - \beta_i)} \tag{2.34}$$

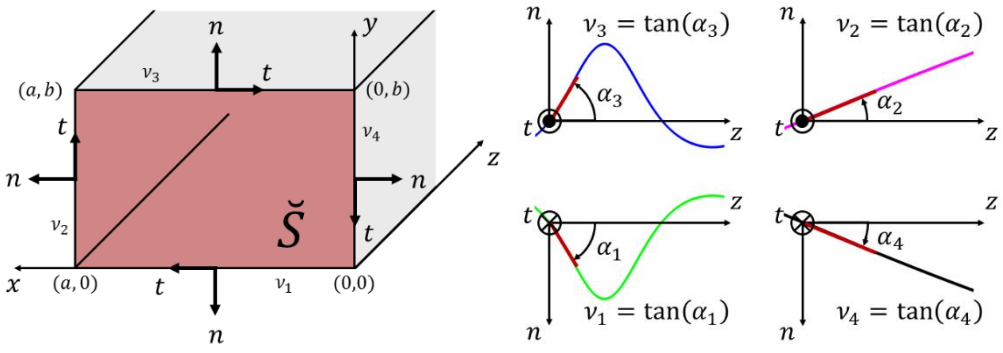

(a) (b)

Fig. 2.3. (a) Auxiliary uniform waveguide associated to the cross section selected in Fig. 2.1 and the correspondence between each local t, n and global x, y coordinate systems for the four metal-dielectric interfaces. (b) Detail of the angles α_1, α_2, α_3, α_4 that determine ν_1, ν_2, ν_3, ν_4, respectively, for each metal-dielectric interface of the cross section of Fig. 2.1.

As it has been already mentioned, the closed-curve integral of (2.34) must be performed following the t direction, which is tangential to the metallic-dielectric interface and is contained in the plane of the cross section of interest. If that broad definition is applied for the rectangular waveguide case, it will be possible to perform four different identities (one per each metal-dielectric interface) between the n, t and the x, y coordinate systems. Indeed, following the convention of Fig. 2.3a, $t = x$ and $n = -y$ for the lower interface ($y = 0$); $t = y$ and $n = x$ for the leftmost wall ($x = a$), $t = -x$ and $n = y$ for the upper interface ($y = b$); and $t = -y$ and $n = -x$ for the interface placed at the right part of the waveguide ($x = 0$).

Moreover, the general definition of the angle α, which determines ν in (2.34), can be applied to the rectangular cross section giving rise to four different angles α_1, α_2, α_3, and α_4, that yield to their corresponding tangents ν_1, ν_2, ν_3, and ν_4, as it is shown in Fig. 2.3b. It must be noted that in Fig. 2.3b, each one of these angles are related with each interface that was highlighted in Fig. 2.2, by following the same color code. Taking into account the ν_1, ν_2, ν_3, and ν_4 definitions, they can be also expressed by means of different derivatives as:

$$\nu_1 = -\frac{dy_d(z)}{dz} \tag{2.64}$$

$$\nu_2 = \frac{dx_l(z)}{dz} \tag{2.65}$$

$$\nu_3 = \frac{dy_u(z)}{dz} \tag{2.66}$$

$$\nu_4 = -\frac{dx_r(z)}{dz} \tag{2.67}$$

where $x_r(z)$, $x_l(z)$, $y_d(z)$, and $y_u(z)$ are the functions that describe the profile of the right, left, down and up metal-dielectric interfaces, respectively, according to the x, y, z general coordinate system of the nonuniform waveguide structure (see Fig. 2.2). It is worth noting that $x_r(z)$, $x_l(z)$, $y_d(z)$, and $y_u(z)$ are related with the width and height dimensions, $a(z)$ and $b(z)$, respectively, as follows:

$$a(z) = x_l(z) - x_r(z) \tag{2.68}$$

$$b(z) = y_u(z) - y_d(z) \tag{2.69}$$

Now, if the ν_1, ν_2, ν_3, and ν_4 variables, as well as the aforementioned identities between t, n and x, y, are applied in (2.34), a general coupling coefficient expression can be developed for rectangular waveguide technology:

$$C_{mi} = \frac{-\pi \cdot f}{2 \cdot N_m \cdot (\beta_m - \beta_i)} \cdot$$

$$\cdot \left[\int_0^a \nu_1 \cdot \left[\mu_0 \cdot H_z^m \cdot H_z^i - \mu_0 \cdot H_x^m \cdot H_x^i + \varepsilon \cdot \left(-E_y^m\right) \cdot \left(-E_y^i\right) \right] \Big|_{y=0} \cdot dx + \right.$$

$$+ \int_0^b \nu_2 \cdot \left[\mu_0 \cdot H_z^m \cdot H_z^i - \mu \cdot H_y^m \cdot H_y^i + \varepsilon \cdot E_x^m \cdot E_x^i \right] \Big|_{x=a} \cdot dy + \tag{2.70}$$

$$+ \int_0^a \nu_3 \cdot \left[\mu_0 \cdot H_z^m \cdot H_z^i - \mu \cdot \left(-H_x^m\right) \cdot \left(-H_x^i\right) + \varepsilon \cdot E_y^m \cdot E_y^i \right] \Big|_{y=b} \cdot dx +$$

$$\left. + \int_0^b \nu_4 \cdot \left[\mu_0 \cdot H_z^m \cdot H_z^i - \mu \cdot \left(-H_y^m\right) \cdot \left(-H_y^i\right) + \varepsilon \cdot \left(-E_x^m\right) \cdot \left(-E_x^i\right) \right] \Big|_{x=0} \cdot dy \right]$$

It is important to note that in this equation (2.70), and in the subsequent equations (2.71), (2.77), (2.78), (2.79), (2.80), the x, y coordinate system employed corresponds to the local coordinate system of the auxiliary uniform waveguide associated to the cross section of interest, see Fig. 2.3(a). This local coordinate system will be different from the global coordinate system employed for the nonuniform waveguide structure, see Fig. 2.2.

Nevertheless, the procedure to calculate the coupling coefficient between different modes (including their forward and backward travelling waves) can be greatly simplified by applying several properties of the coupling coefficient that have been already presented. Indeed, if a pair of coupling coefficients, $C_{m,+i}$ and $C_{m,-i}$ (or briefly, $C_{m,\pm i}$), with $m > 0$ and $i > 0$, is known, then $C_{-m,\mp i}$ will be directly solved using (2.41). Moreover, considering the sign conventions stated in (2.15)-(2.20) for the electric and magnetic field components, and in (2.13) for the phase constant of waves that propagate in opposite directions, equation (2.70) can be updated to calculate $C_{m,\pm i}$ (with $m > 0$ and $i > 0$) in the following manner:

$$C_{m,\pm i} = \frac{-\pi \cdot f}{2 \cdot N_m \cdot (\beta_m \mp \beta_i)} \cdot$$

$$\cdot \left[\int_0^a \nu_1 \cdot \left[\mu_0 \cdot H_z^m \cdot H_z^i \mp \mu_0 \cdot H_x^m \cdot H_x^i + \varepsilon \cdot \left(-E_y^m\right) \cdot \left(-E_y^i\right) \right] \Big|_{y=0} \cdot dx + \right.$$

$$+ \int_0^b \nu_2 \cdot \left[\mu_0 \cdot H_z^m \cdot H_z^i \mp \mu \cdot H_y^m \cdot H_y^i + \varepsilon \cdot E_x^m \cdot E_x^i \right] \Big|_{x=a} \cdot dy + \tag{2.71}$$

$$+ \int_0^a \nu_3 \cdot \left[\mu_0 \cdot H_z^m \cdot H_z^i \mp \mu \cdot \left(-H_x^m\right) \cdot \left(-H_x^i\right) + \varepsilon \cdot E_y^m \cdot E_y^i \right] \Big|_{y=b} \cdot dx +$$

$$\left. + \int_0^b \nu_4 \cdot \left[\mu_0 \cdot H_z^m \cdot H_z^i \mp \mu \cdot \left(-H_y^m\right) \cdot \left(-H_y^i\right) + \varepsilon \cdot \left(-E_x^m\right) \cdot \left(-E_x^i\right) \right] \Big|_{x=0} \cdot dy \right]$$

At this point, it is necessary to take into account that only TE and TM modes can be found in a rectangular waveguide and four different coupling coefficients should be calculated as a consequence, i.e. $C_{m,\pm i}^{TE-TE}$, when both, m and i, are TE modes; $C_{m,\pm i}^{TE-TM}$, in case of m being a TE and i belonging to the TM mode category; $C_{m,\pm i}^{TM-TE}$, when m is TM and i is TE; and finally $C_{m,\pm i}^{TM-TM}$ will be the coupling coefficient when two TM modes, m and i, are under consideration.

However, if (2.40) is applied for the $C_{m,\pm i}^{TM-TE}$ or $C_{m,\pm i}^{TE-TM}$ cases, the following relationships are obtained:

$$C_{m,\pm i}^{TM-TE} = \frac{-C_{\pm i,m}^{TE-TM} \cdot N_{\pm i}}{N_m} \tag{2.72}$$

$$C_{m,\pm i}^{TE-TM} = \frac{-C_{\pm i,m}^{TM-TE} \cdot N_{\pm i}}{N_m} \tag{2.73}$$

Therefore, only $C_{m,\pm i}^{TM-TE}$ or $C_{m,\pm i}^{TE-TM}$ needs to be directly calculated since the other one will be automatically attained by means of (2.72) or (2.73). For this reason, in the subsequent steps of this chapter, a closed-form equation will be obtained for the $C_{m,\pm i}^{TE-TM}$ case, being this arbitrary choice free of practical consequences.

Finally, the relevant components of the electric and magnetic fields of (2.51)-(2.56) and (2.58)-(2.63) for forward travelling waves ($m > 0$ and $i > 0$) are incorporated in (2.71). After several mathematical manipulations, the sought closed-form expressions will be achieved:

$$C_{m,\pm i}^{TE-TE} = \frac{r_m \cdot r_i \cdot k_{cm} \cdot k_{ci} \cdot \sqrt{N_i}}{2 \cdot \sqrt{N_m} \cdot (\beta_m \mp \beta_i) \cdot a \cdot b \cdot \sqrt{\beta_m} \cdot \sqrt{\beta_i}} \cdot$$
$$\cdot \left\{ \left[c_{p,a} + \frac{\pi^2 \cdot p_m \cdot p_i \cdot s_{p,a} \cdot (\pm\beta_m \cdot \beta_i - k^2)}{(a \cdot k_{cm} \cdot k_{ci})^2} \right] \cdot [\nu_1 + \nu_3 \cdot (-1)^{q_m + q_i}] + \right. \tag{2.74}$$
$$\left. + \left[c_{q,b} + \frac{\pi^2 \cdot q_m \cdot q_i \cdot s_{q,b} \cdot (\pm\beta_m \cdot \beta_i - k^2)}{(b \cdot k_{cm} \cdot k_{ci})^2} \right] \cdot [\nu_4 + \nu_2 \cdot (-1)^{p_m + p_i}] \right\}$$

$$C_{m,\pm i}^{TE-TM} = \frac{\pm\pi^2 \cdot r_m \cdot k \cdot \sqrt{N_i}}{\sqrt{N_m} \cdot (a \cdot b)^2 \cdot \sqrt{\beta_m} \cdot \sqrt{\beta_i} \cdot k_{cm} \cdot k_{ci}} \cdot$$
$$\{ p_m \cdot q_i \cdot s_{p,a} \cdot [\nu_1 + \nu_3 \cdot (-1)^{q_m + q_i}] + \tag{2.75}$$
$$- q_m \cdot p_i \cdot s_{q,b} \cdot [\nu_4 + \nu_2 \cdot (-1)^{p_m + p_i}] \}$$

$$C_{m,\pm i}^{TM-TM} = \frac{2 \cdot \pi^2 \cdot \sqrt{N_i} \cdot (\pm k^2 - \beta_m \cdot \beta_i)}{\sqrt{N_m} \cdot (\beta_m \mp \beta_i) \cdot (a \cdot b)^3 \cdot \sqrt{\beta_m} \cdot \sqrt{\beta_i} \cdot k_{cm} \cdot k_{ci}} \cdot$$
$$\{ [a^2 \cdot q_m \cdot q_i \cdot s_{p,a}] \cdot [\nu_1 + \nu_3 \cdot (-1)^{q_m + q_i}] + \tag{2.76}$$
$$+ [b^2 \cdot p_m \cdot p_i \cdot s_{q,b}] \cdot [\nu_4 + \nu_2 \cdot (-1)^{p_m + p_i}] \}$$

where it is assumed that $m > 0$ and $i > 0$ ($C_{-m,\mp i}$ can be immediately calculated using (2.41)), and the auxiliary parameters $c_{p,a}$, $s_{p,a}$, $c_{q,b}$, and $s_{q,b}$, are the result of several trigonometric integrals that depend on the particular combination of modal indexes involved, i.e. p_m, p_i, q_m, and q_i. The explicit integrals of $c_{p,a}$, $s_{p,a}$, $c_{q,b}$, and $s_{q,b}$, as well as their corresponding results are provided below:

$$c_{p,a} = \int_0^a \cos\left(p_m \cdot \pi \cdot \frac{x}{a}\right) \cdot \cos\left(p_i \cdot \pi \cdot \frac{x}{a}\right) \cdot dx = \begin{cases} a \text{ for } p_m = p_i = 0 \\ \frac{a}{2} \text{ for } p_m = p_i \neq 0 \\ 0 \text{ otherwise} \end{cases} \tag{2.77}$$

$$s_{p,a} = \int_0^a \sin\left(p_m \cdot \pi \cdot \frac{x}{a}\right) \cdot \sin\left(p_i \cdot \pi \cdot \frac{x}{a}\right) \cdot dx = \begin{cases} \frac{a}{2} \text{ for } p_m = p_i \neq 0 \\ 0 \text{ otherwise} \end{cases} \tag{2.78}$$

$$c_{q,b} = \int_0^b \cos\left(q_m \cdot \pi \cdot \frac{y}{b}\right) \cdot \cos\left(q_i \cdot \pi \cdot \frac{y}{b}\right) \cdot dy = \begin{cases} b \text{ for } q_m = q_i = 0 \\ \frac{b}{2} \text{ for } q_m = q_i \neq 0 \\ 0 \text{ otherwise} \end{cases} \tag{2.79}$$

$$s_{q,b} = \int_0^b \sin\left(q_m \cdot \pi \cdot \frac{y}{b}\right) \cdot \sin\left(q_i \cdot \pi \cdot \frac{y}{b}\right) \cdot dy = \begin{cases} \frac{b}{2} \text{ for } q_m = q_i \neq 0 \\ 0 \text{ otherwise} \end{cases} \tag{2.80}$$

If the attained expressions of (2.74)-(2.76) for the calculation of $C_{m,\pm i}^{TE-TE}$, $C_{m,\pm i}^{TE-TM}$, and $C_{m,\pm i}^{TM-TM}$, are carefully inspected, taking also into consideration the parameters $c_{p,a}$, $s_{p,a}$, $c_{q,b}$, and $s_{q,b}$, of (2.77)-(2.80), it is clear that only certain modes can be coupled between each other, i.e. $C_{m,i} \neq 0$, depending on the value of p_m, p_i, q_m, q_i, and on the specific geometry of the nonuniform rectangular waveguide through the v_1, v_2, v_3, v_4 variables defined in (2.64)-(2.67).

It must be highlighted that in the most frequent situation that will be applicable for the cases that will be addressed in this thesis, the rectangular waveguide is excited with the first mode that reaches the propagation regime, which is the fundamental TE_{10} ($p_m = 1$, $q_m = 0$) mode. Accordingly, it is worth to perform a deep assessment of the different modes that can couple energy to (or receive that energy from) the TE_{10} mode, depending on the type of perturbation of the rectangular waveguide. Indeed, the most useful classification of the waveguide profile variations for this purpose is based on the presence of symmetries between metallic walls that are parallel to each other. The different relationships that can be found following this criterion are summarized below in terms of derivatives of $x_r(z)$, $x_l(z)$, $y_d(z)$, $y_u(z)$ and their corresponding identities in v_1, v_2, v_3, v_4 for the sake of clarity:

$$\frac{x_r(z)}{dz} \neq \left|\frac{x_l(z)}{dz}\right| \; \forall\, z \Leftrightarrow v_2 \neq |v_4| \; \forall\, z \tag{2.81}$$

$$\frac{x_r(z)}{dz} = \frac{x_l(z)}{dz} \neq 0 \Leftrightarrow v_2 = -v_4 \neq 0 \; \forall\, z \tag{2.82}$$

$$\frac{x_r(z)}{dz} = -\frac{x_l(z)}{dz} \neq 0 \Leftrightarrow v_2 = v_4 \neq 0 \; \forall\, z \tag{2.83}$$

$$\frac{x_r(z)}{dz} = \frac{x_l(z)}{dz} = 0 \; \forall\, z \Leftrightarrow v_2 = v_4 = 0 \; \forall\, z \tag{2.84}$$

$$\frac{y_d(z)}{dz} \neq \left|\frac{y_u(z)}{dz}\right| \; \forall\, z \Leftrightarrow \nu_1 \neq |\nu_3| \; \forall\, z \tag{2.85}$$

$$\frac{y_d(z)}{dz} = \frac{y_u(z)}{dz} \neq 0 \forall\, z \Leftrightarrow \nu_1 = -\nu_3 \neq 0 \; \forall\, z \tag{2.86}$$

$$\frac{y_d(z)}{dz} = -\frac{y_u(z)}{dz} \neq 0 \; \forall\, z \Leftrightarrow \nu_1 = \nu_3 \neq 0 \; \forall\, z \tag{2.87}$$

$$\frac{y_d(z)}{dz} = \frac{y_u(z)}{dz} = 0 \; \forall\, z \Leftrightarrow \nu_1 = \nu_3 = 0 \; \forall\, z \tag{2.88}$$

Now, it will be assumed that the excitation is carried out with the forward travelling wave of the TE_{10} mode ($p_m = 1, q_m = 0$) for the different symmetry conditions of (2.81)-(2.88) so as to find the different values of p_i and q_i that lead to $C_{m,\pm i} \neq 0$ by means of (2.74)-(2.76). The obtained modes constitute the set of modes that have direct coupling with the TE_{10} forward travelling wave, and they are summarized in Table 2.1. If the waveguide profile varies in its width as well as in its height, the modes that will be directly coupled to the TE_{10} will be the combination of the modes that are coupled due to each symmetry condition.

	TE		**TM**	
	$\boldsymbol{p_i}$	$\boldsymbol{q_i}$	$\boldsymbol{p_i}$	$\boldsymbol{q_i}$
$\boldsymbol{\nu_1 \neq \lvert\nu_3\rvert}$	1	0, 1, 2, …	1	1, 2, 3, …
$\boldsymbol{\nu_1 = -\nu_3}$	1	1, 3, 5, …	1	1, 3, 5, …
$\boldsymbol{\nu_1 = \nu_3}$	1	0, 2, 4, …	1	2, 4, 6, …
$\boldsymbol{\nu_1 = \nu_3 = 0}$	-	-	-	-
$\boldsymbol{\nu_2 \neq \lvert\nu_4\rvert}$	1, 2, 3, …	0	-	-
$\boldsymbol{\nu_2 = -\nu_4}$	2, 4, 6, …	0	-	-
$\boldsymbol{\nu_2 = \nu_4}$	1, 3, 5, …	0	-	-
$\boldsymbol{\nu_2 = \nu_4 = 0}$	-	-	-	-

Table 2.1. Modal indexes, p_i and q_i, of the TE and TM modes that are directly coupled with the forward travelling TE10 mode ($p_m = 1$, $q_m = 0$) considering different symmetry relations of the pairs ν_2, ν_4 and ν_1, ν_3. The combination for TE mode with $p_i = 1$ and $q_i = 0$ means that the power is coupled to the backward travelling wave of the TE10 mode.

It is worth noting that in those rectangular waveguide structures where the variations in height and width are symmetrical, i.e. $\nu_1 = \nu_3$ and $\nu_2 = \nu_4$, respectively, it will be verified that $\nu_1 = \nu_3 = \frac{1}{2} \cdot \frac{db(z)}{dz}$ and $\nu_2 = \nu_4 = \frac{1}{2} \cdot \frac{da(z)}{dz}$ according to (2.64)-(2.67), (2.68), and (2.69). In this situation, the coupling coefficient between two modes m and i, $C_{m,i}$ (see (2.74)-(2.76) and (2.77)-(2.80)), will not be equal to zero only if one of the indexes of a mode is the same as the corresponding index of the other mode, and the other pair of indexes is of the same parity. Thus, except for the case of the forward and backward travelling waves of the same mode ($m = -i$) in

which the coupling coefficient has contributions of both $\nu_2 = \nu_4 = \frac{1}{2} \cdot \frac{da(z)}{dz}$ and $\nu_1 = \nu_3 = \frac{1}{2} \cdot \frac{db(z)}{dz}$ (see (2.74)-(2.76)), the coupling coefficient will be proportional to $\nu_2 = \nu_4 = \frac{1}{2} \cdot \frac{da(z)}{dz}$ if $q_m = q_i$ and $p_m + p_i$ is an even number. On the other hand, if $p_m = p_i$ and $q_m + q_i$ is an even number, then the coupling coefficient will be proportional to $\nu_1 = \nu_3 = \frac{1}{2} \cdot \frac{db(z)}{dz}$. Hence, if $|m| \neq |i|$, in the coupling coefficient expressions of (2.74)-(2.76) we should calculate either only the term proportional to $\frac{da(z)}{dz}$ (if $q_m = q_i$ and $p_m + p_i$ is an even number) or only the term proportional to $\frac{db(z)}{dz}$ (if $p_m = p_i$ and $q_m + q_i$ is an even number). For example, if the forward travelling wave of the TE_{10} mode is incident ($p_m = 1$, $q_m = 0$), the odd order waves TE_{30}, TE_{50}, …, are excited in both directions with an amplitude of the coupling coefficient proportional to $\nu_2 = \nu_4 = \frac{1}{2} \cdot \frac{da(z)}{dz}$. On the other hand, the mode pairs TE_{12}-TM_{12}, TE_{14}-TM_{14}, …, are also excited in both directions with the amplitudes of the coupling coefficients proportional to $\nu_1 = \nu_3 = \frac{1}{2} \cdot \frac{db(z)}{dz}$. Finally, the backward travelling wave of the TE_{10} mode is excited with a coupling coefficient that depends on the terms associated with both $\nu_2 = \nu_4 = \frac{1}{2} \cdot \frac{da(z)}{dz}$ and $\nu_1 = \nu_3 = \frac{1}{2} \cdot \frac{db(z)}{dz}$, see [21].

Nonetheless, it must be stressed that the modes of Table 2.1 may likewise couple power to other modes that do not have direct coupling with the TE_{10}. The study of these indirect links between the TE_{10} and other modes may be a complex and time-consuming task when different combinations of symmetry conditions for all ν_1, ν_2, ν_3, and ν_4 variables are considered. The Table 2.2 and Table 2.3 summarize the p_i and q_i permutations that may receive power in either direct or indirect way from the fundamental TE_{10} mode.

	$\boldsymbol{\nu_1 \neq \lvert\nu_3\rvert}$				$\boldsymbol{\nu_1 = -\nu_3 \neq 0}$			
	TE		**TM**		**TE**		**TM**	
	$\boldsymbol{p_i}$	$\boldsymbol{q_i}$	$\boldsymbol{p_i}$	$\boldsymbol{q_i}$	$\boldsymbol{p_i}$	$\boldsymbol{q_i}$	$\boldsymbol{p_i}$	$\boldsymbol{q_i}$
$\boldsymbol{\nu_2 \neq \lvert\nu_4\rvert}$	0,1,2,…	0,1,2,…	1,2,3,…	1,2,3,…	0,1,2,…	0,1,2,…	1,2,3,…	1,2,3,…
$\boldsymbol{\nu_2 = -\nu_4 \neq 0}$	0,1,2,…	0,1,2,…	1,2,3,…	1,2,3,…	0,1,2,…	0,1,2,…	1,2,3,…	1,2,3,…
$\boldsymbol{\nu_2 = \nu_4 \neq 0}$	1,3,5,…	0,1,2,…	1,3,5,…	1,2,3,…	1,3,5,…	0,1,2,…	1,3,5,…	1,2,3,…
$\boldsymbol{\nu_2 = \nu_4 = 0}$	1	0,1,2,…	1	1,2,3,…	1	0,1,2,…	1	1,2,3,…

Table 2.2. Different permutations for modal indexes, p_i and q_i, of TE and TM modes that receive power from TE10 mode ($p_m = 1$, $q_m = 0$) by means of direct or intermediate-mode coupling by considering the different symmetry combinations of the pair ν_2, ν_4; with the cases $\nu_1 \neq |\nu_3|$ and $\nu_1 = -\nu_3 \neq 0$. The pair of values $p_i = 0$ and $q_i = 0$ is forbidden.

	$\nu_1 = \nu_3 \neq 0$				$\nu_1 = \nu_3 = 0$			
	TE		**TM**		**TE**		**TM**	
	p_i	q_i	p_i	q_i	p_i	q_i	p_i	q_i
$\nu_2 \neq \lvert\nu_4\rvert$	0,1,2,…	0,2,4,…	1,2,3,…	2,4,6,…	1,2,3,…	0	-	-
$\nu_2 = -\nu_4 \neq 0$	0,1,2,…	0,2,4,…	1,2,3,…	2,4,6,…	1,2,3,…	0	-	-
$\nu_2 = \nu_4 \neq 0$	1,3,5,…	0,2,4,…	1,3,5,…	2,4,6,…	1,3,5,…	0	-	-
$\nu_2 = \nu_4 = 0$	1	0,2,4,…	1	2,4,6,…	-	-	-	-

Table 2.3. Different permutations for modal indexes, p_i and q_i, of TE and TM modes that receive power from TE_{10} mode ($p_m = 1$, $q_m = 0$) by means of direct or intermediate-mode coupling by considering the different symmetry combinations of the pair ν_2, ν_4; with the cases $\nu_1 = \nu_3 \neq 0$ and $\nu_1 = \nu_3 = 0$. The pair of values $p_i = 0$ and $q_i = 0$ is forbidden.

In order to conclude this subsection, it is important to highlight that closed-form expressions have been obtained for the coupling coefficients of a nonuniform rectangular waveguide as a function of its physical dimensions. Moreover, the relevant modes that are directly coupled to the fundamental TE_{10} have been determined, and the ones that may indirectly receive power from it have been identified for the different symmetries that can be found between the metallic walls of the rectangular waveguide. Therefore, the electromagnetic behavior of the nonuniform waveguide structure, as well as its frequency response, can be completely determined just by solving the coupled-mode equation system of (2.44). In the following section, the single-mode operation assumption will be employed to calculate the waveguide height and width dimensions so as to satisfy a certain coupling coefficient. Moreover, the relationship between the coupling coefficient and the dimensions of the waveguide will be obtained for transmission lines that support TEM or QTEM modes, and specific expressions will be obtained for microstrip and microstrip coupled line technologies through the characteristic impedance of the transmission line.

2.2. SINGLE MODE OPERATION ASSUMPTION FOR THE SOLUTION OF THE SYNTHESIS PROBLEM

In the previous section 2.1, the Coupled-Mode Theory has been carefully formulated without taking any approximation, leading to a theoretical framework that allows us to describe completely the electromagnetic behavior of a general nonuniform waveguide structure. However, the problem addressed by the Coupled-Mode Theory can be greatly simplified by performing several reasonable approximations that lead to the single-mode operation assumption, which is necessary to address the synthesis with Inverse Scattering techniques as it will be shown in CHAPTER 4.

Consequently, the general Coupled-Mode Theory will be reassessed for modelling a nonuniform waveguide structure when a unique mode is considered. Closed-form relationships will be found between the coupling coefficient and the frequency response, as well as between the coupling coefficient and the physical dimensions of the waveguide, as a result of the single-mode assumption. In fact, the relation with the physical dimensions will be specifically studied for the cases of rectangular waveguide and transmission lines that support TEM or QTEM modes, paying special attention to single and coupled microstrip line technologies.

Furthermore, in order to allow the implementation of synthetized responses using waveguide technologies where the variation of the physical dimensions drives to a change of the phase constant along the propagation direction, a novel modelling method based on a normalized propagation axis where the phase constant remains unaltered will be presented in detail.

Finally, the possible parasitic effects caused by the neglected contributions of cut-off modes, that may degrade the expected frequency response under single-mode approximation, will be modelled as a continuous variation of the phase constant of the fundamental mode along the propagation direction. Thanks to this modelling, two methods to assimilate the effects of these higher-order modes into the single-mode equation system will be presented for the case of closed-boundary waveguides.

2.2.1. Relationship between the Coupling Coefficient, the Frequency Response and the Physical Dimensions under Single-Mode Operation

A general relationship between the coupling coefficient and the frequency response of a nonuniform waveguide structure can be achieved when considering that only a single mode is excited, taking into account its associated forward and backward travelling waves, as it was shown in [18]-[20]. For doing so, the continuous spectrum modes will be neglected since the energy of these modes is mainly radiated. The error caused by this approximation will be minimum regarding this thesis, since the aim is to synthesize non-radiating smooth structures in open waveguides, while radiation in closed-boundary waveguides will be completely null indeed. Referring to the discrete spectrum modes, in the operational bandwidth of interest only one propagating mode is assumed, being the rest under the cut-off regime. In this case, the more the structure prevents the coupling to other modes, the more the ideal single-mode operation will fit reality. Thus, if only one mode is considered, the total electric, $\hat{\vec{E}}(x,y,z)$, and magnetic, $\hat{\vec{H}}(x,y,z)$, fields along the nonuniform waveguide of (2.1) and (2.2) will be simplified to [18]-[20]:

$$\hat{\vec{E}}(x,y,z) = a^{+}(z)\cdot\vec{E}^{+}(x,y,z) + a^{-}(z)\cdot\vec{E}^{-}(x,y,z) \tag{2.89}$$

$$\hat{\vec{H}}(x,y,z) = a^{+}(z)\cdot\vec{H}^{+}(x,y,z) + a^{-}(z)\cdot\vec{H}^{-}(x,y,z) \tag{2.90}$$

where a^{+} and a^{-} stand for the complex amplitude of the forward and backward travelling waves of the mode along the propagation direction, respectively; while $\vec{E}^{+}(x,y,z)$ and $\vec{H}^{+}(x,y,z)$ are the vector mode patterns of the electric and magnetic fields of the forward travelling wave for the cross section of interest; and finally $\vec{E}^{-}(x,y,z)$ and $\vec{H}^{-}(x,y,z)$ are the vector mode patterns but for the backward propagating case.

Regarding the two coupling coefficients, $C_{1,-1}$ and $C_{-1,1}$, that affect both, forward and backward travelling waves, it must be noted that they will be identical due to (2.41). Therefore, they will be denoted by K, with $K = C_{1,-1} = C_{-1,1}$. On the other hand, the other relevant coupling coefficients, $C_{1,1}$ and $C_{-1,-1}$, will be null due to (2.38), since the normalization factor

of the mode, $N_1 = -N_{-1}$, will remain constant with z. Thus, the general couple-mode equation system of (2.3), (2.4) can be simplified to [18]:

$$\frac{da^+}{dz} = -j \cdot \beta \cdot a^+ + K \cdot a^- \tag{2.91}$$

$$\frac{da^-}{dz} = j \cdot \beta \cdot a^- + K \cdot a^+ \tag{2.92}$$

being β, the phase constant of the mode. An expression to calculate K is directly obtained by setting $i = -m$ in (2.34), giving rise to (2.93).

$$K = C_{1,-1} = C_{-1,1} = \frac{-\pi \cdot f \cdot \oint \nu \cdot [\mu_0 \cdot (H_z^1 \cdot H_z^{-1} - H_t^1 \cdot H_t^{-1}) + \varepsilon \cdot E_n^1 \cdot E_n^{-1}] \cdot dt}{N_1 \cdot (\beta_1 - \beta_{-1})} \tag{2.93}$$

In order to obtain a more compact equation for K, the sign convention of (2.15)-(2.20) can be applied to the n, t, z coordinate system as follows:

$$E_t^{-i} = E_t^i \tag{2.94}$$

$$E_n^{-i} = E_n^i \tag{2.95}$$

$$E_z^{-i} = -E_z^i \tag{2.96}$$

$$H_t^{-i} = -H_t^i \tag{2.97}$$

$$H_n^{-i} = -H_n^i \tag{2.98}$$

$$H_z^{-i} = H_z^i \tag{2.99}$$

If the set of sign conventions (2.11), (2.13), (2.94)-(2.98) are applied to (2.93), the coupling coefficient gets reduced to:

$$K = \frac{-\pi \cdot f \cdot \oint \nu \cdot \{\mu_0 \cdot [(H_z^+)^2 + (H_t^+)^2] + \varepsilon \cdot (E_n^+)^2\} \cdot dt}{2 \cdot N^+ \cdot \beta} \tag{2.100}$$

where H_z^+ and H_t^+ are the z and t components of the magnetic field of the forward travelling wave, respectively; E_n^+ is the n component of the electric field of that wave; and N^+ is the normalization factor of that forward travelling wave, which is defined as:

$$N^+ = \iint_{\check{S}} \left(\vec{E}^+ \times \vec{H}^+\right) \cdot \hat{z} \cdot d\check{S} = -N^- \tag{2.101}$$

It is demonstrated in [18] that the coupling coefficient expression of (2.100) can be even further simplified to:

$$K = C_{-1,1} = C_{1,-1} = \frac{1}{2 \cdot \beta} \cdot \frac{d\beta}{dz} - \frac{\pi \cdot f}{N^+ \cdot \beta} \cdot \oint \nu \cdot \mu_0 \cdot (H_t^+)^2 \cdot dt \tag{2.102}$$

It must be highlighted that the coupling coefficient completely determines the complex amplitudes $a^+(z)$ and $a^-(z)$, once the boundary (excitation) conditions for $a^+(z)$ and $a^-(z)$ have been fixed, because of the coupled-mode equation system of (2.91), (2.92) and hence, it also determines the amplitude of the fields of (2.89) and (2.90). Since the scattering parameters under single-mode operation will be also a function of the amplitude of that waves at certain points of z, it can be concluded that the coupling coefficient governs the frequency response of the structure. In fact, the scattering parameter definition of (2.26) can be adjusted for a two-port waveguide structure where only one mode is allowed:

$$S_{lk} = \left.\frac{b_l}{a_k}\right|_{a_r=0 \; \forall \; r \neq k} \tag{2.103}$$

Thereby, the scattering matrix allows us to relate the complex amplitudes of the reflected waves at the ports 1 and 2, b_1 and b_2, respectively, with the incident ones at those ports, a_1 and a_2, by means of [27]-[31]:

$$\begin{bmatrix} b_1 \\ b_2 \end{bmatrix} = \begin{bmatrix} S_{11} & S_{12} \\ S_{21} & S_{22} \end{bmatrix} \cdot \begin{bmatrix} a_1 \\ a_2 \end{bmatrix} \tag{2.104}$$

Now that the scattering parameters have been defined in (2.103), and considering the complex amplitudes of (2.91), (2.92), a^+ and a^-, as well as the normalization factor of (2.101), the scattering parameters can be rewritten as [19]:

$$\begin{aligned} S_{11}(f) = \left.\frac{b_1(f)}{a_1(f)}\right|_{a_2=0} &= \left.\frac{\sqrt{N^+(z=0)} \cdot a^-(z=0,f)}{\sqrt{N^+(z=0)} \cdot a^+(z=0,f)}\right|_{a^-(z=L,f)=0} = \\ &= \left.\frac{a^-(z=0,f)}{a^+(z=0,f)}\right|_{a^-(z=L,f)=0} \end{aligned} \tag{2.105}$$

$$S_{21}(f) = \left.\frac{b_2(f)}{a_1(f)}\right|_{a_2=0} = \left.\frac{\sqrt{N^+(z=L)}\cdot a^+(z=L,f)}{\sqrt{N^+(z=0)}\cdot a^+(z=0,f)}\right|_{a^-(z=L,f)=0} \tag{2.106}$$

$$S_{12}(f) = \left.\frac{b_1(f)}{a_2(f)}\right|_{a_2=0} = \left.\frac{\sqrt{N^+(z=0)}\cdot a^-(z=0,f)}{\sqrt{N^+(z=L)}\cdot a^-(z=L,f)}\right|_{a^+(z=0,f)=0} \tag{2.107}$$

$$S_{22}(f) = \left.\frac{b_2(f)}{a_2(f)}\right|_{a_2=0} = \left.\frac{\sqrt{N^+(z=L)}\cdot a^+(z=L,f)}{\sqrt{N^+(z=L)}\cdot a^-(z=L,f)}\right|_{a^+(z=0,f)=0} = \left.\frac{a^+(z=L,f)}{a^-(z=L,f)}\right|_{a^+(z=0,f)=0} \tag{2.108}$$

It must be noted that if the normalization factor at $z = 0$ and $z = L$ is identical, a condition that implies that both ports have the same dimensions, or that the normalization factor remains constant with z, then (2.106) and (2.107) get compacted to:

$$S_{21}(f) = \left.\frac{b_2(f)}{a_1(f)}\right|_{a_2=0} = \left.\frac{a^+(z=L,f)}{a^+(z=0,f)}\right|_{a^-(z=L,f)=0} \tag{2.109}$$

$$S_{12}(f) = \left.\frac{b_1(f)}{a_2(f)}\right|_{a_2=0} = \left.\frac{a^-(z=0,f)}{a^-(z=L,f)}\right|_{a^+(z=0,f)=0} \tag{2.110}$$

As in the general multimode case of the Coupled-Mode Theory, an implicit relationship has been established for single-mode operation between the coupling coefficient and the frequency response by means of the coupled-mode equation system of (2.91), (2.92). This relationship is based on the dependence of the complex amplitudes, $a^+$and a^-, with the coupling coefficient, K, being the formers evaluated at $z = 0$ and $z = L$, the basis of the scattering parameters. Thus, it can be concluded that K determines the frequency response of the waveguide structure under the single-mode operation. However, this relationship is not mathematically clarified since there is not an expression that directly relates any S-parameter, S_{lk}, with K, something that will be the aim of the synthesis methods of CHAPTER 4-CHAPTER 6. In fact, the different equations for K presented in this subsection, (2.93), (2.100), and (2.102), are more directly related with the physical parameters of the waveguide. It is interesting to note that, in the general case, the coupling coefficient is frequency dependent, since the phase constant also depends on frequency, as well as on the propagation direction. Indeed, for the development of the inverse scattering methods, the phase constant must be assumed not to vary along the

propagation direction. Nevertheless, this limitation will be overcome for the cases where this assumption is not satisfied, as it will be thoroughly explained in section 2.2.2.

2.2.1.1. Relationship between the Coupling Coefficient and the Physical Dimensions in Rectangular Waveguide Technology

The relationship between the different coupling coefficients and the physical dimensions of the nonuniform rectangular waveguide was obtained in subsection 2.1.2.1 by considering the different modes and all the symmetry conditions that can be found between its metal-dielectric interfaces. However, as it can be expected, this relationship is greatly simplified by assuming single-mode operation as it was firstly studied in [19]. Since the fundamental (first propagating) mode of a rectangular waveguide is the TE_{10}, something that is satisfied if $a(z) > b(z)\ \forall\ z$, the coupling coefficient, K, will be the one that concerns the forward and backward travelling waves of that mode. Consequently, if the modal indexes $p_m = p_i = 1$ and $q_m = q_i = 0$ in the $C_{m,\pm i}^{TE-TE}$ equation (2.74) are taken, and the lower sign is chosen to select $C_{m,-i}^{TE-TE}$, the coupling coefficient for single-mode operation will be obtained, i.e. $K = C_{1,-1} = C_{1,-1}^{TE-TE}$. It is important to stress that the modal indexes $p_m = p_i = 1$ and $q_m = q_i = 0$ lead to: $N_m = N_i$, $r_m = r_i = \sqrt{2}$ (2.57), $k_{cm}(z) = k_{ci}(z) = \frac{\pi}{a(z)}$ (2.49), $\beta(z) = \beta_m(z) = \beta_i(z)$ (2.45), $c_{p,a}(z) = a(z)$ (2.77), $s_{p,a}(z) = \frac{a(z)}{2}$ (3.15), $c_{q,b} = b(z)$ (2.79), and $s_{q,b}(z) = 0$ (2.80). If the value of the previous parameters is incorporated in (2.74), the result will be the one that is given below [19], [21]:

$$K(z) = C_{1,-1}^{TE-TE}(z) = \frac{\pi^2}{2 \cdot \beta^2(z) \cdot a^3(z) \cdot b(z)} \cdot \cdot \left\{ \left[\frac{a(z)}{2} - \frac{a^3(z) \cdot \beta^2(z)}{2 \cdot \pi^2} - \frac{a^3(z) k^2}{2 \cdot \pi^2} \right] \cdot (v_1 + v_3) + b(z) \cdot (v_4 + v_2) \right\} \tag{2.111}$$

After performing some mathematical manipulations, (2.111) can be rewritten as [19]:

$$K(z) = C_{1,-1}^{TE-TE}(z) = -\frac{1}{2 \cdot b(z)} \cdot (v_1 + v_3) + \frac{\pi^2}{2 \cdot \beta^2(z) \cdot a^3(z)} \cdot (v_4 + v_2) \tag{2.112}$$

Then, taking into account the identities of ν_1, ν_2, ν_3, and ν_4 given in (2.64)-(2.67), $K(z)$ can be expressed as a function of the derivatives of the profiles of each metallic wall, i.e.:

$$K(z) = C_{1,-1}^{TE-TE}(z) = -\frac{1}{2 \cdot b(z)} \cdot \left[-\frac{dy_d(z)}{dz} + \frac{dy_u(z)}{dz} \right] + \frac{\pi^2}{2 \cdot \beta^2(z) \cdot a^3(z)} \cdot \left[-\frac{dx_r(z)}{dz} + \frac{dx_l(z)}{dz} \right] \tag{2.113}$$

In view of (2.68) and (2.69), it is clear that the derivative terms of (2.113) can be formulated in terms of the derivatives of the waveguide width, $a(z)$, and height, $b(z)$, as follows:

$$\frac{da(z)}{dz} = \frac{dx_l(z)}{dz} - \frac{dx_r(z)}{dz} \tag{2.114}$$

$$\frac{db(z)}{dz} = \frac{dy_u(z)}{dz} - \frac{dy_d(z)}{dz} \tag{2.115}$$

Thus, when (2.114) and (2.115) are introduced in (2.113), it is obtained that [19]:

$$K(z) = C_{1,-1}^{TE-TE}(z) = -\frac{1}{2 \cdot b(z)} \cdot \frac{db(z)}{dz} + \frac{\pi^2}{2 \cdot \beta^2(z) \cdot a^3(z)} \cdot \frac{da(z)}{dz} \tag{2.116}$$

At this point, it is important to highlight that $K(z)$ depends on the dimensions of the cross section of interest, $a(z)$ and $b(z)$, and on their derivatives with z. Nonetheless, $K(z)$ also has an inherent dependence on the frequency, f, since $\beta(z)$ must be determined by means of f, i.e. $\beta(z,f)$, as it is demonstrated below for $p_m = 1$ and $q_m = 0$ (TE_{10} mode) by using (2.45), (2.46), and (2.49):

$$\beta(z,f) = \sqrt{k^2 - k_c^2(z)} = \frac{2 \cdot \pi \cdot f}{c} \cdot \sqrt{1 - \left[\frac{f_c^{TE_{10}}(z)}{f} \right]^2} \tag{2.117}$$

where $f_c^{TE_{10}}(z)$ is the cut-off frequency of the fundamental TE_{10} mode along the propagation direction [27]-[31], which is calculated by means of (2.50):

$$f_c^{TE_{10}}(z) = \frac{c}{2 \cdot a(z)} \tag{2.118}$$

Thus, an alternative expression for $\beta(z,f)$ based exclusively on $a(z)$ and f can be provided:

$$\beta(z,f) = \frac{2\cdot\pi\cdot f}{c}\cdot\sqrt{1-\left[\frac{c}{2\cdot a(z)\cdot f}\right]^2} \tag{2.119}$$

Accordingly, the coupling coefficient is no longer a sole function of the dimensions of the cross section of interest, $a(z)$ and $b(z)$, and becomes also frequency dependent, i.e. $K(z,f)$. Then, equation (2.116) can be rewritten considering that f-dependence, yielding to:

$$K(z,f) = -\frac{1}{2\cdot b(z)}\cdot\frac{db(z)}{dz} + \frac{\pi^2}{2\cdot\beta^2(z,f)\cdot a^3(z)}\cdot\frac{da(z)}{dz} \tag{2.120}$$

Indeed, if the $\beta(z,f)$ definition of (2.119) is introduced into $K(z,f)$, (2.120) can be expressed exclusively in terms of the dimensions $b(z)$, $a(z)$, and f, as:

$$\begin{aligned} K(z,f) &= -\frac{1}{2\cdot b(z)}\cdot\frac{db(z)}{dz} + \frac{\pi^2}{2\cdot\beta^2(z,f)\cdot a^3(z)}\cdot\frac{da(z)}{dz} = \\ &= -\frac{1}{2\cdot b(z)}\cdot\frac{db(z)}{dz} + \frac{c^2}{8\cdot f^2\cdot a(z)\cdot\left[a^2(z)-\left(\frac{c}{2\cdot f}\right)^2\right]}\cdot\frac{da(z)}{dz} \end{aligned} \tag{2.121}$$

Now, by inspecting (2.116), (2.120), (2.121), it is clear that $K(z,f)$ can be divided into two parts: the first, $K_b(z)$, only depends on $b(z)$, while the other one is a function of $a(z)$ and f, $K_a(z,f)$. Following this criterion:

$$K(z,f) = K_b(z) + K_a(z,f) \tag{2.122}$$

where:

$$K_b(z) = -\frac{1}{2\cdot b(z)}\cdot\frac{db(z)}{dz} \tag{2.123}$$

$$K_a(z,f) = \frac{\pi^2}{2\cdot\beta^2(z,f)\cdot a^3(z)}\cdot\frac{da(z)}{dz} = \frac{c^2}{8\cdot f^2\cdot a(z)\cdot\left[a^2(z)-\left(\frac{c}{2\cdot f}\right)^2\right]}\cdot\frac{da(z)}{dz} \tag{2.124}$$

It is very important to stress that the coupling coefficient under the single-mode operation assumption, $K(z,f)$, for the case of nonuniform rectangular waveguides has been expressed just in terms of its dimensions, $b(z)$ and $a(z)$, and of the considered frequency, f, even though the latter only applies for structures that exhibit variations in $a(z)$. This frequency dependence may

be troublesome regarding the synthesis methods that will be presented in CHAPTER 3-CHAPTER 6, since all of them rely on the premise that $K(z)$ is not a function of frequency. Therefore, it is clear that when a certain synthesized $K(z)$ is intended to be implemented by means of any variation in $a(z)$, the result is expected to be exclusively exact for a single frequency, something that does not happen when considering the same $K(z)$ but for being implemented by means of changes in the $b(z)$ dimension. Once this point has been clarified it is very important to highlight that the dimensions $b(z)$ and $a(z)$ can be deduced from their corresponding terms of $K(z,f)$, $K_b(z)$ and $K_a(z,f)$, respectively, by solving the necessary first order differential equations to extract $b(z)$ in (2.123) as well as $a(z)$ in (2.124). By doing so, it will be possible to satisfy any synthesized $K(z) = K_b(z) + K_a(z,f)$, and its associated frequency response under the single-mode assumption, by imposing suitable profiles in $b(z)$ and $a(z)$.

2.2.1.1.1. Deduction of Rectangular Waveguide Height

As it has been already mentioned, the height dimensions, $b(z)$, of the nonuniform rectangular waveguide can be obtained by solving the differential equation in $b(z)$ from the $K_b(z)$ expression of (2.123). For doing so, z and $b(z)$ are going to be substituted by the dummy variables r and $p(r)$ (or briefly p, for the sake of simplicity), respectively, in (2.123), i.e.:

$$K_b(r) = -\frac{1}{2 \cdot p} \cdot \frac{dp}{dr} \tag{2.125}$$

Firstly, both sides of the equation (2.125) are multiplied by dr yielding to:

$$K_b(r) \cdot dr = -\frac{1}{2 \cdot p} \cdot dp \tag{2.126}$$

Then, the left-hand side of (2.126) is integrated in r with lower and upper integration limits of 0 and z, respectively. Regarding the right-hand side, the integration variable will be p, defining its limits from $b(0)$ to $b(z)$. As a consequence, (2.126) yields to an identity between those integrals of the following form:

$$\int_0^z K_b(r) \cdot dr = \int_{b(0)}^{b(z)} \left[-\frac{1}{2 \cdot p}\right] \cdot dp \tag{2.127}$$

The right hand side of (2.127) can be analytically solved [33], and hence:

$$\int_0^z K_b(r)\cdot dr = \int_{b(0)}^{b(z)} \left[-\frac{1}{2\cdot p}\right]\cdot dp = -\frac{1}{2}\cdot\int_{b(0)}^{b(z)}\frac{1}{p}\cdot dp = \\ = -\frac{1}{2}\cdot \ln[p]\Big|_{b(0)}^{b(z)} = -\frac{1}{2}\cdot\{\ln[b(z)]-\ln[b(0)]\} = -\frac{1}{2}\cdot\ln\left[\frac{b(z)}{b(0)}\right] \tag{2.128}$$

Now, taking the exponential of both sides of (2.128), it is obtained that:

$$e^{-2\cdot\int_0^z K_b(r)\cdot dr} = \frac{b(z)}{b(0)} \tag{2.129}$$

Finally, the corresponding waveguide height for $K_b(z)$ is attained by solving for $b(z)$ in the last equation (2.129) as:

$$b(z) = b(0)\cdot e^{-2\cdot\int_0^z K_b(r)\cdot dr} \tag{2.130}$$

where $b(0)$ is the waveguide height value at $z = 0$ that can be arbitrarily chosen.

2.2.1.1.2. Deduction of Rectangular Waveguide Width

The procedure to determine the waveguide width, $a(z)$, from $K_a(z,f)$ is similar to the one carried out in the previous subsection for $b(z)$, although the integrals involved are slightly more complex. Firstly, the auxiliary dummy variable r will substitute again z, while $p = p(r)$ will substitute now $a(z)$, and (2.124) gets rewritten as:

$$K_a(r,f) = \frac{c^2}{8\cdot f^2\cdot p\cdot\left[p^2-\left(\frac{c}{2\cdot f}\right)^2\right]}\cdot\frac{dp}{dr} \tag{2.131}$$

The denominator of (2.131) can be factorized and isolated by determining its roots. After doing so, the resulting sides of the equation are multiplied by dr, and hence:

$$2\cdot\left(\frac{2\cdot f}{c}\right)^2\cdot K_a(r,f)\cdot dr = \frac{dp}{p\cdot\left[p+\frac{c}{2\cdot f}\right]\cdot\left[p-\frac{c}{2\cdot f}\right]} \tag{2.132}$$

Then, (2.132) is ready to be integrated with integration limits of 0 and z in r (left side) as well as $a(0)$ and $a(z)$ in p (right side), with $a(0)$ being the width of the waveguide at its

beginning, which can be freely selected. By doing so, the integral form of the identity (2.132) will be the following:

$$2 \cdot \left(\frac{2 \cdot f}{c}\right)^2 \cdot \int_0^z K_a(r,f) \cdot dr = \int_{a(0)}^{a(z)} \frac{dp}{p \cdot \left(p + \frac{c}{2 \cdot f}\right) \cdot \left(p - \frac{c}{2 \cdot f}\right)} \tag{2.133}$$

Unfortunately, it is not possible to solve the right-hand side integral of (2.133) as directly as in the case of the previous section, devoted to the determination of $b(z)$. Nevertheless, the considered integrand can be divided into a sum of three different terms (applying partial fraction decomposition) that lead to the following three integrals, due to the linear property of integration:

$$\begin{aligned} &\int_{a(0)}^{a(z)} \frac{dp}{p \cdot \left(p + \frac{c}{2 \cdot f}\right) \cdot \left(p - \frac{c}{2 \cdot f}\right)} = \\ &= -\left(\frac{2f}{c}\right)^2 \cdot \int_{a(0)}^{a(z)} \frac{dp}{p} + 2\left(\frac{f}{c}\right)^2 \cdot \int_{a(0)}^{a(z)} \frac{dp}{\left(p + \frac{c}{2f}\right)} + 2\left(\frac{f}{c}\right)^2 \cdot \int_{a(0)}^{a(z)} \frac{dp}{\left(p - \frac{c}{2f}\right)} \end{aligned} \tag{2.134}$$

where the resultant integrals already have direct solutions that are available in [33]. For the concerning case, those solutions yield to:

$$\begin{aligned} &-\left(\frac{2f}{c}\right)^2 \cdot \int_{a(0)}^{a(z)} \frac{dp}{p} + 2\left(\frac{f}{c}\right)^2 \cdot \int_{a(0)}^{a(z)} \frac{dp}{\left(p + \frac{c}{2f}\right)} + 2\left(\frac{f}{c}\right)^2 \cdot \int_{a(0)}^{a(z)} \frac{dp}{\left(p - \frac{c}{2f}\right)} = \\ &= -\left(\frac{2f}{c}\right)^2 \cdot \ln[p]\Big|_{a(0)}^{a(z)} + 2 \cdot \left(\frac{f}{c}\right)^2 \cdot \ln\left[p + \frac{c}{2f}\right]\Bigg|_{a(0)}^{a(z)} + 2 \cdot \left(\frac{f}{c}\right)^2 \cdot \ln\left[p - \frac{c}{2f}\right]\Bigg|_{a(0)}^{a(z)} = \\ &= 2 \cdot \left(\frac{f}{c}\right)^2 \cdot \ln\left\{\left[\frac{a(0)}{a(z)}\right]^2\right\} + 2 \cdot \left(\frac{f}{c}\right)^2 \cdot \ln\left[\frac{a(z) + \frac{c}{2 \cdot f}}{a(0) + \frac{c}{2 \cdot f}}\right] + 2 \cdot \left(\frac{f}{c}\right)^2 \cdot \ln\left[\frac{a(z) - \frac{c}{2 \cdot f}}{a(0) - \frac{c}{2 \cdot f}}\right] = \\ &= 2 \cdot \left(\frac{f}{c}\right)^2 \cdot \left(\ln\left\{\left[\frac{a(0)}{a(z)}\right]^2\right\} + \ln\left[\frac{a(z) + \frac{c}{2 \cdot f}}{a(0) + \frac{c}{2 \cdot f}}\right] + \ln\left[\frac{a(z) - \frac{c}{2 \cdot f}}{a(0) - \frac{c}{2 \cdot f}}\right]\right) = \end{aligned} \tag{2.135}$$

$$= 2 \cdot \left(\frac{f}{c}\right)^2 \cdot \ln\left[\frac{a^2(0) \cdot a^2(z) - a^2(0) \cdot \left(\frac{c}{2 \cdot f}\right)^2}{a^2(z) \cdot a^2(0) - a^2(z) \cdot \left(\frac{c}{2 \cdot f}\right)^2}\right]$$

Therefore, the combination of the identity (2.134) and the solution of (2.135) gives rise to:

$$\int_{a(0)}^{a(z)} \frac{dp}{p \cdot \left(p + \frac{c}{2 \cdot f}\right) \cdot \left(p - \frac{c}{2 \cdot f}\right)} = 2 \cdot \left(\frac{f}{c}\right)^2 \cdot \ln\left[\frac{a^2(0) \cdot a^2(z) - a^2(0) \cdot \left(\frac{c}{2 \cdot f}\right)^2}{a^2(z) \cdot a^2(0) - a^2(z) \cdot \left(\frac{c}{2 \cdot f}\right)^2}\right] \quad (2.136)$$

Now, by introducing (2.136) into (2.133), it is obtained that:

$$4 \cdot \int_0^z K_a(r,f) \cdot dr = \ln\left[\frac{a^2(0) \cdot a^2(z) - a^2(0) \cdot \left(\frac{c}{2 \cdot f}\right)^2}{a^2(z) \cdot a^2(0) - a^2(z) \cdot \left(\frac{c}{2 \cdot f}\right)^2}\right] \quad (2.137)$$

If the exponentials of both sides of (2.137) are taken, the following relation is attained:

$$e^{4 \cdot \int_0^z K_a(r,f) \cdot dr} = \frac{a^2(0) \cdot a^2(z) - a^2(0) \cdot \left(\frac{c}{2 \cdot f}\right)^2}{a^2(z) \cdot a^2(0) - a^2(z) \cdot \left(\frac{c}{2 \cdot f}\right)^2} \quad (2.138)$$

Finally, by performing the necessary rearrangements in order to solve for $a(z)$, it is lastly obtained that:

$$a(z) = \frac{c}{2 \cdot f} \cdot \frac{e^{-2 \cdot \int_0^z K_a(r,f) \cdot dr}}{\sqrt{e^{-4 \cdot \int_0^z K_a(r,f) \cdot dr} + \left(\left[\frac{c}{2 \cdot a(0) \cdot f}\right]\right)^2 - 1}} \quad (2.139)$$

In order to conclude this subsection, which is devoted to determine the width of a nonuniform rectangular waveguide for a given $K_a(z,f)$, it must be pointed out that in view of (2.139), $a(z)$ depends on the particular frequency that is being considered, something that is fully coherent with the $K_a(z,f)$ definition of (2.124). This conclusion is very important for the physical implementation of microwave components in rectangular waveguide technology, since the synthesis of the device must be focused on obtaining the desired coupling coefficient for a

single frequency value, which must be employed subsequently in the $a(z)$ calculation, because if we don't proceed in that way, the resulting device will neither achieve the desired dimensions at its output port, nor the expected frequency response.

2.2.1.2. Relationship between the Coupling Coefficient and the Physical Dimensions for Transmission Lines that Support TEM or QTEM Modes

This subsection is focused on the relationship between the coupling coefficient and the physical dimensions for the case of waveguides that are able to propagate TEM or QTEM modes by applying the single-mode operation assumption. The collection of waveguides that support these modes are commonly known as transmission lines.

Firstly, the pure TEM mode is a mode category for those that feature null electric and magnetic field components in the propagation direction [27]-[30], i.e. $E_z = 0$ and $H_z = 0$. This kind of mode is inherent from ideal lossless waveguides composed by two conductors that are placed in parallel to each other in a homogeneous dielectric medium, being the stripline and the coaxial line classical examples of these transmission lines (see Fig. 2.4).

However, in some cases both conductors are not enclosed into a homogeneous dielectric medium, something that forcibly leads to $E_z \neq 0$ and $H_z \neq 0$. Nevertheless, if the dielectric thickness is much smaller than the operating wavelength [29], the z-components of both fields, electric and magnetic, will tend to be approximately null, $E_z \approx 0$ and $H_z \approx 0$, so the mode is called Quasi-TEM (QTEM) and its behavior is assumed to be quite close to a TEM mode from a practical point of view. Typical transmission lines that support QTEM modes are the microstrip and the coplanar waveguides that are depicted in Fig. 2.5, among others.

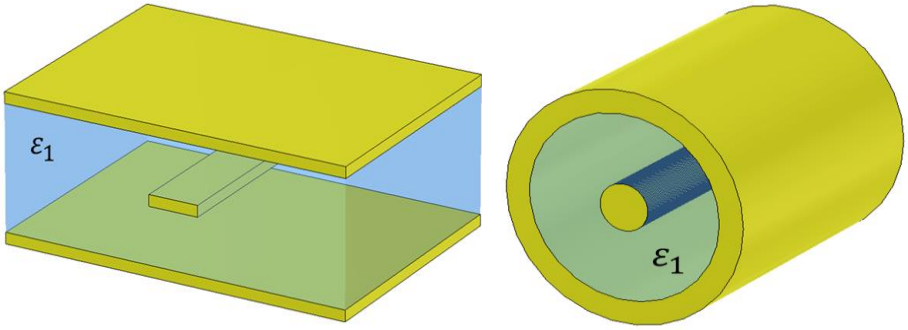

(a) (b)

Fig. 2.4. Sketch of some examples of transmission lines that allow TEM-mode propagation: (a) Stripline. (b) Coaxial line.

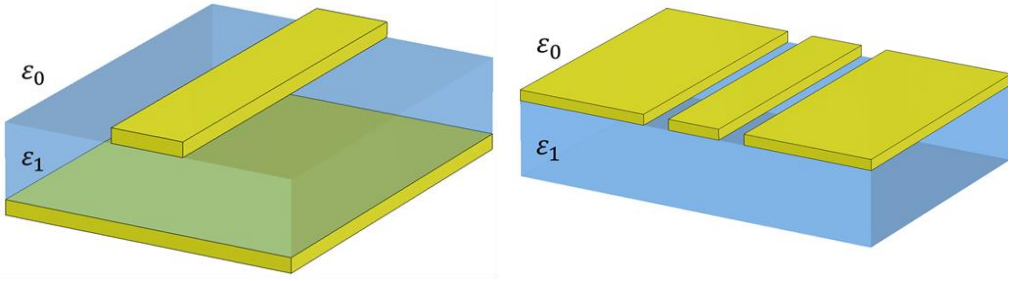

(a) (b)

Fig. 2.5. Sketch of some transmission lines that propagate a QTEM mode: (a) Microstrip line. (b) Coplanar line.

If the Coupled-Mode Theory is applied to the case of a fundamental m TEM or QTEM mode, the discrete-spectrum mode $C_{m,i}$ equation of (2.34), for $i = -m$, i.e. $C_{m,-m}$, can be conveniently rewritten in terms of the characteristic impedance of the mode, Z_{0m}, as it was demonstrated in [18], where alternative expressions for the modes of the discrete and continuous spectrum are besides provided. Therefore, by starting from (2.34) and after performing several mathematical manipulations, it can be demonstrated [18] that for any m discrete spectrum mode and assuming that N_m is constant with z, the resulting $C_{m,-m}$ can be expressed as:

$$C_{m,-m} = -\frac{1}{2 \cdot Z_{0m}} \cdot \frac{dZ_{0m}}{dz} + \frac{1}{N_m} \cdot \iint_{\check{S}} \left(\vec{e}^{\,m} \times \frac{\partial \vec{h}^{\,m}}{\partial z} \right) \cdot \hat{z} \cdot d\check{S} \tag{2.140}$$

where the normalized vector mode patterns, $\vec{e}^{\,m}$ and $\vec{h}^{\,m}$, are related with the vector mode patterns of the m mode, $\vec{E}^{\,m}$ and $\vec{H}^{\,m}$, of the uniform waveguide associated with the cross section of interest, as they were defined in (2.1) and (2.2), in the following manner:

$$\vec{E}^m = \sqrt{Z_{0m}} \cdot \vec{e}^m \tag{2.141}$$

$$\vec{H}^m = \frac{1}{\sqrt{Z_{0m}}} \cdot \vec{h}^m \tag{2.142}$$

Regarding the concept of characteristic impedance, it is well known [29] that when dealing with TEM modes, the voltage, V, and the current, I, can be defined in a univocal way, so the characteristic impedance of the m mode, Z_{0m}, is accordingly defined as:

$$Z_{0m} = \frac{V^+}{I^+} = -\frac{V^-}{I^-} \tag{2.143}$$

where V^+ and V^- stand for the voltage forward and backward travelling waves, respectively; while I^+ and I^- represent the corresponding current waves.

However, when dealing with no pure TEM modes, i.e. QTEM modes, the definitions of V and I are no longer unique and depend on the choice of the specific points within the cross section selected, so Z_{0m} cannot be univocally specified. In this case, a suitable definition of Z_{0m} for determining the coupling coefficient $C_{m,-m}$ must be found. Moreover, the sought Z_{0m} must feature the variations that the cross section presents along the waveguide. Indeed, the most suitable Z_{0m} is the one that accomplishes the same reflection coefficient as the one that is directly produced by the forward and backward travelling waves of the m mode [18], [19]. Taking into account this definition, the field-dependent part of (2.140) can be neglected and $C_{m,-m}$ can be approximated for the discrete spectrum modes as:

$$C_{m,-m} \approx -\frac{1}{2 \cdot Z_{0m}} \cdot \frac{dZ_{0m}}{dz} \tag{2.144}$$

Since single-mode operation is assumed, $K = C_{1,-1}$, yielding to:

$$K(z) = -\frac{1}{2 \cdot Z_0(z)} \cdot \frac{dZ_0(z)}{dz} \tag{2.145}$$

It is important to note that (2.145) can be solved so as to calculate $Z_0(z)$ from $K(z)$. Indeed, equation (2.145) has the same form as (2.123) but for $Z_0(z)$ instead of $b(z)$, and $K(z)$ instead of $K_b(z)$. If the mathematical procedure that is fully detailed in subsection 2.2.1.1.1 within equations (2.125)-(2.130) is applied for (2.145), it will be obtained that:

$$Z_0(z) = Z_0(0) \cdot e^{-2 \cdot \int_0^z K(r) \cdot dr} \tag{2.146}$$

where $Z_0(0)$ is the characteristic impedance of the line at its beginning that can be arbitrarily chosen, while r is just a dummy variable of integration.

The planar transmission lines are of great interest in the design of microwave components due to their flexibility and high integration capability between their different specific technologies. Therefore, the following subsection will be devoted to relate the characteristic impedance with the physical dimensions for the microstrip case, which is one of the most employed planar technologies because it can be fabricated by means of low-cost photolithographic processes and it is easily miniaturized and integrated with both passive and active microwave devices as well [29]. However, similar relationships can be found in the literature for other planar technologies [19], [20] ,[29]-[31], [34].

2.2.1.2.1. Deduction of the Physical Dimensions for Microstrip Lines

The microstrip line consists on a single thin metallic strip of width W, placed on a dielectric substrate of thickness, h, that is situated, in turn, over a metallic plane, as it is shown in Fig. 2.6a.

As it has been stated, the microstrip propagation medium is inhomogeneous, as it can be observed in Fig. 2.6b, so the mode under consideration will be QTEM since the different propagation velocity in the dielectric, $v_{p,diel}$, and in the air, $v_{p,air}$, will lead to the appearance of a z-component in the fields, being:

$$v_{p,diel} = \frac{c_0}{\sqrt{\varepsilon_r}} = \frac{v_{p,air}}{\sqrt{\varepsilon_r}} \tag{2.147}$$

$$v_{p,air} = c_0 = v_{p,diel} \cdot \sqrt{\varepsilon_r} \tag{2.148}$$

In order to describe the electromagnetic properties of the microstrip line, an effective value of the electric relative permittivity, ε_{eff}, is introduced. The ε_{eff} can be interpreted as the electric relative permittivity that would equivalently correspond if an auxiliary homogeneous medium were considered instead of the actual inhomogeneous one. Thus, ε_{eff} will have an intermediate value between the relative permittivities of the air and the dielectric, i.e. $1 < \varepsilon_{eff} < \varepsilon_r$. The value of ε_{eff} can be calculated by taking into account the electric relative permittivity of the dielectric, ε_r, the substrate thickness, h, and the conductor width, W, as [29]:

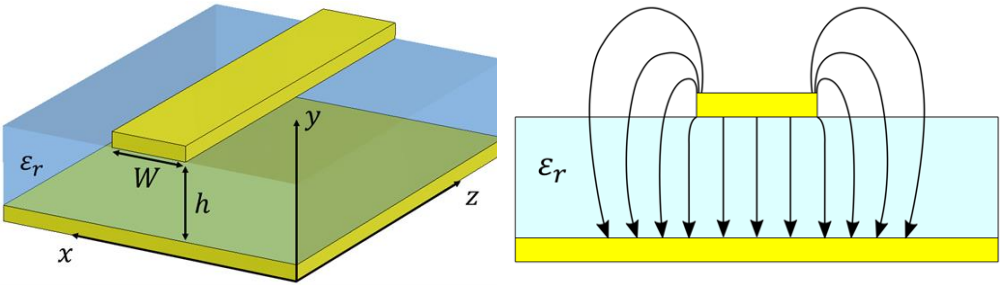

(a) (b)

Fig. 2.6. Sketch of the microstrip line: (a) Structure and relevant dimensions. (b) Distribution of the electric field.

$$\varepsilon_{eff} = \frac{\varepsilon_r + 1}{2} + \frac{\varepsilon_r - 1}{2} \frac{1}{\sqrt{1 + \frac{12 \cdot h}{W}}} \tag{2.149}$$

Thereby, the propagation velocity of the QTEM wave is taken as:

$$v_p = \frac{c_0}{\sqrt{\varepsilon_{eff}}} \tag{2.150}$$

Therefore, when dealing with a microstrip line, the phase constant β can be calculated as follows:

$$\beta = \frac{2 \cdot \pi \cdot f}{v_p} = \frac{2 \cdot \pi \cdot f}{c_0} \cdot \sqrt{\varepsilon_{eff}} \tag{2.151}$$

In view of (2.149) it is clear that ε_{eff} will depend on the strip width, which is a function of the characteristic impedance in turn. Thus, if the characteristic impedance varies along the propagation z axis, ε_{eff} will be also a function of z, i.e. $\varepsilon_{eff}(z)$, and the phase constant will carry that dependence. Fortunately, the dependence on z can be compensated exactly for a single frequency by using the technique that will be detailed in section 2.2.2, which results in a modified propagation axis. More sophisticated models reveal also a relationship between ε_{eff} and frequency [35]-[43], leading to $\varepsilon_{eff}(z, f)$. Therefore, the correspondence between the interconnected variables ε_{eff}, Z_0 and W is only exact for a single frequency value, and the microstrip technology is considered as a dispersive waveguide technology as a consequence.

It is possible to relate the physical dimensions of the microstrip line with the characteristic impedance, Z_0, for each combination of relative permittivity of the substrate, ε_r, dielectric thickness, h, and line width, W, as [29]:

$$\frac{W}{h} = \begin{cases} \dfrac{8e^{A}}{e^{2A}-2} & \text{for } \dfrac{W}{h} < 2 \\ \dfrac{2}{\pi}\cdot\left\{B-1-\ln(2B-1)+\dfrac{\varepsilon_r-1}{2\varepsilon_r}\left[(B-1)+0.39-\dfrac{0.61}{\varepsilon_r}\right]\right\} & \text{for } \dfrac{W}{h} > 2 \end{cases} \tag{2.152}$$

being:

$$A = \frac{Z_0}{60}\sqrt{\frac{\varepsilon_r+1}{2}} + \frac{\varepsilon_r-1}{\varepsilon_r+1}\left(0.23+\frac{0.11}{\varepsilon_r}\right) \tag{2.153}$$

$$B = \frac{377\pi}{2Z_0\sqrt{\varepsilon_r}} \tag{2.154}$$

More refined relationships between the characteristic impedance and the physical dimensions of the microstrip line can be obtained by means of *Keysight*™ *ADS Linecalc* Tool, which are based on [35]-[41], where the frequency and the thickness of the upper conductor are employed for the accurate calculation of the impedance value.

Finally, it must be stressed that in order to guarantee the assumed single-mode operation, while avoiding the coupling to higher order modes, the selection of a suitable dielectric may become critical depending on the specific structure considered to be implemented using microstrip technology. This effect could limit the frequency operation range due to strong coupling between the fundamental QTEM mode and the lowest TM mode. Besides, additional frequency restrictions should be taken into account to avoid the so-called transverse-resonant mode. In order to operate in a safe frequency range, the expressions that approximate the frequencies where the coupling to the higher TM mode, $f_{c,TM}$, and the transversal-resonance, $f_{c,TR}$, may start to be troublesome, are provided below [42], [43]:

$$f_{c,TM} = \frac{c_0 \cdot \tan^{-1}(\varepsilon_r)}{\pi \cdot h \cdot \sqrt{2\cdot(\varepsilon_r-1)}} \tag{2.155}$$

$$f_{c,TR} = \frac{c_0}{\sqrt{\varepsilon_r}\cdot(2\cdot W_{max}+0.8\cdot h)} \tag{2.156}$$

where W_{max} in (2.156) is the maximum width of the metallic strip.

To finish this subsection, it must be highlighted that the characteristic impedance and the physical dimensions of the microstrip line are related between them. Since the characteristic impedance has been already linked with the coupling coefficient under single-mode operation by means of (2.145) and (2.146), it can be concluded that a complete relationship has been

established between that coupling coefficient and the dimensions of the microstrip line. Therefore, using the methods that will be thoroughly detailed in CHAPTER 4-CHAPTER 6 to calculate the coupling coefficient required to obtain a target frequency response, it will be possible to implement that coupling coefficient by providing a suitable microstrip line that feature the necessary variations in the dimensions of its cross section. These changes will be actually performed in the width of the metallic strip, since it is not currently possible to modify the thickness of the substrate. Hence, the target frequency response will be satisfied by the resulting device.

2.2.1.3. Relationship between the Coupling Coefficient, the Frequency Response, and the Physical Dimensions for TEM or QTEM Symmetrical Edge Coupled Transmission Lines

The coupled line configurations were early employed for coupler design [44]-[46], but recent examples can be also found in the literature [47], [48]. Besides, it has been recently employed to implement several analog signal processors in transmission operation mode [49], also in the context of the Coupled-Mode Theory and the inverse scattering synthesis methods [50].

The study of the symmetrical edge coupled transmission lines, from the point of view of the Coupled-Mode Theory, can be easily carried out thanks to the mode decomposition that can be performed to the total fields that actually propagate along this kind of structures, giving rise to the so-called even and odd modes [51], [52]. Since two modes are going to be taken into account, the single-mode operation assumption will not be rigorously valid, and hence it should be presented in section 2.1. However, it will be shown that the foundations of the single-mode operation can be reasonably employed for dealing with the symmetrical edge coupled line structures.

Regarding the structure of the symmetrical edge coupled transmission lines, it strongly depends on the specific technology employed to implement them (see Fig. 2.7), although their common characteristic may be described by considering two transmission lines that are placed

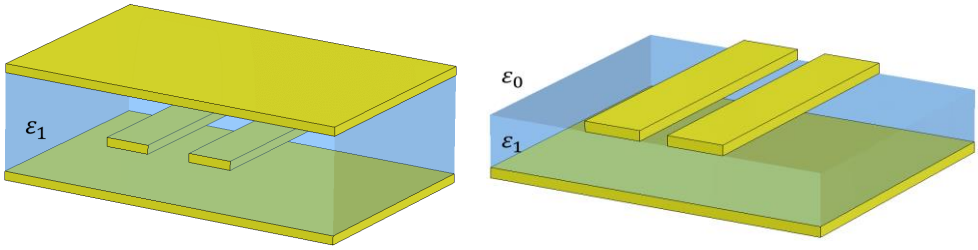

(a) (b)

Fig. 2.7. Sketch of some examples of coupled transmission lines in different planar technologies: (a) Stripline. (b) Microstrip.

sufficiently close so as to couple energy between each other, being the profile of both lines symmetric with respect to the longitudinal plane to the propagation direction.

If the presence of higher-order spurious modes is avoided, the mode decomposition of an ideal symmetrical edge coupled transmission line will result in orthogonal even and odd modes. Moreover, it will be assumed that those modes belong to the discrete spectrum mode category and they are not be able to couple energy between each other. By doing so, the coupled-mode equation system of (2.3) can be rewritten as:

$$\frac{da_e^+}{dz} = -j \cdot \beta_e \cdot a_e^+ + C_{e,-e} \cdot a_e^- \tag{2.157}$$

$$\frac{da_e^-}{dz} = j \cdot \beta_e \cdot a_e^- + C_{-e,e} \cdot a_e^+ \tag{2.158}$$

$$\frac{da_o^+}{dz} = -j \cdot \beta_o \cdot a_o^+ + C_{o,-o} \cdot a_o^- \tag{2.159}$$

$$\frac{da_o^-}{dz} = j \cdot \beta_o \cdot a_o^- + C_{-o,o} \cdot a_o^+ \tag{2.160}$$

where a_e^+ and a_e^- are the complex amplitudes of the forward and backward travelling waves of the even mode, respectively, whereas a_o^+ and a_o^- are the complex amplitudes of the same waves but for the odd mode case; β_e and β_o stand for the phase constant of the even and odd modes, respectively; and the set of $C_{\pm e,\pm e}$ and $C_{\pm o,\pm o}$ are the coupling coefficients between the forward and backward travelling waves of the even and odd modes, respectively.

It is important to note that the equation system of (2.157)-(2.160) can be divided into two independent systems, since there is not a coupling between the waves of the even and odd modes. Furthermore, if the property (2.41) is considered, the coupling coefficients can be denoted as

$K_e = C_{e,-e} = C_{-e,e}$ for the even mode, and as $K_o = C_{o,-o} = C_{-o,o}$ for the odd mode. Thus, the resulting system for the even mode results in [19], [20]:

$$\frac{da_e^+}{dz} = -j \cdot \beta_e \cdot a_e^+ + K_e \cdot a_e^- \tag{2.161}$$

$$\frac{da_e^-}{dz} = j \cdot \beta_e \cdot a_e^- + K_e \cdot a_e^+ \tag{2.162}$$

while for the odd mode case it is obtained that:

$$\frac{da_o^+}{dz} = -j \cdot \beta_o \cdot a_o^+ + K_o \cdot a_o^- \tag{2.163}$$

$$\frac{da_o^-}{dz} = j \cdot \beta_o \cdot a_o^- + K_o \cdot a_o^+ \tag{2.164}$$

Therefore, it can be considered that both systems (2.161), (2.162) and (2.163), (2.164) are fully identical to the single transmission line case of (2.91), (2.92) and hence, it can be demonstrated by following the same reasoning employed in section 2.2.1.2 that [19], [20]:

$$K_e(z) = -\frac{1}{2 \cdot Z_{0,e}(z)} \cdot \frac{dZ_{0,e}(z)}{dz} \tag{2.165}$$

$$K_o(z) = -\frac{1}{2 \cdot Z_{0,o}(z)} \cdot \frac{dZ_{0,o}(z)}{dz} \tag{2.166}$$

being $Z_{0,e}(z)$ and $Z_{0,o}(z)$ the characteristic impedances of the even and odd modes Moreover, taking into account the solution of (2.146) for the case of a single TEM or QTEM line, it will be automatically satisfied that $Z_{0,e}(z)$ and $Z_{0,o}(z)$ can be obtained from $K_e(z)$ and $K_o(z)$, respectively, as [19], [20]:

$$Z_{0,e}(z) = Z_{0,e}(0) \cdot e^{-2 \cdot \int_0^z K_e(r) \cdot dr} \tag{2.167}$$

$$Z_{0,o}(z) = Z_{0,o}(0) \cdot e^{-2 \cdot \int_0^z K_o(r) \cdot dr} \tag{2.168}$$

being $Z_{0,e}(0)$ and $Z_{0,o}(0)$ the characteristic impedance of the even and odd modes, respectively, that can be arbitrarily chosen.

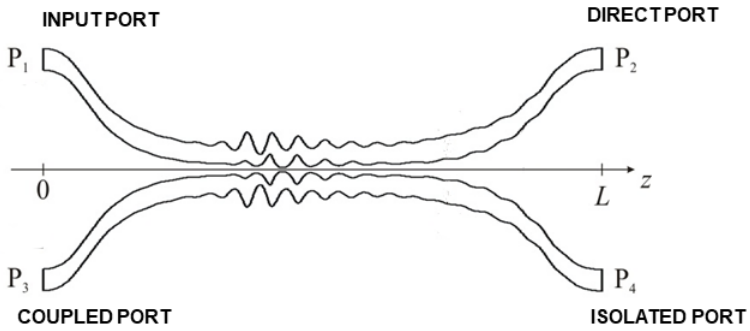

Fig. 2.8. Assignation of port numbers for a generic symmetrical edge coupled transmission line and port naming under the classical coupler nomenclature for the sake of clarity [34].

Regarding the frequency response of the symmetrical edge coupled transmission lines, the following useful relationship between the four port scattering parameters and the reflection and transmission coefficients of even and odd modes can be stated [34]:

$$S_{11}(f) = \frac{\Gamma_e(f) + \Gamma_o(f)}{2} \tag{2.169}$$

$$S_{21}(f) = \frac{T_e(f) + T_o(f)}{2} \tag{2.170}$$

$$S_{31}(f) = \frac{\Gamma_e(f) - \Gamma_o(f)}{2} \tag{2.171}$$

$$S_{41}(f) = \frac{T_e(f) - T_o(f)}{2} \tag{2.172}$$

where $\Gamma_e(f)$ and $T_e(f)$ are the reflection and transmission coefficients of the even mode, while $\Gamma_o(f)$ and $T_o(f)$ are the concerning ones of the odd mode. The nomenclature of the S-parameters follows the port-convention defined in Fig. 2.8.

If the Coupled-Mode Theory notation of (2.161), (2.162) and (2.163), (2.164) is applied to $\Gamma_e(f)$, $T_e(f)$, $\Gamma_o(f)$, and $T_o(f)$, it will be obtained that:

$$\Gamma_e(f) = \left.\frac{b_{1,e}(f)}{a_{1,e}(f)}\right|_{a_{2,e}=0} = \left.\frac{\sqrt{N_e^+(z=0)}\cdot a_e^-(z=0,f)}{\sqrt{N_e^+(z=0)}\cdot a_e^+(z=0,f)}\right|_{a_e^-(z=L,f)=0} = \left.\frac{a_e^-(z=0,f)}{a_e^+(z=0,f)}\right|_{a_e^-(z=L,f)=0} \tag{2.173}$$

$$T_e(f) = \left.\frac{b_{2,e}(f)}{a_{1,e}(f)}\right|_{a_{2,e}=0} = \left.\frac{\sqrt{N_e^+(z=L)}\cdot a_e^+(z=L,f)}{\sqrt{N_e^+(z=0)}\cdot a_e^+(z=0,f)}\right|_{a_e^-(z=L,f)=0} \tag{2.174}$$

$$\begin{aligned}\Gamma_o(f) = \left.\frac{b_{1,o}(f)}{a_{1,o}(f)}\right|_{a_{2,o}=0} &= \left.\frac{\sqrt{N_o^+(z=0)}\cdot a_o^-(z=0,f)}{\sqrt{N_o^+(z=0)}\cdot a_o^+(z=0,f)}\right|_{a_o^-(z=L,f)=0} \\ &= \left.\frac{a_o^-(z=0,f)}{a_o^+(z=0,f)}\right|_{a_o^-(z=L,f)=0}\end{aligned} \tag{2.175}$$

$$T_o(f) = \left.\frac{b_{2,o}(f)}{a_{1,o}(f)}\right|_{a_{2,o}=0} = \left.\frac{\sqrt{N_o^+(z=L)}\cdot a_o^+(z=L,f)}{\sqrt{N_o^+(z=0)}\cdot a_o^+(z=0,f)}\right|_{a_o^-(z=L,f)=0} \tag{2.176}$$

where N_e^+ and N_o^+ are the normalization factors of the forward travelling wave of the even and odd modes, respectively. If it is assumed that these normalization factors are constant along z, it will be concluded that:

$$T_e(f) = \left.\frac{a_e^+(z=L,f)}{a_e^+(z=0,f)}\right|_{a_e^-(z=L,f)=0} \tag{2.177}$$

$$T_o(f) = \left.\frac{a_o^+(z=L,f)}{a_o^+(z=0,f)}\right|_{a_o^-(z=L,f)=0} \tag{2.178}$$

Finally, the most important conclusion of this section devoted to symmetrical edge coupled transmission lines is that a relationship has been exposed between de coupling coefficients, K_e and K_o, and the frequency response of the structure, since they govern the complex amplitudes a_e^+, a_e^-, a_o^+, and a_o^- along the propagation direction and therefore, the reflection and transmission coefficients of both modes at the ports as well as the S-parameters. Thus, the next subsection will be focused on defining the relation between the characteristic impedance of both modes with the physical dimension for the microstrip case, due to the fact that the symmetrical edge coupled transmission line configuration in this technology will be particularly interesting because it features the low-cost and easy manufacturing advantages mentioned for the single line case. Nonetheless, the concerning relationships for other coupled transmission line technologies such as stripline can be found in the literature [29]-[31], [34].

2.2.1.3.1. Deduction of the Physical Dimensions for Symmetrical Edge Coupled Microstrip Lines

The physical structure of a symmetrical edge coupled microstrip transmission line consists of two metallic strips of width W, that are placed close enough between each other with a distance, s, that allows the coupling of energy between them. The strips are situated over a grounded dielectric substrate of relative permittivity, ε_r, and thickness, h, as it can be seen in Fig. 2.9a.

As it has been previously explained, the even an odd mode decomposition may be employed if the coupling to spurious modes is avoided. The corresponding distribution of the electric field of the even and odd modes is represented in Fig. 2.9b and Fig. 2.9c, respectively.

In view of Fig. 2.9b and Fig. 2.9c, it is clear that the propagation medium for both modes is not homogeneous and consequently, the propagation velocity is going to be different at the air and at the dielectric substrate, yielding to a z-component of the electromagnetic fields for both modes. Therefore, the even and odd modes belong to the QTEM mode category. In order to deal with this difference in the electrical permittivity, an effective value of the latter is defined as it

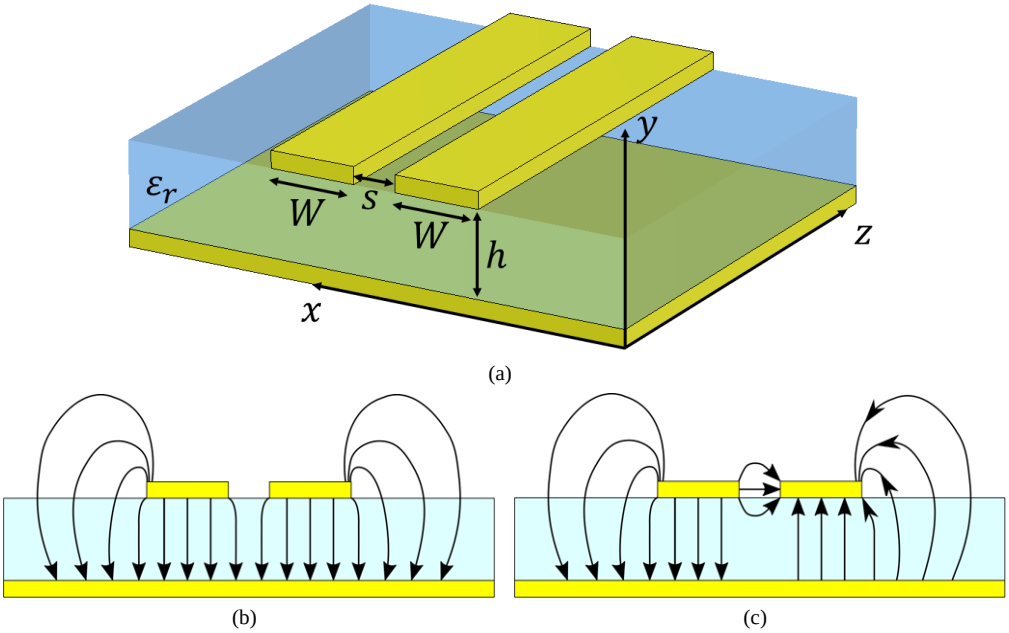

Fig. 2.9. Sketch of microstrip coupled-lines: (a) Structure and relevant dimensions. Distribution of the electric field for the even (b) and odd (c) modes.

was already done in for the case of a single microstrip transmission line. However, in this case, a different effective relative electrical permittivity needs to be defined for the even, $\varepsilon_{eff,e}$, and odd, $\varepsilon_{eff,o}$, mode cases, since their field distributions depicted in Fig. 2.9b and Fig. 2.9c do not cover the same parts of air and substrate. The immediate consequence of this difference is that both modes will propagate with different velocities, being $v_{p,e}$ the proper from the even mode, and $v_{p,o}$ the corresponding one for the odd case. These velocities can be calculated as:

$$v_{p,e} = \frac{c_0}{\sqrt{\varepsilon_{eff,e}}} \tag{2.179}$$

$$v_{p,o} = \frac{c_0}{\sqrt{\varepsilon_{eff,o}}} \tag{2.180}$$

It is noticeable that due to (2.179) and (2.180), the phase constant of the two modes will be also different, as it is shown below:

$$\beta_e = \frac{2 \cdot \pi \cdot f}{v_{p,e}} = \frac{2 \cdot \pi \cdot f}{c_0} \cdot \sqrt{\varepsilon_{eff,e}} \tag{2.181}$$

$$\beta_o = \frac{2 \cdot \pi \cdot f}{v_{p,o}} = \frac{2 \cdot \pi \cdot f}{c_0} \cdot \sqrt{\varepsilon_{eff,o}} \tag{2.182}$$

The value of $\varepsilon_{eff,e}$ can be calculated for a symmetrical edge coupled transmission lines that feature a width in their metallic strips of W, that are also separated a distance s, over a substrate of relative electrical permittivity of ε_r, and thickness h, by means of [34]:

$$\varepsilon_{eff,e} = 0.5 \cdot (\varepsilon_r + 1) + 0.5 \cdot (\varepsilon_r - 1) \cdot \left(1 + \frac{10}{v}\right)^{-[a_e(v) \cdot b_e(\varepsilon_r)]} \tag{2.183}$$

where:

$$v = u \cdot \frac{(20 + g^2)}{(10 + g^2)} + g \cdot e^{-g} \tag{2.184}$$

$$a_e(v) = 1 + \frac{1}{49} \cdot \ln\left[\frac{v^4 + \left(\frac{v}{52}\right)^2}{v^4 + 0.432}\right] + \frac{1}{18.9} \cdot \ln\left[1 + \left(\frac{v}{18.1}\right)^3\right] \tag{2.185}$$

$$b_e(\varepsilon_r) = 0.564 \cdot \left(\frac{\varepsilon_r - 0.9}{\varepsilon_r + 3}\right)^{0.053} \tag{2.186}$$

and being,

$$u = \frac{W}{h} \tag{2.187}$$

$$g = \frac{s}{h} \tag{2.188}$$

Similar expressions are available for calculating $\varepsilon_{eff,o}$, taking into account the identities of (2.187) and (2.188) [34]:

$$\varepsilon_{eff,o} = \left[0.5 \cdot (\varepsilon_r + 1) + a_o(u, \varepsilon_r) - \varepsilon_{eff,in}\right] \cdot e^{(-c_o \cdot g^{d_o})} + \varepsilon_{eff,in} \tag{2.189}$$

where:

$$a_o(u, \varepsilon_r) = 0.7287 \cdot \left[\varepsilon_{eff,in} - 0.5 \cdot (\varepsilon_r + 1)\right] \cdot \left[1 - e^{(-0.179 \cdot u)}\right] \tag{2.190}$$

$$c_o = b_o(\varepsilon_r) - [b_o(\varepsilon_r) - 0.207] \cdot e^{(-0.414 \cdot u)} \tag{2.191}$$

$$d_o = 0.593 + 0.694 \cdot e^{(-0.562 \cdot u)} \tag{2.192}$$

being

$$b_o = \frac{0.747 \cdot \varepsilon_r}{0.15 + \varepsilon_r} \tag{2.193}$$

where $\varepsilon_{eff,in}$, is the effective relative electrical permittivity of a single microstrip line of width W.

It must be highlighted that this difference in the propagation velocity as well as in the phase constants may result troublesome when synthetizing a device in microstrip coupled lines technology. Moreover, the values of $\varepsilon_{eff,e}$ and $\varepsilon_{eff,o}$ will depend on W and s, that will be related in turn with the characteristic impedances of both modes. Accordingly, if the characteristic impedances of both modes are not constant along z, then $\varepsilon_{eff,e}$ and $\varepsilon_{eff,o}$ will be also a function of z. Nonetheless, the differences in the phase constant as well as in the propagation velocities of both modes will be compensated by using the procedure that is fully detailed in section 2.2.2.1 that will lead to a modified propagation axis. As in the case of the single microstrip line, the most accurate models also employ the frequency [53], [54] for determining $\varepsilon_{eff,e}$ and $\varepsilon_{eff,o}$, so in general it can be concluded that $\varepsilon_{eff,e} = \varepsilon_{eff,e}(z, f)$ and $\varepsilon_{eff,o} = \varepsilon_{eff,o}(z, f)$ and thus, the width of the metallic strips, as well as the characteristic impedances of the modes, will be frequency dependent.

Regarding the characteristic impedances of the even and odd modes, $Z_{0,e}$ and $Z_{0,o}$, respectively, they must satisfy that:

$$Z_{0,e} \cdot Z_{0,o} = Z_0^2 \tag{2.194}$$

where Z_0 is the characteristic impedance of the coupled lines. Thus, the quasi-static even-mode characteristic impedance, $Z_{0,e}$, can be calculated using (2.187) and (2.188) from the physical dimensions of the line as [34]:

$$Z_{0,e} = Z_0 \cdot \frac{\sqrt{\frac{\varepsilon_{eff,in}}{\varepsilon_{eff,e}}}}{1 - \frac{Z_0}{377} \cdot \sqrt{\varepsilon_{eff,in}} \cdot Q_4} \tag{2.195}$$

being:

$$Q_4 = \frac{2 \cdot Q_1}{Q_2} \cdot \frac{1}{e^{-g} \cdot u^{Q_3} + (2 - e^{-g}) \cdot u^{-Q_3}} \tag{2.196}$$

with:

$$Q_1 = 0.8695 \cdot u^{0.194} \tag{2.197}$$

$$Q_2 = 1 + 0.7519 \cdot g + 0.189 \cdot g^{2.31} \tag{2.198}$$

$$Q_3 = 0.1975 + \left[16.6 + \left(\frac{8.4}{g}\right)^6\right]^{-0.387} + \frac{\ln\left[\frac{g^{10}}{1 + \left(\frac{g}{3.4}\right)^{10}}\right]}{241} \tag{2.199}$$

With regard to the quasi-static odd-mode characteristic impedance, $Z_{0,o}$, it can be calculated taking under consideration again (2.187) and (2.188), as follows [34]:

$$Z_{0,o} = Z_0 \cdot \frac{\sqrt{\frac{\varepsilon_{eff,in}}{\varepsilon_{eff,o}}}}{1 - \frac{Z_0}{377} \cdot \sqrt{\varepsilon_{eff,in}} \cdot Q_{10}} \tag{2.200}$$

being:

$$Q_{10} = \frac{Q_2 \cdot Q_4 - Q_5 \cdot e^{\ln(u) \cdot Q_6 \cdot u^{-Q_9}}}{Q_2} \tag{2.201}$$

with:

$$Q_5 = 1.794 + 1.14 \cdot \ln\left(1 + \frac{0.638}{g + 0.517 \cdot g^{2.43}}\right) \tag{2.202}$$

$$Q_6 = 0.2305 + \frac{\ln\left[\frac{g^{10}}{1 + \left(\frac{g}{5.8}\right)^{10}}\right]}{281.3} + \frac{\ln(1 + 0.598 + g^{1.154})}{5.1} \tag{2.203}$$

$$Q_7 = \frac{10 + 190 \cdot g^2}{1 + 82.3 \cdot g^3} \tag{2.204}$$

$$Q_8 = e^{-6.5 - 0.95 \cdot \ln(g) - \left(\frac{g}{0.15}\right)^5} \tag{2.205}$$

$$Q_9 = \ln(Q_7) \cdot \left(Q_8 + \frac{1}{16.5}\right) \tag{2.206}$$

As in the case of the single microstrip transmission line, more accurate expressions that take into account the thickness of the metallic strips and the frequency can be obtained by using the *Keysight*™ *ADS Linecalc* software tool, which is based on [34], [36], [53], [54].

In order to conclude this subsection, it must be highlighted that closed-form expressions have been found to relate the characteristic impedance of the even and odd modes with the physical dimensions of the symmetrical edge coupled microstrip transmission lines. Since these characteristic impedances are related with the coupling coefficients of both modes, the dimensions of the coupled microstrip transmission lines can be calculated so as to satisfy those coupling coefficients as well as the frequency response determined by them.

2.2.2. Modelling of Non-Uniform Waveguides that Exhibit a Variable Phase Constant along the Propagation Direction

As it has been already mentioned, the single-mode operation assumption will allow us to solve the synthesis problem under the coupled-mode formulation, using the analytical expressions of CHAPTER 3, as well as the inverse scattering techniques that will be covered in depth throughout CHAPTER 4, CHAPTER 5, and CHAPTER 6. However, it will be also exposed that an additional assumption must be performed in order to be able to reach a solution for the synthesis problem: the nonuniform waveguide structure, and specifically the operation mode, must be assumed to feature a phase constant that remains unaltered along the propagation direction. This principle means that the phase constant for a certain frequency must not vary along the propagation variation, being only a function of frequency, i.e. $\beta(f,z)=\beta(f)$.

However, in many cases the change of the electrical or dimensional properties of a nonuniform waveguide leads to an implicit change of the phase constant along the propagation direction, i.e., $\beta=\beta(f,z)$. For instance, the variation of the width, a, of a rectangular waveguide along the propagation direction involves a variation of β along z, something that becomes obvious by checking (2.117). On the other hand, when dealing with a microstrip transmission line with changes in its strip width, W, an inherent variation of the effective electric permittivity in the propagation direction will be caused due to (2.149), i.e. $\varepsilon_{eff}(z)$. Therefore, in view of (2.151) it will be clear that if ε_{eff} is a function of z, then β will also show a dependence on the position, i.e. $\beta=\beta(f,z)$. Finally, it is worth noting that the phase constants of the even, β_e, and odd, β_o, modes associated to microstrip coupled lines will also exhibit this undesired aspect when the width, W, or the gap, g, between the metallic strips do not remain unaltered along z. In this case $\varepsilon_{eff,e}$ and $\varepsilon_{eff,o}$ will be also z-dependent because of (2.183)-(2.186) and (2.189)-(2.193), respectively, leading in turn to $\beta_e=\beta_e(f,z)$ and $\beta_o=\beta_o(f,z)$, see (2.181) and (2.182).

However, in these cases where $\beta=\beta(f,z)$, it will be possible to model approximately the electromagnetic behavior of the structure under the single-mode operation assumption by means of a reference phase constant, β_{ref}, that will be assumed not to vary along a normalized propagation axis, χ. The approximation made using β_{ref} and χ will be exact for an arbitrarily

selected frequency, f_t, although the accuracy will decrease as the frequency under consideration deviates from f_t.

Firstly, the relationship between the frequency, f, and the reference phase constant, β_{ref}, must be univocal, while also being a monotonically increasing function in the operation bandwidth. For example, if the dimensions of the final device along z are unknown, β_{ref} can be calculated from that of the input port of the device, $\beta_{ref} = \beta(f, z = 0)$, since it is the only point where the dimensions can be chosen as desired, because of (2.130), (2.139) for rectangular waveguide and (2.146) for transmission line technologies. However, any other point of the propagation axis can be selected to determine the relationship $\beta_{ref}(f)$, and it can be even calculated as the average phase constant, for each frequency, between the two extremes of the device, $z = 0$ and $z = L$, i.e. $\beta_{ref}(f) = \frac{\beta(f,z=0)+\beta(f,z=L)}{2}$, as it was done in [55] for the design of tapered matching sections in rectangular waveguide.

In order to carry out the synthesis process, it will be assumed that β_{ref} will not vary along a normalized propagation axis, χ. For the mathematical formulation to be consistent, the differential electrical length achieved along a certain $d\chi$, i.e., $\beta_{ref} \cdot d\chi$, must be the same caused by the actual β in dz, i.e., $\beta_{ref} \cdot d\chi = \beta \cdot dz$. This relationship implies that:

$$\frac{dz}{d\chi} = \frac{\beta_{ref}}{\beta} \tag{2.207}$$

In view of (2.207), the actual propagation axis z can be calculated from the normalized propagation axis χ, by means of (2.208):

$$z(f_t, \chi) = \int_0^{\chi} \frac{\beta_{ref}(f_t)}{\beta(f_t, r)} \cdot dr \tag{2.208}$$

where r is a dummy variable of integration.

Let's consider now the single-mode coupled-mode equations of (2.91), (2.92) that are shown again below for the sake of clarity:

$$\frac{da^+}{dz} = -j \cdot \beta \cdot a^+ + K \cdot a^- \tag{2.91}$$

$$\frac{da^-}{dz} = j \cdot \beta \cdot a^- + K \cdot a^+ \tag{2.92}$$

In order to rewrite (2.91) as a function of the normalized propagation axis χ, and of the reference propagation constant, β_{ref}, the following procedure will be applied:

$$\frac{da^+}{dz} = \frac{da^+}{d\chi} \cdot \frac{d\chi}{dz} \tag{2.209}$$

Proceeding in the same way, and taking into account the dependence of the coupling coefficient $K(z)$ on ν, see (2.93) and (2.100), with $\nu = \tan(\alpha)$, calculated as the derivative with z of the corresponding physical dimension, it will be possible to rewrite:

$$K(z) = K(\chi) \cdot \frac{d\chi}{dz} \tag{2.210}$$

Moreover, taking into account (2.207), β can be also expressed as a function of β_{ref} and $d\chi/dz$:

$$\beta = \beta_{ref} \cdot \frac{d\chi}{dz} \tag{2.211}$$

Now, by substituting (2.209), (2.210) and (2.211) into (2.91), equation (2.212) is finally obtained. Moreover, proceeding in a similar manner with (2.92), equation (2.213) will be found:

$$\frac{da^+}{d\chi} = -j \cdot \beta_{ref} \cdot a^+ + K(\chi) \cdot a^- \tag{2.212}$$

$$\frac{da^-}{d\chi} = j \cdot \beta_{ref} \cdot a^- + K(\chi) \cdot a^+ \tag{2.213}$$

It is important to highlight that (2.212) and (2.213) constitute a system of coupled-mode equations, fully analogous to (2.91), (2.92), but formulated for the normalized position χ, and the reference propagation constant β_{ref}, that does not vary with χ. This will allow us to consider a medium where β does not vary with the normalized position, which is one of the main requirements of the synthesis techniques that will be presented between CHAPTER 3-CHAPTER 6, but it will be necessary to employ β_{ref} and χ instead of β and z. In the last step of the synthesis process $z(\chi)$ will be calculated by means of (2.208). By doing so, the result of the synthesis will be fully suitable for a position dependent β, and the undesired effects will be avoided. Nevertheless, it must be noted that the $z(\chi)$ transformation is done for a single frequency, f_t, and it works properly for the frequency range where the quotient $\beta_{ref}(f)/\beta(f,z)$ does not vary much with respect to $\beta_{ref}(f_t)/\beta(f_t,z)$. Due to this fact, it is advisable to perform

the transformation for a f_t located at the center of the operation bandwidth of the device under consideration.

Finally, in order to summarize the contents of this section, it must be highlighted that the modelling proposed for nonuniform waveguide structures that present a variation of β along the propagation axis allows us to synthetize structures assuming that β remains constant along a normalized axis χ. Once the synthesis has been performed, it will be necessary to denormalize χ, or in other words to calculate $z(\chi)$ using (2.208), so as to obtain a device that meets the pursued frequency response despite of being implemented in a waveguide structure where β varies with the position z.

2.2.2.1. Modelling for Microstrip Edge Coupled Transmission Lines

In the previous section, a method has been proposed to model a waveguide technology whose phase constant, β, can vary along the propagation axis z, as a waveguide where it remains always constant along the propagation direction, so as to allow the application of the synthesis procedures using a reference phase constant, β_{ref}, and a normalized propagation axis, χ. In the last step of the synthesis the actual propagation axis, z, is calculated by means of (2.208), considering the β_{ref} selected as well as the actual phase constant that is achieved at each point of the normalized propagation axis, i.e. $\beta(f_t, \chi)$. It must be noted that this modelling method can be only applied when considering single mode operation. However, when considering edge coupled transmission lines, the mode decomposition that has been employed in section 2.2.1.3 for the analysis of this kind of structures results in the so-called even and odd modes. In that section it was shown how that modes have their independent coupled-mode equations, being (2.61), (2.62) the concerning ones for the even case, while (2.63), (2.64) are the proper ones for the odd mode case. Thus, if the modelling method of (2.208) is directly applied to each mode, and the same β_{ref} is considered for both modes, the corresponding transformations will lead to different propagation axis for the even and odd modes, $z_e(\chi)$ and $z_o(\chi)$, respectively, that will be obtained by applying (2.208) as:

$$z_e(f_t, \chi) = \int_0^{\chi} \frac{\beta_{ref}(f_t)}{\beta_e(f_t, r)} \cdot dr \tag{2.214}$$

$$z_o(f_t,\chi) = \int_0^{\chi} \frac{\beta_{ref}(f_t)}{\beta_o(f_t,r)} \cdot dr \tag{2.215}$$

where $\beta_e(f_t,r)$ and $\beta_o(f_t,r)$ stand for the actual phase constant of the even and odd mode, respectively. Indeed, if the expressions for β_e and β_o provided in (2.181) and (2.182), respectively, are incorporated into (2.214) and (2.215), it will be found that $z_e(\chi)$ and $z_o(\chi)$ can be expressed in terms of the effective electrical permittivity of both modes as:

$$z_e(f_t,\chi) = \int_0^{\chi} \sqrt{\frac{\varepsilon_{eff,ref}(f_t)}{\varepsilon_{eff,e}(f_t,r)}} \cdot dr \tag{2.216}$$

$$z_o(f_t,\chi) = \int_0^{\chi} \sqrt{\frac{\varepsilon_{eff,ref}(f_t)}{\varepsilon_{eff,o}(f_t,r)}} \cdot dr \tag{2.217}$$

where $\varepsilon_{eff,ref}(f_t)$ can be defined as the reference effective electrical permittivity of both modes at the frequency f_t, which will be determined as:

$$\varepsilon_{eff,ref}(f_t) = \left[\frac{\beta_{ref}(f_t)\cdot c_0}{2\cdot\pi\cdot f}\right]^2 \tag{2.218}$$

It is important to note that since β_{ref} can be arbitrarily chosen, the value of $\varepsilon_{eff,ref}(f_t)$ can be also selected as desired so as to achieve a certain sought value of β_{ref}. For example, in those cases where $Z_{0,e}(\chi) \geq Z_{0,e}(\chi=0)$ and $Z_{0,o}(\chi) \leq Z_{0,o}(\chi=0)$, one of the most useful choices that can be performed for the $\varepsilon_{eff,ref}(f_t)$ value is $\varepsilon_{eff,ref}(f_t) = \varepsilon_{eff,in}(f_t, z=0)$, with $\varepsilon_{eff,in}(f_t, z=0)$ defined as in section 2.2.1.3.1, i.e. the effective relative electrical permittivity of a single microstrip line of width W. By doing so, χ will be a good first approximation of z_e and z_o, since $\varepsilon_{eff,o}(f_t) < \varepsilon_{eff,in}(f_t) < \varepsilon_{eff,e}(f_t)$. An example of this choice is provided in Fig. 2.10a.

Therefore, if it is required to maintain a certain relationship between $K_e(\chi)$ and $K_o(\chi)$ (or alternatively between $Z_{0,e}(\chi)$ and $Z_{0,o}(\chi)$), due to (2.167) and (2.168), respectively, for the achievement of a desired frequency response of a microstrip coupled line structure (see section 2.2.1.3), it will be necessary to denormalize the χ propagation axis in z_e and z_o for the even and odd modes respectively. Thus, the final impedance profiles will be $Z_{0,e}(z_e)$ and $Z_{0,o}(z_o)$ as it is

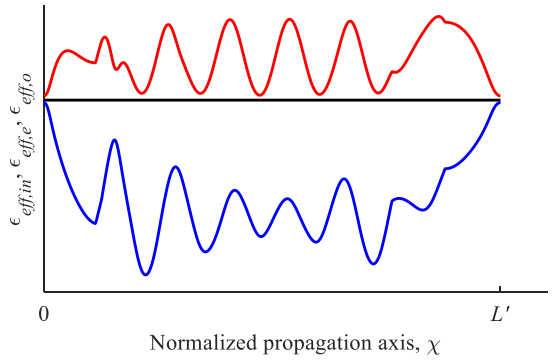

(a)

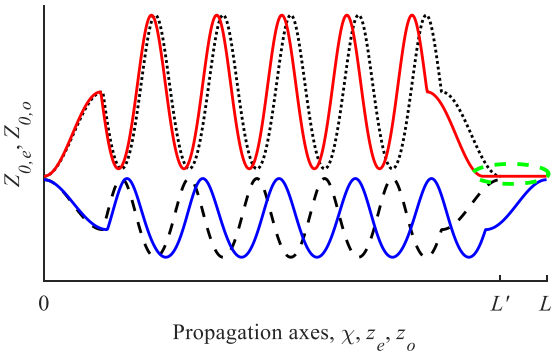

(b)

Fig. 2.10. Sketch of the modelling of a generic microstrip coupled-line structure: (a) the constant value of $\varepsilon_{eff,ref}(f_t)$ has been selected following the criterion $\varepsilon_{eff,ref}(f_t) = \varepsilon_{eff,in}(f_t, z = 0)$ and the actual values of $\varepsilon_{eff,e}(f_t, \chi)$ and $\varepsilon_{eff,o}(f_t, \chi)$ are also provided. (b) $Z_{0,e}$ and $Z_{0,o}$ profiles in the normalized χ propagation axis (dotted and dashed black traces, respectively) and in the actual z axis (red and blue traces, respectively). The uniform transmission line section added to reach the length $L = L_e = L_o$ is highlighted with a green dashed circle.

depicted in the sketch of Fig. 2.10. By doing so, the difference between their corresponding phase constants, β_e and β_o, will be equalized and the frequency response will be the expected for the combination of $K_e(\chi)$ and $K_o(\chi)$. It is noticeable that the device will achieve a length L' in the normalized propagation axis, χ, while different lengths for the even and odd modes, $L_e = \max\{z_e\}$ and $L_o = \max\{z_o\}$, respectively, will be finally obtained as a consequence of the denormalization process. Indeed, it will be always obtained that $L_e < L_o$ since $\varepsilon_{eff,o}(f_t, z) < \varepsilon_{eff,e}(f_t)\ \forall\, z$. Therefore, it will be necessary to complete the shortest even impedance profile with an uniform transmission line section of the final even impedance value, $Z_{0,e}(z_e = L_e)$, so as to artificialy reach the same length for both modes, L, with $L = L_e = L_o$. In the red trace of Fig. 2.10b that corresponds to the even mode impedance profile, the mentioned uniform

transmission line section addition can be appreciated (it is highlighted with a green dashed circle) at the end of the profile.

Nonetheless, as in the case of a single line, this modelling that allows the synthesis is fully exact for the selected frequency, f_t, and approximated around that frequency. Thus, it will be advisable to choose f_t in the center of the operational bandwidth or at a specific frequency where the most accurate modelling is required. It is worth noting that this modelling technique was successfully demonstrated by Chudzik *et al.* in [50] for the design of arbitrary order differentiators implemented in microstrip coupled lines for the achievement of effective transmission operation. Nevertheless, it is obvious that the proposed methodology can be also applied to other kind of coupled transmission lines with characteristics that are not covered in this thesis although they are studied in [19], [20], [34].

2.2.3. Assimilation of the Effects of Cut-Off Modes in Closed-Boundary Waveguides Using the Single-Mode Operation Approach

The single-mode operation approach must be the starting point to deal with the synthesis problem as it has been stated during this chapter. However, the single-mode coupled-mode equation system of (2.91), (2.92) may not be an accurate enough approximation of the general system of (2.3) so as to represent the frequency response of a certain waveguide device, even in the cases where the fundamental mode is propagating and all the higher-order ones remain under cut-off regime, due to the parasitic reactive couplings between all of them. An intuitive approximation based on the general equation system of the Coupled-Mode Theory can be performed in order to take into account the effects of the cut-off modes in closed-boundary waveguides to make the synthesis procedure more accurate.

Firstly, when the expression (2.3) is particularized for the case of $m = 1$ (forward travelling wave of the fundamental mode), neglecting the continuous spectrum modes due to the closed-boundary condition, its corresponding coupled-mode equation is achieved. Moreover, assuming that the normalization factor of the mode, N_1, remains constant with z (and consequently $C_{1,1} = 0$ due to (2.38)), and extracting the corresponding term of the backward travelling wave of the first mode ($i = -1$) from the summation, the following expression will be attained:

$$\frac{da_1}{dz} = -j \cdot \beta_1 \cdot a_1 + C_{1,-1} \cdot a_{-1} + \sum_{|i|>1} C_{1,i} \cdot a_i \tag{2.219}$$

It is very important to stress that (2.91) and (2.219) are quite similar between them (except for the cut-off modes term) if the following identities, $C_{1,-1} = K$, $a_1 = a^+$, $a_{-1} = a^-$, and $\beta_1 = \beta$ are recalled. In fact, a useful rearrangement can be applied to the cut-off modes term of (2.219), yielding to:

$$\frac{da_1}{dz} = -j \cdot \left[\beta_1 + j \sum_{|i|>1} \frac{C_{1,i} \cdot a_i}{a_1} \right] \cdot a_1 + C_{1,-1} \cdot a_{-1} \tag{2.220}$$

Now, by inspecting (2.220), and comparing it with (2.91), it is clear that the parasitic effect of the higher-order mode couplings can be interpreted as an effective change of the propagation constant of the first mode along the propagation direction. In fact, the effective complex propagation constant, β', can be defined to incorporate the parasitic effects of the cut-off modes to the phase term, leading to:

$$\frac{da_1}{dz} = -j \cdot \beta' \cdot a_1 + C_{1,-1} \cdot a_{-1} \tag{2.221}$$

where $\beta' = \beta_{eff} - j \cdot \alpha_{eff}$, with β_{eff} and α_{eff} being the effective phase and loss constants, respectively, that can be defined as:

$$\beta_{eff} = \beta_1 - Im\left\{\sum_{|i|>1} \frac{C_{1,i} \cdot a_i}{a_1}\right\} \tag{2.222}$$

$$\alpha_{eff} = -Re\left\{\sum_{|i|>1} \frac{C_{1,i} \cdot a_i}{a_1}\right\} \tag{2.223}$$

It is also worth noting that equation (2.221) encompasses the term associated to higher-order modes by means of the definition of β', giving rise to a differential equation that is fully analogous to (2.91).

It is important to stress that the expressions (2.222) and (2.223) can be applied only when the fundamental mode is propagating and the higher order ones are under cut-off regime, since the border between cut-off and propagation may lead to singularities in $C_{1,i}$ and a_i, which will involve infinite values of β_{eff} and α_{eff}.

Therefore, it can be considered that the parasitic couplings to higher-order modes cause a double effect in the expected behavior of the waveguide structure when assuming single-mode operation: firstly, a continuous change in the effective phase constant of the first mode that is represented by β_{eff}. On the other hand, the term associated with α_{eff} mathematically describes the local "loss" or "recovery" of energy by the fundamental mode due to the coupling to cut-off modes that are able to locally store and "give back" the energy.

It must be highlighted that the complex propagation constant, β', will no longer be constant in the propagation direction, z, since it depends on the complex amplitudes a_1 and a_i, as well as on the coupling coefficients of the form $C_{1,i}$, with $|i| > 1$, that are also variable with z. In order to deal with this situation, two different approaches may be followed. The first one can be employed as a first simple approximation, and it will be known as the uniform scaling

method, while the most accurate one will be based on an iterative distributed scaling of the propagation axis.

2.2.3.1. Uniform-Scaling Method

The simplest solution to assimilate the effects of cut-off modes to the single-mode operation assumption is the uniform scaling method. In order to apply it, the first task is to solve the coupled mode equation system (2.3) only for discrete spectrum modes (a closed waveguide is assumed), after having calculated the necessary coupling coefficients, $C_{m,i}$. Thus, the problem that we have to solve is a system of first order linear ordinary differential equations that must be solved between $z = 0$ and $z = L$. If it is assumed that the structure is going to be excited with the forward-travelling wave of the fundamental mode ($m = 1$) at $z = 0$, while featuring the output port matched for all modes, it will be possible to calculate the complex amplitude of each mode (specifically of its forward and backward travelling waves) along the waveguide structure as well as its S parameters. These assumptions will constitute the boundary conditions of the problem and they can be mathematically formulated as follows:

$$a_1(z = 0) = 1 \tag{2.224}$$

$$a_m(z = 0) = 0 \; \forall \; m > 1 \tag{2.225}$$

$$a_m(z = L) = 0 \; \forall \; m < 0 \tag{2.226}$$

It is worth noting that due to (2.224) and (2.225) an exclusive unitary excitation of the fundamental mode is set at the input port of the device, whereas (2.226) represents the matching condition at the output port. With these boundary conditions, the problem of (2.3) becomes a two-point boundary value problem. In order to solve it, the numerical method implemented in the *Matlab* function "bvp4c.m" for the solution of boundary value problems can be employed [56], [57]. By doing so, the complex amplitudes a_1 and a_i will be determined, allowing us to calculate β' as well as β_{eff} and α_{eff} from (2.222) and (2.223). Then, it will be possible to deduce the average value of both parameters as:

$$\bar{\beta}' = \frac{\int_0^L \beta' \cdot dz}{L} = \frac{\int_0^L \left(\beta_{eff} - j \cdot \alpha_{eff}\right) \cdot dz}{L} = \bar{\beta}_{eff} - j \cdot \bar{\alpha}_{eff} \tag{2.227}$$

where $\bar{\beta}_{eff}$ and $\bar{\alpha}_{eff}$ are the average phase and loss constants, respectively.

Now, it is important to realize that the effective loss term is locally not null, i.e., $\alpha_{eff}(z) \neq 0$. However, the Coupled-Mode Theory does not consider dissipative losses and thus, all the power supplied to the waveguide structure in the fundamental mode must leave the structure also in that mode (all the higher order modes are under cut-off) and consequently, the average loss constant must satisfy $\bar{\alpha}_{eff} = 0$. Taking that into account, the average propagation constant is identified with the average phase constant, i.e., $\bar{\beta}' = \bar{\beta}_{eff}$, giving rise to a coupled-mode equation (2.228) that is fully analogous to the one of the single-mode assumption of (2.91), but considering the average effective phase constant, $\bar{\beta}_{eff}$, instead of the one of the fundamental mode, β_1.

$$\frac{da_1}{dz} = -j \cdot \bar{\beta}_{eff} \cdot a_1 + a_{-1} \cdot C_{1,-1} \tag{2.228}$$

Therefore, if the single-mode operation assumption is employed to synthetize a waveguide structure, the expected frequency response will be shifted in frequency, because of the difference between the value used in the synthesis procedure, β_1, and the effective value resulting from the coupling of cut-off modes, $\bar{\beta}_{eff}$. Fortunately, the scaling property of the coupling coefficient (2.229) that was originally reported in [58], can be applied to relate the required scaling of the propagation axis with the shift produced in the frequency response in reflection:

$$\psi \cdot K(z \cdot \psi) \leftrightarrow S_{11}\left(\frac{\beta}{\psi}\right) \tag{2.229}$$

In order to be coherent with (2.229), the final propagation axis must be calculated as z/ψ, and the amplitude of the coupling coefficient must be scaled as $\psi \cdot K(z)$. The scaling factor, ψ, can be calculated from (2.230) as a relation between $\bar{\beta}_{eff}$ and β_1.

$$\psi(f_t) = \frac{\bar{\beta}_{eff}(f_t)}{\beta_1(f_t)} \tag{2.230}$$

where f_t, is the frequency where both phase constants, $\beta_1(f)$ and $\bar{\beta}_{eff}$, are calculated. In fact, it must be noticed that the scaling factor is also frequency dependent and the approximation employed to consider the reactive couplings between the fundamental and the cut-off modes is exact at the frequency where the scaling factor is calculated, i.e., f_t. Accordingly, this approximation becomes less accurate when considering frequencies far away from f_t.

The uniform scaling method may result accurate enough as a first approximation, since it only models the shift of the expected frequency response produced as a result of the parasitic

couplings to cut-off modes that were neglected with the single-mode approximation. However, the effects of these reactive couplings could be not exclusively limited to a frequency displacement, and more dramatical degradation of the frequency response can be caused. Thus, in certain cases, the uniform scaling method could be not accurate enough and it will be necessary to resort to the more complex recursive distributed scaling method.

2.2.3.2. Recursive Distributed Scaling Method

The most accurate method to assimilate the parasitic effects of cut-off modes in the single-mode coupled-mode equation system of (2.91) and (2.92) will lead to a distributed scaling of the propagation axis that is performed in an iterative manner.

As it has been explained in the mathematical procedure carried out between (2.219) and (2.223), the effect of cut-off modes can be modelled using a complex propagation constant, β', that can be divided into effective phase and loss constants as $\beta' = \beta_{eff} - j \cdot \alpha_{eff}$. Furthermore, as it has been previously commented, β' will vary with z since it depends on a_1, a_i, and $C_{1,i}$ that are functions of z, i.e. $\beta'(z) = \beta_{eff}(z) - j \cdot \alpha_{eff}(z)$.

As it was also explained, the loss aspect of the effects of cut-off modes, $\alpha_{eff}(z)$, stands for the reactive energy transferring between the fundamental and higher-order modes. This local energy interchange cannot be compensated up to date, but fortunately its effects will be limited since the average value of $\alpha_{eff}(z)$ will be null as it was previously explained.

However, the term $\beta_{eff}(z)$ implies a continuous variation of the effective phase constant of the fundamental mode along z. As it was studied in detail in section 2.2.2, this kind of variation of β along z for the same frequency, i.e. $\beta = \beta(f, z)$, can be modelled using a normalized axis χ, and a reference phase constant, β_{ref}, which is assumed not to vary along χ. Taking that into account, it will be possible to assimilate that effect associated to higher-order cut-off modes, which is expressed by $\beta_{eff}(z)$, using a single-mode modelling of the waveguide device where β_{ref} remains constant along the normalized propagation axis, χ, as it was done in section 2.2.2. For the case under study in this section, the normalized axis will be denoted by z_1, i.e. $z_1 = \chi$, whereas the fixed phase constant along this axis will correspond to the phase constant of the fundamental mode, β_1, i.e. $\beta_1 = \beta_{ref}$. Regarding the variable effective phase constant and the actual propagation axis, they will be expressed by β_{eff} and z_2, respectively. Therefore, the modelling of the pair z_2, β_{eff} (where β_{eff} varies along the propagation axis) with the pair z_1,

β_1 (where β_1 remains constant along the propagation axis) will be based on the fulfillment of the following relationship:

$$\beta_1 \cdot dz_1 = \beta_{eff} \cdot dz_2 \tag{2.231}$$

Recalling (2.207) and (2.208), equation (2.231) yields to the following expression for the calculation of $z_2(f_t, z_1)$, see section 2.2.2:

$$z_2(f_t, z_1) = \int_0^{z_1} \frac{\beta_1(f_t)}{\beta_{eff}(f_t, r)} \cdot dr \tag{2.232}$$

where r is a dummy variable of integration and f_t is the frequency selected for the modelling, as it is explained in section 2.2.2.

Therefore, when considering a certain closed-boundary waveguide structure, it can be modelled in a first approximation by assuming single-mode operation, with a normalized propagation axis, z_1, and a phase constant, β_1, which will be only a function of frequency. If just the fundamental mode is in propagation along the structure (all the higher order modes are cut-off throughout the device), it will be possible to perform the assimilation of the effect of cut-off modes that are neglected by the single-mode version of the coupled-mode equation system of (2.91) and (2.92). For doing so, the first task is to calculate $C_{1,i}(f_t, z_1)$, together with the rest of the necessary coupling coefficients, to solve the general coupled-mode equation system of (2.3) as it was explained at the beginning of subsection 2.2.3.1, so as to calculate the complex amplitudes $a_1(f_t, z_1)$ and $a_i(f_t, z_1)$. At this point, β_{eff} can be obtained by means of (2.222). If the denormalization $z_2(z_1)$ is performed using (2.232), the obtained structure in z_2 should compensate for the non-ideal behavior predicted by $\beta_{eff}(f_t, z_1)$.

However, it must be noted that if the resulting structure in z_2 is again analyzed using the general coupled-mode equation system of (2.3), the complex amplitudes a_1 and a_i will not be exactly the ones that were predicted with the previous analysis performed considering the structure in z_1, i.e. $a_1[f_t, z_2(z_1)] \neq a_1(f_t, z_1)$ and $a_{\mathrm{i}}[f_t, z_2(z_1)] \neq a_{\mathrm{i}}(f_t, z_1)$. Therefore, the effective phase constant in z_2, $\beta_{eff}(f_t, z_2)$, will be slightly different from the one predicted by $\beta_{eff}(f_t, z_1)$, i.e. $\beta_{eff}[f_t, z_2(z_1)] \neq \beta_{eff}(f_t, z_1)$. Fortunately, it will be possible to perform a recursive denormalization process in order to achieve a sufficiently accurate prediction of β_{eff}. Taking this aim into account, it will be advisable to introduce a small change in the notation in order to avoid the use of confusing nomenclature. Accordingly, $\beta_{eff,1}(z_1) = \beta_{eff}(z_1)$ will be employed as the prediction for the z_2 axis through the function $z_2(z_1)$ of (2.232), as

$\beta_{eff,1}[f_t, z_2(z_1)] = \beta_{eff,1}(f_t, z_1)$. Finally, the actual β_{eff} calculated from the multimode analysis of (2.3) for the structure in z_2 will be expressed by $\beta_{eff,2}(z_2) = \beta_{eff}(z_2)$.

It is worth noting that at this point, a new denormalization step can be carried out by considering the predicted $\beta_{eff,1}[f_t, z_2(z_1)]$ and the actual $\beta_{eff,2}(z_2)$ found. If equation (2.232) is adapted for these phase constants, a new propagation axis, z_3, will be reached as:

$$z_3(f_t, z_2) = \int_0^{z_2} \frac{\beta_{eff,1}[f_t, r(z_1)]}{\beta_{eff,2}(f_t, r)} \cdot dr \tag{2.233}$$

The procedure can be repeated recursively until we achieve a certain z_N that accomplishes a convergence limit in the similarity between z_N and z_{N-1}. Indeed, this limit will be reached when the predicted $\beta_{eff,N-2}[f_t, z_{N-1}(z_{N-2})]$ is close enough to the calculated $\beta_{eff,N-1}(f_t, z_{N-1})$. The distributed scaling method will provide satisfactory results when the following approximated condition is attained:

$$\beta_1(f_t) \cdot dz_1 \approx \beta_{eff,N}(f_t, z_N) \cdot dz_N \tag{2.234}$$

It will be possible to generalize (2.233) for each iteration step l, with $1 \leq l \leq N-1$ as:

$$z_{l+1}(f_t, z_l) = \int_0^{z_l} \frac{\beta_{eff,l-1}[f_t, r(z_{l-1})]}{\beta_{eff,l}(f_t, r)} \cdot dr \tag{2.235}$$

where $\beta_{eff,l-1}[f_t, r(z_{l-1})]$ is the effective phase constant prediction for the structure in the $z_l(z_{l-1})$ axis, obtained from the solution of the multimode coupled-mode equation system of (2.3) considering the structure in the z_{l-1} propagation axis. Regarding $\beta_{eff,l}(f_t, z_l)$, it denotes the effective phase constant that results from (2.222) by performing the multimode analysis of (2.3) for the waveguide device in the z_l propagation axis. It must be noted that in the case of $l = 1$, the resulting $\beta_{eff,0}[f_t, r(z_0)]$ that will be required to evaluate the numerator of (2.235) will correspond to $\beta_1(f_t)$, i.e. $\beta_{eff,0}[f_t, r(z_0)] = \beta_1(f_t, z_1) = \beta_1(f_t)$, being $\beta_1(f_t)$ the phase constant of the fundamental mode for the frequency f_t, which is assumed to remain constant along the normalized axis z_1.

Finally, it must be pointed out that the solution (2.235) depends on the election of f_t, and hence the assimilation of the effects of cut-off modes, as well as the resulting structure, will depend on the specific value of f_t selected. It is advisable to choose f_t as the central frequency of the operation bandwidth, in order to reach the best assimilation in the whole frequency range. Nevertheless, alternative interesting frequency points can be considered for other cases, like the

cut-off frequency of low-pass filters, or the center of the passband for band-pass filters. Moreover, it is worth noting that (2.222) is a generalized version of the solution (2.208) found in the previous section 2.2.2, and therefore it should model properly the cases where the fundamental mode β_1 is not constant along the propagation axis, while taking also into account the effects of cut-off modes.

REFERENCES

[1] J. W. Arnold, and P. F. Bechberger, "Sinusoidal Currents in Linearly Tapered Loaded Transmission Lines," *Proc. IRE*, vol. 19, no. 2, pp. 304-310, Feb. 1931.

[2] T. Starr, "The Nonuniform Transmission Line," *Proc. IRE*, vol. 20, no. 6, pp. 1052-1063, June 1932.

[3] J. Gurley, "Impedance matching by means of nonuniform transmission lines," *Transactions of the IRE Professional Group on Antennas and Propagation*, vol. PGAP-4, pp. 107-109, December 1952.

[4] R. W. Klopfenstein, "Nonuniform, Inhomogeneous, and Anisotropic Waveguides," *IRE Trans. Microw. Theory Tech.*, vol. 4, no. 4, pp. 193-196, October 1956.

[5] L. Solymar, "Spurious Mode Generation in Nonuniform Waveguide," *IRE Trans. Microw. Theory Tech.*, vol. 7, no. 3, pp. 379-383, July 1959.

[6] E. Karbowiak, "Distortion of information in non-uniform multi-mode waveguides," *Proc. IEEE - Part B: Electronic and Communication Engineering*, vol. 106, no. 13, pp. 9-, 1959.

[7] L. Solymar, "A note on the optimum design of non-uniform transmission lines," *Proc. IEEE* - Part C: Monographs, vol. 107, no. 11, pp. 100-104, March 1960.

[8] H. Zucker and G. I. Cohn, "Propagation of TE Modes in Nonuniform Waveguides," *IRE Trans. Microw. Theory Tech.*, vol. 10, no. 3, pp. 202-208, May 1962.

[9] H. J. Gould, A. E. Smell and C. C. Han, "New Non-Uniform Waveguide Taper Design Yielding Low VSWR and High Rejection," *1973 IEEE G-MTT International Microwave Symposium*, Boulder, CO, USA, 1973, pp. 221-223.

[10] W. Snyder, "Optical fiber with nonuniform refractive index," *Electron. Lett.*, vol. 8, no. 7, pp. 183-184, 6 April 1972.

[11] Arnedo, Ivan Arregui, M. Chudzik, F. Teberio, A. Lujambio, D. Benito, T. Lopetegi, and M. A. G. Laso, "Direct and Exact Synthesis: Controlling the Microwaves by Means of Synthesized Passive Components with Smooth Profiles," *IEEE Microw. Mag.*, vol. 16, no. 4, pp. 114-128, May 2015.

[12] J.M. Percaz, I. Arnedo, I. Arregui, F. Teberio, P. Martin-Iglesias, M. A. G. Laso, and T. Lopetegi, "General Synthesis of Tapered Matching Sections for Single-Mode Operation Using the Coupled-Mode Theory," *IEEE Trans. Microw. Theory Tech.*, vol. 67, no. 9, pp. 3511-3526, Sept. 2019.

[13] R. Pierce, ‘‘Coupling of modes of propagation,” *J. Appl. Phys.*, vol. 25, p. 179, 1954.

[14] R. W. Gould, “A Coupled Mode Description of the Backward Wave Oscillator and the Kompfner Dip Condition,” *IRE Trans. Electron. Dev.*, vol. PGED-2, pp. 37-42, 1955.

[15] S. E. Miller, “Coupled wave theory and waveguide applications,” *Bell Syst. Tech. J.*, vol. 33, pp. 661-719, 1954

[16] W. H. Louisell, "Analysis of the single tapered mode coupler," *Bell Syst. Tech. J.*, vol. 33, pp. 853-871, 1954

[17] H. Haus and W.-P. Huang, "Coupled-mode theory," *Proc. IEEE* , vol. 79, no. 10, pp. 1505-1518, Oct. 1991

[18] Txema Lopetegi, "Photonic Bandgap Structures in Microstrip Technology: Study using the Coupled Mode Formalism and Applications," Doctoral Thesis, Universidad Pública de Navarra, España, 2002.

[19] Israel Arnedo, "New Methods for the Synthesis of Microwave Devices Based on the Coupled-Mode Theory," Doctoral Thesis, Universidad Pública de Navarra, España, 2009.

[20] Magdalena Chudzik, "Synthesis Techniques for Novel Devices Based on Smooth Profiles with Application from the Microwave to the Terahertz Regions," Doctoral Thesis, Universidad Pública de Navarra, España, 2013.

[21] B. Z. Katsenelenbaum, L. Mercader, M. Pereyaslavets, M. Sorolla, and M. Thumm, Theory of nonuniform waveguides – the cross-section method, London, UK: IEE Electromagnetic Waves Series, 44, 1998.

[22] V. V. Shevchenko, Continuous Transitions in Open Waveguides – Introduction to the Theory, Boulder, CO: The Golem Press, 1971.

[23] F. Sporleder, and H. G. Unger, Waveguide tapers, transitions and couplers, London, UK: Peter Peregrinus Ltd., 1979.

[24] T. Rozzi and M. Mongiardo, Open Electromagnetic Waveguides, London, UK: IEE Electromagnetic Waves Series, 43, 1997.

[25] J. Uher, J. Bornemann, U. Rosenberg, Waveguide Components for Antenna Feed Systems: Theory and CAD, Artech House, 1993.

[26] R. Savafi-Naini and R. H. MacPhie, "Scattering at rectangular-to-rectangular waveguide junctions," *IEEE Trans. Microw. Theory Tech.*, vol. MTT-30, pp. 2060-2063, Nov. 1982.

[27] S. Ramo, J. R. Whinnery, and T. Van Duzer, Fields and Waves in Communication Electronics, Third Edition, New York, USA: John Wiley & Sons, 1993.

[28] N. Marcuvitz, Waveguide Handbook, McGraw-Hill, 1951.

[29] David M. Pozar, Microwave Engineering, Fourth Edition, New York, USA: John Wiley & Sons, 2001.

[30] R. E. Collin, Foundations for microwave engineering, Second Edition, New York, NY: McGraw Hill, 1992.

[31] R. Sorrentino, and G. Bianchi, Microwave and RF Engineering, New York, USA: John Wiley & Sons, 2010.

[32] J. Teniente, P. Turullols, C. del Río and M. Sorolla, "Fórmulas de Referencia Normalizadas para Propagación y Radiación en Guía Rectangular", *Proceedings of the XIII Simposium Nacional U.R.S.I.*, pp. 677-678, September 1998, Pamplona, Spain.

[33] M. R. Spiegel, Mathematical Handbook of Formulas and Tables, Schaum's Outline Series, New York, McGraw-Hill, 1968.

[34] R. K. Mongia, I. J. Bahl, P. Bhartia, and J. Hong, RF and Microwave Coupled-Line Circuits, Norwood, USA, Artech House, 2007.

[35] W. J. Getsinger, "Measurement and Modeling of the Apparent Characteristic Impedance of Microstrip," *IEEE Trans. Microw. Theory Tech.*, vol. 31, no. 8, pp. 624-632, Aug. 1983.

[36] E. Hammerstad and O. Jensen, "Accurate Models for Microstrip Computer-aided Design," *MTT Symposium Digest*, 1980.

[37] Kirschning and R.H. Jansen, "Accurate Model for Effective Dielectric Constant of Microstrip and Validity up in Millimeter-Wave Frequencies," *Electron. Lett.*, Vol. 18 March 18, 1982, pp. 272-273.

[38] Kobayashi, "Frequency Dependent Characteristics of Microstrips on Ansiotropic Substrates," *IEEE Trans. Microw. Theory Tech.*, vol. 30, pp. 89-92, Nov. 1983.

[39] M. Kobayashi, "A Dispersion Formula Satisfying Recent Requirements in Microstrip CAD," *IEEE Trans. Microw. Theory Tech.*, vol. 36, pp. 1246-1370, Aug. 1990.

[40] E. Yamashita, K. Atshi and T. Hirachata, "Microstrip Dispersion in a Wide Frequency Range," *IEEE Trans. Microw. Theory Tech.*, vol. 29, June 1981, pp. 610-611.

[41] H. A. Wheeler, "Formulas for the Skin Effect," *Proc. IRE*, Vol. 30, September 1942, pp. 412-424.

[42] T. C. Edwards and M. B. Steer, Foundations of Interconnect and Microstrip Design, Third Edition, John Wiley & Sons, Chichester, UK, 2000.

[43] J.-S. Hong, and M. J. Lancaster, Microstrip Filters for RF/microwave Applications, New York, USA: John Wiley & Sons, 2001.

[44] W. W. Mumford, "Directional couplers," *Proc. IRE*, vol. 35, pp. 160-165, February 1947.

[45] F. Bolinder, "Approximate theory of the directional coupler," *Proc. IRE*, vol. 39, pp. 291, March 1951.

[46] B. M. Oliver, "Directional Electromagnetic Couplers," *Proc. IRE*, vol. 42, pp. 1686-1692, Nov. 1954.

[47] M. Chudzik et al., "Microstrip Coupled-Line Directional Coupler with Enhanced Coupling Based on EBG Concept," *Electron. Lett.*, vol. 47, no. 23, pp. 1284-6, November 2011.

[48] M. Chudzik et al., "Design of EBG Microstrip Directional Coupler with High Directivity and Coupling," *2012 42nd European Microwave Conference*, Amsterdam, 2012, pp. 483-486.

[49] A. Lujambio, et al., "Dispersive Delay Line with Effective Transmission-Type Operation in Coupled-Line Technology," *IEEE Microw. Wirel. Compon. Lett.*, vol. 21, no. 9, pp. 459–461, September 2011.

[50] M. Chudzik, et al., “Design of Transmission-Type Nth-Order Differentiators in Planar Microwave Technology,” *IEEE Trans. Microw. Theory Tech.*, vol. 60, no. 11, Nov. 2012.

[51] J. Reed, and G. J. Wheeler, “A method of analysis of symmetrical four-port networks,” IRE Trans. Microwave Theory Tech., vol. 4, no. 4, pp. 246–252, October 1956.

[52] E. M. T. Jones and J. T. Bolljahn, “Coupled-strip-transmission-line filters and directional couplers,” *IRE Trans. Microw. Theory Tech.*, vol. 4, no. 2, pp. 75-81, April 1956.

[53] M. Kirschning and R. H. Jansen, "Accurate Wide-Range Design Equations for the Frequency-Dependent Characteristic of Parallel Coupled Microstrip Lines," *IEEE Trans. Microw. Theory Tech.*, vol. 32, no. 1, pp. 83-90, Jan. 1984.

[54] M. Kirschning and R. H. Jansen, "Accurate Wide-Range Design Equations for the Frequency-Dependent Characteristics of Parallel Coupled Microstrip Lines (Corrections)," *IEEE Trans. Microw. Theory Tech.*, vol. 33, no. 3, pp. 288-288, Mar. 1985.

[55] J. M. Percaz *et al.*, "General Synthesis of Tapered Matching Sections for Single-Mode Operation Using the Coupled-Mode Theory," *IEEE Trans. Microw. Theory Techn.*, vol. 67, no. 9, pp. 3511-3526, Sept. 2019.

[56] L. F. Shampine and J. Kierzenka, "A BVP Solver based on residual control and the MATLAB PSE," *ACM Trans. Math. Softw.*, Vol. 27, Number 3, 2001, pp. 299–316.

[57] L. F. Shampine, M. W. Reichelt, and J. Kierzenka, "Solving Boundary Value Problems for Ordinary Differential Equations in MATLAB with bvp4c," Available at https://www.mathworks.com/matlabcentral/fileexchange/3819-tutorial-on-solving-bvps-with-bvp4c.

[58] I. Arnedo, M. A. G. Laso, F. Falcone, D. Benito, T. Lopetegi, “A Series Solution for the Single-Mode Synthesis Problem Based on the Coupled-Mode Theory," *IEEE Trans. Microw. Theory Tech.*, vol. 56, no. 2, pp.457-466, Feb. 2008.

CHAPTER 3. SYNTHESIS USING ANALYTICAL EXPRESSIONS: ELECTROMAGNETIC BAND GAP STRUCTURES

An Electromagnetic Bandgap (EBG) may be defined as a microwave or millimeter waveguide structure that features periodical perturbations of its cross section along the propagation direction [1]-[4], causing the prohibition of propagation for certain frequency bands.

The roots of the EBGs originally come from the concept of Photonic Bandgap (PBG) structures or Photonic Crystals (PC) that were introduced by Yablonovich in the latest ’80 [5] from the point of view of physics. The PBGs are periodic structures where the propagation of certain frequency bands is prohibited, giving rise to stopbands in the frequency response. In 1991, the same author proposed one of the firsts PBGs by drilling holes periodically in a dielectric substrate of high dielectric constant [6]. The PBG research was firstly focused on the design of optical filters, distributed feedback lasers (DFB), distributed Bragg reflector (DBR) lasers, grating couplers, phase matching in nonlinear interactions and signal processing [7]-[9]. However, the physical operating principle can be automatically extended to different wavelengths or frequency ranges, leading to the concept of EBG when it is applied for microwave and millimeter wave regions [4]. Nonetheless, the term PBG was shared between the

optic and microwave ranges in the early research stage of EBGs and indeed, the relationship between the period of the perturbation and the central frequency of the rejection band was explained in terms of the Bragg's law [10].

The simplicity of the concept and features of the EBG made it very attractive for the design of a wide variety of components for different applications [11]. Due to the inherent selectivity characteristics of EBG structures, they have been employed for designing controllable band-pass and stop-band filters [12], [13]. Regarding this utility, several examples can be found in the literature for EBG-based filters implemented in different planar technologies [12]-[19] as well as in rectangular waveguide [20], [21]. Taking also advantage of that frequency-selective behavior, different couplers [22], [23] and multiplexers [24] have been recently proposed. Moreover, the EBG did not promote only the most obvious filtering applications and important contributions were also performed in the scope of Analog Signal Processing (ASP) [25], such as chirped-delay lines [26], [27] and real-time Fourier transformers [28], [29]. Additionally, the performance of antennas, reflectors, absorbers, and frequency selective surfaces, among others, have been also benefited from the EBG concept [30]-[36].

Regarding the electromagnetic analysis of an EBG, it is noticeable that like any other nonuniform waveguide structure, they can be analyzed from the point of view of the Coupled-Mode Theory, as it was deeply studied in [18], [37]. In fact, if the appropriate circumstances that were commented in CHAPTER 2 are applicable to the case under study, the single-mode operation can be assumed and thus, the frequency response of an EBG will be determined by means of the single-mode equation system (2.91), (2.92) that is conveniently provided below.

$$\frac{da^+}{dz} = -j \cdot \beta \cdot a^+ + K \cdot a^- \tag{2.91}$$

$$\frac{da^-}{dz} = j \cdot \beta \cdot a^- + K \cdot a^+ \tag{2.92}$$

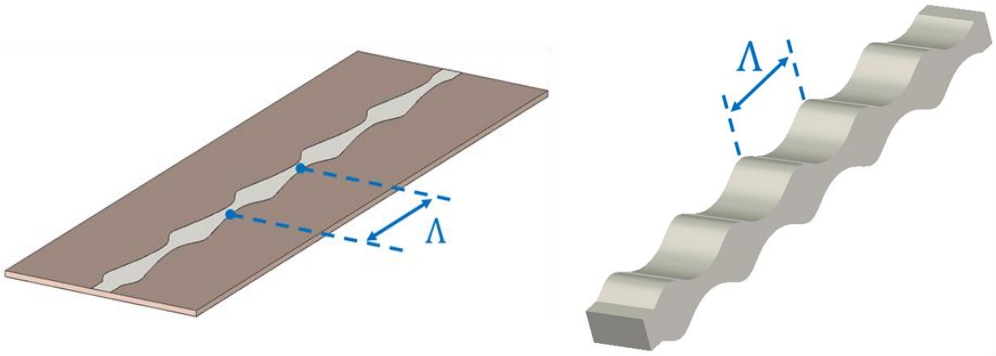

(a) (b)

Fig. 3.1. Example of periodic structures implemented in (a) microstrip and (b) rectangular waveguide. In both cases, the period, Λ, is highlighted.

It can be demonstrated that if an EBG structure of certain length, L, is periodic with a period, Λ, along the propagation direction, z, then the coupling coefficient, $K(z)$, will also exhibit the same period. In order to illustrate this relation, let's consider a periodic microstrip or rectangular waveguide (with exclusive height variations for the sake of simplicity) structure like the ones that are depicted in Fig. 3.1. As it was explained in CHAPTER 2, in absence of variations of the width dimension, the waveguide height, $b(z)$ is directly related with the coupling coefficient, $K(z) = K_b(z)$, by (2.122)-(2.124). On the other hand, the width of the microstrip line rules the characteristic impedance, $Z_0(z)$, which in turn determines $K(z)$, due to (2.145). Therefore, if it is satisfied that $b(z) = b(z + m \cdot \Lambda)$ for rectangular waveguide or $Z_0(z) = Z_0(z + m \cdot \Lambda)$ for the microstrip line case, with $m = 1, 2, \ldots$, then the result of the derivatives (2.123), (2.145) will be also a periodic function, i.e. $K(z) = K(z + m \cdot \Lambda)$. Therefore, the coupling coefficient can be expanded in its Fourier series [38] as:

$$K(z) = \sum_{n=-\infty}^{n=\infty} K_n \cdot e^{j \cdot \frac{2 \cdot \pi}{\Lambda} n \cdot z} \tag{3.1}$$

$$K_n = \frac{1}{\Lambda} \cdot \int_{\Lambda} K(z) \cdot e^{-j \cdot \frac{2 \cdot \pi}{\Lambda} n \cdot z} \cdot dz \tag{3.2}$$

where K_n is the amplitude of the n-th term of the Fourier series that will also determine the n-th rejected band, with $n = 1$ for the fundamental one.

At this point, it must be noticed that in the subsequent steps, the frequency response parameters of the EBGs will be formulated in terms of the phase constant, β, for the sake of

generality. The specific relationship between the frequency, f, and β will depend on the choice of technology for the physical implementation of the EBG.

If the coupling coefficient, K, of (2.91), (2.92) is substituted by its Fourier series expression of (3.1) and several mathematical manipulations are subsequently performed, approximate analytical solutions, valid around the n-th rejected band, will be obtained for the complex amplitudes of the forward and backward travelling waves [37], a^+ and a^-, respectively, in the EBG structure with length L as:

$$a^+(z) = \frac{\Delta\beta \cdot \sinh[\gamma \cdot (z-L)] + j \cdot \gamma \cdot \cosh[\gamma \cdot (z-L)]}{-\Delta\beta \cdot \sinh(\gamma \cdot L) + j \cdot \gamma \cdot \cosh(\gamma \cdot L)} \cdot a^+(0) \cdot e^{-\frac{j \cdot \pi \cdot n \cdot z}{\Lambda}} \tag{3.3}$$

$$a^-(z) = \frac{-j \cdot K_n \cdot \sinh[\gamma \cdot (z-L)]}{-\Delta\beta \cdot \sinh(\gamma \cdot L) + j \cdot \gamma \cdot \cosh(\gamma \cdot L)} \cdot a^+(0) \cdot e^{\frac{j \cdot \pi \cdot n \cdot z}{\Lambda}} \tag{3.4}$$

where:

$$\Delta\beta = \beta - \frac{n \cdot \pi}{\Lambda} \tag{3.5}$$

$$\gamma = +\sqrt{|K_n|^2 - \Delta\beta^2} \tag{3.6}$$

Taking advantage of the approximate expressions of (3.3) and (3.4) for a^+ and a^-, respectively, analytical expressions can be deduced [37] for the S-parameters of the EBG structure using (2.105)-(2.110), also valid around the n-th rejected band. A typical example of for the S_{11} and S_{21} parameters of a general EBG is depicted in Fig. 3.2, while the analytical expressions to calculate them are provided below:

$$S_{11} = \left.\frac{a^-(z=0,f)}{a^+(z=0,f)}\right|_{a^-(z=L,f)=0} = \frac{-j \cdot K_n \cdot \sinh[\gamma \cdot (z-L)]}{-\Delta\beta \cdot \sinh(\gamma \cdot L) + j \cdot \gamma \cdot \cosh(\gamma \cdot L)} \tag{3.7}$$

$$S_{21} = \left.\frac{a^+(z=L,f)}{a^+(z=0,f)}\right|_{a^-(z=L,f)=0} = \frac{j \cdot \gamma \cdot e^{-\frac{j \cdot \pi \cdot n \cdot L}{\Lambda}}}{-\Delta\beta \cdot \sinh(\gamma \cdot L) + j \cdot \gamma \cdot \cosh(\gamma \cdot L)} \tag{3.8}$$

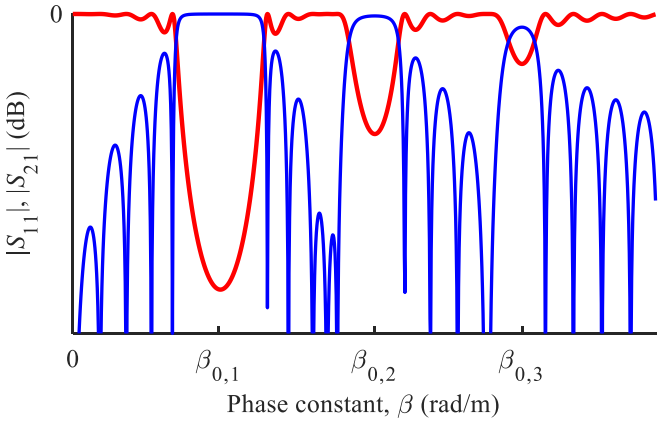

Fig. 3.2. Example of the frequency response of a generic EBG: S_{11} (blue line) and S_{21} (red line) parameters.

The maximum rejection value that is achieved at the n-th band of an EBG from the point of view of the S_{11} and S_{21} parameteres, $|S_{11}|_{max,n}$ and $|S_{21}|_{min,n}$ respectively, can be determined from (3.7) and (3.8), yielding to:

$$|S_{11}|_{max,n} = \tanh(|K_n| \cdot L) \tag{3.9}$$

$$|S_{21}|_{min,n} = \operatorname{sech}(|K_n| \cdot L) \tag{3.10}$$

Regarding the phase constant value where the n-th rejected band is centered, $\beta_{0,n}$, it can be determined by means of the period of the perturbation, Λ, and the considered band n, with $n = 1, 2, 3, \ldots$, as:

$$\beta_{0,n} = \frac{\pi \cdot n}{\Lambda} \tag{3.11}$$

It must be stressed that the $|S_{11}|_{max,n}$ and $|S_{21}|_{min,n}$ will be reached at the center of each rejection band.

Furthermore, the lower and upper limits of the n-th stopband, $\beta_{l,n}$ and $\beta_{u,n}$, respectively, can be calculated using the expressions (3.12) and (3.13). At this phase constant points, it will be ideally satisfied that $S_{11}(\beta = \beta_{l,n}) = S_{11}(\beta = \beta_{u,n}) = 0$, or alternatively $S_{21}(\beta = \beta_{l,n}) = S_{21}(\beta = \beta_{u,n}) = 1$.

$$\beta_{l,n} = \frac{\pi \cdot n}{\Lambda} - \sqrt{|K_n|^2 + \left(\frac{\pi}{L}\right)^2} \tag{3.12}$$

$$\beta_{u,n} = \frac{\pi \cdot n}{\Lambda} + \sqrt{|K_n|^2 + \left(\frac{\pi}{L}\right)^2} \tag{3.13}$$

The $\beta_{l,n}$, $\beta_{u,n}$ equations of (3.12), (3.13) allow us to define a 0 dB bandwidth for each n-th band, $BW_{\beta,n}^{0\,dB}$, as the expected bandwidth (in terms of β) between the lower and upper nulls of the S_{11} parameter for the same stopband. The $BW_{\beta,n}^{0\,dB}$ can be calculated using (3.12) and (3.13) as:

$$BW_{\beta,n}^{0\,dB} = \beta_{u,n} - \beta_{l,n} = 2 \cdot \sqrt{|K_n|^2 + \left(\frac{\pi}{L}\right)^2} \tag{3.14}$$

3.1. SPURIOUS-FREE EBG

As it has been already explained, a general EBG structure will exhibit the fundamental stopband centered at $\beta_{0,1} = \frac{\pi}{\Lambda}$, while the higher ones will be expected at $\beta_{0,n} = \frac{\pi \cdot n}{\Lambda}$, with $n > 1$ as it can be observed in Fig. 3.2. These last stopbands are also known as spurious bands since they may not be desired for the design in many cases. Fortunately, it is possible to synthesize an EBG structure that does not feature those residual bands (see Fig. 3.3) as it was brilliantly demonstrated in [19]. The method to achieve that spurious-free EBG is based on making null all K_n coefficients of the Fourier series of (3.1), (3.2) that satisfy $1 < |n| < \infty$, while leaving $K_{\pm 1}$ as the only coefficients that feature an amplitude $A/2$, with $A > 0$, and phase, θ, a solution that can be mathematically expressed as:

$$K_n = \begin{cases} \frac{A}{2} \cdot e^{\pm j \cdot \theta} & \text{for } |n| = 1 \\ 0 & \text{otherwise} \end{cases} \tag{3.15}$$

It is straightforward to demonstrate that by following the criterion of (3.15) in the coupling coefficient expression of (3.1), the result will be a simple cosine function given by:

$$K(z) = A \cdot \cos\left(\frac{2 \cdot \pi}{\Lambda} \cdot z + \theta\right) \tag{3.16}$$

being this expression rigorously applicable for waveguides where the phase constant does not vary with the position, being only a function of frequency, i.e. $\beta(z, f) = \beta(f) \ \forall \, z$.

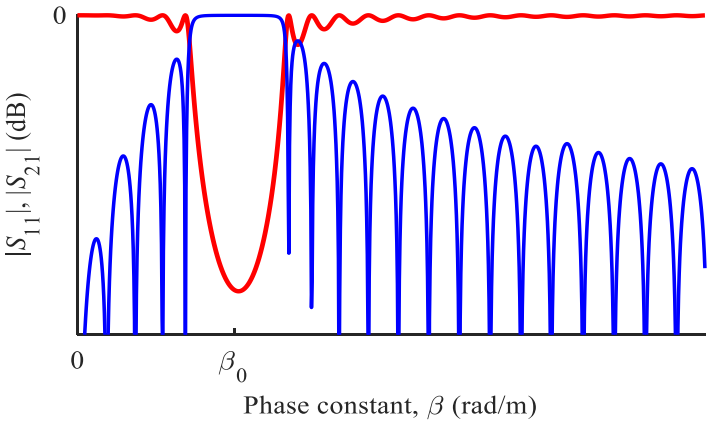

Fig. 3.3. Frequency response of a spurious-free EBG: S_{11} (blue line) and S_{21} (red line) parameters.

The relationship between the center of the unique stopband, β_0, and the period of the spurious-free EBG, Λ, will be obtained by setting $n = 1$ in (3.11), which results in:

$$\beta_0 = \frac{\pi}{\Lambda} \tag{3.17}$$

Moreover, the corresponding 0 dB bandwidth, $BW_\beta^{0\ dB}$, will be also determined if $n = 1$ and $|K_{\pm 1}| = A/2$ are taken in (3.14), leading to:

$$BW_\beta^{0\ dB} = \beta_u - \beta_l = 2 \cdot \sqrt{\left(\frac{A}{2}\right)^2 + \left(\frac{\pi}{L}\right)^2} \tag{3.18}$$

where β_l and β_u obviously stand for the lower and upper limits of the stopband, where $S_{11}(\beta = \beta_l) = S_{11}(\beta = \beta_u) = 0$ and $S_{21}(\beta = \beta_l) = S_{21}(\beta = \beta_u) = 1$. From (3.12) and (3.13), it can be deduced that:

$$\beta_l = \frac{\pi}{\Lambda} - \sqrt{\left(\frac{A}{2}\right)^2 + \left(\frac{\pi}{L}\right)^2} \tag{3.19}$$

$$\beta_u = \frac{\pi}{\Lambda} + \sqrt{\left(\frac{A}{2}\right)^2 + \left(\frac{\pi}{L}\right)^2} \tag{3.20}$$

Furthermore, the maximum value of the S_{11}-parameter, $|S_{11}|_{max}$, and the corresponding minimum one for the $|S_{21}|$, $|S_{21}|_{min}$, are directly inferred from (3.9) and (3.10) as:

$$|S_{11}|_{max} = \tanh\left(\frac{A}{2} \cdot L\right) \tag{3.21}$$

$$|S_{21}|_{min} = \operatorname{sech}\left(\frac{A}{2} \cdot L\right) \tag{3.22}$$

It must be highlighted that it is possible to attain an analytical expression for the characteristic impedance profile, $Z_0(z)$, when dealing with TEM or QTEM transmission lines, by introducing the simple coupling coefficient cosine function of (3.16) into (2.146), giving rise to:

$$Z_0(z) = Z_0(0) \cdot e^{-\frac{A \cdot \Lambda}{\pi} \cdot \left[\sin\left(\frac{2 \cdot \pi}{\Lambda} \cdot z\right) - \sin\theta\right]} \tag{3.23}$$

If it is considered in (3.23) that the number of periods, N_Λ, is an integer number, then it will be directly deduced that $Z_0(L) = Z_0(0)$.

In view of (3.23) it will be possible to calculate the extreme values of $Z_0(z)$, i.e. $Z_{0,max}$ and $Z_{0,min}$, as:

$$Z_{0,min} = Z_0(0) \cdot e^{\frac{A \cdot \Lambda}{\pi} \cdot (\sin\theta - 1)} \tag{3.24}$$

$$Z_{0,max} = Z_0(0) \cdot e^{\frac{A \cdot \Lambda}{\pi} \cdot (\sin\theta + 1)} \tag{3.25}$$

where $Z_{0,min}$ and $Z_{0,max}$ will be the minimum or maximum values of $Z_{0(z)}$.

On the other hand, a closed-form expression for the physical dimensions of EBGs that are implemented introducing exclusive height variations in rectangular waveguide technology can be reached. It must be reminded that in this case, $K(z) = K_b(z)$, see (2.122)-(2.124). Due to the similarity between the expressions (2.130) and (2.146), it is obtained that:

$$b(z) = b(0) \cdot e^{-\frac{A \cdot \Lambda}{\pi} \left[\sin\left(\frac{2 \cdot \pi}{\Lambda} \cdot z\right) - \sin\theta\right]} \tag{3.26}$$

As in the case of transmission lines, an integer number of periods leads to $b(L) = b(0)$.

Moreover, the minimum and maximum values of $b(z)$, b_{min} and b_{max}, respectively, will be obtained if $Z_0(0)$ is substituted by $b(0)$ in (3.24) and (3.25), yielding to:

$$b_{min} = b(0) \cdot e^{\frac{A \cdot \Lambda}{\pi} \cdot (\sin\theta - 1)} \tag{3.27}$$

$$b_{max} = b(0) \cdot e^{\frac{A \cdot \Lambda}{\pi} \cdot (\sin\theta + 1)} \tag{3.28}$$

3.1.1. Spurious-Free EBG with Controlled Extreme Dimensions

If the expressions (3.24), (3.25) and (3.27), (3.28) for the calculation of $Z_{0,min}, Z_{0,max}$ and b_{min}, b_{max}, respectively, are carefully examined, it will be clear that these values will be exclusively determined by the amplitude of the coupling coefficient, A, as well as by the phase of the spurious-free EBG, θ. Indeed, it will be possible to calculate the ratio between extreme impedance values, $\Delta Z_{0,ext}$, and the corresponding ratio for rectangular waveguide extreme heights, Δb_{ext}, that will be necessary to synthetize an EBG of a given amplitude, A, as:

$$\Delta Z_{0,ext} = \frac{Z_{0,max}}{Z_{0,min}} = \frac{Z_0(0)\cdot e^{\frac{A\cdot\Lambda}{\pi}\cdot(\sin\theta+1)}}{Z_0(0)\cdot e^{\frac{A\cdot\Lambda}{\pi}\cdot(\sin\theta-1)}} = e^{\frac{2\cdot A\cdot\Lambda}{\pi}} \tag{3.29}$$

$$\Delta b_{ext} = \frac{b_{max}}{b_{min}} = \frac{b(0)\cdot e^{\frac{A\cdot\Lambda}{\pi}\cdot(\sin\theta+1)}}{b(0)\cdot e^{\frac{A\cdot\Lambda}{\pi}\cdot(\sin\theta-1)}} = e^{\frac{2\cdot A\cdot\Lambda}{\pi}} \tag{3.30}$$

Therefore, if a certain 0-dB bandwidth, $BW_{\beta}^{0\,dB}$, or a maximum rejection level, $|S_{21}|_{min}$, must be satisfied by an EBG of length L, and period Λ, the required amplitude for the coupling coefficient, A, can be deduced from (3.18) and (3.22), respectively, and the extreme characteristic impedance or height ratios will be known through (3.29) or (3.30). It is important to stress that this conclusion leads to the possibility of fixing an extreme value of $Z_0(z)$ and $b(z)$ for given values of A and Λ, while the other extreme will be immediately determined by using the corresponding expressions for $\Delta Z_{0,ext}$ and Δb_{ext} of (3.29) and (3.30), respectively. In fact, this property was successfully employed for the synthesis of a directional coupler with enhanced coupling in microstrip coupled lines in [22], where the value for the minimum gap between the metallic strips of a microstrip coupled-line structure (which is a function of the characteristic impedance of the even and odd mode) was imposed. It is straightforward to demonstrate from (3.29) and (3.30) that:

$$Z_{0,max} = Z_{0,min}^{spec}\cdot e^{\frac{2\cdot A\cdot\Lambda}{\pi}} \tag{3.31}$$

$$Z_{0,min} = Z_{0,max}^{spec}\cdot e^{\frac{-2\cdot A\cdot\Lambda}{\pi}} \tag{3.32}$$

$$b_{max} = b_{min}^{spec}\cdot e^{\frac{2\cdot A\cdot\Lambda}{\pi}} \tag{3.33}$$

$$b_{min} = b_{max}^{spec}\cdot e^{\frac{-2\cdot A\cdot\Lambda}{\pi}} \tag{3.34}$$

where $Z_{0,min}^{spec}$ and $Z_{0,max}^{spec}$ stand for an hypothetic minimum and maximum required value of $Z_0(z)$, while b_{min}^{spec} and b_{max}^{spec} are the corresponding ones when dealing with an EBG implemented in a rectangular waveguide that must only exhibit variations in its height.

However, it must be highlighted that the expressions (3.31)-(3.34) neither specify the characteristic impedance, $Z_0(0)$, nor the waveguide height, $b(0)$, at the input port that are needed to satisfy the corresponding extreme ratios as they were previously defined in (3.29) and (3.30). Due to the inherent periodic essence of the EBG, it is obvious that the impedance or height of that port can be arbitrarily chosen so as to satisfy $Z_{0,min} \leq Z_0(0) \leq Z_{0,max}$ or $b_{min} \leq b(0) \leq$

b_{max}. In order to synthesize an EBG that achieves the expected extreme values $Z_{0,min}$, $Z_{0,max}$ or b_{min}, b_{max} while starting with an input port of $Z_0(0)$ or $b(0)$, respectively, it will be necessary to determine the phase constant term, θ, of the coupling coefficient of (3.16) that satisfies both conditions. For doing so, it must be considered that from (3.24) and (3.25), the product $Z_{0,min} \cdot Z_{0,max}$ will result in:

$$Z_{0,min} \cdot Z_{0,max} = Z_0^2(0) \cdot e^{\frac{2 \cdot A \cdot \Lambda \cdot \sin\theta}{\pi}} \tag{3.35}$$

If we solve equation (3.35) for $\sin\theta$, it will be obtained that:

$$\sin\theta = \frac{\pi}{2 \cdot A \cdot \Lambda} \cdot \ln\left[\frac{Z_{0,min} \cdot Z_{0,max}}{Z_0^2(0)}\right] \tag{3.36}$$

Before performing the last step of the θ deduction, it must be reminded that the following property between the sine and its inverse function is going to fulfilled:

$$\sin\alpha = B \Leftrightarrow \begin{cases} \alpha = \text{asin}(B) \\ \alpha = \pi - \text{asin}(B) \end{cases} \tag{3.37}$$

Taking (3.37) into account, it will be clear that the phase θ will have two different solutions that lead to two dual EBGs that comply with the requirements of featuring a period, Λ, an amplitude of the coupling coefficient, A, and a characteristic impedance, $Z_0(z)$, which satisfies $Z_{0,min} \leq Z_0(z) \leq Z_{0,max}$. The options for the phase term, θ, will be obtained from (3.36) and (3.37) and are given below:

$$\theta = \begin{cases} \text{asin}\left\{\frac{\pi}{2 \cdot A \cdot \Lambda} \cdot \ln\left[\frac{Z_{0,min} \cdot Z_{0,max}}{Z_0^2(0)}\right]\right\} \\ \pi - \text{asin}\left\{\frac{\pi}{2 \cdot A \cdot \Lambda} \cdot \ln\left[\frac{Z_{0,min} \cdot Z_{0,max}}{Z_0^2(0)}\right]\right\} \end{cases} \tag{3.38}$$

It is straightforward to demonstrate that if the mathematical development provided between (3.35)-(3.38) is performed for the rectangular waveguide case with exclusive variations in height, i.e. considering b_{min}, b_{max}, and $b(0)$, as well as (3.27) and (3.28), the necessary values will be given by:

$$\theta = \begin{cases} \text{asin}\left\{\frac{\pi}{2 \cdot A \cdot \Lambda} \cdot \ln\left[\frac{b_{min} \cdot b_{max}}{b^2(0)}\right]\right\} \\ \pi - \text{asin}\left\{\frac{\pi}{2 \cdot A \cdot \Lambda} \cdot \ln\left[\frac{b_{min} \cdot b_{max}}{b^2(0)}\right]\right\} \end{cases} \tag{3.39}$$

An interesting solution can be also deduced so as to obtain equidistant values of $Z_{0,min}$ and $Z_{0,max}$ with respect to $Z_0(0)$, by also choosing the appropriate value for the phase term, θ_{eq}. This equidistant solution implies that:

$$Z_0(0) = \frac{\left(Z_{0,min} + Z_{0,max}\right)}{2} \tag{3.40}$$

Then, by using (3.24), (3.25) it will be possible to develop (3.40) as:

$$\begin{aligned} Z_0(0) = \frac{\left(Z_{0,min} + Z_{0,max}\right)}{2} &= \frac{Z_0(0)\cdot e^{-\frac{A\cdot\Lambda}{\pi}\left[1-\sin\theta_{eq}\right]} + Z_0(0)\cdot e^{\frac{A\cdot\Lambda}{\pi}\left[1+\sin\theta_{eq}\right]}}{2} \\ = Z_0(0)e^{\frac{A\cdot\Lambda}{\pi}\sin\theta_{eq}}\cdot\frac{\left(e^{-\frac{A\cdot\Lambda}{\pi}} + e^{\frac{A\cdot\Lambda}{\pi}}\right)}{2} &= Z_0(0)e^{\frac{A\cdot\Lambda}{\pi}\sin\theta_{eq}}\cdot\cosh\left(\frac{A\cdot\Lambda}{\pi}\right) \end{aligned} \tag{3.41}$$

If we solve equation (3.41) for the term $\sin\theta_{eq}$, it is obtained:

$$\sin\theta_{eq} = \frac{\pi}{A\cdot\Lambda}\cdot\ln\left[\operatorname{sech}\left(\frac{A\cdot\Lambda}{\pi}\right)\right] \tag{3.42}$$

Then, the two possible values of θ_{eq} that allow us to reach the equidistant condition between the extreme values of impedance, $Z_{0,min}$ and $Z_{0,max}$, and the impedance of the input port, $Z_0(0)$, are revealed by taking under consideration (3.37):

$$\theta_{eq} = \begin{cases} \operatorname{asin}\left\{\frac{\pi}{A\cdot\Lambda}\cdot\ln\left[\operatorname{sech}\left(\frac{A\cdot\Lambda}{\pi}\right)\right]\right\} \\ \pi - \operatorname{asin}\left\{\frac{\pi}{A\cdot\Lambda}\cdot\ln\left[\operatorname{sech}\left(\frac{A\cdot\Lambda}{\pi}\right)\right]\right\} \end{cases} \tag{3.43}$$

Finally, it must be highlighted that the result of (3.43) neither depends on characteristic impedances, nor on height values. Indeed, if the reasoning carried out within (3.41) and (3.42) is applied for the rectangular waveguide heights b_1, b_2, and $b(0)$, the expression (3.43) will be also achieved, and thus, this equidistant solution can be considered as general and independent form the selected technology.

3.1.2. Port-Matched Spurious-Free EBG with Non-Integer Number of Periods

One of the most frequent limitations when synthetizing an EBG structure, as well as in the case of almost any other microwave device, is the maximum length, L_{max}, allowed for the device. Moreover, if it is also considered that the characteristic impedance range that can be typically fabricated must belong to the range $Z_{0,min} \leq Z_0(z) \leq Z_{0,max}$ (or $b_{min} \leq b(z) \leq b_{max}$ when dealing with rectangular waveguide technology), due to the inherent limitations of the fabrication techniques, the maximum amplitude of the coupling coefficient, A_{max}, will be also constrained due to the relationships between A and the extreme impedance and height ratios of (3.29) and (3.30), respectively. Therefore, if both L_{max} and A_{max} are limited, it will be clear that the maximum rejection that may be achieved, $|S_{11}|_{max}$ and $|S_{21}|_{min}$, will be also restricted because of (3.21) and (3.22), and the 0-dB bandwidth, $BW_{\beta}^{0\,dB}$, will be also limited in view of (3.18). Furthermore, it must be stressed that in the most frequent case it is desired that $Z_0(L) = Z_0(0)$ or $b(L) = b(0)$, being that condition directly satisfied if an integer number of periods, N_Λ, is enforced to synthetize the EBG. In order to follow this last criterion, N_Λ should be chosen as the highest one that ensures $L_{max} \geq N_\Lambda \cdot \Lambda = L$. It must be pointed out that the situation where the condition $L_{max} = N_\Lambda \cdot \Lambda = L$ is directly satisfied with an integer N_Λ is quite unlikely. Accordingly, both the bandwidth and the rejection level that are achieved by an EBG of length L, will not be the best ones that would be obtained if the device featured a length L_{max}, because of (3.18), (3.21), and (3.22).

Fortunately, it is possible to choose the optimum phase term $\theta = \theta_{opt}$ in (3.16), so as to guarantee that a non-integer number of periods, N_Λ, of the EBG can satisfy $L_{max} = L = N_\Lambda \cdot \Lambda$, as well as the condition $Z_0(L_{max}) = Z_0(0)$ or $b(L_{max}) = b(0)$ at the same time. Thus, the rejection level will be the highest possible. The reasoning of this aspect will be carried out by considering TEM or QTEM transmission lines not to extend unnecessarily the explanation, but it can be automatically translated to the rectangular waveguide height.

Firstly, it is necessary to consider that the condition $Z_0(L_{max}) = Z_0(0)$ implies from (3.23) that:

$$Z_0(L_{max}) = Z_0(0) \cdot e^{-\frac{A \cdot \Lambda}{\pi} \cdot \left[\sin\left(\frac{2 \cdot \pi}{\Lambda} \cdot L_{max}\right) - \sin\theta_{opt}\right]} = Z_0(0) \tag{3.44}$$

and then:

$$e^{-\frac{A\cdot\Lambda}{\pi}\cdot\left[\sin\left(\frac{2\cdot\pi}{\Lambda}\cdot L_{max}\right)-\sin\theta_{opt}\right]}=1 \tag{3.45}$$

It must be realized that (3.45) neither depends on the characteristic impedance of the transmission line, nor on the waveguide height, and hence the reasoning is applicable for both technology realms. In order to satisfy (3.45) the following expression must be fulfilled:

$$\sin\theta_{opt}=\sin\left(\frac{2\cdot\pi}{\Lambda}\cdot L_{max}\right) \tag{3.46}$$

From (3.37) and (3.46) it may be directly inferred that in order to exploit the maximum available length to reach the maximum rejection level with a non-integer number of periods while satisfying that $Z_0(L_{max})=Z_0(0)$ or $b(L_{max})=b(0)$, the phase θ_{opt} should be calculated using one of the two solutions that are provided below:

$$\theta_{opt}=\begin{cases}\dfrac{2\cdot\pi}{\Lambda}\cdot L_{max}\\ \pi-\dfrac{2\cdot\pi}{\Lambda}\cdot L_{max}\end{cases} \tag{3.47}$$

However, it must be noted that due to the fact that a non-integer number of periods is employed, the frequency response of the EBG structure may not completely fit the expected behavior, which is described by the approximated equations (3.3)-(3.14) and (3.17)-(3.22), although the deviations are almost negligible in most of the practical cases (if the number of periods taken is large enough). Moreover, since $\theta=\theta_{opt}$ has been chosen in order to synthetize an EBG with a non-integer number of periods, it will be neither possible to choose the required values of $Z_{0,min}^{spec}$ nor $Z_{0,max}^{spec}$ (or b_{min}^{spec} and b_{max}^{spec}), because the achieved extreme values $Z_{0,min}$ and $Z_{0,max}$ (b_{min} and b_{max}) will be the ones provided by $\theta=\theta_{opt}$ in (3.24) and (3.25), respectively (or (3.27) and (3.28) alternatively when dealing with rectangular waveguide technology). If it is necessary to obtain an EBG that features a non-integer number of periods, as well as $Z_0(L_{max})=Z_0(0)$ or $b(L_{max})=b(0)$, while keeping under control $Z_{0,min}$ and $Z_{0,max}$, or b_{min} and b_{max}, the only remaining option will be to synthesize a so-called tapered spurious-free EBG.

3.1.3. Tapered Spurious-Free EBG

In order to conclude this section focused on the synthesis of optimum EBG structures, the case where the coupling coefficient is tapered using a windowing function, $W(z)$, is going to be

analyzed. This tapering technique is typically devoted to the reduction of the sidelobe level in the S_{11} parameter of an EBG, being the result dependent on the specific $W(z)$ employed. In [22] a microstrip coupled-line EBG-based coupler was synthesized with this windowing method while looking also for an additional objective that was to keep the extreme values of characteristic impedances under control. Indeed, the windowing technique can be employed also with the aim of modulating the profile of the characteristic impedance using an arbitrary function of interest so as to guarantee that the extreme values of the impedance does not lead to physical dimensions that cannot be manufactured. Whatever the case may be under consideration, it is obvious that the synthesis equations of the spurious-free EBG must be reviewed for the case of a tapered EBG, since the coupling coefficient will be altered, and its associated frequency response will be different as a result.

Firstly, the expression (3.17) that links the period of the EBG with the center of the stopband remains unaltered.

Nonetheless, the expression for the highest rejection level of (3.21) and (3.22) will need to be reformulated since the amplitude of the coupling coefficient is going to be modified. Thus, the maximum rejection level will be calculated as a function of an effective EBG length [40], L_{eff}, instead of the physical length, L, as :

$$|S_{11}|_{max} = \tanh\left(\frac{A}{2} \cdot L_{eff}\right) \tag{3.48}$$

where L_{eff} is the effective length of the EBG and will be determined by means of the windowing function, $W(z)$, and the physical length, L, following the relation provided below:

$$L_{eff} = \int_0^L W(z) \cdot dz \tag{3.49}$$

where $|W(z)|$ is assumed to have a unitary maximum amplitude, i.e. $\max\{|W(z)|\} = 1$.

3.1.4. Design of Multiplexer based on EBG concept

The use of the expressions obtained for the synthesis of optimum EBGs, the backward and forward coupling characteristics of symmetrical edge coupled lines, and the different phase velocity of microstrip coupled lines, can be employed to design four-port multiplexers to direct

different frequency components of the same signal to different ports. The central frequency of the backward-coupled band is controlled by the period of the EBG structure, while the frequencies of the forward coupled bands are fixed by the length of the device. The rest of the frequencies go to the direct port giving rise to a device with the input port matched at all the frequencies and where the coupled bands are easily controllable by adjusting the corresponding design parameter.

Coupled lines have been widely used at microwave and millimeter wave frequencies for a long time, with very important applications like the implementation of directional couplers, filters, and transformers [41], [42]. Two different coupling mechanisms have been identified for the coupled line structures: the backward coupling and the forward coupling. Depending on the coupling mechanism employed the structures are classified into two different groups [41]-[43]. The first group comprises the coupled line structures that couple the energy to the port adjacent to the input port (through a wave propagating in the backward direction) and are based on the use of different even and odd characteristic impedances. The second group includes the structures that couple the energy to the port adjacent to the direct port (through a wave propagating in the forward direction) and are based on the use of different even and odd propagation constants [44]. In both groups, the length of the structure controls the central frequency of the coupled band and only the corresponding mechanism (backward or forward coupling) is employed [41].

However, in this thesis a methodology is proposed to produce and exploit simultaneously the forward and backward coupling in coupled line structures. In contrast with the classical designs, the backward coupling will be achieved by introducing an EBG structure that allows to obtain a strong coupling and a single backward-coupled band whose central frequency is independent of the length of the structure [22], [23]. A technology with distinct even and odd propagation constants will be used to obtain the forward-coupled bands. A related EBG structure was also successfully demonstrated but for differential microstrip lines, with the very different application of common-mode suppression, and consequently with very different design methodology and operation [45].

The operation principle of the EBG-assisted coupled line structure proposed here, with independent control of the couplings, rests on the fact that the signal introduced in the input port (P1) is backward-coupled to P3 by the EBG structure, and forward-coupled to P4 by the difference between the even and odd propagation constants, see Fig. 3.4. The central frequency of the single backward-coupled band obtained in P3 solely depends on the period of the EBG structure, Λ, while the central frequencies of the forward-coupled bands obtained in P4 are determined by the total length of the device. The rest of the frequencies go to the direct port (P2), ensuring good matching at the input port (P1) for all the frequencies.

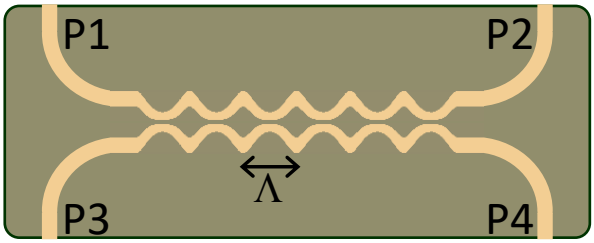

Fig. 3.4. Schematic of the EBG-assisted coupled line structure with EBG period Λ. The ground plane is kept unaltered.

Microstrip technology has been selected for the implementation of the device since it fulfills the required condition of distinct even and odd propagation constants and it ensures low cost, direct integration, and easy fabrication using printed circuit technology.

An EBG structure is implemented in coupled line technology by introducing an adequate periodic variation of the coupled strips width and separation. The resulting four-port side-by-side symmetrical device (see Fig. 3.4) can be studied employing the even and odd mode decomposition of symmetrical edge coupled transmission lines that was mentioned in section 2.2.1.3. The mode decomposition allows us to relate the reflection, $\Gamma_e(f)$ and $\Gamma_o(f)$, and transmission coefficients, $T_e(f)$ and $T_o(f)$, of the even and odd modes, respectively, with the S-parameters of the four-port structure, leading to the identities (2.169)-(2.172) that are rewritten below for the sake of clarity:

$$S_{11}(f) = \frac{\Gamma_e(f) + \Gamma_o(f)}{2} \tag{2.169}$$

$$S_{21}(f) = \frac{T_e(f) + T_o(f)}{2} \tag{2.170}$$

$$S_{31}(f) = \frac{\Gamma_e(f) - \Gamma_o(f)}{2} \tag{2.171}$$

$$S_{41}(f) = \frac{T_e(f) - T_o(f)}{2} \tag{2.172}$$

where the port numbers follow the convention shown in Fig. 3.4.

As it can be seen in (2.169), if the design condition $\Gamma_e(f) = -\Gamma_o(f)$ is satisfied, then $S_{11}(f) = 0$ and $S_{31}(f) = \Gamma_e(f)$ due to (2.171), producing a device with the input port P1 matched for all the frequencies and where the EBG stopband is backward-coupled to P3. If the coupling coefficients of even, $K_e(z)$, and odd, $K_o(z)$, modes are chosen to satisfy, $K_e(z) =$

$-K_o(z)$, then the condition $\Gamma_e(f) = -\Gamma_o(f)$ will be automatically accomplished due to the sign property reported in [19]. Thus, $K_e(z)$ and $K_o(z)$ can be selected as an EBG of initial phase, $\theta = -\frac{\pi}{2}$, and opposite sign, as:

$$K_e(z) = -K_o(z) = A \cdot \sin\left(\frac{2 \cdot \pi}{\Lambda} \cdot z\right) \tag{2.169}$$

then a spurious-free EBG structure that features only the fundamental backward-coupled band is obtained. Taking into account the expression (2.151) that relates the frequency, f, and the phase constant, β, considering a QTEM mode, the EBG period, Λ, will determine the central frequency, f_{31}, of the single backward-coupled band due to (3.17) as:

$$\Lambda = \frac{\pi}{\beta_0} = \frac{\pi \cdot c_0}{2 \cdot \pi \cdot f_{31} \cdot \sqrt{\varepsilon_{eff}}} = \frac{c_0}{2 \cdot f_{31} \cdot \sqrt{\varepsilon_{eff}}} \tag{3.50}$$

Moreover, since the backward wave will be coupled to the port P3, the maximum coupling level will be placed at f_{31}, and according to (3.21) the maximum coupling level, $|S_{31}(f_{31})|$, will be:

$$|S_{31}(f_{31})| = |S_{31}|_{max} = \tanh\left(\frac{A}{2} \cdot L\right) \tag{3.51}$$

Regarding the frequency bandwidth between zeros in the backward coupled band, $BW_{f,31}^{0\,dB}$, it can be calculated by means of the β, f pair relationship of (2.151) and the $BW_{\beta}^{0\,dB}$ expression of (3.18) as:

$$BW_{f,31}^{0\,dB} = BW_{\beta}^{0\,dB} \cdot \frac{c_0}{2 \cdot \pi \cdot \sqrt{\varepsilon_{eff}}} = \frac{c_0}{\pi \cdot \sqrt{\varepsilon_{eff}}} \cdot \sqrt{\left(\frac{A}{2}\right)^2 + \left(\frac{\pi}{L}\right)^2} \tag{3.52}$$

It is important to highlight that by using the EBG structure, the central frequency of the backward-coupled band, f_{31}, is fully independent of L as it can be observed in (3.50).

Considering now the transmission coefficients $T_e(f)$ and $T_o(f)$ used in (2.170) and (2.172), it is important to notice that out of the single backward-coupled band, the reflection coefficients $\Gamma_e(f)$ and $\Gamma_o(f)$ will be negligible since the reflection is governed by the spurious-free EBG structure carefully designed to forbid propagation only around f_{31}. Therefore, out of the single backward-coupled band, the magnitudes of $T_e(f)$ and $T_o(f)$ will be approximately equal to 1, while their phases will be a product, with minus sign, of the propagation constant of the even or odd mode, β_e or β_o, respectively, and the length of the device, L. Inspecting (2.172),

it can be seen that if $T_e(f) = -T_o(f)$, with magnitudes equal to 1, then $|S_{41}(f_{41})| = 1$ and the signal with frequency f_{41} will be forward-coupled to P4. This condition will be satisfied when:

$$\beta_e \cdot L - \beta_o \cdot L = m \cdot \pi \tag{3.53}$$

where $m = 1, 3, 5, ...$, and will give rise to a full coupling of the energy to P4 at the corresponding frequencies.

The length necessary for the EBG-assisted coupled line structure to get the first forward-coupled band to P4 at the frequency f_{41} is obtained from (3.53) when $m = 1$, as [41]:

$$L = \frac{c_0}{2 \cdot f_{41} \cdot \left(\sqrt{\varepsilon_{eff,e}} - \sqrt{\varepsilon_{eff,o}}\right)} \tag{3.54}$$

where $\varepsilon_{eff,e}$ and $\varepsilon_{eff,o}$ are the mean even and odd effective dielectric constants along the device that are directly associated to β_e and β_o through the expressions (2.181) and (2.182), respectively.

For higher values of $m = 3, 5, 7, ...$, additional forward-coupled bands will be obtained at the frequencies $m \cdot f_{41}$, see (3.53). Moreover, when $m = 0, 2, 4, ...$, $T_e(f)$ and $T_o(f)$ will be in phase, see (3.53), and if their magnitudes are equal to 1 then $T_e(f) = T_o(f)$ and $|S_{21}(f_{21})| = 1$, see (2.170). As a result, the signal with frequency f_{21} will be fully routed to the direct port (P2), where f_{21} can take the values $m \cdot f_{41}$ with $m = 0, 2, 4, ...$ It should be noted that in order to avoid the need of an excessive length for the device, a significant difference between $\varepsilon_{eff,e}$ and $\varepsilon_{eff,o}$ is necessary in the implementation technology.

In general, for the frequencies out of the single backward-coupled band produced by the EBG structure (where the magnitudes of $T_e(f)$ and $T_o(f)$ are approximately equal to 1), the frequency behavior of the forward-coupled bands, $|S_{41}(f)|$, and of the direct bands, $|S_{21}(f)|$, is given by [41]:

$$|S_{41}(f)| = \sin\left[\frac{\pi \cdot L \cdot f \cdot \left(\sqrt{\varepsilon_{eff,e}} - \sqrt{\varepsilon_{eff,o}}\right)}{c_0}\right] \tag{3.55}$$

$$|S_{21}(f)| = \cos\left[\frac{\pi \cdot L \cdot f \cdot \left(\sqrt{\varepsilon_{eff,e}} - \sqrt{\varepsilon_{eff,o}}\right)}{c_0}\right] \tag{3.56}$$

Since the coupling coefficient for both modes are known, the expressions (2.167) and (2.168) can be employed to determine their corresponding characteristic impedances, $Z_{0,e}(z)$ and $Z_{0,o}(z)$, leading to:

$$Z_{0,e}(z) = Z_{0,e}(0) \cdot e^{-\frac{A \cdot \Lambda}{\pi} \cdot \left[\cos\left(\frac{2 \cdot \pi}{\Lambda} \cdot z\right) - 1\right]} \tag{3.57}$$

$$Z_{0,o}(z) = Z_{0,o}(0) \cdot e^{\frac{A \cdot \Lambda}{\pi} \cdot \left[\cos\left(\frac{2 \cdot \pi}{\Lambda} \cdot z\right) - 1\right]} \tag{3.58}$$

where $Z_{0,e}(0)$ is the $Z_{0,e}(z)$ value at the beginning of the device, and Λ and L are calculated using (3.50) and (3.54), respectively, to obtain the backward- and forward-coupled bands around the frequencies f_{31} and f_{41}, respectively. The amplitude parameter, A, controls the coupling level, $|S_{31}(f_{31})|$, and bandwidth between zeros, $BW_{f,31}^{0\,dB}$, of the backward-coupled band through (3.51) and (3.52), as explained above, and fixes the maximum value for $Z_{0,e}(z)$, $Z_{0,e\,max}$, due to (3.25).

Finally, a tapering function, $W(z)$, is applied to the $Z_{0,e}(z)$ and $Z_{0,o}(z)$ profiles in order to smoothly adjust the values of the characteristic impedances at the ports P2 and P4, when a non-integer number of periods is necessary to complete the calculated device length, L. Additionally, the tapering function minimizes the ripple (side-lobe level) produced in frequency by the EBG structure, but it also reduces the level of energy coupled throughout the EBG and, consequently, the length L employed in (3.51) and (3.52) needs to be replaced by the effective length of the tapered EBG structure, L_{eff}, that can be calculated using (3.49).

Moreover, due to the fact that the even and odd modes propagate at different speeds, the $Z_{0,e}$ and $Z_{0,o}$ profiles are redistributed along the propagation direction using the $\varepsilon_{eff,e}$ and $\varepsilon_{eff,o}$ values in such a way that both modes are affected at each time instant by the same pair of impedances as in the case of equal speed propagation. The details about the employed compensation procedure are given in section 2.2.2.1. In this way, the design condition $K_e(z) = -K_o(z)$ is still satisfied in our device, although the even and odd modes feature different propagation constants.

The physical parameters of the EBG-assisted microstrip coupled-line structure (strip width and separation) are finally calculated from the obtained $Z_{0,e}(z)$ and $Z_{0,o}(z)$ profiles using the expressions available in [41] and *Agilent ADS LineCalc* tool, where even the thickness of the metallic strips is taken into account.

3.1.4.1. Example of Application: GSM and WLAN Triplexer

As an example of application, a microstrip triplexer working at GSM900 ($f_{21} = 900$ MHz) and both WLAN bands ($f_{31} = 2.4$ GHz and $f_{41} = 5.5$ GHz) has been designed using an EBG-assisted coupled line structure, see Fig. 3.5.

The substrate employed is Rogers RO3010 (ε_r=10.2, $h = 0.635$ mm) with 50 Ω input and output ports. The minimum separation between the metallic strips is fixed to 25 μm, which results in a maximum $Z_{0,e}(z)$ value of $Z_{0,e\,max} = 109.7\,\Omega$ (calculated using *Agilent ADS LineCalc*), guaranteeing a large value for the *A* parameter (see (3.25)) and consequently a high backward-coupling level, see (3.51). Again, using *Agilent ADS LineCalc*, the effective permittivities $\varepsilon_{eff,e} = 7.1$ and $\varepsilon_{eff,o} = 5.7$ are obtained for $f_{31} = 2.4$ GHz, resulting in a mean value of $\varepsilon_{eff} = 6.4$. Taking $Z_{0,e}(0) = 50.5\,\Omega$ and $Z_{0,o}(0) = 49.5\,\Omega$ for convenience, and using (3.50) and (3.25), the parameters to fix the $Z_{0,e}(z)$ and $Z_{0,o}(z)$ profiles (3.57), (3.58) to get the backward-coupled band at $f_{31} = 2.4$ GHz are obtained: $\Lambda = 24.8$ mm, $A = 49.2\,\text{m}^{-1}$. The device length is calculated using (3.54) to get a forward-coupled band at $f_{41} = 5.5$ GHz, with $\varepsilon_{eff,e} = 7.3$ and $\varepsilon_{eff,o} = 5.6$. The result obtained is $L = 81.3$ mm, which gives a number of periods of $N_\Lambda = 3.3$. The direct band will be placed around 0 GHz ($m \cdot f_{41}$, with $m = 0$), encompassing the intended value of $f_{21} = 900$ MHz. Due to the non-integer number of periods, and to minimize the ripple introduced in frequency by the EBG structure, an asymmetrical Bohman window [47] is applied over the $Z_{0,e}(z)$ and $Z_{0,o}(z)$ profiles. Finally, the spatial redistribution process of (2.216) and (2.217) is applied to $Z_{0,e}(z)$ and $Z_{0,o}(z)$, respectively, as it can be seen in Fig. 3.6. The designed device has been simulated using *CST Microwave Studio*,

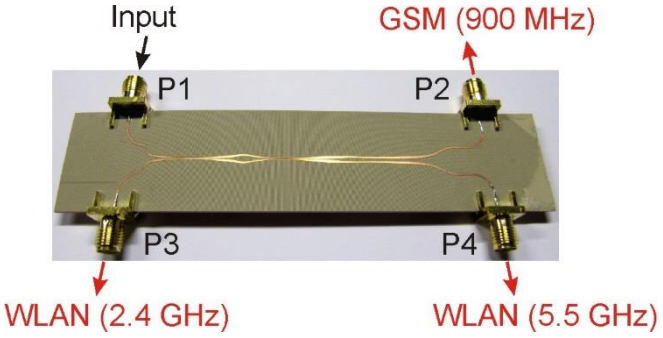

Fig. 3.5. Photograph of the microstrip triplexer, with labeled ports, implemented using an EBG-assisted coupled line structure.

fabricated with a *LPKF ProtoLaser 200* laser PCB milling machine (see Fig. 3.5) and measured by means of an *Agilent™ 8722 VNA*. The results are shown in Fig. 3.7 and Fig. 3.8.

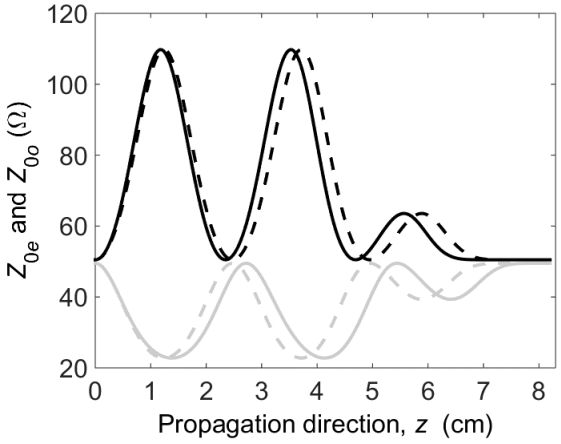

Fig. 3.6. Even (black line) and odd (grey line) characteristic impedances before (dashed line) and after (solid line) the spatial redistribution process.

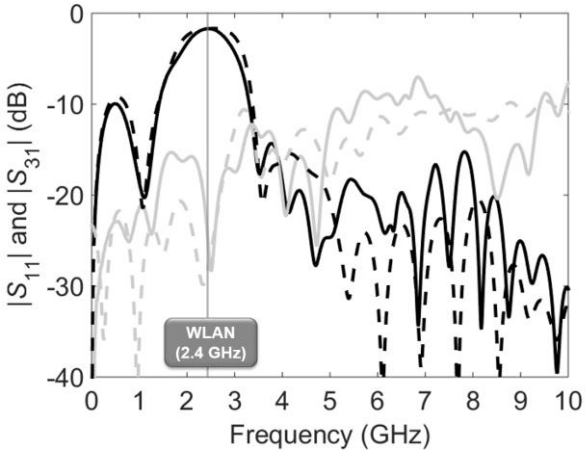

Fig. 3.7. Simulated (dashed line) and measured (solid line) $|S_{11}|$ (grey line) and $|S_{31}|$ (black line) parameters for the triplexer. The WLAN band operating at 2.4-2.45 GHz (IEEE 802.11b/g) backward-coupled to P3 is shaded in grey.

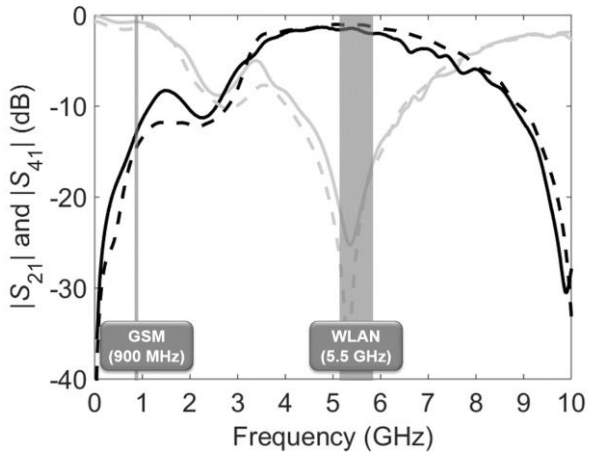

Fig. 3.8. Simulated (dashed line) and measured (solid line) $|S_{21}|$ (grey line) and $|S_{41}|$ (black line) parameters for the triplexer. The GSM band operating at 890-960 MHz (GSM900) directed to P2 and the WLAN band operating at 5.15-5.85 GHz (IEEE 802.11a) forward-coupled to P4 are shaded in grey.

A very good agreement is achieved between the simulated and measured results. As it can be seen, the input port (P1) is matched at all the frequencies, while the bands around $f_{21} = 900$ MHz, $f_{31} = 2.4$ GHz, and $f_{41} = 5.5$ GHz, are routed to the ports P2, P3, and P4, respectively, as intended, with measured coupling levels of $|S_{21}(f_{21})| = -0.7$ dB, $|S_{31}(f_{31})| = -1.7$ dB, and $|S_{41}(f_{41})| = -1.5$ dB. The differences with the theoretical coupling levels (-0.2 dB, -0.8 dB, and 0 dB), calculated using (3.56), (3.51), and (3.55), respectively, can be attributed to the conductor and dielectric losses.

REFERENCES

[1] L. Brillouin, “Wave Propagation in Periodic Structures”, New York: McGraw-Hill, 1946.

[2] A. A. Oliner and W. Rotman, “Periodic Structures in Through Waveguides,” *IRE Trans. Microw. Theory Tech.*, vol. 7, no. 1, pp. 134-142, Jan. 1959.

[3] Charles Elachi, “Waves in Active and Passive Periodic Structures: A Review,” *Proc. IEEE*, vol. 64, no. 12, pp. 1666-1698, Dec. 1976.

[4] Y. Rahmat-Samii and H. Mosallaei, “Electromagnetic band-gap structures: Classification, characterization and applications”, *Proc. Inst. Elect. Eng.-ICAP Symp.*, pp. 560-564, 2001.

[5] E. Yablonovitch, “Inhibited spontaneous emission in solid-state physics and electronics”, *Phys. Rev. Lett.*, vol. 58, no. 20, pp. 2059-2062, 1987

[6] E. Yablonovitch, T. J. Gmitter, K.M. Leung, “Photonic band structure: The face-centered-cubic case employing nonspherical atoms”, *Phys. Rev. Lett.*, no. 67, vol. 17, pp. 2295-2298, 1991.

[7] A. Yariv and M. Nakamura, “Periodic structures for integrated optics”, *IEEE J. Quantum Electron.*, vol. QE-13, pp. 233-253, 1977.

[8] W. S. C. Chang, “Periodic structures and their application in integrated optics”, *IEEE Trans. Microw. Theory Tech.* , vol. 21, pp. 775-785, 1973.

[9] J. Azana and M. A. Muriel, "Real-time optical spectrum analysis based on the time-space duality in chirped fiber gratings," *IEEE J. Quantum Electron.*, vol. 36, no. 5, pp. 517-526, May 2000.

[10] M.A.G. Laso, M.J. Erro, D. Benito, M.J. Garde, T. Lopetegi, F. Falcone, and M. Sorolla, “Analysis and design of 1-D photonic bandgap microstrip structures using a fiber grating model. *Microw. Opt. Technol. Lett.*, vol. 22: 223-226, July 1999.

[11] F. R. Yang, R. Coccioli, Y. Qian, T. Itoh, “Planar PBG structures: basic properties and applications,” *IEICE Trans. Electron.*, vol. E83-C, no. 5, pp .687-696, May 2000.

[12] Y. Qian, V. Radisic, and T. Itoh, “Simulation and experiment of photonic bandgap structures for microstrip circuits”, *Asia-Pacific APMC ‘97*, vol.2, pp.585-588, 2-5 Dec. 1997.

[13] V. Radisic, Y. Qian, R. Coccioli, and T. Itoh, “Novel 2-D photonic bandgap structure for microstrip lines”, *IEEE Microwave Guide Wave Lett.*, vol. 8, pp. 69-71, 1998.

[14] N. V. Nair and A. K. Mallick, “An analysis of a width-modulated microstrip periodic structure”, *IEEE Trans. Microw. Theory Tech.*, vol. MTT-32, pp. 200- 204, 1984.

[15] Miguel A. G. Laso, “Electromagnetic Crystals in optical Fiber and Microstrip Technology,” Doctoral Thesis, Universidad Publica de Navarra, Espana, 2002.

[16] M. A. G. Laso, T. Lopetegi, M. J. Erro, D. Benito, M. J. Garde and M. Sorolla, "Multiple-frequency-tuned photonic bandgap microstrip structures," *IEEE Microwave Guide Wave Lett.*, vol. 10, no. 6, pp. 220-222, June 2000.

[17] F. Falcone, T. Lopetegi, and M. Sorolla, "1-D and 2-D Photonic Band Gap Microstrip Structures," *Microw. Opt. Technol. Lett.*, vol. 22, pp. 411-412, Sep. 1999.

[18] T. Lopetegi, M. A. G. Laso, M. J. Erro, M. Sorolla, and M. Thumm, "Analysis and design of periodic structures for microstrip lines by using the coupled mode theory," *IEEE Microw. Wireless Compon. Lett.*, vol. 12, no. 11, pp. 441-443, Nov. 2002.

[19] I. Arnedo et al., "Analytical solution for the design of planar EBG structures with spurious-free frequency response," *2009 European Microwave Conference (EuMC)*, Rome, 2009, pp. 1299-1302.

[20] M. Sorolla, D. Schmitt, M. Guglielmi, J. Gil, and N. Ortiz, "Microwave bandstop filter for an output multiplexer," U.S. Patent 7468641 B2, Dec. 23, 2008.

[21] I. Arnedo, J. Gil, N. Ortiz, T. Lopetegi, M. A. G. Laso, M. Thumm, M. Sorolla, D. Schmitt, and M. Guglielmi, "Ku-Band High-Power Low-Pass Filter with Spurious Rejection," *IET Electron. Lett.*, vol. 42, no. 25, pp. 1460-1461, Dec 2006.

[22] M. Chudzik et al., "Microstrip coupled-line directional coupler with enhanced coupling based on EBG concept," *IET Electron. Lett.*, vol. 47, no. 23, pp. 1284-1286, 10 Nov. 2011.

[23] M. Chudzik et al., "Design of EBG microstrip directional coupler with high directivity and coupling," *2012 42nd European Microwave Conference*, Amsterdam, 2012, pp. 483-486.

[24] J. M. Percaz et al., "Producing and Exploiting Simultaneously the Forward and Backward Coupling in EBG-Assisted Microstrip Coupled Lines," *IEEE Antennas Wirel. Propag. Lett.*, vol. 15, pp. 873-876, 2016.

[25] C. Caloz, S. Gupta, Q. Zhang and B. Nikfal, "Analog Signal Processing: A Possible Alternative or Complement to Dominantly Digital Radio Schemes," *IEEE Microw. Mag.*, vol. 14, no. 6, pp. 87-103, Sept.-Oct. 2013.

[26] M. A. G. Laso et al., "Chirped delay lines in microstrip technology," *IEEE Microw. Wirel. Compon. Lett.*, vol. 11, no. 12, pp. 486-488, Dec. 2001.

[27] A. Lujambio, I. Arnedo, M. Chudzik, I. Arregui, T. Lopetegi and M. A. G. Laso, "Dispersive Delay Line with Effective Transmission-Type Operation in Coupled-Line Technology," *IEEE Microw. Wirel. Compon. Lett.*, vol. 21, no. 9, pp. 459-461, Sept. 2011.

[28] M. A. G. Laso et al., "Real-time spectrum analysis in microstrip technology," *IEEE Trans. Microw. Theory Tech.*, vol. 51, no. 3, pp. 705-717, March 2003.

[29] J. D. Schwartz, J. Azana and D. V. Plant, "Experimental demonstration of real-time spectrum analysis using dispersive microstrip," *IEEE Microw. Wirel. Compon. Lett.*, vol. 16, no. 4, pp. 215-217, April 2006.

[30] J. D. Schwartz, J. Azana and D. V. Plant. "A fully electronic system for the time magnification of ultra-wideband signals" *IEEE Trans. Microw. Theory Tech.*, vol. 55, no.2, pp. 327-334, Feb. 2007.

[31] R. Gonzalo, P. Maagt, and M. Sorolla, "Enhanced patch-antenna performance by suppressing surface waves using photonic-bandgap substrates", *IEEE Trans. Microw. Theory Tech.*, vol. 47, pp. 2131-2138, 1999.

[32] D. Sievenpiper, L. Zhang, R. F. J. Broas, N. G. Alexopolus, and E. Yablonovitch, "High-impedance electromagnetic surfaces with a forbidden frequency band", *IEEE Trans. Microw. Theory Tech.*, vol. 47, pp. 2059-2074, 1999.

[33] L. Yang, M. Fan, F. Chen, J. She, and Z. Feng, "A novel compact electromagnetic bandgap (EBG) structure and its applications for microwave circuits", *IEEE Trans. Microw. Theory Tech.*, vol. 53, no. 1, pp. 183-190, 2005.

[34] N. Engheta, "Thin absorbing screens using metamaterial surfaces", *IEEE AP-S Int. Symp. Dig.*, vol. 2, pp. 392-395, 2002

[35] J. Kern and D. H. Werner, "Ultra-thin electromagnetic bandgap absorbers synthesized via genetic algorithms," *IEEE AP-S/URSI Symp. Dig.*, vol. 2, pp. 1119- 1122, 2003.

[36] H. Nakano, K. Kikkawa, N. Kondo, Y. Iitsuka, and J. Yamauchi "Low-profile equiangular spiral antenna backed by an EBG reflector", *IEEE Antennas Wirel. Propag. Lett.*, vol. 57, no. 5, pp. 1309-1318, 2009.

[37] Txema Lopetegi, "Photonic Bandgap Structures in Microstrip Technology: Study using the Coupled Mode Formalism and Applications," Doctoral Thesis, Universidad Publica de Navarra, Espana, 2002.

[38] A. Papoulis, The Fourier Integral and its Applications (Electronic Science Series). New York, NY, USA: McGraw-Hill, 1962.

[39] Israel Arnedo, "New Methods for the Synthesis of Microwave Devices Based on the Coupled-Mode Theory," Doctoral Thesis, Universidad Pública de Navarra, España, 2009.

[40] M. A. G. Laso, M. J. Erro, T. Lopetegi, D. Benito, M. J. Garde, and M. Sorolla, "Optimization of Tapered Bragg Reflectors in Microstrip Technology," *J. Infrared Millim. Terahertz Waves*, vol. 21, no. 2, pp. 231-245, Feb. 2000.

[41] R. K. Mongia, I. J. Bahl, P. Bhartia, and J. Hong, RF and Microwave Coupled-Line Circuits, Norwood, USA, Artech House, 2007.

[42] B. M. Oliver, "Directional Electromagnetic Couplers," *Proc. IRE*, vol. 42, pp. 1686-1692, Nov. 1954.

[43] H. Mextorf, R. Knochel, "The intrinsic impedance and its application to backward and forward coupled-line couplers," *IEEE Trans. Microw. Theory Tech.*, vol. 62, no. 2, pp. 224-233, Feb. 2014.

[44] K. Ikalainen, G. L. Matthaei, "Wide-band, forward-coupling microstrip hybrids with high directivity," *IEEE Trans. Microw. Theory Tech.*, vol. 35, no. 8, pp. 719-725, Aug. 1987.

[45] P. Velez, J. Bonache, F. Martin, "Differential Microstrip Lines with Common-Mode Suppression Based on Electromagnetic Band-Gaps (EBGs)," *IEEE Antennas Wireless Propagation Letters*, vol. 14, pp. 40-43, 2015.

[46] M. Chudzik, I. Arnedo, A. Lujambio, I. Arregui, I. Gardeta, F. Teberio, J. Azana, D. Benito, M. A .G. Laso, and T. Lopetegi, "Design of Transmission-Type Nth-Order Differentiators in Planar Microwave Technology," *IEEE Trans. Microw. Theory Tech.*, vol. 60, no. 11, pp. 3384-3394, Nov. 2012.

[47] H. Bohman, "Approximate Fourier analysis of distribution functions," Arkiv för Matematik, vol. 4, no. 2-3, pp. 99-157, 1960.

upna

Universidad Pública de Navarra
Nafarroako Unibertsitate Publikoa

CHAPTER 4. THE GEL'FAND, LEVITAN & MARCHENKO EXACT SERIES SOLUTION FOR THE SYNTHESIS PROBLEM

The one-dimensional Inverse Scattering synthesis problem of how to directly calculate the coupling coefficient, $K(z)$, as a function of the complex frequency response in reflection can be expressed as a system of Gel'fand-Levitan-Marchenko coupled-integral equations [1], [2] as it was firstly demonstrated by Peral *et al.* in [3] in 1996 for the synthesis of fiber gratings for the optics range. In the microwave range, numerical solutions were attained by discretizing the system and using it as a recurrence relation in an iterative manner [4] being this method successfully applied for the synthesis of microwave filters with strict specifications [5]. Similar results were obtained by Kritikos *et al.* for the reconstruction of dielectric profiles [6] using an algorithm that was subsequently refined by other authors in [7], [8]. Finally, the series solution of the coupling coefficient for the microwave domain was brilliantly achieved by Arnedo *et al.* in [9], while an optimized algorithm based in that solution was published by Chudzik *et al.* in [10].

In order to formulate the exact series solution for the coupling coefficient for any causal, stable and passive frequency response in reflection, it is necessary to start from the single-mode coupled-mode equation system of (2.91), (2.92):

$$\frac{da^+}{dz} = -j \cdot \beta \cdot a^+ + K \cdot a^- \tag{2.91}$$

$$\frac{da^-}{dz} = j \cdot \beta \cdot a^- + K \cdot a^+ \tag{2.92}$$

As it was mentioned in CHAPTER 2, when dealing with two propagating waves of the same mode, $K(z)$ is a real function, i.e. $K(z) = K^*(z)$, where $*$ stands for the complex conjugate. Accordingly, (2.91), (2.92) can be expressed as a Zakharov-Shabat system for quantum mechanics [11] as:

$$j \cdot \begin{bmatrix} \frac{d}{dz} & -K \\ K^* & \frac{-d}{dz} \end{bmatrix} \cdot \begin{bmatrix} a^+ \\ a^- \end{bmatrix} = \beta \cdot \begin{bmatrix} a^+ \\ a^- \end{bmatrix} \tag{4.1}$$

We introduce two linearly independent solutions of the Zakharov-Shabat system (two of the so-called Jost functions) which satisfy in the limit [9], [11]:

$$\lim_{z \to -\infty} \begin{bmatrix} \phi_1(z,\beta) \\ \phi_2(z,\beta) \end{bmatrix} = \begin{bmatrix} 1 \\ 0 \end{bmatrix} \cdot e^{-j \cdot \beta \cdot z} \tag{4.2}$$

$$\lim_{z \to -\infty} \begin{bmatrix} \overline{\phi}_1(z,\beta) \\ \overline{\phi}_2(z,\beta) \end{bmatrix} = \begin{bmatrix} 0 \\ 1 \end{bmatrix} \cdot e^{j \cdot \beta \cdot z} \tag{4.3}$$

Now, in order to solve the synthesis problem, the coupling region is assumed to be located within $z = 0$ and $z = L$, and therefore $K(z) = 0$ for $z < 0$ and $z > L$. A solution of the Zakharov-Shabat system (and hence of the coupled-mode equations) with the boundary conditions $a^+(z = 0, \beta) = 1$ and $a^-(z = L, \beta) = 0$ (i.e., output port matched) can be obtained as a linear combination of the previous Jost functions (4.2) and (4.3) of the form [9], [11]:

$$\begin{bmatrix} u_1(z,\beta) \\ u_2(z,\beta) \end{bmatrix} = \begin{bmatrix} \phi_1(z,\beta) \\ \phi_2(z,\beta) \end{bmatrix} + S_{11}(\beta) \cdot \begin{bmatrix} \overline{\phi}_1(z,\beta) \\ \overline{\phi}_2(z,\beta) \end{bmatrix} \tag{4.4}$$

being:

$$S_{11}(\beta) = \left.\frac{a^-(z=0,\beta)}{a^+(z=0,\beta)}\right|_{a^-(z=L,\beta)=0} \tag{4.5}$$

where the solution $a^+(z,\beta) = u_1(z,\beta)$, $a^-(z,\beta) = u_2(z,\beta)$, corresponds to the situation when the output port is matched, and the values at the input port of the filter are $a^+(z=0,\beta) = u_1(z=0,\beta) = 1$ and $a^-(z=0,\beta) = u_2(z=0,\beta) = S_{11}(\beta)$.

Taking into account these considerations, and the behavior of the Jost functions at the limit (4.2) and (4.3) that will remain valid up to the input port of the structure at $z = 0$ (since $K(z) = 0$ for $z < 0$), the validity of (4.4) can be easily verified.

One of the previous Jost functions (solution of the Zakharov-Shabat system) can be represented as [9], [11]:

$$\begin{bmatrix}\phi_1(z,\beta)\\ \phi_2(z,\beta)\end{bmatrix} = \begin{bmatrix}1\\0\end{bmatrix}\cdot e^{-j\cdot\beta\cdot z} + \int_{-\infty}^{\infty}\begin{bmatrix}A_1(z,\tau)\\ A_2(z,\tau)\end{bmatrix}\cdot e^{-j\cdot\beta\cdot\tau}\cdot d\tau \tag{4.6}$$

where the first term corresponds to the propagation of the forward traveling wave in the absence of coupling region (behavior at the limit (4.2)), and $A_1(z,\tau)$, $A_2(z,\tau)$, are the kernel functions that characterize the scattering effect produced by the coupling region (i.e. the synthetized structure).

Additionally, using symmetry properties of the Zakharov-Shabat system (4.1), it can be easily demonstrated that our two Jost functions are related as [11]:

$$\begin{bmatrix}\overline{\phi}_1(z,\beta)\\ \overline{\phi}_2(z,\beta)\end{bmatrix} = \begin{bmatrix}\phi_2^*(z,\beta)\\ \phi_1^*(z,\beta)\end{bmatrix} \tag{4.7}$$

As it was stated in [12], [13], it is important to highlight that β is the independent variable in the Zakharov-Shabat system, while frequency, f, is the final independent variable in the coupled-mode equations. Therefore, it is necessary to assume that variables β and f are univocally related once the technology is chosen, and it means that β does not vary with z for a given frequency. This aspect may be troublesome when considering several technologies, but it can be exactly compensated for a single frequency using the strategy that was presented in section 2.2.2. Moreover, it will be assumed in the application of the synthesis method that β does not depend on z (as it is needed), and the obtained solution will be subsequently corrected when needed using the aforementioned strategy.

In order to solve the synthesis problem by applying causality considerations, it is recalled that the coupling region (i.e. the area of designed device) begins at $z = 0$, and therefore $K(z) = 0$ for $z < 0$. Accordingly, the problem is reformulated in the time domain using the Fourier Transform [14], by introducing the variables $V^+(z,\tau)$ and $V^-(z,\tau)$ that are related to the amplitudes of the forward and backward travelling waves, respectively, as:

$$V^+(z,\tau) = \frac{1}{2\cdot\pi}\cdot\int_{-\infty}^{\infty} a^+(z,\beta)\cdot e^{j\cdot\beta\cdot\tau}\cdot d\beta \tag{4.8}$$

$$V^-(z,\tau) = \frac{1}{2\cdot\pi}\cdot\int_{-\infty}^{\infty} a^-(z,\beta)\cdot e^{j\cdot\beta\cdot\tau}\cdot d\beta \tag{4.9}$$

By taking the inverse Fourier Transform of (4.8), (4.9) in the solution of the Zakharov-Shabat system of (4.4), and after several mathematical manipulations, the subsequent expression can be obtained [9], [11]:

$$\begin{bmatrix}U_1(z,\tau)\\U_2(z,\tau)\end{bmatrix} = \begin{bmatrix}\delta(\tau-z)\\0\end{bmatrix} + \begin{bmatrix}A_1(z,\tau)\\A_2(z,\tau)\end{bmatrix} + \begin{bmatrix}0\\1\end{bmatrix}\cdot F(z+\tau) + \int_{-\infty}^{\infty}\begin{bmatrix}A_2^*(z,y)\\A_1^*(z,y)\end{bmatrix}\cdot F(y+\tau)\cdot dy \tag{4.10}$$

where

$$F(\tau) = \frac{1}{2\cdot\pi}\cdot\int_{-\infty}^{\infty} S_{11}(\beta)\cdot e^{j\cdot\beta\cdot\tau}\cdot d\beta \tag{4.11}$$

and

$$S_{11}(\beta) = \int_{-\infty}^{\infty} F(\tau)\cdot e^{-j\cdot\beta\cdot\tau}\cdot d\tau \tag{4.12}$$

being $F(\tau)$ the inverse Fourier Transform of the $S_{11}(\beta)$-parameter. Due to the causality principle, $F(\tau)$ must satisfy the condition [3], [9]:

$$F(\tau) = 0 \;\forall\; \tau < 0 \tag{4.13}$$

Moreover, applying causality considerations, it follows that [11]:

$$\begin{bmatrix}A_1(z,\tau)\\A_2(z,\tau)\end{bmatrix} = 0 \;\forall\; z < |\tau| \tag{4.14}$$

At this point, new functions $Y_1(z,\tau)$ and $Y_2(z,\tau)$ can be conveniently defined as:

$$\begin{bmatrix} Y_1(z,\tau) \\ Y_2(z,\tau) \end{bmatrix} = \begin{bmatrix} U_1(z,\tau) \\ U_2(z,\tau) \end{bmatrix} - \begin{bmatrix} \delta(\tau - z) \\ 0 \end{bmatrix} \tag{4.15}$$

and considering again the causality principle [11]:

$$\begin{bmatrix} Y_1(z,\tau) \\ Y_2(z,\tau) \end{bmatrix} = 0 \; \forall \; |z| > \tau \tag{4.16}$$

Using (4.13) and (4.14), the integration range of (4.10) can be limited from $-\tau$ to z. Additionally, using (4.10) in (4.15), (4.16), the so-called Gel'fand-Levitan-Marchenko coupled-integral equations can be obtained as it is provided below:

$$A_1(z,\tau) + \int_{-\tau}^{z} A_2^*(z,y) \cdot F(y+\tau) \cdot dy = 0 \qquad ,|z| > \tau \tag{4.17}$$

$$A_2(z,\tau) + F(z+\tau) + \int_{-\tau}^{z} A_1^*(z,y) \cdot F(y+\tau) \cdot dy = 0 \qquad ,|z| > \tau \tag{4.18}$$

At this point, it will be necessary to deduce the relationship between the functions $A_1(z,\tau)$, $A_2(z,\tau)$ that appear in the Gel'fand-Levitan-Marchenko equations of (4.17), (4.18) and the coupling coefficient, $K(z)$, required to obtain the targeted frequency response that is expressed in its time-domain version, $F(\tau)$, of (4.11). In order to achieve that relationship, the problem is formulated in the τ-domain by taking the inverse Fourier Transform of the coupled-mode equation system of (2.91), (2.92), as well as the inverse Fourier Transforms of $a^+(z,\beta)$ and $a^-(z,\beta)$, $V^+(z,\tau)$ and $V^-(z,\tau)$, respectively, of (4.8) and (4.9), leading to [9]:

$$\frac{\partial V^+(z,\tau)}{\partial z} + \frac{\partial V^+(z,\tau)}{\partial \tau} = K(z) \cdot V^-(z,\tau) \tag{4.19}$$

$$\frac{\partial V^-(z,\tau)}{\partial z} - \frac{\partial V^-(z,\tau)}{\partial \tau} = K(z) \cdot V^+(z,\tau) \tag{4.20}$$

It must be highlighted that the transformation is performed assuming that $K(z)$ does not depended on β, or in other words, on frequency, f.

Now, it must be reminded that the functions $u_1(z,\beta)$ and $u_2(z,\beta)$ defined in (4.4) are a solution of the Zhakarov-Shabat system and thus, their corresponding inverse Fourier transformed pairs $U_1(z,\tau)$, $U_2(z,\tau)$ of (4.10), must be also a solution of the τ-domain coupled-mode equations of (4.19) and (4.20). From (4.15), $U_1(z,\tau)$ and $U_2(z,\tau)$ can be rewritten as:

$$\begin{bmatrix} U_1(z,\tau) \\ U_2(z,\tau) \end{bmatrix} = \begin{bmatrix} Y_1(z,\tau) \\ Y_2(z,\tau) \end{bmatrix} + \begin{bmatrix} \delta(\tau - z) \\ 0 \end{bmatrix} \tag{4.21}$$

If the identity (4.21) is introduced into the equation (4.20), it will lead to:

$$\frac{\partial Y_2(z,\tau)}{\partial z} - \frac{\partial Y_2(z,\tau)}{\partial \tau} = K(z) \cdot [Y_1(z,\tau) + \delta(\tau - z)] \tag{4.22}$$

Then, if a coordinate transformation is performed in (4.22) and both sides are integrated by taking into account (4.16), (4.22) will yield to [9]:

$$-Y_2(z,z^+) = \frac{1}{2} \cdot K(z) \tag{4.23}$$

The expression of $K(z)$ can be deduced from (4.23), by getting the expression for $Y_2(z,z^+)$ from (4.15) and (4.10), as well as by taking under consideration (4.14), leading to:

$$K(z) = -2 \cdot F(2z) - 2 \cdot \int_{-z}^{z} A_1^*(z,y) \cdot F(y+z) \cdot dy \tag{4.24}$$

This equation (4.24) allows the analytical calculation of the coupling coefficient, $K(z)$, necessary to obtain the target frequency response (that is expressed in its τ-domain through the function $F(\tau)$ of (4.11)) from the $A_1(z,\tau)$-parameter that is employed in the Gel'fand-Levitan-Marchenko equations of (4.17) and (4.18). It must be noted that since the coupling region have been restricted to $z \geq 0$ due to the consideration of the causality principle, it will be necessary to know $A_1(z,\tau)$ in the región $|\tau| < z$ that is fully included within the limits of the Gel'fand-Levitan-Marchenko equations of (4.17) and (4.18).

If the integral term of (4.24) is neglected, the zero-th order approximation for the coupling coefficient will be obtained as:

$$K(z) \cong -2 \cdot F(2z) \tag{4.25}$$

It must be highlighted that the zero-th order approximation of (4.25) is fully coincident with the classical Fourier Transform approximation that was early reported in [15], [16], which is only valid for devices that feature low reflectivity. The physical meaning of this approximation is that the coupling is so weak that the amplitude of the incident mode can be approximated as constant along the whole structure.

4.1. ITERATIVE SOLUTION

The final necessary step to achieve the series solution for the synthesis problem is to solve the Gel'fand-Levitan-Marchenko system for $A_1(z,\tau)$ by using an iterative method reported originally in [3]. For doing so, the Gel'fand-Levitan-Marchenko system of (4.17) and (4.18) can be rewritten as follows:

$$A_1(z,\tau) = -\int_{-\tau}^{z} A_2^*(z,y)\cdot F(y+\tau)\cdot dy \qquad ,|z|>\tau \tag{4.26}$$

$$A_2(z,\tau) = -F(z+\tau) - \int_{-\tau}^{z} A_1^*(z,y)\cdot F(y+\tau)\cdot dy = 0 \quad ,|z|>\tau \tag{4.27}$$

If the integral term of (4.27) is neglected, the zero-th order approximation for $A_2(z,\tau)$ will be attained:

$$A_2(z,\tau) \cong -F(z+\tau) \tag{4.28}$$

And then, by introducing (4.28) into (4.26), the first-order approximation for $A_1(z,\tau)$ will be obtained as:

$$A_1(z,\tau) \cong \int_{-\tau}^{z} F^*(z+y)\cdot F(y+\tau)\cdot dy \tag{4.29}$$

If the solution of (4.29) is introduced into the coupling coefficient expression of (4.24), the first-order approximate solution for $K(z)$ can be deduced as [9]:

$$K(z) = -2\cdot F(2z) - 2\cdot \int_{-z}^{z} dx_1\cdot F(x_1+z)\cdot \int_{-x_1}^{z} dx_2\cdot F(z+x_2)\cdot F^*(x_1+x_2) \tag{4.30}$$

Proceeding in an iterative manner, i.e. introducing (4.29) into (4.27), and its result subsequently into (4.26), the second-order approximation for $A_1(z,\tau)$ is obtained, which can be used in turn in (4.24) so as to achieve the second-order approximate solution for the coupling coefficient. If the procedure is further iterated while taking into account that $F(\tau)$ must be real for any physical device, the exact analytical series solution for the coupling coefficient will be eventually attained as [9]:

$$
\begin{aligned}
K(z) = &-2 \cdot F(2z) + \\
&-2 \cdot \int_0^{2z} dx_1 F(x_1) \cdot \int_0^{x_1} dx_2' F(x_2') \, F(x_2' - x_1 + 2z) + \\
&-2 \int_0^{2z} dx_1 F(x_1) \int_0^{x_1} dx_2' F(x_2') \int_0^{x_2} dx_3' F(x_3') \int_0^{x_3} dx_4' F(x_4') \, F(x_4' - x_3 + 2z) + \\
&- \cdots + \\
&-2 \int_0^{2z} dx_1 F(x_1) \int_0^{x_1} dx_2' F(x_2') \int_0^{x_2} \ldots \int_0^{x_{2N-1}} dx_{2N}' F(x_{2N}') \, F(x_{2N}' - x_{2N-1} + 2z) + \\
&- \cdots +
\end{aligned}
\tag{4.31}
$$

where $x_i' = x_i + x_{i-1} - 2z$ for $i > 1$.

The analytical solution of (4.31) allows us to calculate the coupling coefficient, $K(z)$, required to implement a target frequency response $S_{11}(\beta)$ that has its counterpart in the τ-domain as $F(\tau) = TF^{-1}\{S_{11}(\beta)\}$, as it was stated in (4.11). It must be highlighted that the only approximations taken to obtain the synthesis solution of (4.31) are the single-mode operation, the assumption that the phase constant, β, does not vary with z for a given frequency along the whole device, and the assumption that $K(z)$ does not depend on frequency.

It must be noted that in order to practically employ (4.31), it will be necessary to truncate the approximation order, N. Indeed, it is worth noting that the higher the approximation order N taken for the solution of (4.31), the higher the reflectivity achievable for the device, and the more accurate the coupling coefficient calculated, as it was demonstrated in [12]. This aspect was also addressed in [10], where an efficient computation algorithm was proposed for the calculation of the N-th approximation of (4.31).

Finally, it is worth noting that the feasibility of synthesizing microwave devices by means of the GLM series solution technique was originally demonstrated in [9] and it has been successfully employed in many cases since then [18]-[21], being some quite recent.

4.2. General Synthesis of Tapered Matching Sections for Single-Mode Operation

Tapered matching sections, or simply tapers, for microwave transmission lines and waveguides are a mature research topic that can be traced back almost a century [22]-[24]. They can be defined as a smooth intermediate structure that allows us to connect two transmission lines or waveguides of different characteristic impedances or cross-sections, with a profile that varies continuously in a smooth fashion from one transmission line or waveguide to the other. The taper is designed to minimize the excitation of unwanted modes (including reflection), keeping the excitation level under a given design value. Following that broad definition, it is easy to understand the importance of tapers, since they solve a common problem in numerous different microwave devices, technologies and systems.

Many different techniques for the design of tapers have been developed using the transmission line theory [25], [26]. Linear, hyperbolic, parabolic and exponential functions, among others, have been proposed. However, two sophisticated solutions must be highlighted. The first one was proposed by Klopfenstein [27] and later on completed by other authors [28]-[30], and it is also known as the Dolph-Chebyshev function. It achieves the optimum taper in the sense that its reflection level is below the maximum specified for the frequencies above the minimum required, with a tapering function of minimum length. However, the taper always exhibits discontinuities (steps) at its extremes that are inherent to the function. These critical steps can result in manufacturability problems and in the excitation of higher order modes that can be troublesome for certain applications. The second solution was proposed by Hecken [31] and it is also known as the modified Dolph-Chebyshev function. It is considered as a near-optimum taper and achieves a performance close to the Klopfenstein optimum proposal, employing a fully smooth tapering function with no discontinuities, but with a slightly larger length. Anyway, both Klopfenstein and Hecken tapers were developed for ideal transmission lines, in terms of the characteristic impedance parameter.

Very interesting proposals have been done to extend the theory of transmission line tapers to non-ideal transmission lines, synthesizing the taper in terms of the characteristic impedance but taking into account dispersion. Implementations in microstrip technology have been proposed [32], [33] and even tapers in finline have been carefully designed. For the finline case,

the synthesis has been done in terms of the wave impedance [32] or using the mode coupling coefficient [34], [35] by introducing several approximations valid for that technology.

Tapers have been also widely studied and employed in microwave waveguide technologies, especially in rectangular and circular waveguides [36], [37]. Initially, simple tapers with linear profiles were proposed for circular (conical taper) [38] and rectangular waveguides (pyramidal taper) [39], [40]. The excitation of parasitic modes (including reflection) in linear tapers is often relatively high, and to reduce it the length of the taper must be increased often to large values. A better taper design was achieved by successive connection of several cones with different contour angles [41], [42]. However, when the number of conical sections employed is large, these tapers approach the superior nonlinear smooth tapers, where the contour angle is changed continuously. Several techniques have been proposed to design nonlinear smooth tapers, most of them resting on the use of the coupled-mode theory [36], [37]. Some elegant and solid synthesis procedures are available for circular waveguide tapers [36], [37], [43]-[45], also applicable to rectangular tapers where the height of the waveguide is kept constant [36]. Guidelines to extend the synthesis procedures to arbitrary cross sections are given in [37] and an analytical solution for parabolic tapers is obtained in [46]. All these synthesis procedures achieve nonlinear smooth tapers for overmoded (highly multimode) waveguides, with very low excitation of the parasitic mode, where only the most strongly coupled unwanted (parasitic) mode is taken into account, and assuming that both modes are far above cutoff. These devices are of high interest in the field of high-power microwaves or to transmit microwave signals with very low losses. If several higher-order parasitic modes need to be taken into account in the synthesis, then a quasidiagonalization of the coupled-mode equations can be performed, [36], [47], [48]. Using this technique, a more accurate synthesis can be achieved but still assuming that all the relevant modes are far above cutoff. More complex taper synthesis techniques (based on the use of horn modes) have been proposed for the case when the parasitic mode is close to cutoff [36], or even when the parasitic mode is below cutoff in a region of the taper [36], [37]. In any case, all these synthesis techniques have been developed assuming multimode operation in the taper and with the aim of minimizing the coupling to the main parasitic mode.

A systematic and general synthesis procedure to design microwave waveguide tapers for single-mode operation able to implement the Klopfenstein and Hecken analytical responses, among others, is not available in the literature. Those single-mode tapers are of high interest for microwave telecommunication devices like filters and couplers. Recently, a novel and interesting design method based on the use of generalized superellipses and optimization algorithms has been proposed, demonstrating successful results in microstrip and rectangular waveguide single-mode tapers [49].

It can be summarized that there is an absence of a technique to translate the Klopfenstein and Hecken analytical responses from the transmission line theoretical background to the general waveguide domain. However, by using the general synthesis workflow that is followed within the present thesis it will be possible to calculate the coupling coefficient, $K(z)$, from both analytical responses, and the specific implementation will depend on the required technology. Furthermore, it will be possible to employ a modified version of the frequency response of multisection Chebyshev transformers so as to synthetize tapered matching sections shorter than the classical approaches of Klopfenstein and Hecken. Last but not least, it must be highlighted that the GLM synthesis technique is very suitable for the design of general waveguide tapers for single-mode operation, since the reflection required for the targeted $S_{11}(\beta)$ will be typically very low, and thus the required coupling coefficient, $K(z)$, will be accurately calculated by taking into account only a few terms (low order solution) of the GLM series solution of (4.31).

The maximum reflectivity, ρ_m, allowed for the taper, i.e. $|S_{11}| \leq \rho_m$, can be formulated in terms of the return loss level, RL, in dBs as:

$$\rho_m = 10^{-RL/20} \tag{4.32}$$

In the case of a tapered matching section, it is worth noting that there is an inherent port mismatch level, $\rho_0 = S_{11}(\beta = 0)$, whose specific value will depend on the difference between the cross-sections of its ports. Following the notation of the single-mode coupled-mode equation system of (2.91), (2.92), ρ_0 can be defined as:

$$\rho_0 = S_{11}(\beta = 0) = \left.\frac{a^-(z = 0, \beta = 0)}{a^+(z = 0, \beta = 0)}\right|_{a^-(z=L)=0} \tag{4.33}$$

where L is the length of the taper. Taking into account the ρ_0 definition of (4.33), and setting $\beta = 0$ and $z = 0$ in the coupled-mode equations (2.91), (2.92), a useful relationship between ρ_0 and $K(z)$ can be obtained after some mathematical manipulations:

$$\rho_0 = \tanh\left[-\int_0^L K(z) \cdot dz\right] \tag{4.34}$$

It is interesting to note that the coupling coefficient, $K(z)$, depends finally on the physical dimensions of the waveguide and, therefore, for a target coupling coefficient obtained through the GLM synthesis method, the waveguide physical parameters can be deduced using the expressions found for the technologies studied in section 2.2.

However, it must be highlighted that the change in the waveguide dimensions may involve a change in the phase constant along the propagation axis, and thus, it will be necessary to employ the modelling method carefully developed in section 2.2.2 for the concerning cases. As it was stated in that section, the application of this modelling requires the definition of a reference phase constant, β_{ref}, that will be assumed to remain constant along a normalized propagation axis χ. Since the dimensions of the ports will be a typical requirement for the taper design, β_{ref} can be conveniently chosen as the average phase constant between the ports, $\bar{\beta}$, defined as:

$$\beta_{ref} = \bar{\beta}(f) = \frac{\beta(f, z = 0) + \beta(f, z = L)}{2} \tag{4.35}$$

It must be reminded that this modelling using a reference phase constant, β_{ref}, of structures with β variable along z, will be exact for an arbitrarily selected frequency, f_t. The selection of f_t will eventually determine the relationship between the normalized propagation axis, χ, and the actual, z. Therefore, taking into account the expression (2.208) that determines the relation $z(\chi)$, and the identity (4.35), it can be concluded that for the synthesis of general waveguide tapers, $z(\chi)$ will be calculated as:

$$z(\chi) = \int_0^{\chi} \frac{\bar{\beta}(f_t)}{\beta(f_t, r)} \cdot dr \tag{4.36}$$

Not only for the propagation axis transformation, but the average propagation constant of (4.35) will be also relevant when the specifications of the starting prototype are defined. Actually, as it will be shown for technologies where the coupling coefficient is a function of the phase constant, it is necessary to consider $K(z, \bar{\beta}_{min})$, with $\bar{\beta}_{min} = \bar{\beta}(f = f_{min})$, where f_{min} is the minimum frequency that is required to satisfy the ρ_m level, in order to extrapolate the ρ_0 level through (4.34) that would correspond to $S_{11}(\beta = 0)$ if $K(z)$ were constant with β. Therefore, when the taper is designed for a waveguide where β varies along the propagation direction, ρ_0 must be calculated for $\bar{\beta}_{min}$ (or its corresponding f_{min}) so as to synthetize a suitable frequency response, $S_{11}(\bar{\beta})$, that will eventually meet the expected performance. Moreover, this criterion must be followed also when relating $K(z)$ with the physical dimensions of the waveguide because, if it is not, the waveguide cross-section achieved at $z = L$ will not result in the required one for the output port.

Finally, as it was commented in section 2.2.2, it must be highlighted that the $z(\chi)$ transformation is performed for f_t and it will be accurate when the quotient $\bar{\beta}(f)/\beta(f, z)$ does

not vary much with respect to $\bar{\beta}(f_t)/\beta(f_t, z)$. Accordingly, it will be recommended to select f_t as the frequency that corresponds to the center of the operational bandwidth of the taper.

4.2.1. Synthesis of the Classical Klopfenstein and Hecken Tapers Based on the Coupled-Mode Theory

Taking advantage of the single-mode approximation of the coupled-mode theory presented in 2.2, together with the GLM inverse scattering synthesis technique found in section 4.1, classical Klopfenstein and Hecken tapers can be synthetized for transmission line and waveguide technologies. In essence, both taper solutions were originally developed for an ideal transmission line model [27], [31] and, consequently, they were intended to match two transmission lines of different characteristic impedances, Z_{p1} and Z_{p2}, being Z_{p1} the characteristic impedance of the incoming transmission line to the taper (port 1) and Z_{p2} the characteristic impedance of the outcoming transmission line (port 2).

Focusing on the Klopfenstein classical taper solution, its ideal frequency response in reflection exhibits an equiripple behavior with a maximum reflection level of ρ_m, when the propagation constant is higher than a given value, β_{min}, as depicted in Fig. 4.1. Its frequency response can be expressed analytically as a function of the propagation constant, β, as [27], [50]:

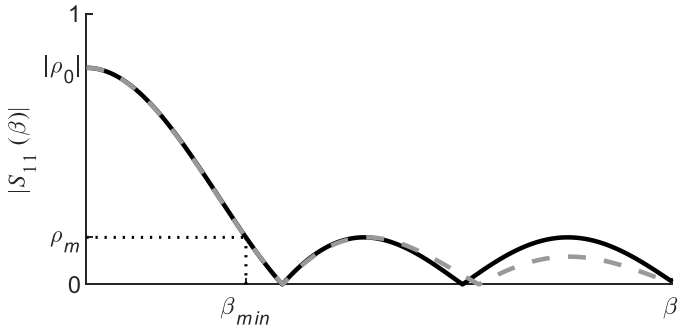

Fig. 4.1. $|S_{11}|$-parameter as a function of the propagation constant for classical tapers: Klopfenstein (black solid line) and Hecken (grey dashed line).

$$S_{11}(\beta) = \rho_0 \cdot \frac{\cos\left(\sqrt{(\beta L)^2 - A^2}\right)}{\cosh(A)} \cdot e^{-j\beta L} \tag{4.37}$$

where A is given in (4.38), ρ_0 is defined in (4.33) and L is the taper length.

$$A = \cosh^{-1}\left(\frac{|\rho_0|}{\rho_m}\right) \tag{4.38}$$

An analogous expression for $S_{11}(\beta)$ is also presented in [50], deduced from [31], for the case of the Hecken taper, see (4.39). As it is shown in Fig. 4.1, the frequency response of the Hecken taper is somewhat different from that of the Klopfenstein taper. In particular, the $|S_{11}(\beta)|$ of the Hecken taper exhibits a decreasing (not equiripple) maximum reflection level beyond β_{min} , where the maximum in-band reflection ρ_m is reached.

$$S_{11}(\beta) = \rho_0 \cdot \frac{B}{\sinh(B)} \cdot \frac{\sin\left(\sqrt{(\beta L)^2 - B^2}\right)}{\sqrt{(\beta L)^2 - B^2}} \cdot e^{-j\beta L} \tag{4.39}$$

The B parameter in (4.39) can be calculated by using (4.40) to achieve the required ρ_m:

$$\frac{B}{\sinh(B)} \cdot 0.21723 = \frac{\rho_m}{|\rho_0|} \tag{4.40}$$

If a transmission line model is used, the coupling coefficient, $K(z)$, is related to the characteristic impedance of the taper along the propagation direction, $Z_0(z)$, through the expression (2.145) that is provided below to ease the following of the procedure:

$$K(z) = -\frac{1}{2 \cdot Z_0(z)} \cdot \frac{dZ_0(z)}{dz} \tag{2.145}$$

Substituting this last expression into (4.34), it is obtained that:

$$\rho_0 = \tanh\left[-\int_0^L K(z) \cdot dz\right] = \tanh\left[\frac{1}{2} \cdot \ln\left(\frac{Z_{p2}}{Z_{p1}}\right)\right] \tag{4.41}$$

Taking into account that $\tanh(x) = (e^x - e^{-x})/(e^x + e^{-x})$, and after some mathematical manipulations, the familiar expression for ρ_0 as a function of the characteristic impedances of the ports [25], [26] can be deduced from (4.41):

$$\rho_0 = \frac{Z_{p2} - Z_{p1}}{Z_{p2} + Z_{p1}} \tag{4.42}$$

Now, in order to calculate the required coupling coefficient for the Klopfenstein and Hecken taper responses, a $N = 0$ (0-th order) approximation of the exact series solution of the synthesis problem (4.31) is taken. As it was demonstrated in [50], this is equivalent to the low reflectivity approximation that was employed in [27], [31]. By following this procedure, an analytical expression for $K(z)$ will be obtained for both cases. Thus, the coupling coefficient for the Klopfenstein taper results in (4.43) as it was presented in [50], deduced from [27]:

$$K(z) = \frac{-\rho_0}{\cosh(A)} \cdot \left[\frac{A^2}{L} \cdot \frac{I_1\left(A \cdot \sqrt{1 - \left(\frac{z - L/2}{L/2} \right)^2} \right)}{A \cdot \sqrt{1 - \left(\frac{z - L/2}{L/2} \right)^2}} + \frac{1}{2} \cdot \delta(z) + \frac{1}{2} \cdot \delta(z - L) \right] \tag{4.43}$$

where $I_1(x)$ is the modified Bessel function of the first kind of first order. The impulse functions $\delta(z)$ and $\delta(z - L)$ present in the coupling coefficient will produce the characteristic step discontinuities at the beginning and at the end of the Klopfenstein taper profile.

In the same way, the expression of $K(z)$ for the Hecken taper results in (4.44), as it was presented in [50], deduced from [31]:

$$K(z) = -\rho_0 \cdot \frac{B/L}{\sinh(B)} \cdot I_0 \left[B \cdot \sqrt{1 - \left(\frac{z - L/2}{L/2} \right)^2} \right] \tag{4.44}$$

where $I_0(x)$ is the modified Bessel function of the first kind of zero order.

It must be noted that the use of the 0-th order (low reflectivity) approximation leads to an inaccuracy in the synthesized coupling coefficient because, if the actual ρ_0 value is taken, the taper will not reach Z_{p2} at $z = L$, with $Z_0(z)$ being calculated by (2.146), as it was shown in [50]. In order to overcome this issue, the actual value of ρ_0 has to be overestimated and given by its 0-th order (low reflectivity) approximation, ρ_0', which can be obtained by performing the Fourier transform of (4.31) for $N = 0$, leading to [14]:

$$\rho_0' = S_{11}(\beta = 0)\Big|_{N=0} = -\int_0^L K(z) \cdot dz \tag{4.45}$$

Now, if (2.145) is substituted into (4.45), it will be obtained ρ_0' as a function of Z_{p1} and Z_{p2}, with an expression identical to that proposed in [27], [31] for an ideal transmission line model:

$$\rho_0' = \frac{1}{2} \cdot \ln\left(\frac{Z_{p2}}{Z_{p1}}\right) \tag{4.46}$$

Hence, ρ_0 in the synthesis equations (4.38), (4.40), (4.43) and (4.44), must be substituted by the new overestimated ρ_0' in order to guarantee that the taper achieves the intended impedance values or cross-section dimensions at its ports. Once the suitable synthesis parameters are known, the resulting length of the Klopfenstein taper will be determined by $L = A/\beta_{min}$ [27], whereas for the Hecken taper case will be $L = \sqrt{B^2 + 6.523}/\beta_{min}$ [31].

However, it must be stressed that when dealing with waveguides where the phase constant does not remain constant with z and the coupling coefficient is a function of the phase constant, it will be necessary to calculate ρ_0' from (4.45) considering $K(z) = K(z, \bar{\beta}_{min})$, or its corresponding $K(z, f_{min})$ in order to synthetize a taper that will meet the expected performance.

Finally, it is worth noting that the inaccuracy of the low reflectivity approximation in these classical tapers was surpassed in [50] by employing a higher order $N > 0$ in the series solution of the synthesis problem. Unfortunately, this solution results in an increase of the taper length that is not practical.

4.2.2. New Taper Solutions Based on Multisection Quarter-Wave Chebyshev Transformers

The use of multisection quarter-wave matching transformers is a classical method to achieve impedance matching between two different transmission lines [25], [26], [51].

The multisection Chebyshev transformer consists of M commensurate transmission lines in cascade, all of them with the same electrical length, but with different characteristic impedances Z_i (with $1 \leq i \leq M$), featuring a Chebyshev frequency response of order M. The commensurate lines have the same frequency behavior due to their identical electrical lengths. In fact, all lines have ideally the same physical length, l, and show the same wavelength, λ_g, and propagation constant, β, at any particular frequency. These properties allow us to define the

frequency behavior of the prototype as a function of the electrical length of the line, θ, or equivalently as a function of β:

$$\theta = \beta \cdot l = \frac{2 \cdot \pi}{\lambda_g} \cdot l \tag{4.47}$$

In order to extend the validity of the multisection Chebyshev transformer prototype to general waveguide technologies, Z_{p1}, Z_{p2} can be employed since they have been defined in such a way that the ρ_0 achieved by them (calculated with (4.42)) is identical to the actual ρ_0 produced by the waveguide ports mismatch, as calculated by (4.34). If Z_{p1}=1 Ω is set for convenience, Z_{p2} can be obtained from (4.42) as:

$$Z_{p2} = \frac{1 + \rho_0}{1 - \rho_0} \tag{4.48}$$

Once the equivalent impedances, Z_{p1} and Z_{p2}, are defined (or the actual values are known for the case of transmission line technologies), the normalized characteristic impedance of each commensurate line, Z_i, can be determined by applying the well-known Richards' transformation and the iterative extraction procedure fully detailed in [52]. Alternative calculation methods for the $Z_i's$ are explained in [25], [26], [51], although they are less convenient when the order M of the multisection transformer is increased. The values of Z_i can be also calculated using commercial software synthesis tools like *S/Filsyn.*

Now the $S_{11}(\beta)$ of the multisection transformer prototype can be deduced by means of the [ABCD] matrix [25], [26], just by cascading the Z_i transmission line sections (multiplying their matrices) and loading the output port with Z_{p2}, employing Z_{p1} as the reference impedance.

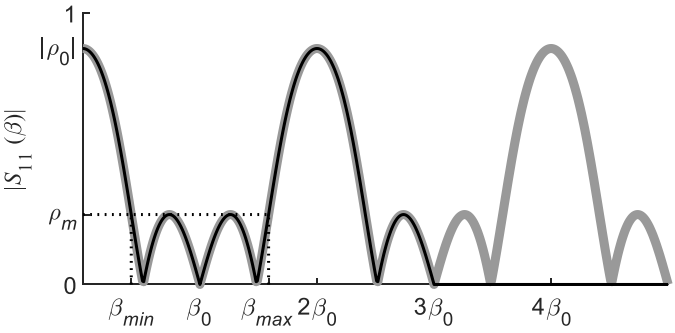

Fig. 4.2. $|S_{11}|$-parameter as a function of the propagation constant for a classical $M = 3$ (3-rd order) multisection quarter-wave Chebyshev transformer (grey line) and an example of target response for the novel taper to be synthetized with $\beta_z = 3 \cdot \beta_0$ (black line).

As it is shown in Fig. 4.2, the frequency response $S_{11}(\beta)$ has a periodic behavior which repeats every $2 \cdot \beta_0$. The matched bandwidth is centered at β_0, that is the propagation constant value at which the electrical length of the commensurate lines is $\theta_0 = \beta_0 \cdot l = \pi/2$, leading to $l = \lambda_{g0}/4$, with $\lambda_{g0} = (2 \cdot \pi)/\beta_0$.

The lower and upper limits of the propagation constant range, β_{min} and β_{max}, that complies with the required ρ_m level for a M-th order multisection Chebyshev transformer can be calculated using (4.49) and (4.50):

$$\beta_{min} = \beta_0 \cdot \frac{2 \cdot \theta_m}{\pi} \tag{4.49}$$

$$\beta_{max} = 2 \cdot \beta_0 \cdot \left(1 - \frac{\theta_m}{\pi}\right) \tag{4.50}$$

where $\theta_m = \cos^{-1}\left\{\text{sech}\left[\frac{1}{M} \cdot \cosh^{-1}\left(\frac{|\rho_0|}{\rho_m} \cdot \sqrt{\frac{1-\rho_m{}^2}{1-\rho_0{}^2}}\right)\right]\right\}$

When obtaining the multisection transformer prototype, it is convenient to consider a transformer whose β_{min} is as close as possible to the required β_{low} for the taper, while fulfilling also the required matched bandwidth. This election will eventually lead to the shortest taper. When a valid multisection transformer prototype is found, the procedure proposed in [53] (and fully detailed in section 5.2.2.2.2) to achieve a fully smooth device from a periodic $S_{11}(\beta)$, as the one obtained here, can be applied. The method requires just to set the $S_{11}(\beta)$ to zero beyond a certain β_z (see Fig. 4.2), retaining just several full periods of the frequency response (with the basic period defined symmetrically around $\beta = 0$). This technique will allow us to synthetize fully smooth tapered matching sections, by applying the exact series solution of (4.31) to the obtained $S_{11}\ (\beta)$, while maintaining a physical length similar to that of the initial multisection Chebyshev transformer prototype.

4.2.3. Rectangular Waveguide: a Specific Application Technology

The series solution of the synthesis problem attained in section 4.1 provides a general method to calculate the coupling coefficient required for both classical and novel tapers. However, in order to extract the physical dimensions of the taper, a specific waveguide technology needs to be chosen and the relationship between physical parameters and coupling

coefficient must be stablished. Several examples will be shown in rectangular waveguide, since it is one of the most widely employed waveguide technologies.

As it was shown in section 2.2.1.1, the propagation constant of the TE_{10} fundamental mode of rectangular waveguide can be calculated with the expression (2.119):

$$\beta(z,f) = \frac{2\cdot\pi\cdot f}{c}\cdot\sqrt{1-\left[\frac{c}{2\cdot a(z)\cdot f}\right]^2} \tag{2.119}$$

Moreover, the coupling coefficient of rectangular waveguide for single mode (TE_{10}) operation exhibits an analytical expression (2.120) that depends on its width and height, $a(z)$ and $b(z)$ respectively, and on the propagation constant, β:

$$K(z,f) = -\frac{1}{2\cdot b(z)}\cdot\frac{db(z)}{dz} + \frac{\pi^2}{2\cdot\beta^2(z,f)\cdot a^3(z)}\cdot\frac{da(z)}{dz} \tag{2.120}$$

being $c = c_0/\sqrt{\varepsilon_r}$, with c_0 the speed of light in vacuum, and ε_r the relative electrical permittivity that fills the inner volume of the rectangular waveguide. It is worth noting that $K(z)$ will exhibit an inherent dependence on frequency, since the propagation constant, β, depends on it, see (2.119).

In order to set the requirements of a taper, the first task is to determine ρ_0 just by introducing (2.120) in (4.34) for the case of rectangular waveguide. The final solution for ρ_0 is shown in (4.51), revealing that it can be calculated just by considering the required values of $a(z)$ and $b(z)$ at $z = 0$ and $z = L$ (i.e. at the input and output ports of the taper):

$$\rho_0 = \tanh\left\{\frac{1}{4}\ln\left[\left(\frac{b(L)}{b(0)}\right)^2\cdot\frac{1-\left(\frac{c}{2\cdot f_{min}\cdot a(0)}\right)^2}{1-\left(\frac{c}{2\cdot f_{min}\cdot a(L)}\right)^2}\right]\right\} \tag{4.51}$$

Regarding the 0-th order (low reflectivity) approximation of ρ_0', which is employed for the case of Klopfenstein and Hecken tapers, it can be calculated by introducing (2.120) in (4.45), again for the case of rectangular waveguide, resulting in:

$$\rho_0' = \frac{1}{4}\ln\left[\left(\frac{b(L)}{b(0)}\right)^2\cdot\frac{1-\left(\frac{c}{2\cdot f_{min}\cdot a(0)}\right)^2}{1-\left(\frac{c}{2\cdot f_{min}\cdot a(L)}\right)^2}\right] \tag{4.52}$$

Furthermore, paying attention to (2.120), it is clear that $K(z)$ can be divided into two parts with respect to the physical dimensions of the rectangular waveguide as it was stated in section 2.2.1.1. The left-side summand is only a function of $b(z)$, while the right-side one has an exclusive dependency with $a(z)$. This allows us to rewrite the coupling coefficient as $K(z) = K_b(z) + K_a(z)$, with $K_b(z)$ and $K_a(z)$ as in (4.53) and (4.54):

$$K_b(z) = \frac{-1}{2 \cdot b(z)} \cdot \frac{db(z)}{dz} = k_b \cdot K(z) \tag{4.53}$$

$$K_a(z) = \frac{\pi^2}{2 \cdot a(z)^3 \cdot {\beta_{min}}^2} \cdot \frac{da(z)}{dz} = k_a \cdot K(z) \tag{4.54}$$

where k_b and k_a are the constants that control which fraction of the general coupling coefficient $K(z)$ corresponds to $K_b(z)$ and $K_a(z)$. The expressions to calculate both constants, k_b and k_a, are available in (4.55) and (4.56), and they exclusively depend on the dimensions of the cross-sections at $z = 0$ and $z = L$, as expected:

$$k_b = \frac{\int_0^L K_b(z) \cdot dz}{\int_0^L K(z) \cdot dz} = \frac{-\frac{1}{2} \cdot \ln\left[\frac{b(z=L)}{b(z=0)}\right]}{-\rho_0'} \tag{4.55}$$

$$k_a = \frac{\int_0^L K_a(z) \cdot dz}{\int_0^L K(z) \cdot dz} = \frac{\frac{1}{4} \cdot \ln\left[\frac{1 - \left(\frac{c}{2 \cdot f_{min} \cdot a(L)}\right)^2}{1 - \left(\frac{c}{2 \cdot f_{min} \cdot a(0)}\right)^2}\right]}{-\rho_0'} \tag{4.56}$$

where ρ_0' is given in (4.52). It is interesting to note that k_b and k_a satisfy $k_b + k_a = 1$, guaranteeing that $K_b(z) + K_a(z) = k_b \cdot K(z) + k_a \cdot K(z) = K(z)$.

The $b(z)$ profile of the rectangular waveguide taper can be calculated with the expression (2.130) originally obtained in section 2.2.1.1.1 and provided here again for the sake of clarity:

$$b(z) = b(0) \cdot e^{-2 \cdot \int_0^z K_b(r) \cdot dr} \tag{4.57}$$

Regarding the $a(z)$ profile, it can be calculated by imposing $f = f_{min}$ in its analytical expression of (2.139) so as to achieve the desired dimensions at the extreme (input and output ports) of the synthetized taper, giving rise to:

$$a(z) = \frac{\frac{c}{2 \cdot f_{min}} \cdot e^{-2 \cdot \int_0^z K_a(r) \cdot dr}}{\sqrt{e^{-4 \cdot \int_0^z K_a(r) \cdot dr} + \left(\frac{c}{2 \cdot a(0) \cdot f_{min}}\right)^2 - 1}} \tag{4.58}$$

where r in (4.57) and (4.58) is a dummy variable of integration.

Finally, it must be highlighted that if we want to synthetize a taper that features a variable width, i.e. $k_a \neq 0$, we will need to apply the ideal modelling of technologies with β variable along z that was thoroughly developed in section 2.2.2, because of the variation of the propagation constant with the position. The denormalization expression for the calculation of the actual z from the normalized χ axis was given in (4.36).

The robustness and flexibility of the proposed taper synthesis method was verified by synthetizing tapers fulfilling certain frequency specifications, between two rectangular waveguides, in three different scenarios: mismatch in cross-section heights, widths and both heights and widths simultaneously.

4.2.3.1. Rectangular Waveguide Tapers Implemented with Variations in Height Only

The possibility of synthetizing tapers by means of the coupled-mode theory with exclusive variation in the height of the rectangular waveguide cross sections is going to be demonstrated for each of the following cases: a Klopfenstein taper, a Hecken taper, and a novel taper based on a multisection Chebyshev transformer. In all cases, they must interconnect a standard WR90 port with a waveguide with half of that height and the same width, while achieving $RL \geq 40$ dB (ρ_m = 0.01 by (4.32)) for the whole WR90 frequency range, between f_{low}= 8.2 GHz and f_{up}= 12.4 GHz. In order to obtain the shortest tapers, f_{min}=f_{low} will be chosen.

Firstly, the mismatch ρ_0 (defined in (4.33)) caused by the height difference needs to be calculated. The waveguide height of the WR90 standard is $b(0) = 10.16$ mm, and thus $b(L) = b(0)/2 = 5.08$ mm. Applying (4.51), $\rho_0 = -1/3$, while $\rho_0' = -0.3465$ by (4.52). Finally, considering that the width of the WR90 standard is $a = 22.86$ mm in (2.119), the corresponding

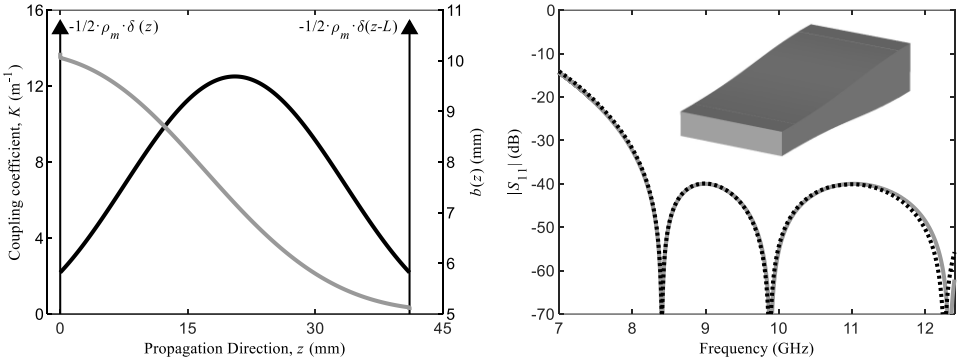

(a) (b)

Fig. 4.3. (a) Coupling coefficient (black line) of the Klopfenstein taper and its rectangular waveguide height variation profile (grey line). (b) Comparison of the $|S_{11}(f)|$-parameters for the Klopfenstein taper: target response (grey solid line) and CST Microwave Studio simulation (black dotted line). Inset: view of the inner hollow volume of the taper.

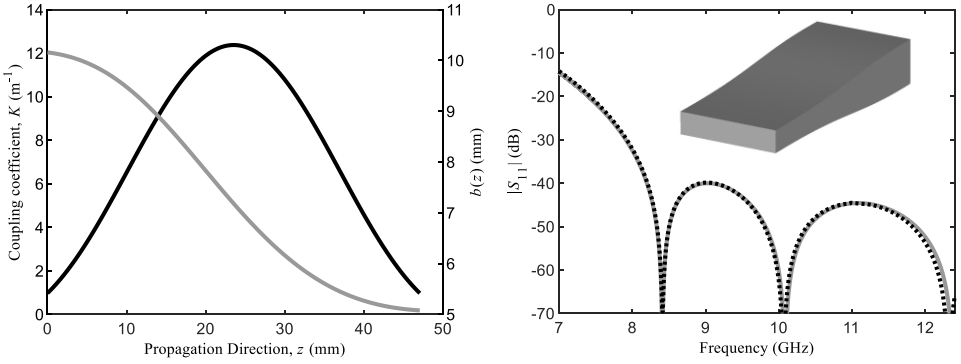

(a) (b)

Fig. 4.4. (a) Coupling coefficient (black line) of the Hecken taper and its rectangular waveguide height variation profile (grey line). (b) Comparison of the $|S_{11}(f)|$-parameters for the Hecken taper: target response (grey solid line) and CST Microwave Studio simulation (black dotted line). Inset: view of the inner hollow volume of the taper.

propagation constant values for $\beta_{min} = \beta(f_{min}) = 103.19$ rad/m and $\beta(f_{up}) = 220.58$ rad/m can be specified.

Since ρ_0', ρ_m, and β_{min} are known, the coupling coefficient, $K(z)$, for the Klopfenstein taper can be immediately calculated by means of (4.43). Since a taper that matches waveguides with different heights only is needed, then $K_a(z) = 0$, and hence $K_b(z) = K(z)$, and consequently $k_b = 1$. Then, calculating $b(z)$ using (4.57), we will obtain the physical dimensions of the Klopfenstein taper with a total length $L = A/\beta_{min} = 41.07$ mm. The coupling coefficient as well as the height profile are depicted in Fig. 4.3a.

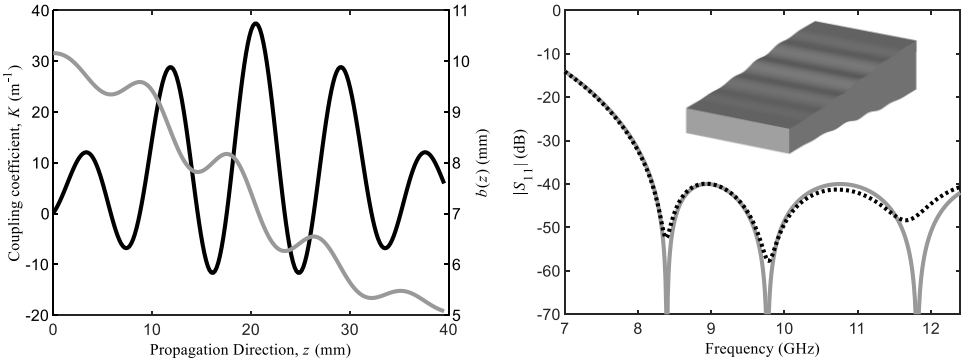

(a) (b)

Fig. 4.5. (a) Coupling coefficient (black line) of the novel taper based on a 4-th order multisection Chebyshev transformer and its rectangular waveguide height variation profile (grey line). (b) Comparison of the $|S_{11}(f)|$-parameters of the novel taper based on a 4-th order multisection Chebyshev transformer: target response (grey solid line) and CST Microwave Studio simulation (black dotted line). Inset: view of the inner hollow volume of the taper.

Regarding the Hecken taper, its $K(z)$ can be calculated by means of (4.44). Then, we can follow a reasoning similar to that of the Klopfenstein taper, ensuring $K_b(z) = K(z)$ and applying (4.57) to obtain $b(z)$. Both, $K(z)$ and $b(z)$ for the Hecken taper are shown in Fig. 4.4a. The final length of this taper is $L = \sqrt{B^2 + 6.523}/\beta_{min}$= 47.08 mm in this case, larger than the Klopfenstein taper as expected.

The last taper that is going to be considered for waveguides with changes only in height is based on the frequency response of a Chebyshev transformer. The first step is to calculate the impedance of the output port assuming an equivalent input port of Z_{p1}= 1 Ω. Considering that $\rho_0 = -1/3$, the impedance for the equivalent output port must be Z_{p2} = 0.5 Ω, see (4.48).

Then, the minimum order, M, of the multisection Chebyshev transformer that is capable of meeting the proposed frequency specifications must be determined, resulting in M=4. The propagation constant β_0=178.798 rad/m at which the commensurate lines exhibit an electrical length of $\theta = \pi/2$ rad is calculated. By using it, the values of β_{min} = 103.19 rad/m and $\beta_{up} < \beta_{max}$ = 254.4 rad/m are obtained by (4.49) and (4.50), respectively.

The calculated normalized characteristic impedances of each commensurate line are: Z_1 = 0.934 Ω, Z_2 = 0.789 Ω, Z_3 = 0.633 Ω, and Z_4 = 0.535 Ω. The $S_{11}(\beta)$ of the transformer is calculated by cascading its transmission lines loaded at the end with Z_{p2}, for an input impedance of Z_{p1}, by employing the [ABCD] matrix for every β value from 0 rad/m to 50·β_0 in regular intervals of β_0/50. Then, the obtained $S_{11}(\beta)$ of the transformer is modified by applying $S_{11}(\beta > \beta_z)$ = 0 for β_z = 3·β_0. The obtained $S_{11}(\beta)$ is synthetized using the exact series solution of (4.31) and (4.11) with an order $N = 4$, see Fig. 4.5a. As for Klopfenstein and Hecken tapers,

the physical dimensions of the novel taper are obtained by means of (4.57) with $K_b(z) = k_b \cdot K(z) = K(z)$. The height profile, $b(z)$, is also depicted in Fig. 4.5a.

It must be highlighted that the resulting taper based on a 4-th order multisection Chebyshev transformer has a length L = 39.53 mm, being a bit shorter than the Klopfenstein taper that was classically considered as the shortest possible taper solution.

Finally, the synthetized structures were simulated with CST Microwave Studio and the results are depicted in Fig. 4.3b (Klopfenstein), Fig. 4.4b (Hecken), and Fig. 4.5b (4-th order multisection Chebyshev transformer-based). In all cases, the frequency requirements are achieved, obtaining $RL \geq$ 40 dB for the whole frequency range of the WR90 waveguide standard.

4.2.3.2. Rectangular Waveguide Tapers Implemented with Variations in Width Only

The synthesis of rectangular waveguide tapers involving width changes along the propagation direction implies that the propagation constant will depend on the position, as it was detailed in section 4.2, where the strategy for dealing with that situation was explained. Taking that into account, two different tapers will be synthetized: a classical Hecken taper and a new taper based on multisection Chebyshev transformers.

Regarding the dimensions of the taper waveguide ports, the incoming waveguide cross-section width will be the WR90 width, i.e., $a(0)$ = 22.86 mm, and the width of the cross-section of the outcoming waveguide will be the WR62 width, i.e., $a(L)$ = 15.799 mm. The height of the cross section will be fixed to the WR62 height, i.e., b = 7.899 mm. In this case, the required performance of the taper must fulfill RL levels higher than 40 dB (ρ_m = 0.01 by (4.32)) in a frequency range defined from f_{low}=f_{min}=11 GHz up to f_{up}=13 GHz.

Due to the change of the propagation constant caused by the width variation, we need to consider the propagation constants $\beta(f, z = 0)$ and $\beta(f, z = L)$ in order to define the average propagation constant, $\bar{\beta}(f)$, see (4.35). Thus, $\beta(f, z = 0)$ is calculated using (2.119) for $a(0)$, while the value of $\beta(f, z = L)$ is obtained employing $a(L)$. Therefore, for $f = f_{min}$ = 11 GHz, $\beta(f_{min}, z = 0) =$ 185.1 rad/m and $\beta(f_{min}, z = L) =$ 116.66 rad/m, and consequently, $\bar{\beta}_{min}(f = f_{min}) =$ 150.88 rad/m by (4.35). Regarding the upper frequency specification, the average propagation constant is $\bar{\beta}_{up}(f = f_{up}) =$ 210.76 rad/m. The use of the average

propagation constant implies that the synthesis process is going to be performed in the normalized propagation axis, χ, and the real position z will be determined in a subsequent step.

Moreover, as it was explained in sections 4.2 and 4.2.1, the values of ρ_0 and ρ_0' for $\bar{\beta}_{min} = \bar{\beta}(f = f_{min})$ must be determined. In the particular case of a rectangular waveguide, ρ_0 and ρ_0' are directly expressed as a function of f_{min} through (4.51) and (4.52). Solving both expressions for f_{min}= 11 GHz, and the aforementioned waveguide dimensions at the taper extremes, it will be finally obtained that ρ_0 = 0.227 and ρ_0' = 0.231.

The coupling coefficient along the normalized propagation axis, $K(\chi)$, of the Hecken taper can be directly calculated by (4.44) using $\bar{\beta}_{min}$ and ρ_0' and it is represented in Fig. 4.6a. Then, due to the fact that the height is constant, $K_b(\chi)$ = 0 because of (4.53) and k_b = 0 as well. Hence, k_a = 1 leads to $K_a(\chi)$=$K(\chi)$ in (4.54) and the a(χ) profile shown in Fig. 4.6a can be calculated employing (4.58). Finally, in order to calculate the waveguide width along the actual propagation axis z, we must choose the transformation frequency, f_t, fixing it at the center of the required matched frequency range, i.e., f_t = 12 GHz. Hence, $\bar{\beta}_t(f = f_t)$ = 182.31 rad/m. By employing $\bar{\beta}_t$ and $\beta_t(f_t, \chi)$ in (4.36), the final width of the waveguide along the propagation direction, $a(z)$, can be obtained as it is depicted in Fig. 4.6a. The length of the resulting Hecken taper is L = 30.04 mm.

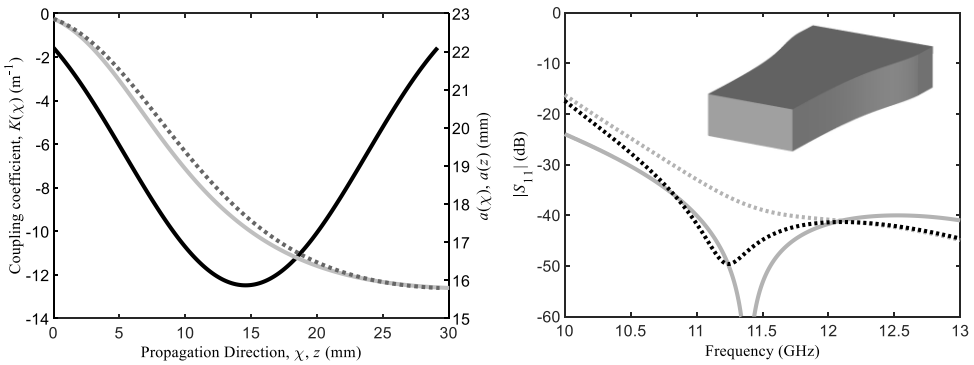

(a) (b)

Fig. 4.6. (a) Hecken taper: Coupling coefficient (black solid line) and width profile dimensions (dark grey dashed line) along the normalized propagation axis, χ. The final width profile along the actual propagation axis, z, is also included (light grey solid line). (b) Comparison of $|S_{11}(f)|$-parameters of the Hecken taper. Target response (grey solid line) and CST Microwave Studio simulations: taper with $a(\chi)$ width profile (grey dotted line) and taper with $a(z)$ width profile (black dotted line). Inset: view of the inner hollow volume of the definitive taper.

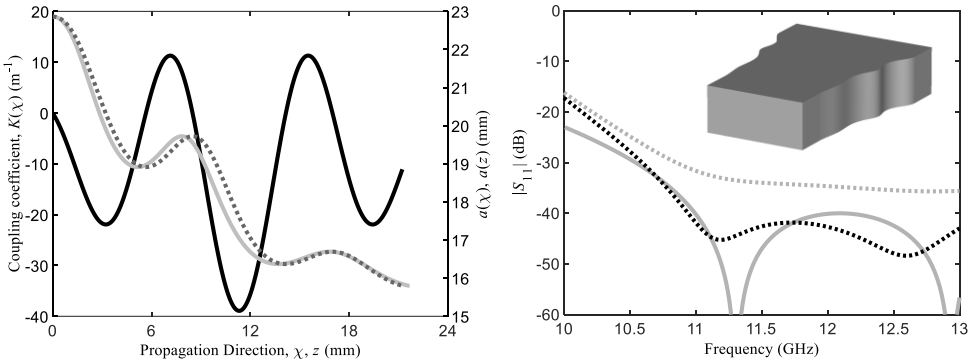

(a) (b)

Fig. 4.7. (a) Novel taper based on a 2-nd order multisection Chebyshev transformer: Coupling coefficient (black solid line) and width profile dimensions (dark grey dashed line) along the normalized propagation axis, χ. The final width profile along the actual propagation axis, z, is also included (light grey solid line). (b) Comparison of $|S_{11}(f)|$-parameters of the novel taper based on 2-nd order multisection Chebyshev transformer. Target response (grey solid line) and CST Microwave Studio simulations: taper with $a(\chi)$ width profile (grey dotted line) and taper with $a(z)$ width profile (black dotted line). Inset: view of the inner hollow volume of the definitive taper.

For the case of the novel multisection Chebyshev transformer-based taper, an output auxiliary impedance, Z_{p2}= 1.587 Ω, is calculated for ρ_0=0.227 and Z_{p1}= 1 Ω by means of (4.48). A minimum order M=2 and $\bar{\beta}_0 = 184.97$ rad/m yields to $\bar{\beta}_{min} = 150.69$ rad/m and $\bar{\beta}_{max} = 219.24$ rad/m using (4.49) and (4.50), respectively, ensuring the fulfilment of the requirements. The normalized characteristic impedances of the multisection Chebyshev transformer are Z_1 = 1.128 Ω and Z_2 = 1.407 Ω. Once these characteristic impedances are known, the $S_{11}(\bar{\beta})$ is calculated making use of the transmission matrix by defining $\bar{\beta}$ from 0 rad/m to $50 \cdot \bar{\beta}_0$ every $\bar{\beta}_0/50$. The final response intended to be synthetized is attained after setting $S_{11}(\bar{\beta} > \bar{\beta}_z) = 0$ for $\bar{\beta}_z = 3 \cdot \bar{\beta}_0$. Then, $K(\chi)$ is calculated with (4.31) and the result is depicted in Fig. 4.7a. As $K_b(\chi)$ must be 0, k_a=1 and $K_a(\chi) = K(\chi)$. The width dimensions of the rectangular waveguide taper along the normalized propagation axis, a(χ), are calculated with (4.58) and are also displayed in Fig. 4.7a. The last transformation step is carried out like in the case of the Hecken taper by means of (4.36) for $\bar{\beta}_t(f_t)$ with f_t = 12 GHz and hence, the relation $z(\chi)$ is obtained. The resulting $a(z)$ profile is presented in Fig. 4.7a. The final Chebyshev transformer-based taper has a length L = 21.67 mm.

A CST Microwave Studio simulation is performed for the Hecken taper as well as for the taper based on the 2-nd order multisection Chebyshev transformer, and the attained $|S_{11}(f)|$-parameters are shown in Fig. 4.6b and Fig. 4.7b, respectively. An excellent agreement is achieved between both simulations and their corresponding target frequency responses. Moreover, the matching specifications are also fulfilled in terms of frequency range and level.

To conclude this subsection that shows the feasibility of the method to synthesize tapers for rectangular waveguides of different widths and same height, a final remark must be done. If we pay attention to the waveguide width profiles, $a(\chi)$ and $a(z)$, that have been obtained and shown in Fig. 4.6a for the Hecken taper as well as in Fig. 4.7a for the novel taper, we can realize that $a(\chi)$ and $a(z)$ are pretty similar to each other in both cases. Therefore, one might think that the propagation axis transformation of (4.36) may not be actually necessary because the transformed width profile, $a(\chi)$, is close enough to the actual one, $a(z)$. As a result, it could be considered that if the taper of $a(z)$ meets the specifications, one defined by $a(\chi)$ perhaps meets them too, something that would render the propagation axis transformation of (4.36) in a trivial and useless synthesis step. Additional CST Microwave Studio simulations have been done with both tapers but defining the width profile with $a(\chi)$ instead of $a(z)$. The results of those simulations are displayed in Fig. 4.6b for the Hecken taper and in Fig. 4.7b for the Chebyshev transformer-based taper. In both cases, the obtained frequency response does not meet the required specifications and, actually, it is quite far from the expected behavior of the taper. This demonstrates the importance of the propagation axis transformation proposed in this thesis.

4.2.3.3. Rectangular Waveguide Tapers Implemented with Variations in Height and Width Simultaneously

Now that in previous subsections several examples have been presented of tapers matching rectangular waveguides where only the width or height changed, this subsection will be devoted to show how to synthetize tapers for the most complicated case where the cross-sections of both waveguides do not have neither the same height, nor same width. A Klopfenstein taper, a Hecken taper, and three different models of multisection Chebyshev transformer-based tapers will be synthetized for this case.

The specifications are going to be the same as with width variations only, i.e. minimum RL level of 40 dB (ρ_m = 0.01) between f_{low}= 11 GHz and f_{up}= 13 GHz. In order to obtain the shortest tapers, f_{low}= f_{min} is imposed.

Regarding the geometry of the taper, the incoming waveguide will be WR90, whereas the outcoming waveguide will be WR62. This means that $a(0)$= 22.86 mm, $b(0)$=10.16 mm, $a(L)$= 15.799 mm, and $b(L)$= 7.899 mm. Thus, ρ_0 = 0.1046 and ρ_0' = 0.105 are calculated by (4.51)

and (4.52). The average propagation constant, calculated by (4.35), for f_{min} is $\bar{\beta}_{min}(f = f_{min})$ = 150.88 rad/m, while for f_{up} is $\bar{\beta}_{up}(f = f_{up})$ =210.76 rad/m.

Both Klopfenstein and Hecken tapers are synthetized by obtaining their coupling coefficients with (4.43) and (4.44) respectively, using the calculated values of $\bar{\beta}_{min}$, ρ_0' and ρ_m. The coupling coefficient along the normalized position is depicted in Fig. 4.8a for the Klopfenstein case, whereas for the Hecken taper it is shown in Fig. 4.9a.

For the synthesis of the three novel tapers, two different starting prototypes of multisection Chebyshev transformers have been considered, being Z_{p2} =1.234 Ω the auxiliary characteristic impedance for ρ_0 and Z_{p1} =1 Ω. The first transformer has an order M = 2 with $\bar{\beta}_0$ = 206.62 rad/m, and hence $\bar{\beta}_{min}$= 150.08 rad/m, $\bar{\beta}_{max}$ = 263.17 rad/m, and the specifications are met as a consequence. The normalized characteristic impedances of the commensurate lines are Z_1 = 1.059 Ω and Z_2 = 1.165 Ω. This allows us to calculate the $S_{11}(\bar{\beta})$ of the transformer that is going to be employed to synthetize two different responses: the first one is modified by applying $S_{11}(\bar{\beta} > \bar{\beta}_z)$ = 0 for $\bar{\beta}_z$=3·$\bar{\beta}_0$, while for the second one $\bar{\beta}_z$ = 5·$\bar{\beta}_0$ is chosen. The synthesis of those responses employing the series solution of (4.31) results in the coupling coefficients that can be seen in Fig. 4.10a for $\bar{\beta}_z$ = 3·$\bar{\beta}_0$ and in Fig. 4.11a for $\bar{\beta}_z$ = 5·$\bar{\beta}_0$. On the other hand, the second initial prototype is a 3-rd order transformer centered at $\bar{\beta}_0$ = 269.39 rad/m, which extends its matched bandwidth from $\bar{\beta}_{min}$ = 150.09 rad/m up to $\bar{\beta}_{max}$ = 388.7 rad/m, with Z_1 = 1.039 Ω, Z_2 = 1.111 Ω, and Z_3 = 1.188 Ω. The frequency response of this initial transformer is calculated and then modified with $\bar{\beta}_z$=3·$\bar{\beta}_0$, and synthetized by means of (4.31). The resulting coupling coefficient is shown in Fig. 4.12a.

Since all the tapers synthetized are intended to have the same cross-sections at their extremes, the constants calculated by (4.55) and (4.56) are the same for all of them: k_b= -1.199 and k_a= 2.199. Then, $K_b(\chi)$ and $K_a(\chi)$ can be determined for each taper and this allows to obtain $b(\chi)$ and $a(\chi)$ afterwards by means of (4.57) and (4.58). Finally, the transformation to the real propagation axis, $z(\chi)$, is performed employing (4.36) for $\bar{\beta}_t(f = f_t)$ = 182.31 rad/m with f_t = 12 GHz. The final width and height profiles of both Klopfenstein and Hecken tapers are shown in Fig. 4.8a and Fig. 4.9a, respectively. The profiles corresponding to the novel tapers based on the M=2 Chebyshev transformer with $\bar{\beta}_z$ = 3·$\bar{\beta}_0$ and $\bar{\beta}_z$ = 5·$\bar{\beta}_0$ are depicted in Fig. 4.10a and Fig. 4.11a. Finally, the taper based on the 3-rd order Chebyshev transformer with $\bar{\beta}_z$ = 3·$\bar{\beta}_0$ is shown in Fig. 4.12a.

The main parameters of all the synthetized tapers, as well as their final lengths, are summarized in Table 4.1.

Taper	M	$\bar{\beta}_0$ (rad/m)	$\bar{\beta}_z$ (rad/m)	L (mm)
Klopfenstein	-	-	-	20.65
Hecken	-	-	-	23.93
MCTB* 1	2	206.62	$3\cdot\bar{\beta}_0$	19.37
MCTB* 2	2	206.62	$5\cdot\bar{\beta}_0$	17.89
MCTB* 3	3	269.39	$3\cdot\bar{\beta}_0$	20.82

* MCTB: Multisection Chebyshev Transformer-Based.

Table 4.1. Synthesis parameters for different WR-90 to WR-62 tapers operating from 11 GHz to 13 GHz with $RL\geq$ 40 dBs, and their lengths.

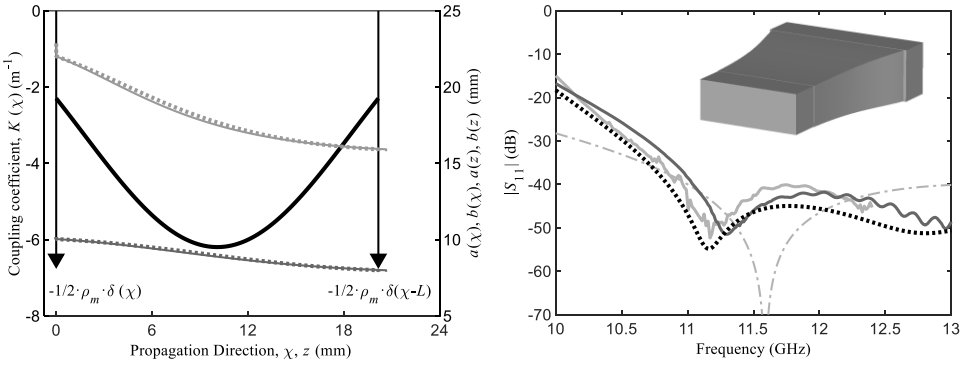

(a) (b)

Fig. 4.8. (a) Klopfenstein taper: Coupling coefficient (black solid line) as well as width (light grey dashed line) and height (dark grey dashed line) profile dimensions along the normalized propagation axis, χ. The final width (light grey solid line) and height (dark grey solid line) profiles along the actual propagation axis, z, are also included. (b) Comparison of $|S_{11}(f)|$-parameters of the Klopfenstein taper: target response (grey dash-dotted line), CST Microwave Studio simulation (black dotted line), measurements performed with WR90 (light grey solid line) and WR62 (dark grey solid line) calibration. Inset: view of the inner hollow volume of the taper.

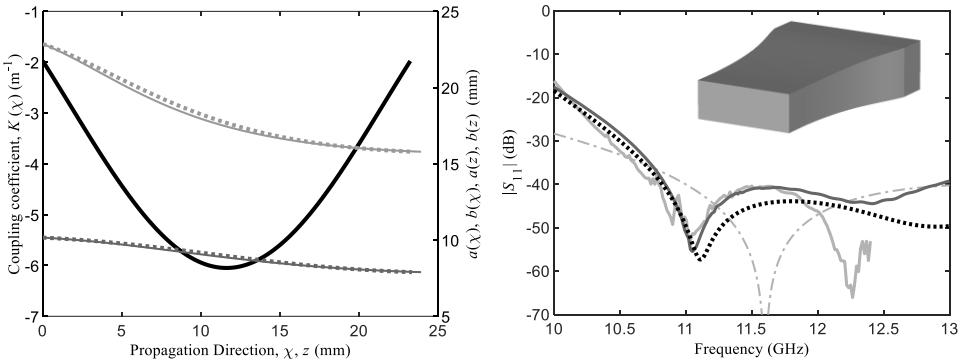

(a) (b)

Fig. 4.9. (a) Hecken taper: Coupling coefficient (black solid line) as well as width (light grey dashed line) and height (dark grey dashed line) profile dimensions along the normalized propagation axis, χ. The final width (light grey solid line) and height (dark grey solid line) profiles along the actual propagation axis, z, are also included. (b) Comparison of $|S_{11}(f)|$-parameters of the Hecken taper: target response (grey dash-dotted line), CST Microwave Studio simulation (black dotted line), measurements performed with WR90 (light grey solid line) and WR62 (dark grey solid line) calibration. Inset: view of the inner hollow volume of the taper.

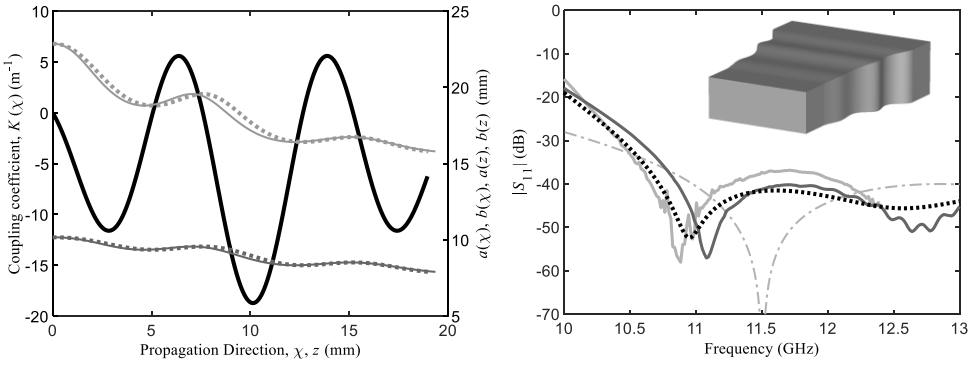

(a) (b)

Fig. 4.10. (a) Novel taper based on a 2-nd order multisection Chebyshev transformer with $\beta_z = 3 \cdot \beta_0$: Coupling coefficient (black solid line) as well as width (light grey dashed line) and height (dark grey dashed line) profile dimensions along the normalized propagation axis, χ. The final width (light grey solid line) and height (dark grey solid line) profiles along the actual propagation axis, z, are also included. (b) Comparison of $|S_{11}(f)|$-parameters of the novel taper based on 2-nd order multisection Chebyshev transformer with $\beta_z = 3 \cdot \beta_0$: target response (grey dash-dotted line), CST Microwave Studio simulation (black dotted line), measurements performed with WR90 (light grey solid line) and WR62 (dark grey solid line) calibration. Inset: view of the inner hollow volume of the taper.

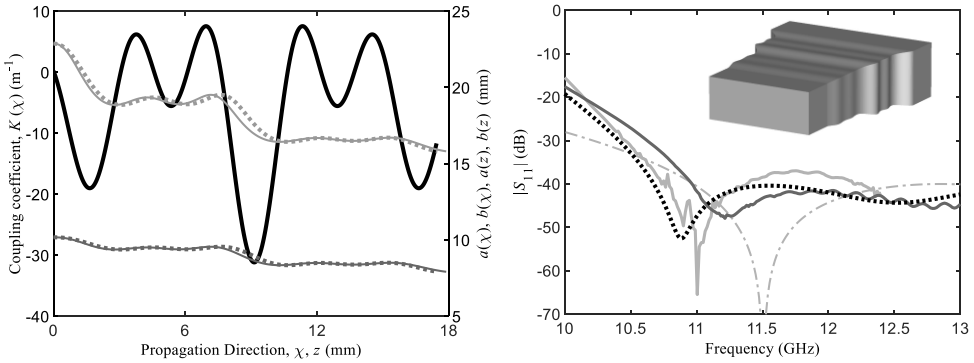

(a) (b)

Fig. 4.11. (a) Novel taper based on a 2-nd order multisection Chebyshev transformer with $\beta_z = 5 \cdot \beta_0$: Coupling coefficient (black solid line) as well as width (light grey dashed line) and height (dark grey dashed line) profile dimensions along the normalized propagation axis, χ. The final width (light grey solid line) and height (dark grey solid line) profiles along the actual propagation axis, z, are also included. (b) Comparison of $|S_{11}(f)|$-parameters of the novel taper based on 2-nd order multisection Chebyshev transformer with $\beta_z = 5 \cdot \beta_0$: target response (grey dash-dotted line), CST Microwave Studio simulation (black dotted line), measurements performed with WR90 (light grey solid line) and WR62 (dark grey solid line) calibration. Inset: view of the inner hollow volume of the taper.

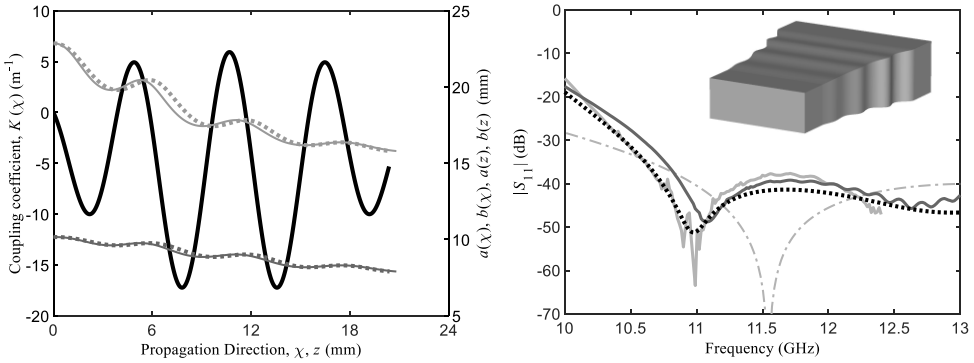

(a) (b)

Fig. 4.12. (a) Novel taper based on a 3-rd order multisection Chebyshev transformer with $\beta_z = 3 \cdot \beta_0$: Coupling coefficient (black solid line) as well as width (light grey dashed line), and height (dark grey dashed line) profile dimensions along the normalized propagation axis, χ. The final width (light grey solid line) and height (dark grey solid line) profiles along the actual propagation axis, z, are also included. (b) Comparison of $|S_{11}(f)|$-parameters of the novel taper based on 3-rd order multisection Chebyshev transformer with $\beta_z = 3 \cdot \beta_0$: target response (grey dash-dotted line), CST Microwave Studio simulation (black dotted line), measurements performed with WR90 (light grey solid line) and WR62 (dark grey solid line) calibration. Inset: view of the inner hollow volume of the taper.

The five different tapers synthetized with height and width variations have been fabricated in AlSi10Mg aluminum alloy, by means of an Additive Manufacturing technique (Direct Metal Laser Sintering), using an EOS M290 printer which allows a maximum building

volume of 250x250x350 mm. All the tapers were fabricated growing the structures from the WR62 to the WR90 port, following the propagation direction in order to avoid overhanging surfaces. A photograph of the prototypes is shown in Fig. 4.13. The DMLS technique was selected since it has been lately employed to fabricate inexpensive RF parts from a few GHz to 30 GHz, approximately [54]. Beyond that frequency, the fabrication accuracy of DMLS begins to become insufficient. Nevertheless, if specifications for higher frequencies are required, metal coated polymer Additive Manufacturing solutions like Stereolithography Apparatus (SLA) or Fused Deposition Modeling (FDM), among others, could be employed, since they achieve significantly better accuracies. Alternatively, the classical electroforming manufacturing technique could be also used for an inexpensive fabrication of these structures, for example.

Since the designed tapers operate between different waveguide standards, two different measurement set-ups had to be employed to test the tapers using a Keysight (Agilent) 8722 Vector Network Analyzer (VNA). The first one (set-up 1) consisted in calibrating the VNA with a WR90 calibration kit and the tapers were tested loading their WR62 port with a waveguide sliding load of a WR62 calibration kit. For the second set-up (set-up 2), the VNA was calibrated using a WR62 calibration kit and the tapers were tested loading the WR90 port with the sliding load of a WR90 calibration kit.

A comparison between the target responses, CST Microwave Studio simulations and measurement results is shown in Fig. 4.8b (Klopfenstein), Fig. 4.9b (Hecken), Fig. 4.10b (2-nd order multisection Chebyshev transformer with $\beta_z = 3 \cdot \beta_0$), Fig. 4.11b (2-nd order multisection Chebyshev transformer with $\beta_z = 5 \cdot \beta_0$), and Fig. 4.12b (3-rd order multisection Chebyshev transformer with $\beta_z = 3 \cdot \beta_0$).

A very good agreement is achieved between simulation and measurement results in all cases. In fact, the aim specifications, $RL \geq 40$ dB from f_{low} = 11 GHz up to f_{up} = 13 GHz, are fully achieved in simulation and very close to be achieved in measurements. The small discrepancies found between simulations and measurements can be attributed to two main reasons. The first one is related to the DMLS manufacturing tolerances, as fabrication inaccuracies of ±100 μm can be easily expected using this technique of Additive Manufacturing of metallic parts. However, the main reason for discrepancies is the measurement set-up itself, because two sliding waveguide loads were employed to load the port that was not connected to the VNA. During the measurements, these loads were not operating in their native frequency range, since the VNA is calibrated for another standard with its own optimal frequency range. Actually, measurements made with set-up 1 are more troublesome than measurements performed with set-up 2, because the WR62 load is operating from 10 GHz to 13 GHz, and the WR62 standard range starts at 12.4 GHz. Nevertheless, the propagation regime is ensured for WR62 in the whole operation bandwidth. On the other hand, set-up 2 employs the WR90 load from 10

GHz to 13 GHz, and the native WR90 bandwidth is defined from 8.2 GHz to 12.4 GHz. Finally, it must be pointed out that a minor shift to lower frequencies can be observed when comparing the target and the simulated frequency responses. That frequency shift is caused by parasitic reactive coupling to higher order modes that are under cut-off but suffer a small excitation somewhat noticeable for these tapers with simultaneous variations in height and width. However, since the minor shift is towards lower frequencies, the tapers obtained continue fulfilling the aim specifications as it has been shown in the simulation and measurement results.

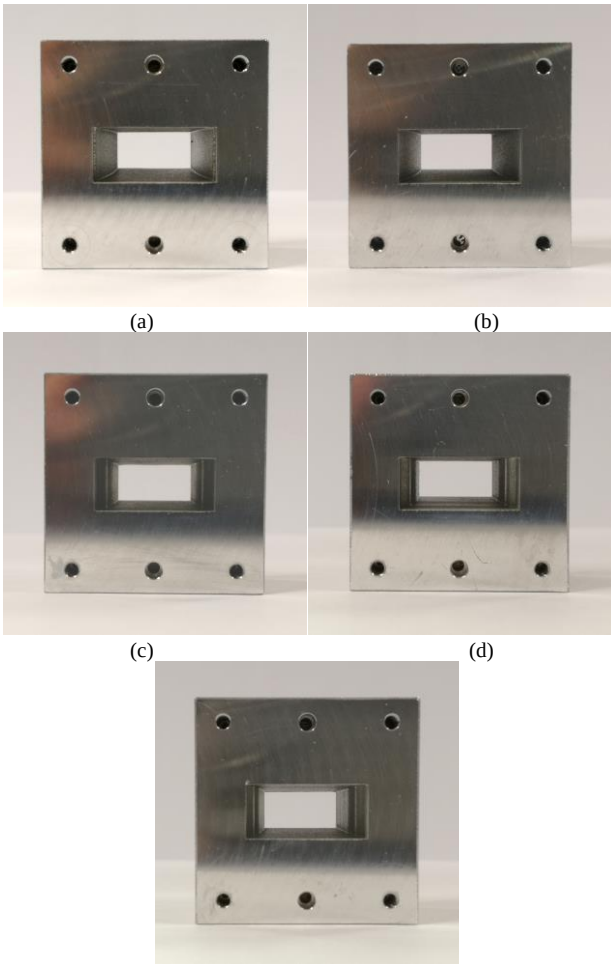

Fig. 4.13. Photographs of the tapers fabricated by means of Direct Metal Laser Sintering technique: (a) Klopfenstein taper; (b) Hecken taper; multisection Chebyshev transformer-based taper with (c) M=2, $\bar{\beta}_z$=3·$\bar{\beta}_0$; (d) M=2, $\bar{\beta}_z$=5·$\bar{\beta}_0$; and (e) M=3, $\bar{\beta}_z$=3·$\bar{\beta}_0$.

REFERENCES

[1] I. M. Gel'fand and B. M. Levitan, "On the determination of a differential equation by its spectral function," Am. Math. SOC. Transl., vol. 1, pp. 253-304, 1955.

[2] V. A. Marchenko, "Reconstruction of the potential energy from the phase of scattered waves," *Dokl. Akad. Nauk. SSR*, vol. 104, pp. 635-698, 1955.

[3] E. Peral, J. Capmany, and J. Marti, "Iterative Solution to the Geld'Fand-Levitan-Marchenko coupled equations and application to synthesis of fiber gratings," *IEEE J. Quantum Electron.*, vol. 32, no. 12, pp. 2078-2084, Dec. 1996.

[4] P. V. Frangos and D. L. Jaggard, "A numerical solution to the Zakharov-Shabat inverse scattering problem," *IEEE Trans. Antennas Propagat.*, vol. 39, pp. 74-79, Jan. 1991.

[5] P. P. Roberts and G. E. Town, "Design of microwave filters by inverse scattering," *IEEE Trans. Microw. Theory Tech.*, vol. 43, no. 4, pp. 739-743, Apr. 1995.

[6] H. N. Kritikos, D. L. Jaggard, and D. B. Ge, "Numeric reconstruction of smooth dielectric profile," *Proc. IEEE*, vol. 70, pp. 296-299, Mar. 1982.

[7] G. Xiao and K. Yashiro, "An efficient algorithm for solving Zakharov-Shabat inverse scattering problem," *IEEE Trans. Antennas Propagat.*, vol. 50, no. 6, pp. 807-811, June 2002.

[8] J. Modelski, A. Synyavskyy, "A New Numerical Method for Zakharov-Shabat's Inverse Scattering Problem Solution" *Proc. of XVI Itern. Conference on Microwaves, Radar and Wireless Communications*, MIKON'2006, Krakow, Poland, vol. 1, pp. 191-194, 2006.

[9] I. Arnedo, M. A. G. Laso, F. Falcone, D. Benito, T. Lopetegi, "A Series Solution for the Single-Mode Synthesis Problem Based on the Coupled-Mode Theory," *IEEE Trans. Microw. Theory Tech.*, vol. 56, no. 2, pp.457-466, Feb. 2008.

[10] M. Chudzik et al., "Novel Synthesis Technique for Microwave Circuits Based on Inverse Scattering: Efficient Algorithm Implementation and Application*", Int. J. RF Microw. C. E.*, vol. 21, no. 2, pp. 164-173, Mar. 2011.

[11] G. H. Song and S. Y. Shin, "Design of Corrugated Waveguide Filters by the Gel'fand-Levitan-Marchenko Inverse-Scattering Method," *J. Opt. Soc. Amer. A*, vol. 2, no. 11, pp. 1905-1915, Nov. 1985.

[12] Israel Arnedo, "New Methods for the Synthesis of Microwave Devices Based on the Coupled-Mode Theory," Doctoral Thesis, Universidad Pública de Navarra, España, 2009.

[13] Magdalena Chudzik, "Synthesis Techniques for Novel Devices Based on Smooth Profiles with Application from the Microwave to the Terahertz Regions," Doctoral Thesis, Universidad Pública de Navarra, España, 2013.

[14] A. Papoulis, The Fourier Integral and its Applications (Electronic Science Series). New York, NY, USA: McGraw-Hill, 1962.

[15] E. F. Bolinder, "The relationship of physical applications of Fourier Transforms in various fields of wave theory and circuitry," *IRE Trans. Microw. Theory Tech.*, pp. 153-158, Apr. 1957.

[16] K. A. Winick and J. E Roman, "Design of corrugated waveguide filters by Fourier Transform techniques," *IEEE J. Quantum Electron.*, vol. 26, no. 11, pp. 1918- 1929, Nov. 1990.

[17] I. Arnedo, I. Arregui, A. Lujambio, M. Chudzik, M. A. G. Laso and T. Lopetegi, "Synthesis of Microwave Filters by Inverse Scattering Using a Closed-Form Expression Valid for Rational Frequency Responses," *IEEE Trans. Microw. Theory Tech.*, vol. 60, no. 5, pp. 1244-1257, May 2012.

[18] I. Arnedo, J. D. Schwartz, M. A. G. Laso, T. Lopetegi, D. V. Plant, and J. Azana, "Passive microwave planar circuits for arbitrary UWB pulse shaping," *IEEE Microw. Wireless Compon. Lett.*, vol. 18, no. 7, pp. 452–454, Jul. 2008.

[19] I. Arnedo et al., "Customized pulses for UWB applications," *in Proc. 40th Eur. Microw. Conf. (EuMC)*, Paris, France, Sep. 2010, pp. 320–323.

[20] M. Chudzik *et al*., "Design of transmission-type Nth-order differentiators in planar microwave technology," *IEEE Trans. Microw. Theory Techn.*, vol. 60, no. 11, pp. 3384–3394, Nov. 2012.

[21] J. M. Percaz *et al*., "General Synthesis of Tapered Matching Sections for Single-Mode Operation Using the Coupled-Mode Theory," *IEEE Trans. Microw. Theory Techn.*, vol. 67, no. 9, pp. 3511-3526, Sept. 2019.

[22] E. Dietze, "Tapered Filter for Alternating Currents of Varying Frequency," U. S. Patent 1,603,329; Oct. 1926.

[23] H. A. Wheeler, "Transmission Lines with Exponential Taper," *Proc. IRE*, vol. 27, no. 1, pp. 65-71, Jan. 1939.

[24] A. W. Gent and P. J. Wallis, "Impedance Matching by Tapered Transmission Lines," *J. Inst. Electr. Eng. 3*, vol. 93, no. 3, pp. 559-563, 1946.

[25] D. M. Pozar, *Microwave Engineering*, 4th ed. Norwood, NJ, USA: Wiley, 2005.

[26] R. E. Collin, *Foundations for Microwave Engineering*, Second Edition, New York, McGraw Hill, 1992.

[27] R. W. Klopfenstein, "A Transmission Line Taper of Improved Design," *Proc. IRE*, vol. 44, pp. 31–35, Jan. 1956.

[28] R. E. Collin, "The Optimum Tapered Transmission Line Matching Section," *Proc. IRE*, vol. 44, no. 4, pp. 539-548, April 1956.

[29] J. A. Fuchs, "Tapered Transmission Line Computer Program Using Collin's Derivation," *Proc. IEEE*, vol. 56, no. 12, pp. 2174-2175, Dec. 1968.

[30] D. Kajfez and J. O. Prewitt, "Correction to "A Transmission Line Taper of Improved Design" (Letters)," *IEEE Trans. Microw. Theory Techn.*, vol. 21, no. 5, pp. 364-364, May 1973.

[31] R. P. Hecken, "A Near Optimum Matching Section without Discontinuities, " *IEEE Trans. Microw. Theory Techn.*, vol. MTT-20, pp. 734–739, Nov. 1972.

[32] P. Pramanick and P. Bhartia, "A Generalized Theory of Tapered Transmission Tine Matching Transformers and Asymmetric Couplers Supporting non-TEM Modes," *IEEE Trans. Microw. Theory Techn.*, vol. 37, no. 8, pp. 1184-1191, Aug. 1989.

[33] M. Kobayashi and N. Sawada, "Analysis and Synthesis of Tapered Microstrip Transmission Lines," *IEEE Trans. Microw. Theory Techn.*, vol. 40, no. 8, pp. 1642-1646, Aug. 1992.

[34] J. H. Hinken, "Simplified Analysis and Synthesis of Fin-line Tapers," *Arch. Elek. Ubertrugung.*, vol. 37, pp. 375-380, Nov.-Dec. 1983.

[35] C. Schieblich, J. K. Piotrowski, and J. H. Hinken, "Synthesis of Optimum Finline Tapers Using Dispersion Formulas for Arbitrary Slot Widths and Locations," *IEEE Trans. Microw. Theory Techn.*, vol. 32, no. 12, pp. 1638-1645, Dec. 1984.

[36] F. Sporleder, and H. G. Unger, *Waveguide Tapers, Transitions and Couplers*, London, UK: Peter Peregrinus Ltd., 1979.

[37] B. Z. Katsenelenbaum *et al*., *Theory of Nonuniform Waveguides-the Cross-Section Method*, London, UK: IEE Electromagnetic Waves Series, 44, 1998.

[38] L. Solymar, "Design of a Conical Taper in Circular Waveguide System Supporting H_{10} Mode," *Proc. IRE*, vol. 46, no. 3, pp. 618-619, March 1958.

[39] R. C. Johnson, "Design of Linear Double Tapers in Rectangular Waveguides," *IRE Trans. Microw. Theory Techn.*, vol. 7, no. 3, pp. 374-378, July 1959.

[40] K. Matsumaru, "Reflection of a Pyramidally Tapered Rectangular Waveguide," *IRE Trans. Microw. Theory Techn.*, vol. 7, no. 2, pp. 192-196, April 1959.

[41] L. Solymar, "Design of a Two-section Conical Taper in Circular Waveguide System Supporting the H_{01} mode," *Proc. IEE - Part B: Electronic and Communication Engineering*, vol. 106, no. 13, pp. 119-120, Jan. 1959.

[42] L. Solymar, "Monotonic Multi-section Tapers for Over-moded Circular Waveguides," *Proc. IEE - Part B: Electronic and Communication Engineering*, vol. 106, no. 13, pp. 121-128, Jan. 1959.

[43] H. G. Unger, "Circular Waveguide Taper of Improved Design," *Bell Syst. Tech. J.*, vol. 37, pp. 899-912, July 1958.

[44] C. C. H. Tang, "Optimization of Waveguide Tapers Capable of Multimode Propagation," *IRE Trans. Microw. Theory Techn.*, vol. 9, no. 5, pp. 442-452, Sept. 1961.

[45] R. P. Hecken and A. Anuff, "On the Optimum Design of Tapered Waveguide Transitions," *IEEE Trans. Microw. Theory Techn.*, vol. 21, no. 6, pp. 374-380, June 1973.

[46] J. L. Doane, "Parabolic Tapers for Overmoded Waveguides," *Int. J. Infrared Millim. Waves*, vol. 5, no. 5, pp. 737-751, May 1984.

[47] F. Sporleder, "Waveguide Transition Design of Improved Accuracy," *Arch. Elek. Ubertrugung.*, vol. 30, pp. 289-296, 1976.

[48] H. Flugel and E. Kuhn, "Computer-aided Analysis and Design of Circular Waveguide Tapers," *IEEE Trans. Microw. Theory Techn.*, vol. 36, no. 2, pp. 332-336, Feb. 1988.

[49] S. Cogollos *et al.*, "Novel Planar and Waveguide Implementations of Impedance Matching Networks Based on Tapered Lines Using Generalized Superellipses," *IEEE Trans. Microw. Theory Techn.*, vol. 66, no. 4, pp. 1874-1884, April 2018.

[50] J. M. Percaz *et al.*, "Synthesis of Tapers Using the Coupled-Mode Theory," *2018 IEEE MTT-S Latin America Microwave Conf. (LAMC)*, Arequipa, 2018, pp. 1-4.

[51] R. E. Collin, "Theory and Design of Wide-Band Multisection Quarter-Wave Transformers," *Proc. IRE*, vol. 43, no. 2, pp. 179-185, Feb. 1955.

[52] R. J. Cameron, C. M. Kudsia, and R. R. Mansour, *Microwave Filters for Communication Systems: Fundamentals*, Design and Applications. Hoboken, NJ, USA: Wiley, 2007.

[53] I. Arnedo *et al*., "Synthesis of One-Dimensional Electromagnetic Bandgap Structures with Fully Controlled Parameters," *IEEE Trans. Microw. Theory Techn.*, vol. 65, no. 9, pp. 3123-3134, Sept. 2017.

[54] R. Sorrentino, and O. A. Peverini, "Additive Manufacturing: a Key Enabling Technology for Next-Generation Microwave and Millimeter-Wave Systems," *Proc. IEEE*, vol. 104, no. 7, pp. 1362-1366, July 2016.

upna

Universidad Pública de Navarra
Nafarroako Unibertsitate Publikoa

CHAPTER 5. THE CONTINUOUS LAYER PEELING (CLP) SYNTHESIS TECHNIQUE

The inverse scattering layer peeling methods arose in the decade of the 80's from the field of geophysics, in order to exploit the physical properties of a layered media in which waves propagate [1]. Their solutions were referred to as dynamic deconvolution methods [1]-[3], and they were formulated in terms of a discretized layered earth model. They were employed to reconstruct the earth medium in a layer-by-layer recursive manner following the algorithm of Schur [4]. The layer peeling method was initially translated to the microwave realm by Bruckstein and Kilath in [5] and [6].

The main basis of the layer peeling techniques is the principle of causality, and its concept can be easily understood from an intuitive point of view by considering a TEM or QTEM transmission line, being the method fully valid for other kind of waveguides such as the rectangular waveguide. However, the reasoning becomes much trickier when dealing with technologies of dispersive nature, since it is not possible to relate the propagation distance and the time employed for that propagation through a unique propagation velocity. Therefore, if a transmission line device is considered by dividing it into infinitesimal layers of thickness dz, being this device excited at its input port ($z = 0$) by an incident wave, the distance that the wave will need to travel to come back to the input port after going forward and being backward reflected at dz will be $d\tau = 2 \cdot dz$, being τ the "reflection distance". It is important to stress that

if the device has a length $z_{max} = L$, the corresponding maximum of the reflection distance will be $\tau_{max} = 2 \cdot z_{max} = 2 \cdot L$.

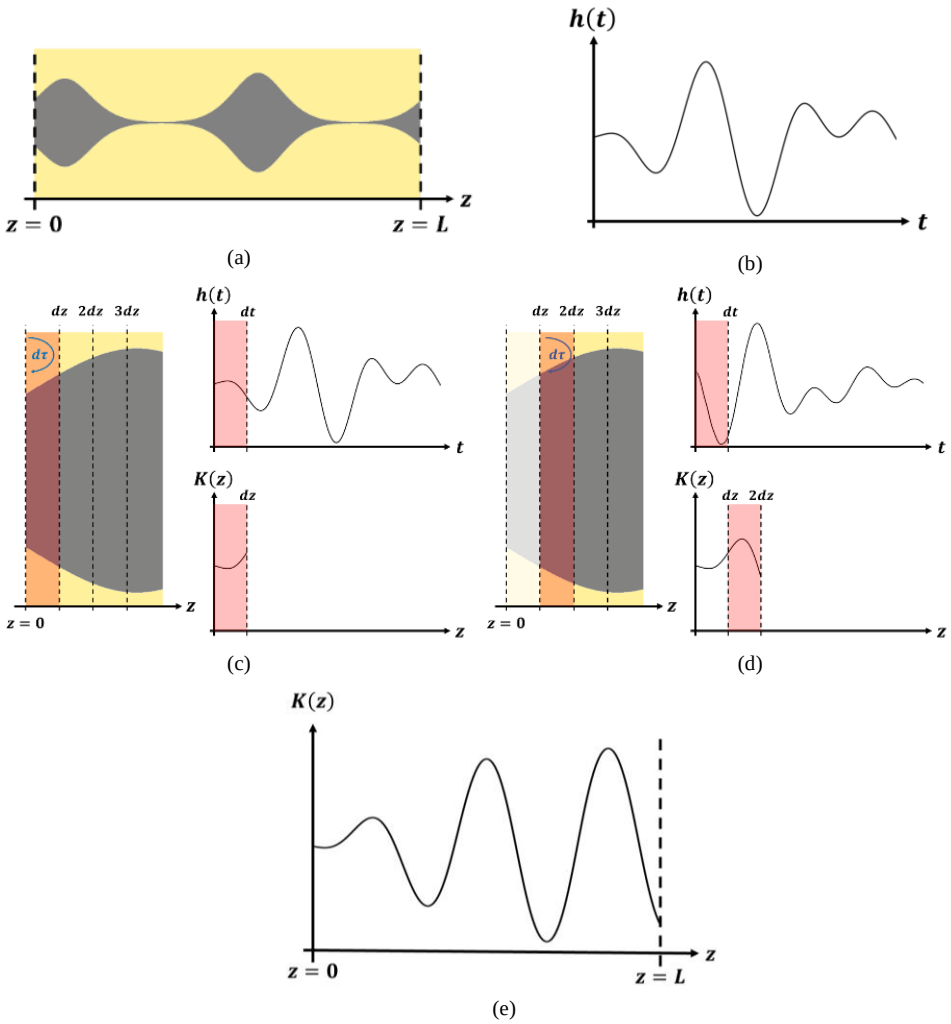

Fig. 5.1. Schematic representation of the operation principle of the CLP method: (a) unknown physical structure intended to be synthetized by calculating its coupling coefficient with CLP and its (b) target impulse response in reflection, $h(t)$. (c) The first dt instant of $h(t)$ must be governed only by the first dz layer of the device due to the causality principle and thus, it is possible to calculate the coupling coefficient, $K(z)$, for dz. (d) Once the first layer is peeled-off, a new $h(t)$ must be accomplished by the rest of the device, and by applying the same procedure of the first layer, the coupling coefficient between dz and $2dz$ can be calculated. (e) Once all layers have been peeled-off, the coupling coefficient of the whole structure is determined.

Thus, if time is denoted by t, the first dt instant, i.e. $0 < t \leq dt$, of the impulse response in reflection, $h(t)$, must be completely determined through the propagation velocity, v_p, due to the causality principle and $dt = \frac{d\tau}{v_p} = \frac{2 \cdot dz}{v_p}$. Therefore, the time domain evolution of the first dt of the impulse response does not depend on the properties of the structure beyond the considered block of dz, which also corresponds to $d\tau$ when considering the reflection distance (see Fig. 5.1). If this last reasoning is reversed, it will be possible to state that the first dt instant of the impulse response in reflection, $h(t)$, will completely determine the properties of the first $dz = v_p/2 \cdot dt$ layer of the structure. Once the sought properties of this first dz layer have been determined, it will be possible to remove the contribution of that layer to the impulse response, giving rise to a different impulse response that must be accomplished by the rest of the structure as it is shown in Fig. 5.1. At this point the first dz layer can be peeled-off, and the initial situation is repeated, but in this case the new target impulse response will characterize the following layer that was originally placed within $dz \leq z \leq 2 \cdot dz$. It is noticeable that if the process is performed for each layer between $z = 0$ and $z = L$, the properties of the whole structure will be revealed, according to the workflow graph of Fig. 5.1. This qualitative description of the method would be strictly valid if the thickness of the layers were finite, something that would give rise to the Discrete Layer Peeling method. However, when the thickness of the layers tends to be infinitesimal, i.e. $dz \to 0$, the layer concept lacks sense and thus, the method is known as Continuous Layer Peeling (CLP).

The Inverse Scattering layer peeling procedure was originally developed in the time domain for the synthesis of fiber Bragg gratings in the optical range by Feced *et al.* [7], but the works of Skaar [8], [9] and Poladian [10], [11] translated the technique to the frequency domain where the computational efficiency is better, although still restricted to Bragg gratings in the optical domain. All these contributions were the basis for the development of the method presented in this thesis, implemented in the frequency domain and valid for the synthesis of microwave and millimeter wave devices.

As it was demonstrated for the GLM series solution of the synthesis problem that has been carefully developed in CHAPTER 4, the coupling coefficient, $K(z)$, can be expressed as a function of the target frequency response in reflection, $S_{11}(\beta)$, through the series solution (4.31) that is conveniently provided again:

$$
\begin{aligned}
K(z) = {} & -2 \cdot F(2z) + \\
& -2 \cdot \int_0^{2z} dx_1 F(x_1) \cdot \int_0^{x_1} dx_2' F(x_2') \, F(x_2' - x_1 + 2z) + \\
& -2 \int_0^{2z} dx_1 F(x_1) \int_0^{x_1} dx_2' F(x_2') \int_0^{x_2} dx_3' F(x_3') \int_0^{x_3} dx_4' F(x_4') \, F(x_4' - x_3 + 2z) + \\
& - \cdots + \\
& -2 \int_0^{2z} dx_1 F(x_1) \int_0^{x_1} dx_2' F(x_2') \int_0^{x_2} \ldots \int_0^{x_{2N-1}} dx_{2N}' F(x_{2N}') \, F(x_{2N}' - x_{2N-1} + 2z) + \\
& - \cdots +
\end{aligned}
\tag{4.31}
$$

where $x_i' = x_i + x_{i-1} - 2z$ for $i > 1$ and $F(\tau)$ is the inverse Fourier transform of the $S_{11}(\beta)$-parameter, as it was originally defined in (4.11):

$$F(\tau) = \frac{1}{2 \cdot \pi} \cdot \int_{-\infty}^{\infty} S_{11}(\beta) \cdot e^{j \cdot \beta \cdot \tau} \cdot d\beta \tag{4.11}$$

Particularizing the series solution of (4.31) for the beginning of the device, $z = 0$, it can be seen that just the first term of the series is not null, whose expression is, rigorously speaking, $-2 \cdot F(\tau = z + z^+)$, obtaining at the beginning of the device:

$$K(z = 0) = -2 \cdot F(\tau = 0^+) \tag{5.1}$$

being $F(\tau = 0^+)$ the right-hand limit of $F(\tau)$ at $\tau = 0$.

Due to the causality principle it must be verified that $F(\tau) = 0, \forall\, \tau < 0$, and thus, $F(\tau = 0^+)$ must be rigorously taken in (5.1). Accordingly, $F(\tau = 0^-) = 0$, and $F(\tau)$ will have a step discontinuity at $\tau = 0$. In order to evaluate the inverse Fourier integral at that discontinuity, the average value at $\tau = 0^-$ and $\tau = 0^+$ needs to be used [12]:

$$F(\tau = 0) = \frac{F(\tau = 0^+) + F(\tau = 0^-)}{2} = \frac{F(\tau = 0^+)}{2} \tag{5.2}$$

and taking into account (4.11) and (5.2) it can be obtained:

$$F(\tau = 0^+) = 2 \cdot F(\tau = 0) = 2 \cdot \frac{1}{2\pi} \int_{-\infty}^{\infty} S_{11}(\beta) \cdot e^{j \cdot \beta \cdot \tau} \cdot d\beta \Big|_{\tau = 0} = \frac{1}{\pi} \int_{-\infty}^{\infty} S_{11}(\beta) \cdot d\beta \tag{5.3}$$

Incorporating this result into (5.1) it can be finally obtained:

$$K(z=0) = -\frac{2}{\pi}\int_{-\infty}^{\infty} S_{11}(\beta)\cdot d\beta \tag{5.4}$$

It is interesting to note that (5.4) allows us to calculate the coupling coefficient at the origin of the device, $z = 0$, as a function of the reflection coefficient also at the origin of the device.

In order to get the most efficient numerical implementation of (5.4), the property satisfied by any real physical device $S_{ij}(-f) = S_{ij}^{*}(f)$ will be taken into account. It implies in our case that $S_{11}(-\beta) = S_{11}^{*}(\beta)$. Therefore, expression (5.4) can be finally rewritten as:

$$K(z=0) = -\frac{4}{\pi}\int_{0}^{\infty} \mathcal{R}e\{S_{11}(\beta)\}\cdot d\beta \tag{5.5}$$

Now, in order to peel-off the synthetized infinitesimal layer, the Riccati equation [13] will be used to propagate the target reflection coefficient along the device. The Riccati equation can be obtained from the single-mode coupled-mode equation system of (2.91), (2.92). The reflection coefficient parameter, ρ, is introduced, being defined as:

$$\rho(z,\beta) = \frac{a^{-}(z,\beta)}{a^{+}(z,\beta)} \tag{5.6}$$

and taking its derivative it results in:

$$\frac{d\rho}{dz} = \frac{\left(\frac{da^{-}}{dz}\cdot a^{+} - \frac{da^{+}}{dz}\cdot a^{-}\right)}{(a^{+})^{2}} \tag{5.7}$$

Introducing the single-mode system of couple-mode equations (2.91), (2.92), it is obtained that:

$$\frac{d\rho}{dz} = \frac{(j\cdot\beta\cdot a^{-} + K\cdot a^{+})\cdot a^{+} - (-j\cdot\beta\cdot a^{+} + K\cdot a^{-})\cdot a^{-}}{(a^{+})^{2}} \tag{5.8}$$

and reorganizing the equation it can be rewritten as:

$$\frac{d\rho}{dz} = j\cdot\beta\cdot\frac{a^{-}}{a^{+}} + K + j\cdot\beta\cdot\frac{a^{-}}{a^{+}} - K\cdot\frac{(a^{-})^{2}}{(a^{+})^{2}} \tag{5.9}$$

Recalling that the reflection coefficient ρ is defined as (5.6), the expression can be finally rewritten as the so-called Riccati equation:

$$\frac{d\rho}{dz} = 2 \cdot j \cdot \beta \cdot \rho + K \cdot (1 - \rho^2) \tag{5.10}$$

Once the coupling coefficient at the origin of the device, $K(0)$, is calculated using (5.5), the Riccati equation (5.10) will be employed to propagate the target reflection coefficient spectrum along the first infinitesimal layer of the device. With this new target spectrum, the first infinitesimal layer is peeled off and the origin of the rest of the device is shifted to the next layer. Then, the next point of the coupling coefficient can be calculated using (5.5). Following in an iterative manner, i.e., propagating the target spectrum with (5.10) and calculating the next value of the coupling coefficient by means of (5.5), the entire coupling coefficient, $K(z)$, for the targeted $S_{11}(\beta)$ is synthesized.

In order to conclude this subsection it must be highlighted that the CLP method is able to synthetize frequency responses that feature a maximum rejection level substantially higher than the one that can be achieved by means of GLM [14], which features an approximate limit for the achievable rejection level of -15 dB, as it was reported in [15].

5.1. Relevant Numerical Aspects for the Implementation of the CLP Method

In order to implement the CLP synthesis method in practice, and due to the inherent limitations of computation, it will be mandatory to employ discretized versions of the target frequency response in reflection, $S_{11}(\beta)$, and of its corresponding inverse Fourier transform, $F(\tau)$. Therefore, it is needed to explore the optimum relationship between the sampling period of the z axis and the resolution employed for the definition of the transform pair variables β and τ. It is important to highlight that this relationship will also determine the optimum number of points, N_z, that must be employed for the correct discretization of the z axis of a structure of length L.Thus, if N_z is the optimum number of points for a length L, then the discretization period for the propagation axis, $T_{D,z}$, will be:

$$T_{D,z} = \frac{L}{N_z} \tag{5.11}$$

Firstly, we must recall the inverse Fourier transform relationship that was previously stablished between $S_{11}(\beta)$ and $F(\tau)$ in (4.11):

$$F(\tau) = \frac{1}{2 \cdot \pi} \cdot \int_{-\infty}^{\infty} S_{11}(\beta) \cdot e^{j \cdot \beta \cdot \tau} \cdot d\beta \tag{4.11}$$

where the forward Fourier transform was provided in (4.12) and is rewritten below:

$$S_{11}(\beta) = \int_{-\infty}^{\infty} F(\tau) \cdot e^{-j \cdot \beta \cdot \tau} \cdot d\tau \tag{4.12}$$

being τ the "reflection distance", which satisfies:

$$\tau = 2 \cdot z \tag{5.12}$$

When dealing with discretized versions of signals that compose a transform pair of the form $S_{11}(\beta) = FT\{F(\tau)\}$, the sequence $F_D[n]$ is defined as the sampled version of $F(\tau)$ and satisfies $F_D[n] = F\left(\tau = n \cdot T_{D,\tau}\right)$, see Fig. 5.2a. The sampled $F_D[n]$ can be alternatively written as:

$$F_D[n] = \sum_{i=0}^{N-1} F\left(\tau = i \cdot T_{D,\tau}\right) \cdot \delta[n-i] \tag{5.13}$$

where $T_{D,\tau}$ is the sampling period of the τ aixs, $\delta[n]$ is the discrete-time unit impulse, and $i = 0, \dots, N-1$, with N being the number of samples. It must be noticed that for the sake of simplicity N will be assumed to be an even number in the subsequent steps.

The set of discrete points along τ, $\tau_{D,n}$, for whom $F(\tau)$ is sampled, i.e. $F_D[n] = F\left(\tau = \tau_{D,n}\right)$, can be deduced according to (5.13) as:

$$\tau_{D,n} = n \cdot T_{D,\tau} = 0 \cdot\ T_{D,\tau}, 1 \cdot T_{D,\tau}, 2 \cdot T_{D,\tau}, \dots, (N-1) \cdot T_{D,\tau} \tag{5.14}$$

Considering the principles of discrete signal processing that are thoroughly discussed in the textbook reference [16], it is possible to define the sampling phase constant, β_S, (in analogy to the sampling frequency employed in the classical sampling theorem [16], see Fig. 5.2b) that is needed to sample the τ axis with period $T_{D,\tau}$ as:

$$\beta_S = \frac{2 \cdot \pi}{T_{D,\tau}} \tag{5.15}$$

If the Fast Fourier Transform (FFT) is applied to a real $F_D[n]$ while taking into account the properties of discrete signal processing [16], the sampled version of the S_{11}-parameter, $S_{11,D}$, will be also composed of N samples (see Fig. 5.2b), given by:

$$S_{11,D}[k] = T_{D,\tau} \cdot FFT\{F_D[n]\} = \sum_{i=0}^{N-1} S_{11}(\beta = i \cdot \Delta\beta_D) \cdot \delta[k-i] \tag{5.16}$$

where $\Delta\beta_D$ is the sampling period in β, which is related in turn with the sampling phase constant, β_S, see Fig. 5.2b, by the expression:

$$\Delta\beta_D = \frac{\beta_S}{N} \tag{5.17}$$

It is important to stress that (5.17) states that the phase constant range between $\beta = 0$ rad/m and β_S will be divided into N uniform portions and hence, each of them covers a bandwidth of $\Delta\beta_D$. Regarding $\Delta\beta_D$, the discrete points of β where the $S_{11,D}(\beta)$ is sampled, $\beta_{D,k}$, can be accordingly determined from (5.16) as:

$$\beta_{D,k} = k \cdot \Delta\beta_D \tag{5.18}$$

On the other hand, if it is desired to calculate $F_D[n]$ from $S_{D,11}[k]$, the inverse FFT will be needed with an additional $\frac{1}{T_{D,\tau}}$ scaling factor, which is fully coherent with (5.16), i.e.:

$$F_D[n] = \frac{1}{T_{D,\tau}} \cdot FFT^{-1}\{S_{D,11}[k]\} = \sum_{i=0}^{N-1} F(\tau = i \cdot T_{D,\tau}) \cdot \delta[n-i] \tag{5.19}$$

Taking under consideration (5.15) in (5.17), alternative expressions for $\Delta\beta_D$ can be attained:

$$\Delta\beta_D = \frac{\beta_S}{N} = \frac{\frac{2\cdot\pi}{T_{D,\tau}}}{N} = \frac{2\cdot\pi}{T_{D,\tau}\cdot N} \tag{5.20}$$

where the term $T_{D,\tau} \cdot N$ of the denominator of (5.20) corresponds to the total duration of the sampled τ axis, $\tau_{D,max}$, that in turn will be two times the total length of the structure along z due to (5.12), i.e.:

$$\tau_{D,max} = 2 \cdot L = T_{D,\tau} \cdot N \tag{5.21}$$

Incorporating the definition of (5.21) in (5.20), the resolution $\Delta\beta_D$ can be directly related with $\tau_{D,max}$ as:

$$\Delta\beta_D = \frac{\beta_S}{N} = \frac{2\cdot\pi}{T_{D,\tau}\cdot N} = \frac{2\cdot\pi}{\tau_{D,max}} \tag{5.22}$$

At this point, it is important to stress that if the z axis of a structure of length L is sampled with an optimum number of points, N_z, it must be automatically satisfied that:

$$N_z = \frac{L}{T_{D,z}} \tag{5.23}$$

where $T_{D,z}$ stands for the sampling period of the z axis, which is obviously related with $T_{D,\tau}$ by (5.12) as:

$$T_{D,z} = \frac{T_{D,\tau}}{2} \tag{5.24}$$

Thus, the z axis will be optimally discretized in the $z_{D,n}$ points that will be defined according to Fig. 5.2c and (5.24) as:

$$z_{D,n} = n \cdot T_{D,z} = 0 \cdot\ T_{D,z}, 1 \cdot T_{D,z}, 2 \cdot T_{D,z}, \ldots, (N-1) \cdot T_{D,z} \tag{5.25}$$

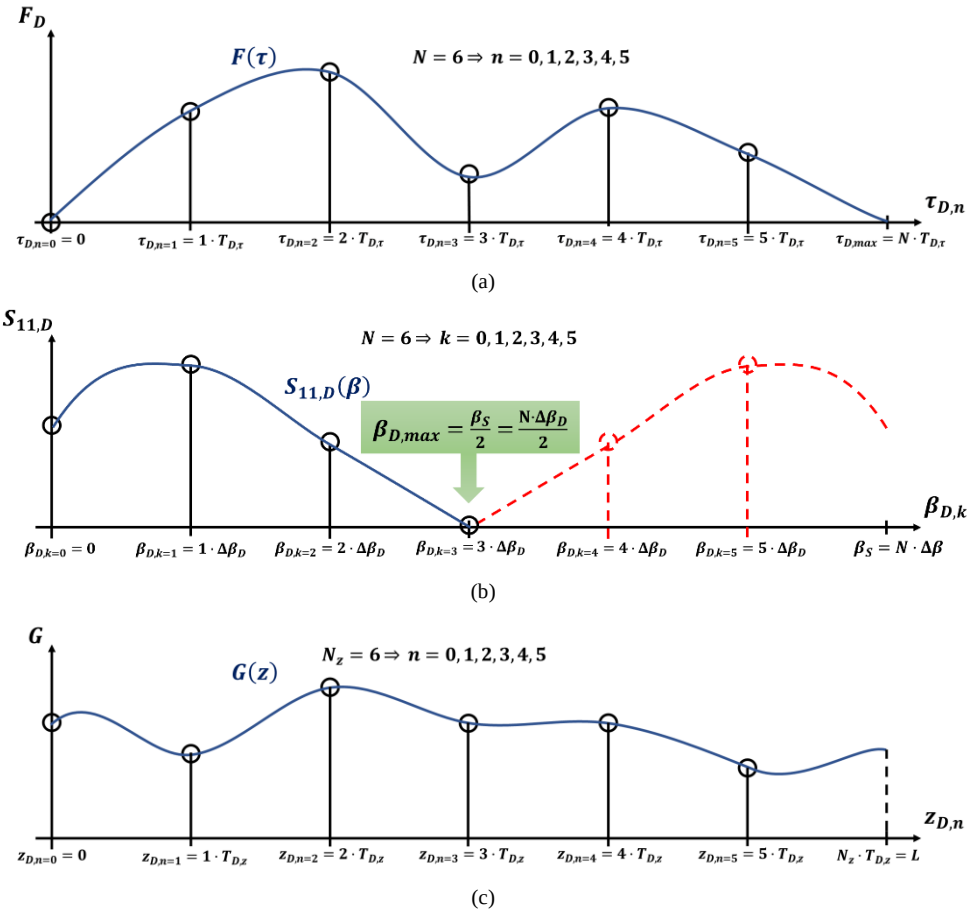

Fig. 5.2. Sketch of the correspondence between the original (blue lines) and discretized (black circles) versions of (a) the impulse response in reflection, $F(\tau)$, (b) the $S_{11}(\beta)$-parameter, and (c) the propagation axis, z, of a physical structure that features a dimensional profile, $G(z)$, for the case of $N = N_z = 6$. In (b), the redundant samples of the $S_{11,D}(\beta_{D,n})$ that are consequence of the discretization are highlighted with a red dashed line.

If the expressions (5.21) and (5.24) are properly incorporated in (5.23), the optimum number of points for the z axis, N_z, will be determined as a result:

$$N_z = \frac{L}{T_{D,z}} = \frac{2 \cdot L}{T_{D,\tau}} = \frac{\tau_{D,max}}{T_{D,\tau}} = \frac{T_{D,\tau} \cdot N}{T_{D,\tau}} = N \tag{5.26}$$

Therefore, the optimum number of points, N_z, that must be considered in the propagation axis z, for the synthesis of a structure of length, L, which is defined by a sampled impulse response in reflection, $F_D[n]$, will be the number of samples, N, of $F_D[n]$, see Fig. 5.2c.

Nevertheless, since the CLP method actually starts from the $S_{11}(\beta)$, it will be worth to relate $T_{D,z}$ and N_z with a parameter of the target $S_{11,D}[k]$.

However, it must be firstly stressed that due to the inherent properties of the FFT [16], only the first $\left(\frac{N}{2}+1\right)$ values of $S_{11,D}[k]$ will be relevant, since the remaining $\left(\frac{N}{2}-1\right)$ values will correspond to the complex conjugate of the former, i.e. $S_{11,D}[k] = S^*_{11,D}[N-k]$ and can be considered redundant as a result, see Fig. 5.2b. Therefore, the useful values of $S_{11,D}[k]$ will be $S_{11,D}[r]$, with $r = 0, \dots, \frac{N}{2}$. Consequently, the spectral information of the frequency response in reflection will be limited up to the sample $S_{11,D}\left[\frac{N}{2}\right]$, which will correspond to the maximum phase constant that can be univocally determined, $\beta_{D,max}$, using the sampling phase constant β_S. It is obvious that $\beta_{D,max}$ can be determined from (5.18) for the last value of r, i.e. $r = \frac{N}{2}$ as:

$$\beta_{D,max} = \beta_{D,k=\frac{N}{2}} = \Delta\beta_D \cdot \frac{N}{2} \tag{5.27}$$

Thus, in view of (5.20) it will be straightforward to deduce:

$$\beta_{D,max} = \Delta\beta_D \cdot \frac{N}{2} = \frac{\beta_S}{2} \tag{5.28}$$

It is important to highlight that the expression (5.28) is fully coherent with the Nyquist-Shannon sampling theorem [17], [18]. Recalling (5.12) and (5.15) it will be deduced that:

$$\beta_{D,max} = \frac{\beta_S}{2} = \frac{\frac{2\cdot\pi}{T_{D,\tau}}}{2} = \frac{\pi}{T_{D,\tau}} = \frac{\pi}{2\cdot T_{D,z}} \tag{5.29}$$

The relationship (5.29) states the maximum phase constant, $\beta_{D,max}$, that can be determined considering a sampling period, $T_{D,z}$, for the z axis. However, the most interesting conclusion is extracted by reversing the last reasoning, i.e. if the frequency response in reflection, $S_{11,D}$, prescribed to apply any synthesis procedure is defined up to $\beta_{D,max}$, then the optimum sampling period for the z axis that should be considered must be $T_{D,z}$, where $T_{D,z}$ can be determined from (5.29) as:

$$T_{D,z} = \frac{\pi}{2\cdot\beta_{D,max}} \tag{5.30}$$

Since the number of non-redundant samples of the $S_{11,D}$ is $\left(\frac{N}{2}+1\right)$, it can be concluded that the number of points in which the z axis must be sampled, N_z, regarding a $S_{11,D}$-parameter

defined with $\left(\frac{N}{2}+1\right)$ non-redundant samples will be $N_z = N$. It must be noted that this result agrees with (5.26).

The number of points, N_z, can be alternatively deduced from $\beta_{D,max}$ and $\Delta\beta_D$ by (5.28) as:

$$N_z = N = \frac{2 \cdot \beta_{D,max}}{\Delta\beta_D} \tag{5.31}$$

Moreover, taking into account the following general relationship between β and λ_g:

$$\beta = \frac{2 \cdot \pi}{\lambda_g} \tag{5.32}$$

where λ_g is the wavelength of the propagating mode in the waveguide, the maximum phase constant, $\beta_{D,max}$, of (5.27)-(5.31) will be forcibly related with the minimum wavelength, $\lambda_{g,D,min}$, that can be described when dealing with a sampled S_{11}-parameter as follows:

$$\beta_{D,max} = \frac{2 \cdot \pi}{\lambda_{g,D,min}} \tag{5.33}$$

In view of (5.30) and (5.33), the optimum sampling period in z, $T_{D,z}$, is related with $\lambda_{g,D,min}$ (see Fig. 5.3a) as:

$$T_{D,z} = \frac{\lambda_{g,D,min}}{4} \tag{5.34}$$

However, in order to finish this section that has been developed considering the relevant numerical aspects for the practical implementation of the layer-peeling synthesis approach, it is

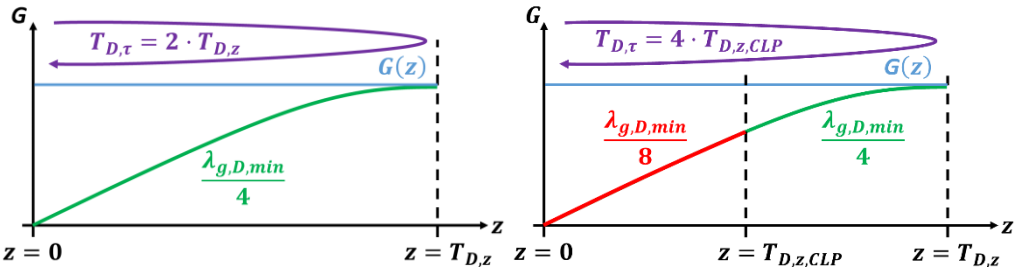

(a) (b)

Fig. 5.3. Sketch of the first $T_{D,z}$ sample in z of a generic structure with physical dimensions G along the propagation axis, z (light blue line): (a) The optimum sampling period selected for z, $T_{D,z}$, should correspond to a the quarter of the minimum wavelength $\lambda_{g,D,min}$ associated with $\beta_{D,max}$. However, the sampling period necessary to implement properly the CLP method (b) is $\frac{\lambda_{g,D,min}}{8}$.

important to highlight a critical peculiarity of the practical implementation of the CLP method. The numerical solution of the Riccati equation of (5.10) that has been implemented using the Matlab ordinary differential equation (ODE) solver "*ode45.m*", needs to consider half of the discretization period $T_{D,z}$ that has been deduced in (5.30) and (5.34) for a frequency response in reflection defined up to $\beta_{D,max}$, in order to propagate correctly the reflection coefficient through the z axis. Consequently, (5.30) and (5.34) must be reformulated taking into account the extra factor of 2 for the concerning CLP synthesis technique, yielding to a necessary non-optimum sampling period for the numerical implementation of CLP (see Fig. 5.3b), $T_{D,z,CLP}$, that will be determined by means of (5.30) and (5.34) as:

$$T_{D,z,CLP} = \frac{T_{D,z}}{2} = \frac{\pi}{4 \cdot \beta_{D,max}} = \frac{\lambda_{g,D,min}}{8} \tag{5.35}$$

Therefore, the number of points that will be needed to ensure a proper convergence of the numerical implementation of the CLP method, $N_{z,CLP}$, will be the two times the optimum N_z, i.e. $N_{z,CLP} = 2 \cdot N_z$, as it is shown in Fig. 5.4. Thus, considering (5.35) in (5.26) as well as in (5.31), it is obtained that:

$$N_{z,CLP} = 2 \cdot N = \frac{4 \cdot \beta_{D,max}}{\Delta\beta_D} \tag{5.36}$$

where N is the number of samples numerically provided for the target $F(\tau)$, $F_D[n]$. It must be highlighted that the result of (5.36) is coherent with the relationship reported in [19], where a deduction only valid for transmission line was carried out.

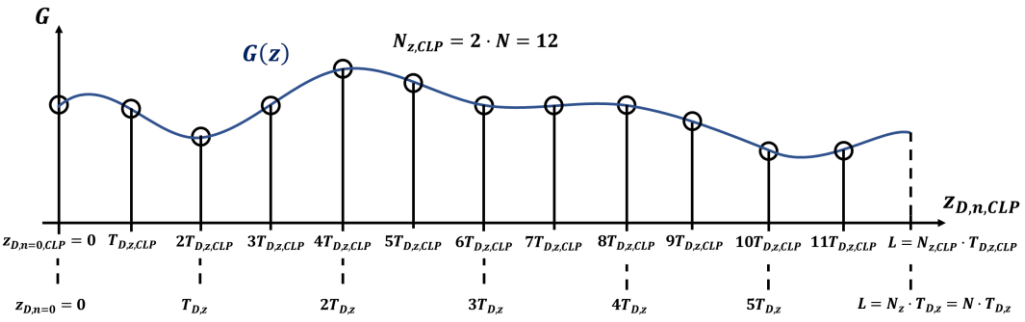

Fig. 5.4. Sketch of the discretization that must be employed for the z axis for the practical implementation of the CLP method regarding a structure with physical dimensions $G(z)$. In this example, the discretized version of the impulse response in reflection of $G(z)$, $F_D[n] = F(\tau = n \cdot T_{D,\tau})$, as well as its associated frequency response, $S_{11,D}[k] = S_{11}(\beta = k \cdot \Delta\beta_D)$, are defined with $N = 6$ samples. Thus, the z axis must be divided into $N_{z,CLP} = 2 \cdot N = 12$ points with a sampling period $T_{D,z,CLP} = \frac{T_{D,z}}{2}$

Finally, the necessary discretized points of the z axis for the CLP method, $z_{D,n,CLP}$, must be adjusted by considering $n_{CLP} = 0, 1, \dots, N_{z,CLP} - 1$, as it is depicted in Fig. 5.4, where $N_{z,CLP} = 2 \cdot N$, i.e.:

$$z_{D,n,CLP} = n_{CLP} \cdot T_{D,z,CLP} =$$

$$= 0 \cdot T_{D,z,CLP}, 1 \cdot T_{D,z,CLP}, 2 \cdot T_{D,z,CLP}, \dots, \left(N_{z,CLP} - 1\right) \cdot T_{D,z,CLP} = \tag{5.37}$$

$$= 0 \cdot T_{D,z}, 1 \cdot \frac{T_{D,z}}{2}, 2 \cdot \frac{T_{D,z}}{2}, \dots, (2 \cdot N_z - 1) \cdot T_{D,z}$$

5.2. Design Procedure for Low-pass and Band-pass Filters without Spurious Stopbands

Microwave filters are one of the most widely employed components for microwave systems since they are two-port structures that provide a transmission feature between these ports for frequencies within a passband range, while other frequencies that belong to the stopband get attenuated. The definition of the characteristics of both passband and stopband determines the general behavior of the frequency response, leading to the four different categories of filters that can be typically distinguished: low-pass, high-pass, band-pass, and reject-band filter.

A wide variety of design techniques based on different physical approaches have been proposed for the diverse technologies employed for the implementation of microwave components. Many specialized books have been published covering the topic of design of microwave filters, where a reduced selection is provided in [20]-[25], although an overview of the classical design techniques is gathered in the review papers [26]-[28]. However, a great part of the filter design techniques rests on the so-called insertion loss method [20], which employs the theory developed for the synthesis of filters based on discrete elements (resistors, capacitors, inductors,…) that are appropriate for lower frequencies where the wavelength is much longer than the physical size of these elements. The values and the association between the discrete components are chosen so as to obtain a frequency response given by a rational function such as the Butterworth, Chebyshev, Zolotarev, or Cauer. Nevertheless, the discrete elements are no longer suitable for the microwave range due to their excessive size with respect to the concerning wavelengths. Thus, the microwave distributed structures are designed and connected so as to achieve the functionality of one (or a set) of the discrete elements that would be needed to obtain the frequency response of the filter by following the insertion loss method. However, the equivalence between the behavior of a discrete and a distributed element is only exact for a single design frequency and the frequency response far from this point is rapidly degraded when it is compared with the one that may be expected from the use of ideal discrete elements. As a result, the selectivity provided by the microwave filter is poorer than that of the initial discrete element prototype. Furthermore, the appearance of spurious passbands or stopbands cannot be easily avoided due to the periodic essence of the frequency response of transmission lines and to the excitation of higher-order modes. This lack of control of the out of band behavior of the filter can lead to the breach of the requirements when broadband specifications are demanded.

In this section, a method for the design of low-pass and band-pass filtering structures that do not feature spurious rejection bands will be detailed. The resulting physical dimensions of the filters will vary in a smooth fashion along the propagation direction.

In 2012, a method based on an Inverse Scattering technique was successfully proposed by Arnedo *et al.* [29] to synthetize smooth-shaped filters, although it was limited to pure rational frequency responses in reflection, i.e. responses that must be expressed as rational functions with a finite number of poles and zeros in the complex Laplace plane, $s = \sigma + j \cdot \omega$. Moreover, an additional drawback of that technique was the lack of control by the designer over the final dimensions of the resulting device. Indeed, this kind of responses leads to structures that ideally feature an infinite length, and their coupling coefficient must be truncated with a long length in practice. Furthermore, the physical dimensions of the perturbations of the cross-section along the propagation direction are completely unknown until the structure is synthetized. Conversely, the design method that is going to be presented and demonstrated here drives to finite-length structures, while also providing an approximate insight of the physical dimensions that will be eventually featured by the cross-section of the synthetized device along the propagation direction.

As a general description of the design method proposed here, the response in reflection of a classical commensurate-line filter prototype that fulfills the desired specifications will be properly modified by means of a bandlimited interpolation, giving rise to the target response for the CLP technique. The synthetized filter will feature a dimensional profile that will vary in a smooth fashion, while retaining similar length and physical dimensions to those of the initial commensurate-line prototype. Since the inverse scattering synthesis techniques are exact for the intended bandwidth, the frequency response of the resulting structure will not exhibit spurious passbands or stopbands. In order to verify the proposed design technique, a first design example in microstrip technology will be provided. The feasibility of the synthesis of rectangular waveguide filters for a subsequent fabrication with Additive Manufacturing techniques in metal will be also addressed in a second design example, requiring realistic specifications in terms of rejection levels for the target response.

5.2.1. Classical Low-Pass Commensurate-Line Unit-Element Prototype

The first stage to achieve the target response for the synthesis is to obtain a commensurate-line distributed prototype that fulfills the frequency specifications required for

the filter. The prototype is formed by a cascade of *N* line-sections, all of them with the same electrical length (commensurate) and different characteristic impedances, plus an additional input and output line-section with the port impedances (see Fig. 5.5).

The synthesis of commensurate-line distributed networks (composed in general of commensurate lossless line-sections and lumped resistors) can be formulated on an analogous basis to the synthesis of lumped-element networks by using the Richards' transformation [30]-[32]:

$$t = \tanh\left(\frac{a \cdot s}{2}\right) \tag{5.38}$$

where the complex frequency (Laplace) variable *s* is transformed to a new complex variable *t*, and the constant $a = l/c$ is the ratio between the length of a commensurate line, *l*, and the velocity of propagation of electromagnetic waves in the line, *c*. Using the Richards' transformation, the driving-point impedance of a commensurate distributed network, as well as the parameters of its scattering, transfer, and immittance matrices, can be expressed as rational functions in *t* [30]-[32]. The use of the half-argument $a \cdot s/2$ in the hyperbolic tangent in (5.38) is required so that the transmittances become rational functions in *t*. However, if the full argument $a \cdot s$ is employed, the driving-point impedance and all the matrix parameters remain rational functions in *t*, except for the possible appearance of irrational factors of the form $(1 - t^2)^{1/2}$ in the transmittances [21], [31], [32]. In this case, the Richards' transformation is defined as:

$$t = \tanh\left(a \cdot s\right) \tag{5.39}$$

and the degree of the rational functions in *t* of the scattering, transfer, and immittance matrices, and of the driving-point impedance, is reduced by half when compared to the original transformation of (5.38). Actually, this last form of the Richards' transformation is preferred and used in the vast majority of books and papers published in the last decades [21], [22], [31]-[37], where expressions identical or equivalent to (5.39) are employed, and it will be used here.

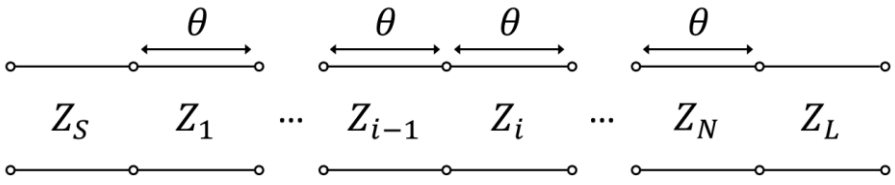

Fig. 5.5. Commensurate-line distributed prototype. Each line-section has the same electrical length, θ, and different characteristic impedance, Z_i.

As it was presented in (5.38) and (5.39), the Richards' transformation can be applied only to ideal transmission lines, since a constant velocity of propagation, c (not variable with frequency) is assumed in the definition of $a = l/c$. However, it can be easily extended to waveguides (where a phase velocity, v_p, variable with frequency must be considered), by introducing the concept of electrical length of the commensurate lines, $\theta = \beta \cdot l$, where $\beta = \omega/v_p$ is the phase constant of the waveguide operation mode, $\omega = 2\pi f$ is the frequency in rad/s, and f is the frequency in Hz [21], [22]. Thus, the Richards' transformation of (5.39) can be rewritten as [22]:

$$t = \tanh(j\theta) = j \cdot \tan(\theta) \tag{5.40}$$

since the argument $j\theta = j\omega l/v_p = sl/v_p$, where $\omega = s/j$ is employed to perform the analytic continuation to the complex frequency plane, *s*.

Inspecting (5.39) and (5.40) it can be seen that the Richards' transformation maps the (imaginary) frequency axis ($j\omega$) of the complex frequency (Laplace) plane, *s*, to the (imaginary) frequency axis ($j\Omega$) of the Richards' transform plane, *t*, through the equation [31]-[33]:

$$\Omega = \tan(\theta) \tag{5.41}$$

where:

$$\theta = \beta l = \omega l/v_p \tag{5.42}$$

is the electrical length of the commensurate lines (either transmission or waveguide line-sections). Therefore the mapping between frequency axes is periodic in θ, and actually all responses of commensurate distributed networks will be periodic with respect to θ (and to ω for the case of ideal transmission lines where v_p does not vary with frequency [31], [32], [34]-[37]). Additionally, it can be demonstrated that the right half of the *s* plane maps on the right half of the *t* plane, while the left half *s* plane maps on the left half *t* plane. Consequently the Richards' transformation behaves adequately and a positive real function of *t* has the same property with respect to *s* [31], [32].

The input impedance, in the Richards' transform plane, of a commensurate-line section (with electrical length θ and characteristic impedance Z_0) terminated in a short-circuit is given by $Z_{sc} = Z_0 \cdot t$. In the same way, it can be easily demonstrated using (5.40) that the input impedance of a commensurate-line section terminated in an open-circuit is $Z_{oc} = Z_o/t$. Therefore, a short-circuited stub and an open-circuited stub behave, in the Richards' transform

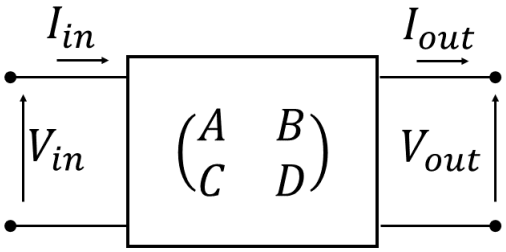

Fig. 5.6. Transmission matrix model of generic two-port element with the definition of the sign convention for the equivalent voltages and currents.

plane, as a lumped inductor and a lumped capacitor, respectively [21], [22], [31]-[37]. However,a commensurate-line section (with electrical length, θ, and characteristic impedance, Z_0), viewed as a two-port component, has no lumped-element counterpart and is termed unit element (UE) [21], [22], [31]-[37]. In order to model the frequency response of the commensurate line filter, it will be advisable to employ the transmission matrix defined as [38]:

$$\begin{pmatrix} V_{in} \\ I_{in} \end{pmatrix} = \begin{pmatrix} A & B \\ C & D \end{pmatrix} \cdot \begin{pmatrix} V_{out} \\ I_{out} \end{pmatrix} \tag{5.43}$$

where the equivalent voltages V_{in}, V_{out} and currents I_{in}, I_{out} follow the convention stated by the Fig. 5.6.

If (5.43) is developed, it will be obtained that:

$$V_{in} = A \cdot V_{out} + B \cdot I_{out} \tag{5.44}$$

$$I_{in} = C \cdot V_{out} + D \cdot I_{out} \tag{5.45}$$

The transmission matrix of a UE, i.e. a transmission or waveguide line section of length l, and characteristic impedance Z_0, for a specific phase constant β, is [38]:

$$\begin{pmatrix} A & B \\ C & D \end{pmatrix}_{UE} = \begin{pmatrix} \cos(\beta l) & jZ_0 \sin(\beta l) \\ \dfrac{j}{Z_0} \cdot \sin(\beta l) & \cos(\beta l) \end{pmatrix} \tag{5.46}$$

Therefore, the transmission matrix of a UE in the Richards' transform plane can be obtained from (5.46) by taking into account (5.40) and (5.42), resulting in [21], [22], [32], [34], [35], [37]:

$$\begin{pmatrix} A & B \\ C & D \end{pmatrix}_{UE} = \frac{1}{\sqrt{1-t^2}} \begin{bmatrix} 1 & Z_0 t \\ t/Z_0 & 1 \end{bmatrix} \tag{5.47}$$

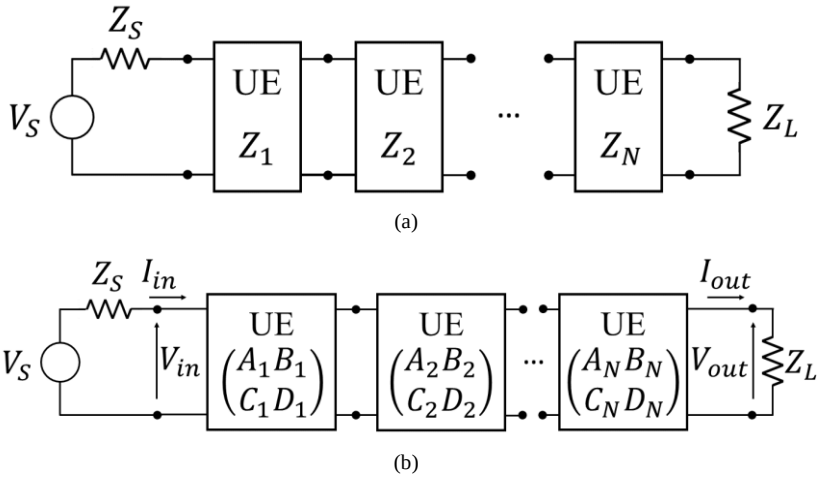

Fig. 5.7. Commensurate-line distributed prototype represented as a cascade of *N* UEs with their corresponding (a) impedances and (b) transmission matrices.

Let's focus now on the starting commensurate-line distributed prototype of interest. It is formed by a cascade of *N* line-sections, all of them with the same electrical length and different characteristic impedances, with an additional input and output line-section with the port impedances (see Fig. 5.5). Therefore, in the Richards' transformation domain, it can be modelled as a cascade of *N* UEs, plus the input and output ports, see Fig. 5.7a.

By multiplying the transfer matrices of the *N* UEs as they are depicted in Fig. 5.7b it can be demonstrated that the transmission coefficient of a lossless two-port network obtained by cascading *N* UEs, as shown in Fig. 5.7a, satisfies [21], [22], [32]:

$$S_{21}(t) = \frac{(1-t^2)^{N/2}}{P_N(t)} \tag{5.48}$$

where $P_N(t)$ is a strictly Hurwitz polynomial in t of order N (a polynomial with real positive coefficients and all its roots in the open left half plane, $\mathrm{Re}(t) < 0$), and $|S_{21}(t = j\Omega)| \leq 1$.

Inspecting (5.47) and (5.48) it can be seen that each UE produces a half-order transmission zero at $t = \pm 1$. Other transmission zeros (even at infinity) are not possible with this structure [22], [31]. Therefore in order to implement the classical all-pole functions (Butterworth, Chebyshev, Zolotarev,…), which have all the transmission zeros at infinity, a mapping must be first applied to move all the transmission zeros of the all-pole function from $s = \pm j\infty$ to $t = \pm 1$ [22]. Starting from the normalized all-pole transfer function (with cutoff frequency $\omega_c = 1$ rad/s, see Fig. 5.8), the following mapping function is applied:

$$\omega = \frac{\sin\theta}{\sin\theta_c} = \alpha \cdot \sin\theta \tag{5.49}$$

where θ_c is the electrical length of the commensurate lines at the cutoff frequency and $\alpha = 1/\sin\theta_c$. Then the Richards' transformation is employed in the form of (5.40), and using $\omega = s/j$ to perform the analytic continuation to the complex frequency plane s, and taking advantage of the identity $\sin\theta = \tan\theta/\sqrt{1+\tan^2\theta}$, it results [22],:

$$s = \frac{\alpha \cdot t}{\sqrt{1-t^2}} \tag{5.50}$$

$$t = \frac{\pm s}{\sqrt{\alpha^2 + s^2}} \tag{5.51}$$

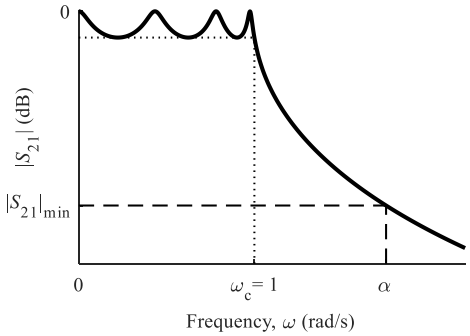

Fig. 5.8. Frequency response of the normalized all-pole Chebyshev function taken as example. The transmission value obtained at $\omega = \alpha$ is labeled $|S_{21}|_{min}$, since it will correspond to the minimum transmission (maximum attenuation) achieved by the commensurate-line distributed prototype.

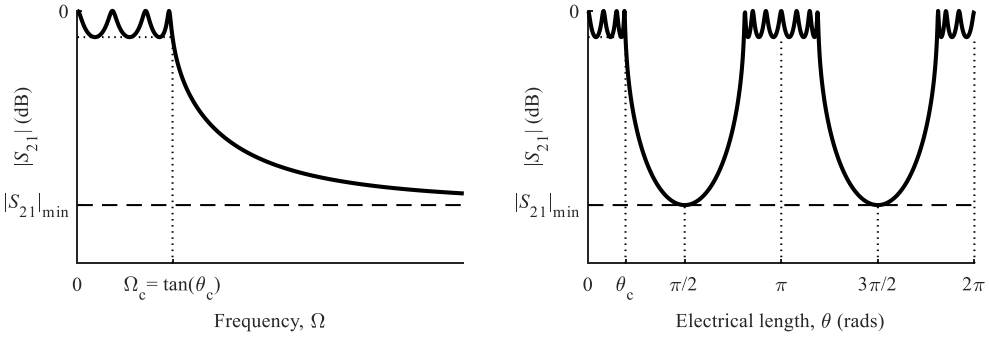

Fig. 5.9. Frequency response of the commensurate–line distributed Unit Element prototype of Fig. 5.5 and Fig. 5.7 for the all-pole Chebyshev function of Fig. 5.8 (taken as example). a) $|S_{21}|$ in the Richards' transform domain, as a function of the frequency axis $t = j \cdot \Omega$. b) $|S_{21}|$ in the natural frequency domain, as a function of the electrical length of the commensurate lines (or UEs), θ.

As it can be seen, by changing the complex frequency variable *s* of the all-pole transfer function $S_{21}(s) = 1/P'_N(s)$ to t using (5.50), the half-order transmission zeros at $t = \pm 1$ are introduced, replacing the original transmission zeros at infinity, and obtaining a transfer function of the form of (5.48) as intended [22]. The order of the all-pole transfer function, *N*, is equal to the number of UEs required for the implementation. The resulting frequency responses are shown in Fig. 5.9 for the all-pole Chebyshev function taken as example.

The frequency responses are given in the Richards' transform domain (in the frequency axis $t = j\Omega$), and in the natural frequency domain (as a function of the electrical length of the commensurate lines, θ), with both frequency axes related through (5.41). Additionally, they are related to the normalized frequency response of Fig. 5.8 through (5.49). As it can be seen, the passband characteristics are identical to those of the normalized frequency response of Fig. 5.8 (equiripple responses with identical ripple levels in our Chebyshev case), with a cutoff frequency of $\Omega_c = \tan(\theta_c)$ in the Richards' domain, and θ_c in the natural frequency domain (electrical length axis). Moreover, the maximum attenuation (minimum transmission $|S_{21}|_{min}$) is achieved for $\Omega \longrightarrow \infty$ (in the Richards' domain) and for $\theta = \pi/2$ (in the natural frequency domain). The maximum attenuation value is equal to the attenuation of the normalized all-pole transfer function at the frequency $\omega = \alpha = 1/\sin\theta_c$, see (5.49) and Fig. 5.8. Beyond $\theta = \pi/2$ the frequency response repeats periodically (as indicated by (5.41), taking into account that the frequency responses will have Hermitian symmetry, $S_{21}(-\Omega) = S_{21}^*(\Omega)$), and as it happens in any commensurate distributed network. Equivalent methods to implement all-pole functions with commensurate–line distributed UE networks of the form of Fig. 5.5 and Fig. 5.7 are proposed in [21], [31], [32], [39], relying all of them on mapping functions of the form of (5.49).

Once the required transfer function in the Richards' transform plane, $S_{21}(t)$, fulfilling (5.48) is chosen, the values (characteristic impedances) of the UEs that form the commensurate-line distributed prototype (see Fig. 5.7a) can be calculated.

5.2.1.1. Determination of the Unit Elements of the Commensurate-Line Prototype

Different methods can be employed to perform the calculations of the Unit Elements of the low-pass commensurate-line filter prototype. In this section, the two most widely employed will be thoroughly explained.

The first method is based on the iterative application of the Richards' theorem, which allows us to extract the UEs sequentially from the input impedance of the network, leaving a

remainder impedance after each extraction [31], [32], [37]. The second method is easier to program and is based on the iterative extraction of the UEs from the transfer matrix [ABCD] of the network, leaving a remainder transfer matrix after each extraction [22].

In both cases, the first task is to determine the frequency response in reflection defined in the complex Laplace frequency plane, $s = \sigma + j \cdot \omega$, i.e. $S_{11}(s)$. This frequency response must be normalized with $\omega_c = 1\ \mathrm{rad/s}$ and $R_g = 1\ \Omega$. In order to reach the $S_{11}(s)$, two different approaches can be employed.

The first way to determine $S_{11}(s)$ requires the frequency response in transmission also defined in the Laplace s plane, with identical normalization ($\omega_c = 1\ \mathrm{rad/s}$ and $R_g = 1\ \Omega$), i.e. $S_{21}(s)$. The $S_{11}(s)$ and $S_{21}(s)$-parameters of a lossless network must fulfill the following condition [22]:

$$|S_{11}(s = j\omega)|^2 + |S_{21}(s = j\omega)|^2 = 1 \tag{5.52}$$

The relationship (5.52) can be alternatively expressed as:

$$S_{11}(s = j\omega) \cdot S_{11}(s = j\omega)^* = 1 - S_{21}(s = j\omega) \cdot S_{21}(s = j\omega)^* \tag{5.53}$$

Then, $S_{11}(s)$ can be obtained from (5.53) by performing the analytic continuation to the complex Laplace frequency plane, s, by using $\omega = s/j$.

The alternative method to obtain $S_{11}(s)$ is based on the values $g_1, g_2, \ldots, g_N, g_{N+1}$ of the lumped-element LC ladder network that conforms the low-pass filter prototype of order N with $\omega_c = 1\ \mathrm{rad/s}$ and $R_g = 1\ \Omega$, which can be found in numerous textbooks like [13], [20], [22], [38], or using several software tools like *Keysight Genesys* or *Filsyn*, among others. The input impedance in the complex s plane, $Z_{in}(s)$, can be deduced from the LC network following the scheme shown in Fig. 5.10.

Once $Z_{in}(s)$ is achieved, the sought $S_{11}(s)$-parameter can be finally determined with the following expression:

$$S_{11}(s) = \frac{Z_{in}(s) - 1}{Z_{in}(s) + 1} \tag{5.54}$$

Now that the $S_{11}(s)$ has been calculated following one of the procedures explained, it must be expressed as the ratio of the N-degree polynomials $F(s)$ and $E(s)$ as:

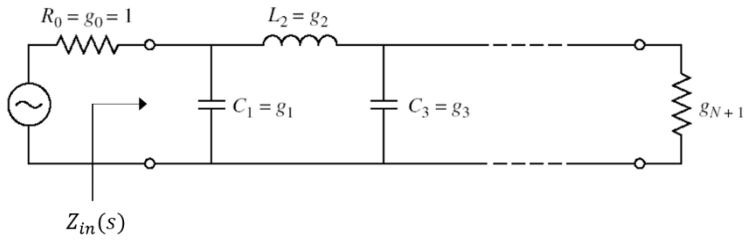

(a)

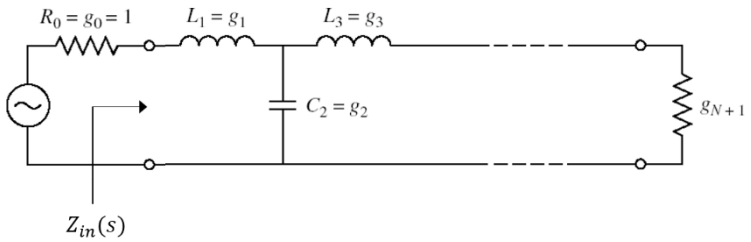

(b)

Fig. 5.10. Definition of the *LC* ladder network of the low-pass filter prototype. There are two dual implementations for the same response with equal magnitude an opposite phase. (a) First option: the first element is a shunt capacitor and (b) second option: the first element is a series inductor.

$$S_{11}(s) = \frac{F(s)}{E(s)} \tag{5.55}$$

The roots of $F(s)$ and $E(s)$ must be extracted and subsequently mapped into the Richards' transform plane using (5.51) and (5.49), allowing us to reconstruct the polynomials $F(t)$ and $E'(t)$ that define $S_{11}(t)$ as [22]:

$$S_{11}(t) = \frac{F(t)/\varepsilon_{Rt}}{E'(t)} \tag{5.56}$$

being ε_{Rt} the constant lost when reconstructing the polynomials with their roots, that can be recovered as:

$$\varepsilon_{Rt} = \frac{\varepsilon_t}{\sqrt{\varepsilon_t^2 - 1}} \tag{5.57}$$

and

$$\varepsilon_t = \frac{(1-t^2)^{\frac{N}{2}}}{\left(\sqrt{1-10^{-RL/10}}\right)\cdot |E'(t)|}\Bigg|_{t=t_c} \tag{5.58}$$

where $t_c = j \cdot tan\,\theta_c$, RL is the required return loss level in dB, and N is the order of the filter.

At this point, is where the two methods for the calculation of the UEs begin to differ, even though the final result is the same.

The first method is based on the iterative application of the Richards' theorem [31], [32], [37], and in order to use it the input impedance in the Richards' transform plane, $Z_{in}(t)$, must be deduced from $S_{11}(t)$ as:

$$Z_{in}(t) = \frac{1 + S_{11}(t)}{1 - S_{11}(t)} \tag{5.59}$$

Following the Richards' theorem, the characteristic impedance of the first UE, Z_1 (see Fig. 5.7a), can be calculated from $Z_{in}(t)$ as follows:

$$Z_1 = Z_{in}(t)|_{t=1} \tag{5.60}$$

Moreover, the residual impedance of the network, $Z'_{in}(t)$, after having extracted the first UE with value Z_1 will be given by:

$$Z'_{in}(t) = Z_1 \cdot \frac{t \cdot Z_1 - Z_{in}(t)}{t \cdot Z_{in}(t) - Z_1} \tag{5.61}$$

Then, the impedance of the second UE can be calculated from $Z'_{in}(t)$, yielding to a new residual impedance. If we proceed iteratively, i.e. extracting the UE impedances with (5.60) from the residuals of (5.61), we will find a common factor of the form $(t^2 - 1)$ in both, numerator and denominator, that will be cancelled between each other. Hence, the order of the residual impedance, $Z'_{in}(t)$, will be reduced in a unity at each UE impedance extraction. The procedure finishes when $Z'_{in}(t) = R_L$, i.e. the output impedance of the UE prototype, see Fig. 5.7a. It is important to notice that the UE prototype obtained is normalized in impedance (it has been calculated assuming $R_g = 1\,\Omega$) and therefore all the impedances must be multiplied by Z_S in order to obtain the final denormalized UE prototype of Fig. 5.7a.

The second method for the calculation of the characteristic impedances of the UEs is based on the iterative extraction of each UE from the transfer matrix [ABCD] of the network [22]. From the $S_{11}(t)$ definition of (5.56), the polynomials $A(t)$, $B(t)$, $C(t)$, and $D(t)$ are calculated from the coefficients of $E'(t)$, e_i, and $\frac{F(t)}{\varepsilon_{Rt}}$, f_i, with $i = 0, \dots, N$, as:

$$A(t) = (e_0 + f_0) + (e_2 + f_2) \cdot t^2 + (e_4 + f_4) \cdot t^4 + \cdots \tag{5.62}$$

$$B(t) = (e_1 + f_1) \cdot t + (e_3 + f_3) \cdot t^3 + (e_5 + f_5) \cdot t^5 + \cdots \tag{5.63}$$

$$C(t) = (e_1 + f_1) \cdot t + (e_3 + f_3) \cdot t^3 + (e_5 + f_5) \cdot t^5 + \cdots \tag{5.64}$$

$$D(t) = (e_0 + f_0) + (e_2 + f_2) \cdot t^2 + (e_4 + f_4) \cdot t^4 + \cdots \tag{5.65}$$

It is worth noting that $A(t)$ and $D(t)$ will be even polynomials, and $B(t)$ and $D(t)$ will be odd polynomials for N even, and vice versa for N odd.

The characteristic impedance of the first UE, Z_1, will be calculated as follows:

$$Z_1 = \left.\frac{A(t)}{C(t)}\right|_{t=1} = \left.\frac{B(t)}{D(t)}\right|_{t=1} \tag{5.66}$$

Next, the residual network will be given by the residual polynomials $A_{res}(t)$, $B_{res}(t)$, $C_{res}(t)$, and $D_{res}(t)$ that can be obtained with the expressions (5.67)-(5.70) provided here:

$$A_{res}(t) = \frac{A(t) - t \cdot Z_1 \cdot C(t)}{1 - t^2} \tag{5.67}$$

$$B_{res}(t) = \frac{B(t) - t \cdot Z_1 \cdot D(t)}{1 - t^2} \tag{5.68}$$

$$C_{res}(t) = \frac{C(t) - \frac{t}{Z_1} \cdot A(t)}{1 - t^2} \tag{5.69}$$

$$D_{res}(t) = \frac{D(t) - \frac{t}{Z_1} \cdot B(t)}{1 - t^2} \tag{5.70}$$

where all numerators of (5.67)-(5.70) will have a common factor of $(1 - t^2)$ and hence, this term will be eliminated from the $A_{res}(t)$, $B_{res}(t)$, $C_{res}(t)$, and $D_{res}(t)$ polynomials.

Then, if we proceed iteratively, the characteristic impedances of the rest of the UEs will be calculated from the residual networks until the latter will only contain the output impedance of the filter, see Fig. 5.7a. The value of the output impedance can be easily calculated as $R_L = (e_0 + f_0)/(e_0 - f_0)$. Again, it is important to highlight that the UE prototype obtained is normalized in impedance (it has been calculated assuming $R_g = 1\ \Omega$) and therefore all the

impedances must be multiplied by Z_S in order to obtain the final denormalized UE prototype of Fig. 5.7a.

To finish this section, it is important to note that the values of the UEs can be also calculated using commercial software tools, like *Keysight Genesys S/Filter* or *Filsyn*, among others.

5.2.2. Determination of the Target Response for the Synthesis

In the previous section, a commensurate-line distributed UE prototype has been obtained fulfilling the required frequency specifications. The prototype is formed by a cascade of N transmission line sections, all of them with the same electrical length and different characteristic impedances, see Fig. 5.5. From this stepped-impedance prototype, a filter with smooth profile will be obtained while retaining similar length and physical dimensions to those of the original UE prototype.

The time/frequency response of the commensurate-line UE prototype will be modified using a bandlimited interpolation procedure, that will be presented in both τ and β domains, producing a target $F(\tau)$ and $S_{11}(\beta)$ responses corresponding to a smooth-profiled filter, that will be subsequently synthesized using the CLP technique.

5.2.2.1. Determination of the Target Response in the τ Domain

The method to calculate the Unit Elements of the starting commensurate-line prototype has been thoroughly detailed in the previous section 5.2.1. In order to synthetize a smooth-profiled low-pass or band-pass filter without spurious rejection bands using the CLP synthesis, the UE prototype response in the τ domain will be firstly calculated. Then it will be carefully modified exploiting properties of the relationship between the impulse response and the frequency response of a linear time-invariant device. In order to ease the explanation of the procedure followed, the simplest case where the filter is implemented in ideal transmission line technology will be initially considered. Next, the more complex case of implementation in waveguide technology will be studied.

5.2.2.1.1. Case of Ideal Transmission Line Technology

For the case of ideal transmission line, the phase velocity, v_p, does not vary with frequency, and it represents the propagation velocity along the line-sections of the UE prototype. All the commensurate (same electrical length) line-sections will have the same physical length l, see (5.42), and the propagation time through a line-section will be l/v_p. Therefore, the impulse response, $h_{UE}(t)$, of the UE prototype (the time domain response to an impulse or Dirac delta function, $\delta(t)$) will be an impulse train formed by a sequence of equidistant impulses separated T seconds apart, see Fig. 5.11a:

$$h_{UE}(t) = \sum_{n=0}^{\infty} a_n \cdot \delta(t - nT) \tag{5.71}$$

where $T = 2 \cdot l/v_p$ is the time taken by the impulse to go through a line-section, multiplied by 2. The form of the impulse response given in (5.71) is valid for the transmission and reflection responses of the UE prototype, and it can be easily verified by "following" the propagation of the input impulse $\delta(t)$ through the UE prototype, as it reflects and transmits at the junctions between the line-sections with different characteristic impedances, see Fig. 5.5. The transmission impulse response would also include an initial propagation delay. The coefficients of the impulses in (5.71), a_n, could be seen as samples of an underlying continuous impulse response, $h_c(t)$, multiplied by T as:

$$a_n = h_c(t = nT) \cdot T \tag{5.72}$$

In this way, the frequency response of the UE prototype, $S_{11,UE}(\omega)$, can be expressed as a periodic replication and superposition of the frequency response corresponding to the underlying continuous impulse response, $S_{11,c}(\omega)$ [12], [16]:

$$S_{11,UE}(\omega) = \sum_{n=-\infty}^{\infty} S_{11,c}(\omega + 2\omega_0 n) \tag{5.73}$$

where

$$\omega_0 = \frac{\pi}{T} \tag{5.74}$$

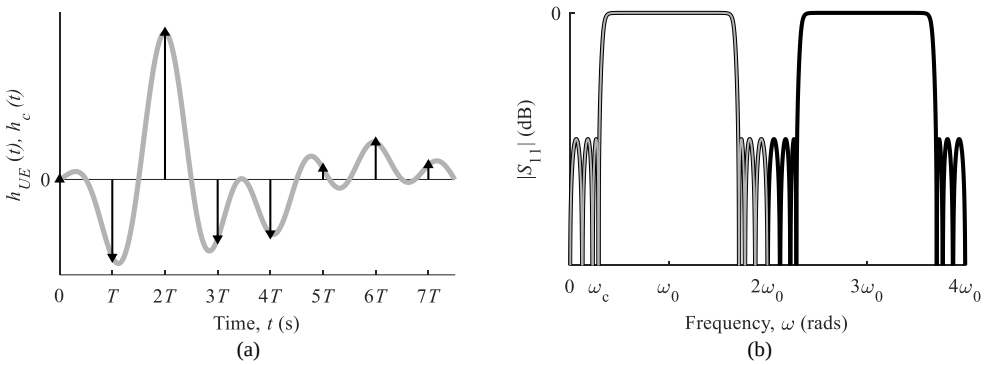

Fig. 5.11. Responses in the time and frequency domains for the case of ideal transmission line. (a) Impulse response in reflection of the Unit Element prototype, $h_{UE}(t)$, formed by a sequence of equidistant impulses (black line), and underlying continuous impulse response, $h_c(t)$, obtained by performing an ideal bandlimited interpolation with $m = 2$ (grey line). (b) Frequency response in reflection of the UE prototype periodic in ω (black line), and frequency response corresponding to the continuous impulse response obtained by performing an ideal bandlimited interpolation with $m = 2$ (grey line).

Actually, as it is shown in Fig. 5.11b for $S_{11}(\omega)$, the frequency response of the UE prototype will be periodic in ω, since it is periodic in θ (see Fig. 5.9), and the constant v_p and l of our transmission line case will make it also periodic in ω, see (5.42). Thus, the frequency response of the UE prototype can be seen indeed as the periodic replication and superposition of (5.73).

Additionally, by applying the sampling theorem [12], performing an ideal bandlimited interpolation of the UE prototype impulse response of (5.71), the underlying continuous $h_c(t)$, see Fig. 5.11a, can be calculated as [12], [16]:

$$h_c(t) = \sum_{n=-\infty}^{\infty} a_n \cdot \frac{\sin\big(\omega_{max}(t - nT)\big)}{\pi(t - nT)} \tag{5.75}$$

where ω_{max} is the maximum frequency of the interpolated impulse response, $h_c(t)$, in the sense that its frequency response, $S_{11,c}(\omega)$, is equal to $S_{11,UE}(\omega)$ up to ω_{max}, and zero beyond that frequency. In the classical ideal bandlimited interpolation $\omega_{max} = \pi/T = \omega_0$ [12], [16]. However, in our case of interpolating the UE prototype impulse response, $h_{UE}(t)$, to obtain a continuous $h_c(t)$ to synthesize a filter with smooth profile, it is possible and more convenient to take $\omega_{max} = m \cdot \omega_0$, with m integer, where $m = 2$ will be used to implement a low-pass filter, see Fig. 5.11b, and $m = 4$ could be taken to implement a band-pass filter. The introduction of the m factor in ω_{max} can be compensated in (5.75) simply by introducing the same factor in a_n as:

$$a_n = h_c(t = nT) \cdot T/m \tag{5.76}$$

For the case studied in this subsection of ideal transmission line technology (phase velocity, v_p, constant with frequency), a simple and direct relationship can be stablished between the inverse Fourier Transform pair of the form:

$$F(\tau) = \frac{1}{2\pi}\int_{-\infty}^{\infty} S_{11}(\beta) \cdot e^{j\beta\tau} \cdot d\beta \tag{4.11}$$

and the classical time-frequency pair. Actually, by applying the Fourier Transform property of time and frequency scaling [12], [40], it can be obtained:

$$v_p \cdot F(v_p \cdot t) \leftrightarrow S_{11}\left(\frac{\omega}{v_p}\right) \tag{5.77}$$

since $\beta = \omega/v_p$ and v_p is a positive real constant. Therefore, the impulse response in reflection will satisfy $h(t) = v_p \cdot F(v_p \cdot t)$ and $\tau = v_p \cdot t$, and from (5.71) it can be deduced that the impulse response of the commensurate-line prototype in the τ domain, $F_{UE}(\tau)$, will have the form (see Fig. 5.12a):

$$F_{UE}(\tau) = \sum_{n=0}^{\infty} a_n \cdot \delta(\tau - nT_\tau) \tag{5.78}$$

since $\delta(v_p \cdot t) = \delta(t)/v_p$, where $T_\tau = v_p \cdot T$:

$$T_\tau = 2 \cdot l \tag{5.79}$$

being l the physical length of the commensurate-line sections of the UE prototype. Additionally, by employing the relationships that have been obtained, the ideal bandlimited interpolation of (5.75) can be rewritten for $F_{UE}(\tau)$, giving rise to the continuous underlying response, $F_c(\tau)$, as:

$$F_c(\tau) = \sum_{n=-\infty}^{\infty} a_n \cdot \frac{\sin\left(\beta_{max}(\tau - nT_\tau)\right)}{\pi(\tau - nT_\tau)} \tag{5.80}$$

where

$$\beta_{max} = m \cdot \beta_0 \tag{5.81}$$

with m integer and $\beta_0 = \omega_0/v_p$ defined from (5.74) as:

$$\beta_0 = \frac{\pi}{T_\tau} \tag{5.82}$$

and the coefficients of the impulses in (5.78), a_n, satisfying a similar relationship to that of (5.76):

$$a_n = F_c(\tau = nT_\tau) \cdot T_\tau/m \tag{5.83}$$

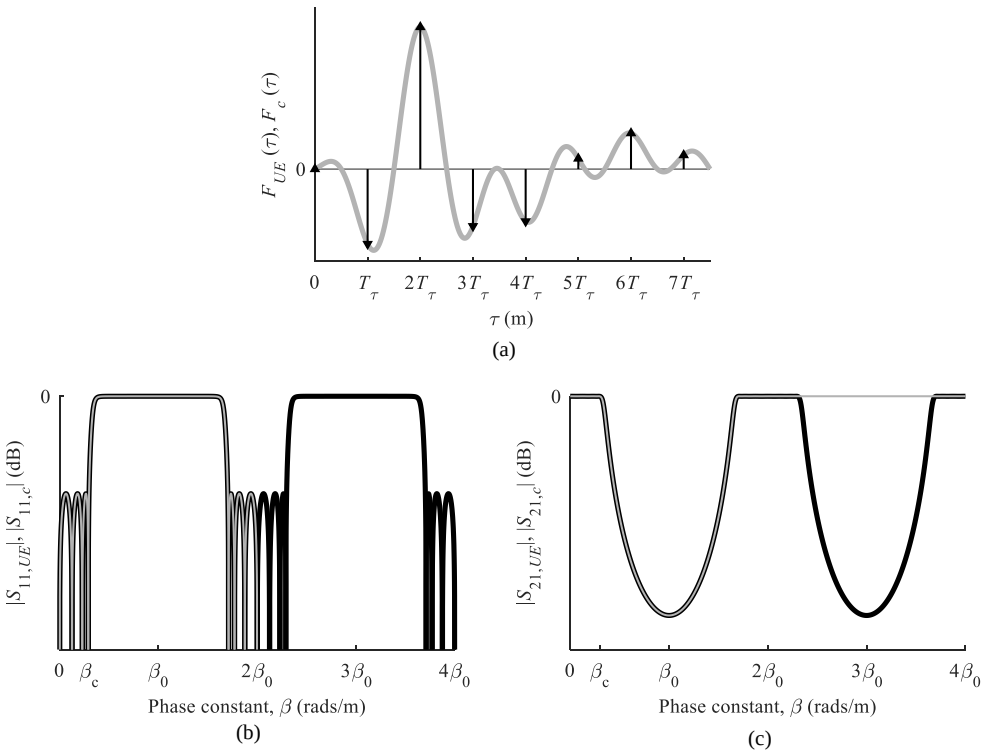

Fig. 5.12. Responses in the τ and β domains for the cases of ideal transmission line and rectangular waveguide. (a) Impulse response in reflection of the Unit Element prototype, $F_{UE}(\tau)$, formed by a sequence of equidistant impulses (black line), and underlying continuous impulse response, $F_c(\tau)$, obtained by performing an ideal bandlimited interpolation with $m = 2$ (grey line). Periodic frequency responses of the UE prototype (black lines) and the resulting response from the application of a bandlimited interpolation procedure with $m = 2$ (grey lines) in β: (b) in reflection, $|S_{11}|$-parameters, and (c) in transmission, $|S_{21}|$-parameters (grey line).

Thus, by interpolating the impulse response in reflection of the UE prototype of (5.78), as shown in (5.80), a continuous $F_c(\tau)$ is obtained to synthesize a filter with smooth profile whose frequency response in reflection, $S_{11,c}(\beta)$, is identical to that of the UE prototype up to β_{max}, and zero beyond that frequency (see Fig. 5.12b). The coefficients of the impulses in (5.78), a_n, are equal to those of (5.71) (identical impulse coefficients in the time and τ domains), and they can be easily calculated from the characteristic impedances of the UE prototype, Z_i, see section 5.2.2.1.3.

Finally, it is worth noting that $S_{11,c}(\beta)$ can be obtained by performing the Fourier Transform of (4.12) for $F_c(\tau)$, i.e.:

$$S_{11,c}(\beta) = \int_{-\infty}^{\infty} F_c(\tau) \cdot e^{-j\beta\tau} \cdot d\tau \tag{5.84}$$

It is important to highlight that the $S_{11,c}(\beta)$ obtained as a result of (5.84) will be the same that is obtained by following the alternative procedure that will be detailed in section 5.2.2.2.

5.2.2.1.2. Case of Rectangular Waveguide Technology

In the case of rectangular waveguide technology, the fundamental TE_{10} mode will be employed, keeping the width of the waveguide constant, and varying its height along the device. In this way, the phase constant, β, will not vary along the filter, and will remain constant for a given frequency [38]. Consequently, the frequency response of the UE prototype that is periodic in θ (see Fig. 5.9b) will be also periodic in β, as it can be easily deduced from (5.42), with all the line-sections having the same physical length, l. Thus, the frequency response of the UE prototype will have the form of Fig. 5.12b and Fig. 5.12c, and can be seen as a periodic replication and superposition in β of the form of (5.73), where ω is substituted by β:

$$S_{11,UE}(\beta) = \sum_{n=-\infty}^{\infty} S_{11,c}(\beta + 2\beta_0 n) \tag{5.85}$$

Therefore, the impulse response of the UE prototype in the τ domain, $F_{UE}(\tau)$, will have the form of Fig. 5.12a, with an expression given by (5.78), (5.79), where the coefficients of the impulses, a_n, can be seen as samples of an underlying continuous impulse response, $F_c(\tau)$, satisfying (5.83). By applying the ideal bandlimited interpolation of (5.80), a continuous impulse response $F_c(\tau)$ is obtained (see Fig. 5.12a), corresponding to a rectangular waveguide filter with smooth profile. The resulting filter will have a length and profile excursion similar to those of the UE prototype, with a frequency response $S_{11,c}(\beta)$ identical to that of the UE prototype up to

β_{max}, and zero beyond that frequency. The value of β_{max} is fixed through (5.81) and (5.82), where $\beta_{max} = 2 \cdot \beta_0$ is taken to implement a low-pass filter ($m = 2$), and $\beta_{max} = 4 \cdot \beta_0$ could be used to implement a band-pass filter ($m = 4$). The introduction of the m factor in β_{max} must be formally compensated in (5.85) by introducing a $1/m$ factor on the right-hand side of the equation.

As it can be seen, the equations employed to modify the UE prototype response to subsequently synthesize a filter with smooth profile, are identical in the case of rectangular waveguide and ideal transmission line. This is due to the fact that both technologies produce UE prototypes with frequency responses $S_{11,UE}(\beta)$ periodic in β, and impulse responses $F_{UE}(\tau)$ formed by a sequence of equidistant impulses in τ, that can be interpolated using the same procedure and equations. In the same way, the coefficients of the impulses of $F_{UE}(\tau)$, a_n, can be calculated from the Z_i's of the UE prototype (see section 5.2.2.1.3) using also identical procedures for the case of rectangular waveguide and for ideal transmission line. It is interesting to note, however, that the expressions for the impulse response in the time domain (5.71), the frequency response in the frequency domain ω (5.73), and of course the interpolation in the time domain (5.75), are not valid for rectangular waveguide technology due to its inherent dispersion (phase velocity v_p variable with frequency). However, the corresponding expressions in the τ and β domains are indeed valid as it has been explained, and they will be the equations employed for our inverse scattering synthesis procedure.

5.2.2.1.3. Calculation of the Impulse Response in Reflection of the Commensurate-Line Unit Element Prototype

The impulse response in reflection of the commensurate-line UE prototype of Fig. 5.5 and Fig. 5.7a can be readily calculated from the values of the characteristic impedances, Z_i, of the prototype. If an ideal excitation impulse $\delta(t)$ in the time domain (please note that in this section *t* is used as the time variable) is assumed for the input port, which is equivalent to consider a $\delta(\tau)$ for the τ domain, the resulting impulse response in reflection will consist on a sequence of equidistant impulses, $a_n \cdot \delta(t - n \cdot T)$ or $a_n \cdot \delta(\tau - n \cdot T_\tau)$, where the coefficients a_n are identical in the t and τ domains, as it was demonstrated in the previous section 5.2.2.1.1. These coefficients, a_n, can be calculated following the method detailed below.

The procedure is based on the fact that a wave injected at the input port of the commensurate-line UE prototype will be scattered by each discontinuity encountered while

propagating throughout the structure. As it is shown in Fig. 5.5 and Fig. 5.7a, the prototype can be represented as a cascade of N commensurate lines, or UEs, all with the same electrical length, $\theta = \beta l$, but with different characteristic impedances, Z_i, plus an additional input and output line-section with the port impedances, named as $Z_0 = Z_S$ and $Z_{N+1} = Z_L$ for our calculations, see Fig. 5.13. At the junction between two commensurate lines with different characteristic impedances Z_{j-1} and Z_j a discontinuity will arise, giving rise to a reflection and a transmission coefficient for the impinging wave with values [38]:

$$\Gamma_{j-1,j} = \frac{Z_j - Z_{j-1}}{Z_j + Z_{j-1}} \tag{5.86}$$

$$T_{j-1,j} = 1 + \Gamma_{j-1,j} = \frac{2 \cdot Z_j}{Z_j + Z_{j-1}} \tag{5.87}$$

Thus, wave propagation along the analyzed prototype can be described in terms of an infinite sum of the transmitted and reflected waves at each junction between two consecutive commensurate lines, taking into account the multiple reflection and transmission events arising throughout the structure.

If the incident wave at the input port of the prototype is a unit impulse, then the impulse response will be obtained. We are interested in calculating the impulse response in reflection, in the time or τ domain. For doing so, we need to calculate the coefficients a_n of the impulse train. In order to determine them, we are going to define a time index, i, with time $t = i \cdot l/v_p$ for ideal transmission line, and $\tau = i \cdot l$ for the more general case of β constant with position. Additionally, the number of the commensurate line will be represented by the j index, including the input and output port lines, numbered 0 and $N + 1$, respectively, see Fig. 5.13. The forward travelling impulses are tracked just at the end of the commensurate lines and are represented at the F columns. The backward travelling impulses are tracked just at the beginning of the commensurate lines and are represented at the B columns. The straight and dashed arrows represent the transmission and reflection events, respectively. The circles, on the other hand, represent each contribution to the tracked impulses, see Fig. 5.13. It is interesting to note that a forward travelling impulse, when reflected, produces a new backward travelling impulse, and when transmitted a new forward travelling impulse. Conversely, a backward travelling impulse, when reflected, produces a new forward travelling impulse, and when transmitted a new backward travelling impulse. These reflection and transmission calculations will be the core of the algorithm employed to obtain the impulse response in reflection of the prototype. The algorithm is described now in detail.

- *Step* 1: Initialize the coefficients of the forward and backward travelling impulses tracked in the calculations, assuming excitation by a unit impulse at the input port.

//for all the considered time instants
$\forall i = 0, 1, \ldots, i_{max}$
//for all the commensurate lines
$\forall j = 0, 1, \ldots, (N + 1)$
//coefficients of forward traveling impulses
$F(i, j) = 0$
//coefficients of backward travelling impulses
$B(i, j) = 0$
//unit impulse injected at the input port
$F(i = 1, j = 0) = 1$

- *Step* 2: Propagation and scattering (reflection and transmission) of the impulses, through the commensurate line prototype and the time or τ domain.

//for all the considered time instants
For $i = 1, 2, \ldots, (\, i_{max} - 1)$
{
//for all the commensurate lines
For $j = 0, 1, \ldots, N$
{
//contributions of the forward travelling impulse, with
//coefficient $F(i, j)$, located at the i time instant at the end of
//the j commensurate line, for the next $i + 1$ time instant
$F(i + 1, j + 1) = F(i + 1, j + 1) + F(i, j) \cdot T_{j,j+1}$
$B(i + 1, j) = B(i + 1, j) + F(i, j) \cdot \Gamma_{j,j+1}$
//contributions of the backward travelling impulse, with
//coefficient $B(i, j)$, loc. at the i time instant at the beginning
//of the j commensurate line, for the next $i + 1$ time instant
If $j \neq 0$
{$F(i + 1, j) = F(i + 1, j) + B(i, j) \cdot \Gamma_{j,j-1}$
$B(i + 1, j - 1) = B(i + 1, j - 1) + B(i, j) \cdot \mathrm{T}_{j,j-1}$}
}
}

- *Step* 3: Extract the impulse response in reflection of the analyzed prototype, formed by a sequence of equidistant impulses, separated $T = 2 \cdot l/v_p$ or $T_\tau = 2 \cdot l$, by recovering the values of the a_n coefficients.

```
//coefficients of the backward travelling impulses at the
//input line (j = 0), and at the even time instants, since in the
//algorithm t = i · l/v_p or τ = i · l
a_n = B(i = 2 · n, j = 0)
```

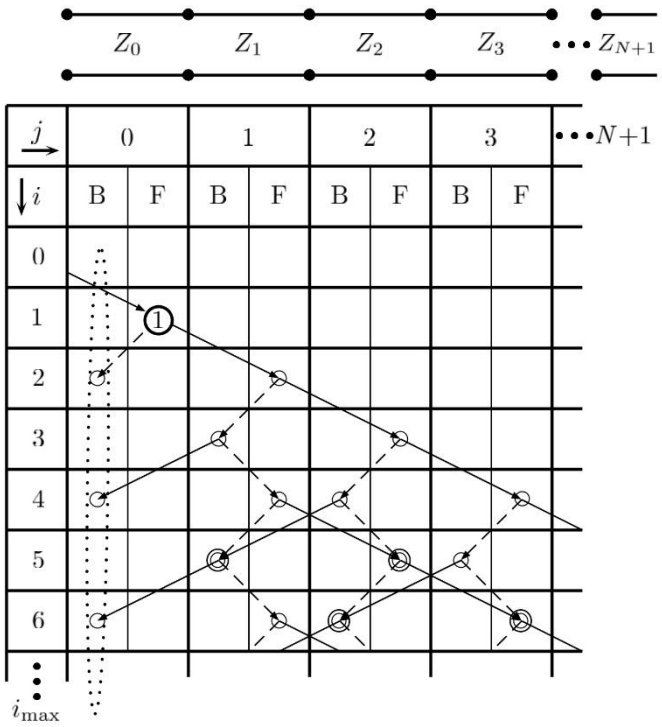

Fig. 5.13. Schematic representation for the algorithm to calculate the impulse response in reflection of the commensurate-line UE prototype shown above. A time index, i, with time $t = i \cdot l/v_p$ or $\tau = i \cdot l$, and a position index, j, where j is the number of commensurate line (including the input and output port lines, 0 and $N + 1$), are employed. The forward and backward travelling impulses are tracked just at the end and beginning of the commensurate lines, respectively, and are represented at the corresponding F and B columns. To obtain the impulse response, the prototype is excited with a unit impulse injected at the input port, $F(i = 1, j = 0) = 1$. Straight and dashed arrows represent the transmission and reflection events, respectively, while the circles represent each contribution to the tracked impulses. The sought impulse response in reflection is formed by a sequence of equidistant impulses, separated $T = 2 \cdot l/v_p$ or $T_\tau = 2 \cdot l$ apart, with coefficients a_n, encircled by a dotted line at the input port line $a_n = B(i = 2 \cdot n, j = 0)$.

5.2.2.2. Determination of the Target Response in the β Domain

Once the Unit Elements of the commensurate-line prototype have been determined by means of the procedure detailed in section 5.2.1, the necessary target frequency response for the synthesis of low-pass and band-pass filters, with smooth profile and without spurious rejection bands, can be directly calculated in the phase constant, β, domain.

The procedure is divided into two stages, where the first one consists in the deduction of the frequency response of the commensurate-line UE prototype, $S_{11,UE}(\beta)$, by means of the transmission matrix properties that were partially introduced in section 5.2.1. In a second step, the final target frequency response intended to be synthetized using the CLP method, $S_{11,c}(\beta)$, will be obtained by a simple numerical modification of the $S_{11,UE}(\beta)$.

5.2.2.2.1. Calculation of the Frequency Response in Reflection of the Commensurate-Line Unit Element Prototype

In order to obtain a valid frequency response in reflection for the synthesis, the first step will be to calculate the S_{11}-parameter of the starting classical commensurate-line UE prototype. For doing so, it will be necessary to consider the N UEs of the filter, as well as their corresponding transmission matrixes of Fig. 5.7. It will be possible to calculate the transmission matrix of the whole commensurate-line filter by multiplying the individual transmission matrices of its UEs (given by equation (5.47) in the Richards transform plane) as [38]:

$$\begin{pmatrix} A & B \\ C & D \end{pmatrix} = \prod_{i=1}^{N} \frac{1}{\sqrt{1-t^2}} \begin{bmatrix} 1 & Z_i \cdot t \\ \dfrac{t}{Z_i} & 1 \end{bmatrix} = (1-t^2)^{-\frac{N}{2}} \cdot \prod_{i=1}^{N} \begin{bmatrix} 1 & Z_i \cdot t \\ \dfrac{t}{Z_i} & 1 \end{bmatrix} \tag{5.88}$$

where Z_i is the characteristic impedance of the i-th UE.

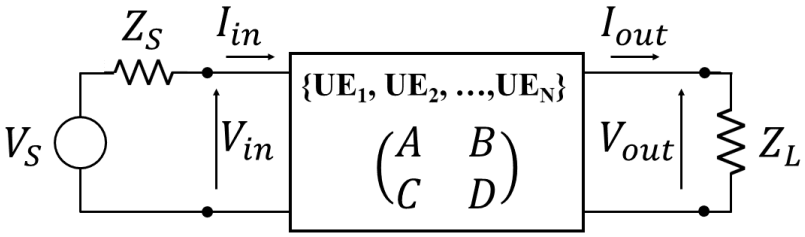

Fig. 5.14. Transmission matrix model of the whole commensurate line filter.

Therefore, the transmission matrix of the commensurate-line filter will follow the schematic of Fig. 5.14, and hence, it will be possible to define the input impedance of the filter, Z_{in}, as:

$$Z_{in} = \frac{V_{in}}{I_{in}} \tag{5.89}$$

Then, taking advantage of the definition of the transmission matrix given in (5.44) and (5.45), as well as of the result of (5.88), it will be possible to develop (5.89) as:

$$Z_{in}(t) = \frac{V_{in}(t)}{I_{in}(t)} = \frac{A(t) \cdot V_{out}(t) + B(t) \cdot I_{out}(t)}{C(t) \cdot V_{out}(t) + D(t) \cdot I_{out}(t)} \tag{5.90}$$

Moreover, in view of Fig. 5.14, it will be possible to relate V_{out} and I_{out} through the load impedance, Z_L, as:

$$I_{out} = \frac{V_{out}}{Z_L} \tag{5.91}$$

If the relationship of (5.91) is introduced in (5.90), it will be obtained that:

$$Z_{in}(t) = \frac{V_{in}(t)}{I_{in}(t)} = \frac{A(t) + \frac{B(t)}{Z_L}}{C(t) + \frac{D(t)}{Z_L}} = \frac{A(t) \cdot Z_L + B(t)}{C(t) \cdot Z_L + D(t)} \tag{5.92}$$

It is important to stress that the input impedance, Z_{in}, allows us to calculate the reflection coefficient at the input port, ρ_{in}, by considering a real characteristic impedance of the source (input port), Z_S, as (see Fig. 5.5 and Fig. 5.14):

$$\rho_{in}(t) = \frac{Z_{in}(t) - Z_S}{Z_{in}(t) + Z_S} \tag{5.93}$$

Moreover, the definition of the S_{11}-parameter is an special case of ρ_{in} when the output port is matched, something that will be accomplished when the load impedance is equal to the characteristic impedance of the output port, i.e. Z_L (see Fig. 5.5 and Fig. 5.14). Taking that into account in (5.92) and incorporating the result in (5.93), the S_{11}-parameter of the commensurate-line UE prototype, $S_{11,UE}$, will be deduced as:

$$S_{11,UE}(t) = \frac{\frac{A(t)\cdot Z_L + B(t)}{C(t)\cdot Z_L + D(t)} - Z_S}{\frac{A(t)\cdot Z_L + B(t)}{C(t)\cdot Z_L + D(t)} + Z_S} = \frac{A(t)\cdot Z_L + B(t) - Z_s\cdot[C(t)\cdot Z_L + D(t)]}{A(t)\cdot Z_L + B(t) + Z_s\cdot[C(t)\cdot Z_L + D(t)]} \tag{5.94}$$

Finally, the S_{11}-parameter of the commensurate-line UE prototype calculated in the Richards transform domain of (5.94) can be easily converted to the phase constant domain, β, by applying the previously studied transformations (5.40) and (5.42), i.e.:

$$S_{11,UE}(\beta) = S_{11,UE}(t = j\cdot\tan(\beta\cdot l)) \tag{5.95}$$

As example, the frequency response of a 7-th order low-pass Chebyshev commensurate-line UE filter is provided in Fig. 5.15.

It is worth noting that β_0 in Fig. 5.15 is the phase constant value that corresponds with the electrical length $\theta = \frac{\pi}{2}$ rad, see Fig. 5.9b. It is straightforward to demonstrate from (5.42) that the length of each transmission or waveguide line-section of the initial commensurate-line UE prototype can be related with β_0 as:

$$\theta_0 = \frac{\pi}{2} = \beta_0\cdot l \tag{5.96}$$

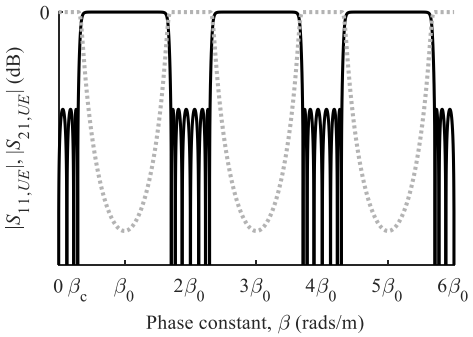

Fig. 5.15. Frequency response of the UE prototype periodic in β: in reflection, $|S_{11,UE}|$-parameter (black line), and in transmission, $|S_{21,UE}|$-parameter (grey dotted line)

The identity (5.96) allows us to express l as a function of the wavelength, λ_{g0}, that corresponds to β_0 in the waveguide. The relationship between β and λ_g is:

$$\beta = \frac{2 \cdot \pi}{\lambda_g} \tag{5.97}$$

According to (5.96) and (5.97), the length l will be:

$$l = \frac{\lambda_{g0}}{4} \tag{5.98}$$

Furthermore, taking advantage of the identity (5.96), it will be also possible to relate the cut-off phase constant of the filter, β_c, (see Fig. 5.15) with the electrical length θ_c (see Fig. 5.9b) of (5.49) as:

$$\theta_c = \frac{\pi}{2} \cdot \frac{\beta_c}{\beta_0} \tag{5.99}$$

5.2.2.2.2. Modification of the Frequency Response in Reflection of the Commensurate-Line Unit Element Prototype

Finally, as it was firstly demonstrated in [14] for planar technologies, it is possible to synthetize a smooth-profiled low-pass filter by performing simple modifications to the attained $S_{11,UE}(\beta)$. In [14] it was also shown how the physical dimensions featured by the synthetized filter are similar to those of the initial commensurate-line UE prototype in terms of device length and maximum and minimum values of the characteristic impedance. In order to provide the suitable target frequency response for the CLP synthesis method, the target $S_{11,c}(\beta)$ will be defined from $S_{11,UE}(\beta)$ as:

$$S_{11,c}(\beta) = \begin{cases} S_{11,UE}(\beta) \text{ , for } 0 \leq \beta \leq m \cdot \beta_0 \\ 0 \quad \text{ , for } \beta \geq m \cdot \beta_0 \end{cases} \tag{5.100}$$

where m is the same parameter that has been previously employed in section 5.2.2.1 for the bandlimited interpolation procedure carried out in the τ domain.

Therefore, the target low-pass response attained with $m = 2$ will only feature the fundamental stopband of $S_{11,UE}(\beta)$ centered at β_0, while the higher-order replicas will be

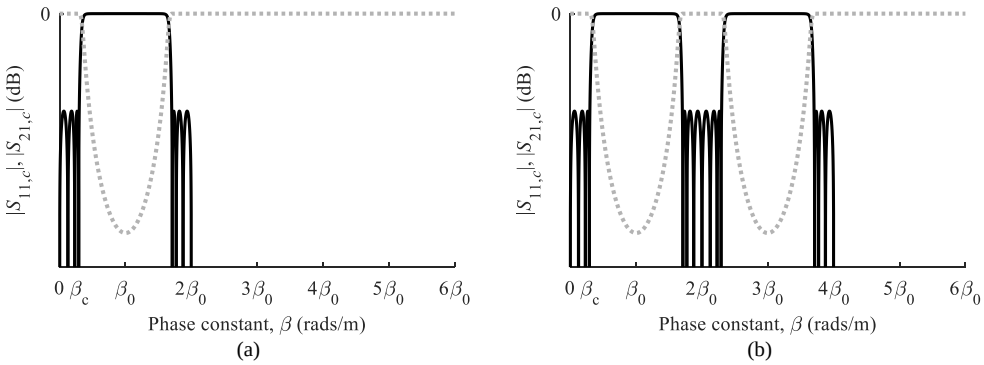

Fig. 5.16. Target frequency responses for an example of Chebyshev (a) low-pass and (b) band-pass filter to be synthetized: in reflection, $|S_{11}|$-parameter (black line), and in transmission, $|S_{21}|$-parameter (grey dotted line)

eliminated, as it is depicted in Fig. 5.16a. However, if $m = 4$ is taken, the associated band-pass filter response will be characterized by unique lower and upper stopbands centered at β_0 and $3 \cdot \beta_0$, respectively, while the center of the passband will be placed at $2 \cdot \beta_0$ (see Fig. 5.16b).

In order to conclude the present subsection devoted to the determination of the target frequency response to be synthesized using the CLP method, it must be stated that the method explained is valid for general all-pole frequency responses. The synthesis of this kind of responses will lead to waveguide structures that feature smooth variations of their cross-sections along the propagation direction.

Moreover, the target frequency responses that are achieved with this method can be also translated to the τ domain by performing the inverse Fourier transform of (4.11) to the $S_{11,c}(\beta)$:

$$F_c(\tau) = \int_{-\infty}^{\infty} S_{11,c}(\beta) \cdot e^{j\beta\tau} \cdot d\beta \tag{5.101}$$

The impulse response, $F_c(\tau)$, that results from (5.101) will match the response obtained from the bandlimited interpolation performed to the impulse response in reflection of the commensurate-line UE filter, $F_{UE}(\tau)$, as it was thoroughly explained in 5.2.2.1.

5.2.3. Microstrip Low-Pass Filter with Smooth Profile and without Spurious Rejection Bands

The filter design methodology carefully developed in the previous sections will be tested now with the practical design of a low-pass filter with smooth profile and without spurious stopbands in microstrip technology. The design requirements are the following: central frequency of the stopband $f_0 = 1$ GHz, maximum attenuation of 30 dB, cut-off frequency $f_c = 447.45$ MHz, and return loss level, $RL = 20$ dB. In order to satisfy these requirements, a canonical Chebyshev response will be employed. Following the procedure detailed in section 5.2.1, the first step is to determine the characteristic impedance of the starting N-th order classical commensurate-line UE filter.

It must be reminded that when dealing with microstrip technology, the relation between β and f will be determined by means of the expression (2.151), which is provided again below for the sake of convenience:

$$\beta = \frac{2 \cdot \pi \cdot f}{v_p} = \frac{2 \cdot \pi \cdot f}{c_0} \cdot \sqrt{\varepsilon_{eff}} \tag{2.151}$$

It is worth noting that ε_{eff} will eventually depend on the width of the upper conductor strip of the microstrip line along the propagation direction, $W(z)$, as well as on the characteristics of the substrate, a *Rogers RO3035*™ with thickness $h = 1.524$ mm, and dielectric constant $\varepsilon_r = 3.5$. Taking into account the provided substrate parameters, a line with 50 Ω characteristic impedance (that will be subsequently required for the input port) results in $\varepsilon_{eff} = 2.744$, see equations (2.149) and (2.152). In order to apply the modelling for technologies with β variable along the propagation axis, z, presented in section 2.2.2, a reference electrical permittivity, $\varepsilon_{eff,ref} = 2.744$, will be employed for the definition of a reference phase constant, $\beta_{ref} = \beta(f, \varepsilon_{eff,ref})$, that will be assumed to remain fixed along a normalized propagation axis, χ. In the last synthesis step, a denormalization of the propagation axis will be needed to compensate for the variations of ε_{eff} along the actual propagation axis. Therefore, from (2.151) it can be calculated that $\beta(f_0, \varepsilon_{eff,ref}) = 34.69$ rad/m and $\beta(f_c, \varepsilon_{eff,ref}) = 15.52$ rad/m. Then, the use of (5.99) will lead to $\theta_c = 0.703$ rad. Once the value of θ_c is known, the normalized frequency for the maximum rejection level, $\alpha = 1.547$ rad/s, can be deduced from (5.49).

The minimum filter order $N = 7$ for the Chebyshev response case that is required to satisfy the demanded performance can be calculated by means of the expression (5.102) as [14]:

$$N = \frac{\operatorname{acosh}\left(\sqrt{\left(\frac{1}{|S_{21}|^2_{min}} - 1\right) \cdot \left(10^{\frac{RL}{10}} - 1\right)}\right)}{\operatorname{asech}\left(\frac{1}{\alpha}\right)} \tag{5.102}$$

where $|S_{21}|_{min}$ is the minimum linear magnitude of the S_{21}-parameter that will be achieved at $\beta(f = f_0)$. Considering the required 30 dB value for the maximum rejection level, $|S_{21}|_{min} = 10^{(-30/20)}$.

Once both the order $N = 7$ and return loss level $RL = 20$ dB parameters have been determined, it is possible to reach the normalized all-pole Chebyshev response. Next, from the $\alpha = 1.547$ rad/s parameter and using (5.51), the normalized low-pass prototype is translated to the Richards transform domain. Then, applying the procedure detailed in section 5.2.1 and imposing a value of $Z_0 = 50\ \Omega$ for the input port, the characteristic impedance of each UE is deduced: $Z_1 = Z_7 = 34.61\ \Omega$, $Z_2 = Z_6 = 85.54\ \Omega$, $Z_3 = Z_5 = 22.40\ \Omega$, $Z_4 = 104.02\ \Omega$. The characteristic impedances of the commensurate-line UE prototype are depicted in Fig. 5.17.

The length of each commensurate-line section is $l = 4.528$ cm, being a value that can be calculated by means of (5.98) and (2.151) by considering $\varepsilon_{eff,ref} = 2.744$.

The frequency response of the 7th-order commensurate-line UE filter is computed by means of the transmission matrix multiplication method developed in section 5.2.2. The results

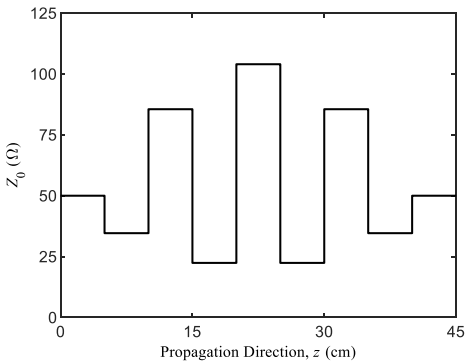

Fig. 5.17. Characteristic impedances of the 7th-order classical Chebyshev commensurate-line UE filter along the propagation direction.

have been translated to the frequency domain for the sake of clarity by means of (2.151) and they are provided in Fig. 5.18, where all the target specifications are satisfied apart from the appearance of the inherent spurious stopbands. The next step is to remove those spurious stopbands by introducing null values in the $S_{11,UE}(f)$ response for frequencies higher than $f_{max} = 2 \cdot f_0 = 2$ GHz, which is equivalent to impose the design condition of (5.100) with $m = 2$, but in the frequency domain, see (2.151). The resulting target frequency response is represented in Fig. 5.19 and Fig. 5.20.

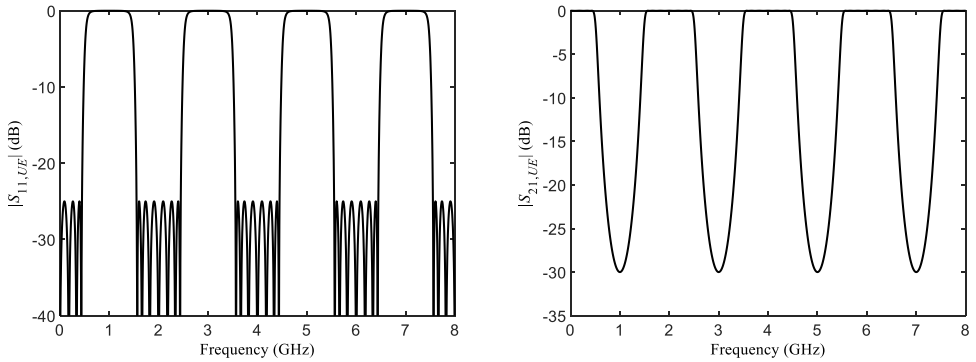

(a) (b)

Fig. 5.18. Magnitude of the frequency response of the 7th-order Chebyshev UE prototype: the periodic (a) $S_{11,UE}$ and (b) $S_{21,UE}$ parameters are provided.

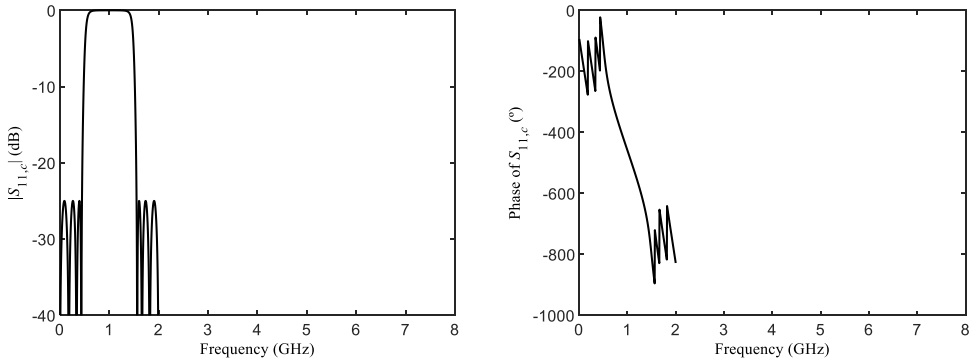

(a) (b)

Fig. 5.19. Magnitude (a) and phase (b) of the target $S_{11,c}$-parameter for the low-pass filter with smooth profile and without spurious rejection bands designed as an example.

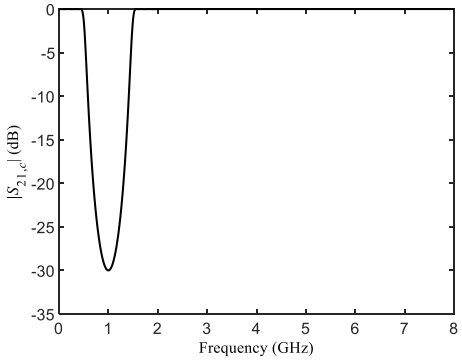

Fig. 5.20. Target $|S_{21,c}|$-parameter for the low-pass filter with smooth profile and without spurious rejection bands designed as an example.

Once the target frequency response has been determined, the necessary coupling coefficient for the low-pass filter that does not feature spurious rejection bands can be obtained employing the CLP synthesis technique. Thus, from the complex (magnitude and phase) target $S_{11,c}(f)$, defined numerically from $f_{D,n=0} = 0$ GHz to $f_{D,max} = 200$ GHz every Δf_D =4 MHz, and partially shown in Fig. 5.19, is translated to β-domain by means of (2.151). This discretized definition of $S_{11,c}(f)$ yields to $N_{z,CLP} = 200000$ points for the sampled z axis by (5.36). Then, the coupling coefficient at $z = 0$, $K(0)$, is obtained by means of (5.5). Using this value of $K(0)$, the Riccati equation of (5.10) is solved using the *Matlab*™ ODE solver function "ode45.m". By doing so, the first layer is peeled-off and $S_{11}(f)$ is propagated to the following layer. The next sample of the coupling coefficient is straightforwardly calculated by means of (5.5). In a layer by layer iterative routine, the whole coupling coefficient is calculated and shown in Fig. 5.21a. The required characteristic impedance for the microstrip line is finally calculated by imposing $Z_0(0) = 50\ \Omega$ in the expression (2.146), which is rewritten below for the sake of convenience:

$$Z_0(z) = Z_0(0) \cdot e^{-2 \cdot \int_0^z K(r) \cdot dr} \tag{2.146}$$

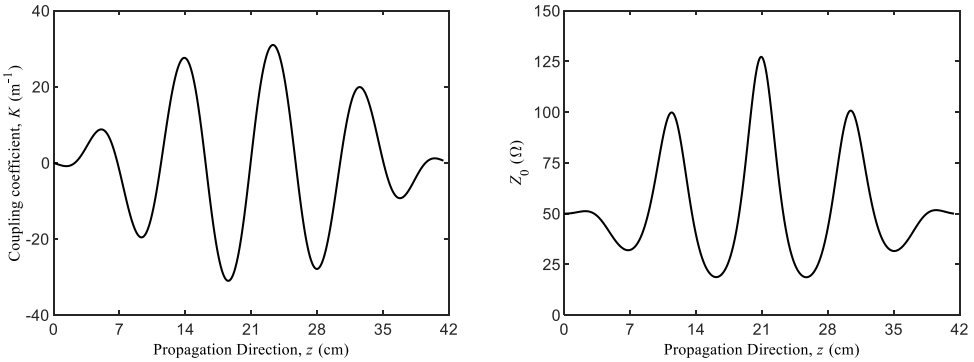

(a) (b)

Fig. 5.21. (a) Coupling coefficient and (b) characteristic impedance along the propagation direction of the designed low-pass filter without spurious rejection bands.

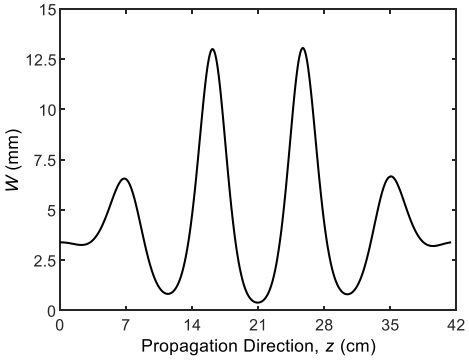

Fig. 5.22. Conductor strip width, W, of the microstrip structure along the propagation axis, z, for the low-pass filter without spurious rejection bands designed.

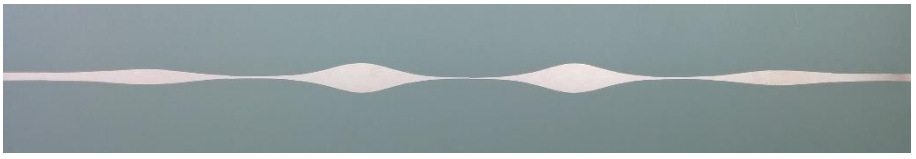

Fig. 5.23. Photograph of the fabricated microstrip low-pass filter with smooth profile and without spurious rejection bands designed as an example.

The obtained characteristic impedance profile is displayed in Fig. 5.21b. The physical dimensions as well as the actual $\varepsilon_{eff}(z)$ values of the microstrip structure are obtained by means of the *Keysight™ Linecalc* software tool. The denormalization process explained in section 2.2.2 is applied to the *z*-axis (propagation direction) using the equation (2.208) in order to compensate for the variation of the phase constant that is caused by the changing of the effective dielectric constant along the microstrip structure. For doing so, it is necessary to consider the actual phase constant given by $\varepsilon_{eff}(z)$ as well as the reference phase constant calculated with $\varepsilon_{eff,ref} = 2.744$ that was employed for the synthesis process. The transformation of (2.208) was performed at $f_t = f_c = 447.45$ MHz. The width of the conductor strip along the propagation direction of the final structure is depicted in Fig. 5.22. The final length of the device is 41.43 cm. A photograph of the fabricated prototype is shown in Fig. 5.23.

The designed low-pass filter structure without spurious rejection bands was simulated using *Keysight™ ADS Momentum* and measured with an *Agilent™* 8722 Vector Network Analyzer. The simulated and measured results are depicted in Fig. 5.24. A detail of the measured frequency response around the rejected band is given in Fig. 5.25 and Fig. 5.26, together with the target response.

The excellent agreement found between the target response, the simulations, and the measurements confirms the accuracy of the novel synthesis methodology proposed. Specifically, no spurious stopbands appear up to the 15th harmonic ($15 \cdot f_0$), and the return loss level out of the stopband is better than 20 dB in measurement up to 8 GHz ($8 \cdot f_0$). The return loss level decreases beyond that frequency due to the connectors and to the dispersion of the microstrip

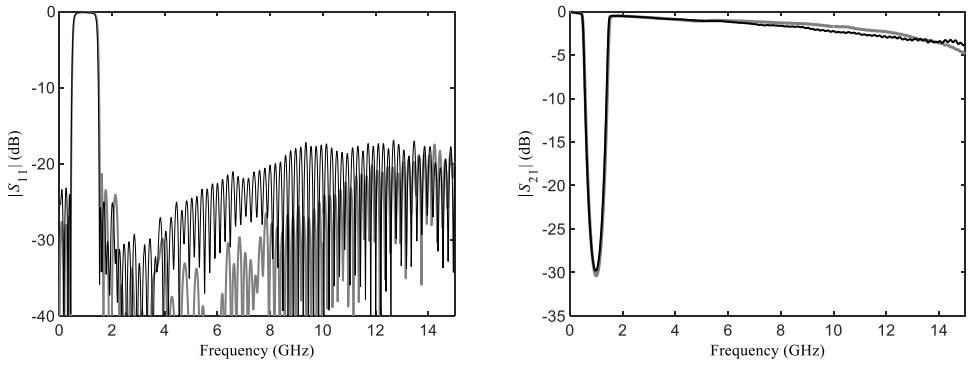

Fig. 5.24. Simulated (grey line) and measured (black line) magnitudes of the (a) S_{11} and (b) S_{21} parameters of the low-pass filter without spurious rejection bands designed as an example.

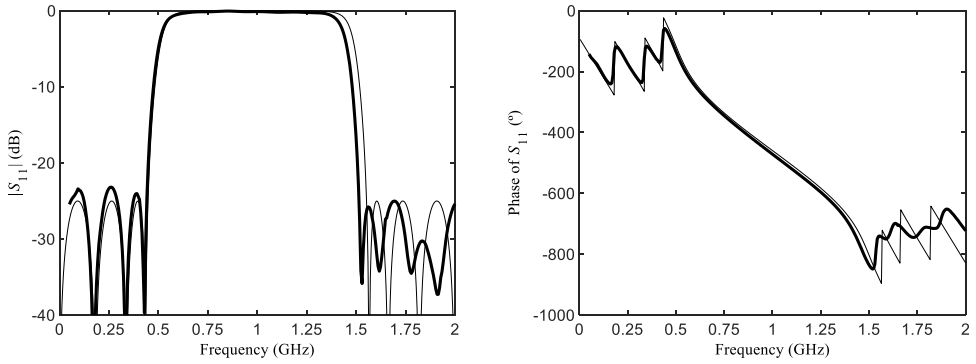

Fig. 5.25. Target (thin black line) and measured (thick black line) magnitude (a) and phase (b) of the S_{11}-parameter of the low-pass filter without spurious rejection bands designed as an example.

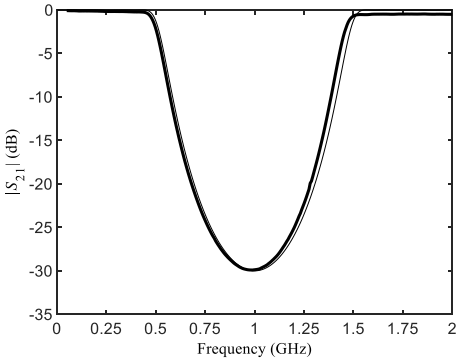

Fig. 5.26. Target (thin black line) and measured (thick black line) magnitude of the S_{21}-parameter of the low-pass filter without spurious rejection bands designed as an example.

line, but it remains better than 17 dB in measurement up to 15 GHz ($15 \cdot f_0$). Focusing on Fig. 5.25 and Fig. 5.26 it can be seen that the target specifications are achieved in measurement with remarkable accuracy: central frequency of the stopband, $f_0 = 1$ GHz, cut-off frequency, $f_c =$ 447.45 MHz, maximum rejection of 30 dB, and return loss level better than 20 dB. The small discrepancies found can be attributed to the fabrication tolerances, to the uncertainty in the dielectric constant of the substrate and to the connectors.

It is worth noting that the frequency response achieved by the prototype (see Fig. 5.24) may be considered more characteristic from a band-stop filter than from a low-pass filter. However, this practical appearance of band-stop responses is inherent to the design method of classical low-pass filters based on commensurate lines, as it was thoroughly exposed in section 5.2.1. Hence, the final frequency response featured by the present smooth-profiled filter is also classified here as a low-pass response (without spurious rejection bands), since its synthesis was

performed using a modified version of the frequency response in reflection of a classical commensurate-line low-pass filter, which also exhibits that periodical band-stop characteristic in practice as it can be observed in Fig. 5.18.

To finish this section, it can be considered that the methodology proposed to synthetize low-pass filters with smooth profile and without spurious rejection bands provides quasi-periodic structures that can be considered like a fully optimum EBG. As in the case of the optimum EBG of section 3.1, the spurious bands are avoided while providing the required maximum rejection level. However, unlike in the case of EBGs, the filters proposed in the present section feature a passband behavior that can be fully controlled without degrading the rejection level achieved in the stopband.

5.2.4. Rectangular Waveguide Low-Pass Filters Suitable for Direct Metal Laser Sintering Fabrication (I)

The technique intended for the design of low-pass and band-pass filters with smooth profiles and without spurious rejection bands is going to be oriented for the synthesis of rectangular waveguide low-pass filters with smooth height profiles. The expected geometrical properties of the resulting structure will be very suitable for a final fabrication by means of Direct Metal Laser Sintering (DMLS) additive manufacturing techniques. Since the final filter will feature smooth variations, it will not feature overhanging surfaces in the propagation direction and hence, the necessity of auxiliary supports will be avoided by growing the piece in that direction. It is important to stress that the necessity of auxiliary supports is one of the most troublesome aspects for metal Additive Manufacturing (AM) techniques. Indeed, several approaches have been recently proposed so as to adapt or modify classical filtering structures in order to allow a latter DMLS fabrication. In [41], step-shaped geometries are employed for the design of filters, showing the necessity of using support structures attached to the building platform to sustain overhangs. In that paper, as well as in previous works [42], [43], an insightful analysis is performed to show the importance of determining a suitable angle to try to improve the fabrication tolerances of a specific device, revealing also the difficulty, the resources, and the post-processing required to obtain acceptable results when support structures are needed.

In order to facilitate the manufacturing process, ellipsoid cavities and hyperbolic blended irises are used to obtain rounded geometries in [44], [45]. Following this approach of using

smooth surfaces, lollypop-shaped resonators (spheres balanced on top of poles) have been considered in [46] to design band-pass filters. However, the same classical design method employed to design conventional filters (with step-shaped geometries) is considered in the previous references, which is not convenient since, for example, long optimization processes (that are especially inadvisable with rounded profiles) are required. Therefore, it is of special interest to have a design technique, which allows us to directly obtain devices with smooth profile that can be always manufactured in the same growing direction and avoiding the use of support structures.

Nevertheless, it must be pointed out that typical requirements for rectangular waveguide filters include higher rejection levels than those demanded for planar devices. Regarding this concern, it is clear that the CLP synthesis method increases the rejection level that can be achieved when compared to the exact series solution of GLM [14], [15], but perhaps it might not be enough to reach the challenging specifications typically required for rectangular waveguide filters.

For this design example, the demanded passband of the filter will be defined from 10.65 to 11.65 GHz, and a Return Loss (RL) level greater than 20 dB must be provided within the whole passband range. On the other hand, a minimum rejection level of 80 dB must be guaranteed for a stopband located between 14 GHz and 15 GHz. However, if the typical ±100 μm fabrication tolerances associated to the DMLS manufacturing technique and the uncertain effects that they may carry in the frequency response of the filter are considered, it will be advisable to include additional security margins in the frequency response that will be eventually synthetized, in order to ensure the achievement of the aforementioned specifications at the measurement stage. Following this security margin criterion that is widely employed as a practical filter design rule, a low-pass Chebyshev frequency response was chosen to provide $RL \geq 25$ dB between 10.6 GHz and 11.95 GHz, while the minimum rejection level of 80 dB must be achieved from 13.95 GHz up to 15 GHz. The filter will be implemented with WR75 standard ports, which feature a width, $a = 19.05$ mm, and a height, $b = 9.525$ mm.

In order to satisfy the design margins for the frequency response, the cut-off frequency of the filter, f_c, was chosen as the upper limit for the passband, i.e. $f_c = 11.95$ GHz, while a value of 16.045 GHz was selected for the frequency at which the maximum rejection level will be achieved, f_0.

For the present design example, it is convenient to consider the relationship between the frequency and the phase constant for the fundamental TE_{10} mode of a rectangular waveguide that was firstly provided in (2.117):

$$\beta(f) = \frac{2 \cdot \pi \cdot f}{c} \cdot \sqrt{1 - \left[\frac{f_c^{TE_{10}}}{f}\right]^2} \tag{2.117}$$

where $f_c^{TE_{10}}$ is the cut-off frequency of the TE_{10} fundamental mode, which can be calculated by means of (2.118):

$$f_c^{TE_{10}}(z) = \frac{c}{2 \cdot a(z)} \tag{2.118}$$

The values of $\beta_c = \beta(f = f_c) = 188.496$ rad/m and $\beta_0 = \beta(f = f_0) = 293.058$ rad/m are obtained with (2.117) by imposing the width, $a = 19.05$ mm, of the WR75 standard in (2.118). Then, the electrical lengths, θ_c and θ_0, as well as the normalized frequencies, ω_c and α, associated with β_c and β_0, respectively, can be subsequently deduced. Since the electrical length for β_0 is $\theta_0 = \frac{\pi}{2}$ rad by definition (see Fig. 5.9b), $\theta_c = 1.01$ rad can be calculated from (5.99). Therefore, the expected normalized cut-off frequency $\omega_c = 1$ rad/s for the canonical starting prototype is obtained, and $\alpha = 1.181$ rad/s is calculated using (5.49). Moreover, it is necessary to consider the corresponding electrical length, $\theta_r = 1.294$ rad (calculated from (5.99) by changing the *c* index to *r*), and normalized frequency, $\omega_r = 1.136$ rad/s (calculated from (5.49)), for the minimum frequency for which the rejection level of 80 dB is required, i.e., $f_r = 13.95$ GHz. Then, the minimum order *N* of the Chebyshev filter that is necessary to reach the aforementioned specifications can be deduced as the closest upper integer to the result of the following expression:

$$N = \frac{\operatorname{acosh}\left(\sqrt{\left(10^{\frac{RJL}{10}} - 1\right) \cdot \left(10^{\frac{RL}{10}} - 1\right)}\right)}{\operatorname{acosh}(\omega_r)} \tag{5.103}$$

where RJL in (5.103) stands for the minimum rejection level that must be achieved at ω_r.

Therefore, evaluating (5.103) for $RJL = 80$ dB, $RL = 25$ dB, and $\omega_r = 1.136$ rad/s, a minimum order $N = 25$ is calculated, and the corresponding normalized Chebyshev response (with $N = 25$, $RL = 25$ dB) can be translated to the Richards transform plane using (5.51). Then, applying the procedure detailed in section 5.2.1 and imposing a value of $Z_0 = b_S = 9.525$ mm for the input port (height of the WR75 standard at the input port), the characteristic impedance of each UE is deduced, with a value equal to the height of the UE in rectangular waveguide [22]. The values obtained are given in Table 5.1. Furthermore, the length of each commensurate-line is calculated using (5.98) as $l = 5.36$ mm and thus, the commensurate-line UE starting prototype in rectangular waveguide technology will feature the height profile depicted in Fig. 5.27.

Unit Element	Height (mm)
$b_S = b_L$	9.525
$b_1 = b_{25}$	7.808
$b_2 = b_{24}$	11.794
$b_3 = b_{23}$	6.148
$b_4 = b_{22}$	14.235
$b_5 = b_{21}$	5.439
$b_6 = b_{20}$	15.305
$b_7 = b_{19}$	5.215
$b_8 = b_{18}$	15.688
$b_9 = b_{17}$	5.138
$b_{10} = b_{16}$	15.837
$b_{11} = b_{15}$	5.107
$b_{12} = b_{14}$	15.892
b_{13}	5.099

Table 5.1. Height values of the 25th-order Chebyshev commensurate-line UE prototype in rectangular waveguide technology for WR75 standard ports ($b_S = b_L = 9.525$ mm).

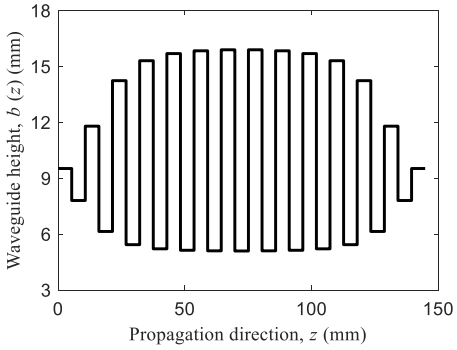

Fig. 5.27. Heights of the 25th-order Chebyshev commensurate-line UE prototype along the propagation direction.

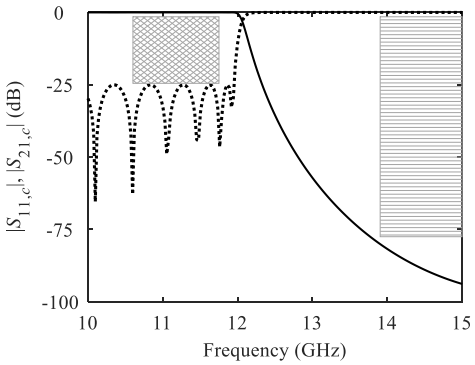

Fig. 5.28. Magnitude of the $S_{11,c}$ (dashed black line) and $S_{21,c}$ (solid black line)-parameters for the target 25-th order Chebyshev low-pass response. The specification masks for the frequency response in terms of return losses (grey diamond pattern) and the rejection level (grey rectangle pattern) are also provided.

Once the Unit Elements of the starting prototype have been determined, its corresponding $S_{11,UE}(\beta)$ is calculated by transfer matrix multiplication, following the procedure detailed in section 5.2.2.2. The final target frequency response, $S_{11,c}(\beta)$, intended to be synthetized is obtained after applying the modification procedure of (5.100) with $m = 2$ (low-pass filter case). The aimed $S_{11,c}(\beta)$ is partially shown in Fig. 5.28, where the specification masks are also included. The $S_{11,c}(\beta)$ parameter was defined from $\beta_{D,n=0} = 0$ rad/m to $\beta_{D,max} = 200 \cdot \beta_0$ every $\Delta\beta_D = \frac{\beta_0}{400}$. The use of these synthesis parameters results in a z axis that must be divided into $N_{z,CLP} = 320000$ points, according to (5.36).

The required coupling coefficient, $K(z)$, obtained by applying the CLP synthesis technique to the target $S_{11,c}(\beta)$ is depicted in Fig. 5.29a. This coupling coefficient will be implemented by exclusively performing variations in the waveguide height profile, $b(z)$, and thus $K(z) = K_b(z)$, see (2.122) and (2.123). Thereby, the corresponding waveguide height profile along the propagation direction, $b(z)$, can be calculated using the expression (2.130) that is rewritten below:

$$b(z) = b(0) \cdot e^{-2 \cdot \int_0^z K_b(r) \cdot dr} \tag{2.130}$$

The dimensions of $b(z)$ are attained by requiring the height of the WR75 standard for the input port in (2.130), i.e. $b(0) = 9.525$ mm, and the result is provided in Fig. 5.29b.

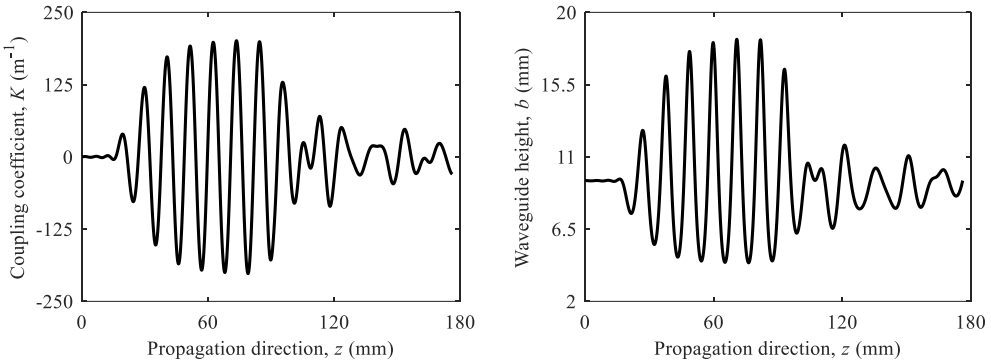

Fig. 5.29. Synthetized (a) coupling coefficient along the propagation direction calculated using the CLP synthesis technique and corresponding (b) waveguide height profile.

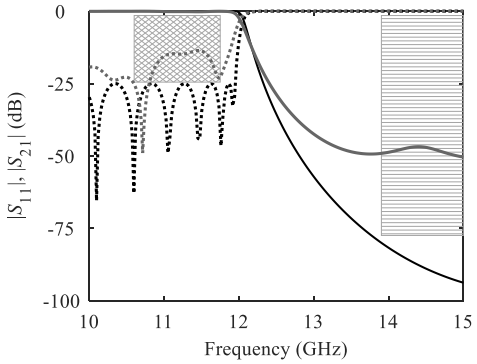

Fig. 5.30. Targeted (black lines) and simulated (dark grey lines) magnitude of the S_{11} (dashed lines) and S_{21} (solid lines)-parameters for the 25th-order Chebyshev low-pass filter. The simulation of the synthetized waveguide structure was done by solving the single-mode coupled-mode equation system of (2.91) and (2.92). The specification masks for the frequency response in terms of return loss (grey diamond pattern) and the rejection level (grey rectangle pattern) are also provided.

In order to perform an evaluation of the frequency response associated with the synthetized $K(z)$, the single-mode coupled-mode equation system of (2.91), (2.92) is solved for the complex amplitudes a^+ and a^- using the Matlab "*bvp4c.m*" function for the frequency range $\beta(f = 10\text{ GHz}) \leq \beta(f) \leq \beta(f = 15\text{ GHz})$. The $S_{11}(\beta)$ and $S_{21}(\beta)$-parameters can be deduced from a^+ and a^- using (2.105) and (2.106), respectively, and the results are given in Fig. 5.30.

As it can be seen in Fig. 5.30, the result of the synthesis procedure was not accurate enough and the frequency response featured by the synthetized $K(z)$ neither achieves the desired passband behavior, nor the required rejection level for the stopband. It is important to stress that the results of Fig. 5.30 correspond to a single-mode analysis of (2.91), (2.92) and hence, the lack of agreement between the target and the obtained frequency responses can be only explained by

a wrong calculation of $K(z)$. Indeed, the approximate maximum rejection level of 55 dB achieved by the synthetized structure is in accordance with the maximum rejection levels for the CLP synthesis method that were reported in [19].

It is worth noting that the reason for the inaccurate $K(z)$ synthetized must be attributed to the numerical implementation of the CLP method, since its theoretical foundations that have been developed in depth between (5.1) and (5.10) are fully exact. However, besides the constraints associated to the limited bandwidth employed to define $S_{11,c}(\beta)$ and $F_c(\tau)$, the solution of the Riccati equation of (5.10) is based on the use of the numerical method implemented in the "*ode45.m*" Matlab function, as it has been mentioned during the development of the CLP method. Since the Riccati equation is numerically solved at each discretized point in order to propagate the reflection coefficient, $\rho(\beta, z)$, from $z = z_0$ to $z = z_0 + T_{D,z}$ so as to determine the reflection coefficient that must be satisfied at $z_0 + T_{D,z}$, i.e. $\rho(\beta, z = z_0 + T_{D,z})$, the solution for $\rho(\beta, z = z_0 + T_{D,z})$ contains a certain quantity of numerical error. Moreover, the coupling coefficient $K\left(z = z_0 + T_{D,z}\right)$ is calculated as a function of $\rho\left(\beta, z = z_0 + T_{D,z}\right) = S_{11}(\beta, z = z_0 + T_{D,z})$, see (5.5). Accordingly, the coupling coefficient at $z = z_0 + T_{D,z}$ incorporates the numerical error that was added in the calculation of $\rho(\beta, z = z_0 + T_{D,z})$. Indeed, it is important to realize that once the coupling coefficient has been determined, the reflection coefficient must be propagated again so as to determine $\rho(\beta, z = z_0 + 2 \cdot T_{D,z})$ using (5.10) that depends both on $\rho(\beta, z = z_0 + T_{D,z})$ and $K\left(z = z_0 + T_{D,z}\right)$. Therefore, the solution of $\rho(\beta, z = z_0 + 2 \cdot T_{D,z})$ will add again numerical error to the solution that will be obtained using the variables $\rho(\beta, z = z_0 + T_{D,z})$ and $K\left(z = z_0 + T_{D,z}\right)$ that already contain numerical error. Following this reasoning, it is clear that the numerical error gets accumulated at each layer, and its effect in the $K(z)$ calculation becomes critical when z approaches L for the cases where high rejection values are required, since the last layers are the ones that accumulate the larger numerical errors. In fact, the error in the calculation of $K(z)$ is typically found at the end of the structure, where $K(z)$ seems not to converge to zero at the final part of the device. This is the case for the synthesis carried out in this example, as it can be observed in Fig. 5.29a. The accuracy of the CLP synthesis solution cannot be strongly improved by using better synthesis parameters for the definition of the target $S_{11,c}$, such as the use of a higher maximum phase constant, $\beta_{D,max}$, that implies thinner layers due to (5.35), or a finer resolution for the phase constant, $\Delta\beta_D$, see [19] and [47]. Thus, the main source of errors, i.e. the limited bandwidth and the numerical solving of the Riccati equation, cannot be completely avoided and accordingly, the rejection level that can be obtained from the CLP synthesis method is limited approximately to the highest value of 55 dB that was obtained for this example. Therefore, if higher rejection levels are required, it will be necessary to employ a more accurate synthesis technique for the

coupling coefficient calculation. The use of the Integral Layer Peeling synthesis method that will be presented in CHAPTER 6 will allow us to accurately determine the coupling coefficient even in these challenging situations.

REFERENCES

[1] R. G. Newton, “Inversion of reflection data for layered media – A review of Exact Methods,” *Geophysical Journal of the Royal Astronomical Society*, vol. 65, no. 1, pp. 191-215, 1981.

[2] J. F. Clerbout, “Fundamentals of Geophysical Data Processing”, McGraw-Hill, New York, 1976.

[3] E. A. Robinson, “Spectral Approach to Geophysical Inversion by Lorentz, Fourier and Radon Transforms,” *Proc. IEEE*, vol 70/9, pp. 1039-1054, 1982.

[4] I. Schur, “Uber Potentzreihen, die im Innern des Einheitskreises Beschramnkt Sind (Bounded Factorial Series within the Unity Circle),” *J. fur die Reine und Angewandte Mathematik*, vol. 147, pp. 205-232, 1917.

[5] A. M. Bruckstein and T. Kailath, “Inverse scattering for discrete transmission- line models,” *SIAM Rew.*, vol. 29, pp. 359-389, Sept. 1987.

[6] A. M. Bruckstein and T. Kailath, “An inverse scattering framework for several problems in signal processing,” *IEEE ASSP Magazine*, pp. 6-20, Jan. 1987.

[7] R. Feced, M. N. Zerbas, and M. A. Muriel, “An Efficient Inverse Scattering Algorithm for the Design of Nonuniform Fiber Bragg Gratings,” *IEEE J. Quantum Electron.*, vol. 35, no. 8, pp. 1105-1115, August 1999.

[8] J. Skaar, “Synthesis and Characterization of Fiber Bragg Gratings” PhD Dissertation, The Norwegian University of Science and Technology, Norway, 2000.

[9] J. Skaar, L. Wang, T. Erdogan, “On the Synthesis of Fiber Bragg Gratings by Layer Peeling,” *IEEE J. Quantum Electron.*, vol. 37, no. 2, pp. 165-173, February 2001.

[10] L. Poladian, “Simple Grating Synthesis Algorithm,” *Opt. Lett.*, vol. 25, no. 11, pp. 787-789, June 2000.

[11] L. Poladian, “Simple Grating Synthesis Algorithm: Errata,” *Opt. Lett.*, vol. 25, no. 18, pp. 1400-1400, September 2000.

[12] A. Papoulis, The Fourier Integral and its Applications (Electronic Science Series). New York, NY, USA: McGraw-Hill, 1962.

[13] R. E. Collin, “Foundations for Microwave Engineering”, Second Edition, New York, McGraw Hill, 1992.

[14] I. Arnedo *et al.*, "Synthesis of One-Dimensional Electromagnetic Bandgap Structures with Fully Controlled Parameters," *IEEE Trans. Microw. Theory Tech.*, vol. 65, no. 9, pp. 3123-3134, Sept. 2017.

[15] Israel Arnedo, “New Methods for the Synthesis of Microwave Devices Based on the Coupled-Mode Theory,” Doctoral Thesis, Universidad Pública de Navarra, España, 2009.

[16] A. V. Oppenheim and R. W. Schafer, *Discrete-Time Signal Processing*, 3rd ed. New York, NY, USA: Pearson, 2013.

[17] H. Nyquist, "Certain Topics in Telegraph Transmission Theory," *IEEE Trans. of the AIEE*, vol. 47, no. 2, pp. 617-644, April 1928.

[18] C. E. Shannon, "Communication in the Presence of Noise," *Proc. of the IRE*, vol. 37, no. 1, pp. 10-21, Jan. 1949.

[19] Magdalena Chudzik, "Synthesis Techniques for Novel Devices Based on Smooth Profiles with Application from the Microwave to the Terahertz Regions," Doctoral Thesis, Universidad Pública de Navarra, España, 2013.

[20] G. Matthaei, L. Young, E. M. T. Jones, Microwave filters, impedance-matching networks, and coupling structures, Artech House, Inc., 1980.

[21] I. Hunter, *Theory and Design of Microwave Filters. London*, U.K.: IEE Press, 2001.

[22] R. J. Cameron, C. M. Kudsia, R. R. Mansour, "Microwave filters for communication systems: fundamentals, design and applications", Hoboken, NJ: John Wiley & Sons, 2007.

[23] J. S. Hong and M. J. Lancaster, "Microstrip Filters for RF/Microwave Applications", New York, NY: John Wiley & Sons, 2001.

[24] J. A. G. Malherbe, "Microwave Transmission Line Filters", Dedham, MA: Artech House, 1979.

[25] R. W. Rhea, "HF Filter Design and Computer Simulation", Tucker, GA: Noble Publishing, 1994.

[26] R. Levy and S. B. Cohn, "A history of microwave filter research, design, and development," *IEEE Trans. Microwave Theory Tech.*, vol. 32, no. 9, pp. 1055- 1067, Sept. 1984.

[27] R. Levy, R. V. Snyder, and G. Matthaei, "Design of Microwave Filters," *IEEE Trans. Microwave Theory Tech.*, vol. 50, no. 3, pp. 783-793, Mar. 2002.

[28] I. C. Hunter, L. Billonet, B. Jarry, and P. Guillon, "Microwave Filters – Applications and Technology," *IEEE Trans. Microwave Theory Tech.*, vol. 50, no. 3, pp. 794-805, Mar. 2002.

[29] I. Arnedo, I. Arregui, A. Lujambio, M. Chudzik, M. A. G. Laso and T. Lopetegi, "Synthesis of Microwave Filters by Inverse Scattering Using a Closed-Form Expression Valid for Rational Frequency Responses," *IEEE Trans. Microw. Theory Tech.*, vol. 60, no. 5, pp. 1244-1257, May 2012.

[30] P. I. Richards, "Resistor-transmission-line circuits," *Proc. IRE*, vol. 36, no. 2, pp. 217-220, Feb. 1948.

[31] H. J. Carlin, P. P. Civalleri, *Wideband Circuit Design*. Boca Raton, FL, USA: CRC Press, 1998.

[32] H. Baher, *Synthesis of Electrical Networks*. New York, NY, USA: John Wiley & Sons, 1984.

[33] R. Levy, I. Whiteley, “Synthesis of distributed elliptic-function filters from lumped-constant prototypes,” *IEEE Trans. Microw. Theory Tech.*, vol. 14, no. 11, pp. 506-517, Nov. 1966.

[34] H. Ozaki and J. Ishii, “Synthesis of a class of strip-line filters,” *IRE Trans. Circuit Theory*, vol. 5, no. 2, pp. 104–109, Jun. 1958.

[35] R. J. Wenzel, “Exact design of TEM microwave networks using quarter-wave lines,” *IEEE Trans. Microw. Theory Tech.*, vol. 12, no. 1, pp. 94–111, Jan. 1964.

[36] M. C. Horton and R. J. Wenzel, “General theory and design of optimum quarter-wave TEM filters,” *IEEE Trans. Microw. Theory Tech.*, vol. 13, no. 5, pp. 316–327, May 1965.

[37] B. J. Minnis, *Designing Microwave Circuits by Exact Synthesis.* Norwood, MA, USA: Artech House, 1996.

[38] David M. Pozar, Microwave Engineering, Fourth Edition, New York, USA: John Wiley & Sons, 2001.

[39] R. Levy, “Tables of element values for the distributed low-pass prototype filter,” *IEEE Trans. Microw. Theory Tech.*, vol. 13, no. 5, pp. 514–536, Sep. 1965.

[40] A. V. Oppenheim, A. S. Willsky, and S. H. Nawab, *Signals & Systems*, 2nd ed. Upper Saddle River, NJ, USA: Prentice Hall, 1997.

[41] O. A. Peverini, M. Lumia, F. Calignano, G. Addamo, M. Lorusso, E. P. Ambrosio, D. Manfredi, and G. Virone, "Selective laser melting manufacturing of microwave waveguide devices," *Proc. IEEE*, vol. 105, no. 4, pp. 620-631, April 2017.

[42] F. Calignano, “Design optimization of supports for overhanging structures in aluminium and titanium alloys by selective laser melting, ”*Mater. Design*, vol. 64, pp. 203-213, December 2014.

[43] P. Das, R. Chandran, R. Samant, and S. Anand, “Optimum part build orientation in additive manufacturing for minimizing part errors and support structures,” *Procedia Manuf.*, vol. 1, pp. 343-354, 2015.

[44] P. Booth and E. Valles-Lluch, "Enhancing the performance of waveguide filters using Additive Manufacturing," *Proc. IEEE*, vol. 105, no. 4, pp. 613-619, April 2017.

[45] P. Booth and E. Valles-Lluch, "Realising advanced waveguide pas filters using additive manufacturing," *IET Microw. Antenna P.*, vol. 11, no. 14, pp. 1943-1948, December 2017.

[46] S. W. Sattler, F. Gentili, R. Teschl, and W. Bösch, "Direct metal printed 4th order stepped impedance filter in the C/X band", *IEEE MTT-S Int. Microw. Symp. Dig.*, Philadelphia, PA, pp. 145-148, June 2018.

[47] A. Rosenthal and M. Horowitz, "Inverse scattering algorithm for reconstructing strongly reflecting fiber Bragg gratings," *IEEE J. Quantum Electron.*, vol. 39, no. 8, pp. 1018-1026, Aug. 2003.

upna

Universidad Pública de Navarra
Nafarroako Unibertsitate Publikoa

CHAPTER 6. THE INTEGRAL LAYER PEELING (ILP) SYNTHESIS TECHNIQUE

The Integral Layer Peeling (ILP) one dimensional Inverse Scattering synthesis technique belongs to the same layer peeling approach as the Continuous Layer Peeling (CLP) method that has been carefully developed in CHAPTER 5. In fact, the qualitative explanation that was provided in CHAPTER 5 about the essence of the layer peeling approach, whereby the method is based in the causality principle and allows us to relate the layer coupling coefficient with the beginning of the target impulse response, can be immediately applied for the ILP technique. Nonetheless, several differences in the initial assumptions as well as in the implementation of the technique will lead to accurate results for the synthesized coupling coefficient even when very high rejection levels are required for the frequency response.

As in the case of GLM and CLP, the ILP Inverse Scattering synthesis technique was initially developed in the optics realm, for the synthesis of Fiber Bragg Gratings (FBG). Specifically, Rosenthal and Horowitz originally proposed the method for reconstructing strongly reflective FBGs in [1], where a thorough description of the method and its properties is also provided, being this work a great support for the development of the ILP technique in the range of microwave and millimeter waves.

The ILP method is based on an approximate analytical solution of the GLM equations, combined with the layer-peeling procedure. The structure is divided into layers that are neither uniform, nor infinitesimal. An approximate analytical solution of the GLM equation system of (4.26), (4.27) is employed for the propagation of the reflection coefficient through the layer, in contrast to the numerical solution of the Riccati equation that is employed in CLP. The approximate analytical solution of the GLM equations for each layer is also used to extract its coupling coefficient. The procedure is repeated layer by layer until the coupling coefficient of the entire structure is determined. It must be highlighted that since we need to solve the GLM equations for a narrow layer (where a large variation of the coupling coefficient is not typically expected) a low order of the GLM analytical series solution will be needed for reaching accurate results for the coupling coefficient of the layer. Therefore, the complexity of the ILP method remains on the same order as previous inverse scattering methods. Indeed, the computational complexity of ILP will be below the level reached by GLM and CLP, even when the error acceptable is small.

Furthermore, as it will be later explained in detail, the ILP method is implemented by jointly using both β- and τ-domains for the calculations, something that may be initially considered as a disadvantage when compared with CLP, since the latter is exclusively developed in the β-domain due to computational efficiency reasons. However, ILP requires for its numerical implementation almost only the highly-efficient FFT algorithm and does not need to solve the Riccati equation by using complex numerical methods.

It must be highlighted that the main source of error for the inverse scattering methods comes from the fact that the target response needs to be defined and computed by using a finite and discretized version of the $S_{11}(\beta)$ (or its associated $F(\tau)$), which is characterized by a limited spectrum resolution in β (equivalent to a non-infinite duration in τ) and a limited maximum β (related to the shortest discretization period in τ that can be employed) [1]. In GLM, the discretization of the $S_{11}(\beta)$-parameter leads to errors of relevant magnitude when solutions of high order are needed for the synthesis of a highly reflective response. In the same way, the limited bandwidth affects CLP. At each layer, the calculation of the coupling coefficient, as well as the target reflection coefficient for the subsequent layer, adds a certain quantity of numerical error in an accumulative fashion. Therefore, in the highest reflectivity responses, synthesis errors tend to appear at the end of the resulting coupling coefficient. As it was explained in [1] for FBGs in the optics range, and as it will be equally seen in the results found in this thesis for the application of the ILP method for microwave devices, the error caused by the use of limited bandwidth for dealing with the target response in ILP is significantly smaller than the error obtained with the other methods. Thus, the coupling coefficient can be calculated with better accuracy, and higher maximum rejection levels can be achieved with ILP as a result.

In order to formulate the ILP method, the single-mode coupled-mode equation system of (2.91) and (2.92) must be firstly considered:

$$\frac{da^+}{dz} = -j \cdot \beta \cdot a^+ + K \cdot a^- \tag{2.91}$$

$$\frac{da^-}{dz} = j \cdot \beta \cdot a^- + K \cdot a^+ \tag{2.92}$$

As it was stated in CHAPTER 4, the coupled-mode equation system of (2.91) and (2.92) can be reformulated as a Zakharov-Shabat system of quantum mechanics obtaining [2], [3]:

$$j \cdot \begin{bmatrix} \frac{d}{dz} & -K \\ K^* & \frac{-d}{dz} \end{bmatrix} \cdot \begin{bmatrix} a^+ \\ a^- \end{bmatrix} = \beta \cdot \begin{bmatrix} a^+ \\ a^- \end{bmatrix} \tag{4.1}$$

where $*$ stands for complex conjugate.

It must be also reminded that (4.1) has two linearly independent solutions (two of the so-called Jost functions) firstly introduced in (4.2) and (4.3), which satisfy in the limit [3]:

$$\lim_{z \to -\infty} \begin{bmatrix} \phi_1(z,\beta) \\ \phi_2(z,\beta) \end{bmatrix} = \begin{bmatrix} 1 \\ 0 \end{bmatrix} \cdot e^{-j \cdot \beta \cdot z} \tag{4.2}$$

$$\lim_{z \to -\infty} \begin{bmatrix} \overline{\phi}_1(z,\beta) \\ \overline{\phi}_2(z,\beta) \end{bmatrix} = \begin{bmatrix} 0 \\ 1 \end{bmatrix} \cdot e^{j \cdot \beta \cdot z} \tag{4.3}$$

Now, in order to solve the synthesis problem, it must be assumed that the coupling region (i.e., the synthetized structure) starts at $z = 0$ and ends at $z = L$, and therefore $K(z) = 0$ for $z < 0$ and $z > L$. As it was already commented in CHAPTER 4, a solution of the system of (4.1) (and hence of the coupled-mode equations, (2.91) and (2.92)) with the boundary conditions $a^+(z = 0, \beta) = 1$ and $a^-(z = L, \beta) = 0$ (i.e., output port matched) can be obtained as a linear combination of the previous functions (4.2) and (4.3) of the form [1]-[3]:

$$\begin{bmatrix} u_1(z,\beta) \\ u_2(z,\beta) \end{bmatrix} = \begin{bmatrix} \phi_1(z,\beta) \\ \phi_2(z,\beta) \end{bmatrix} + S_{11}(\beta) \cdot \begin{bmatrix} \overline{\phi}_1(z,\beta) \\ \overline{\phi}_2(z,\beta) \end{bmatrix} \tag{4.4}$$

where the formal definition of the $S_{11}(\beta)$ in terms of the complex amplitudes, a^+ and a^-, was originally given in (4.5) as:

$$S_{11}(\beta) = \left.\frac{a^-(z=0,\beta)}{a^+(z=0,\beta)}\right|_{a^-(z=L,\beta)=0} \tag{4.5}$$

and the solution $a^+(z,\beta) = u_1(z,\beta)$, $a^-(z,\beta) = u_2(z,\beta)$, corresponds to the situation when the output port is matched, and the values at the input port of the structure are $a^+(z=0,\beta) = u_1(z=0,\beta) = 1$ and $a^-(z=0,\beta) = u_2(z=0,\beta) = S_{11}(\beta)$.

One of the previous Jost functions (solution of the Zakharov-Shabat system) can be represented as [2], [3]:

$$\begin{bmatrix}\phi_1(z,\beta)\\ \phi_2(z,\beta)\end{bmatrix} = \begin{bmatrix}1\\0\end{bmatrix}\cdot e^{-j\cdot\beta\cdot z} + \int_{-\infty}^{\infty}\begin{bmatrix}A_1(z,\tau)\\ A_2(z,\tau)\end{bmatrix}\cdot e^{-j\cdot\beta\cdot\tau}\cdot d\tau \tag{4.6}$$

where the first term corresponds to the propagation of the forward traveling wave in the absence of coupling region (behavior at the limit (4.2)), and $A_1(z,\tau)$, $A_2(z,\tau)$, are the kernel functions that characterize the scattering effect produced by the coupling region (i.e., the synthetized structure).

Now, by considering the relationship (4.7) between the solutions $\phi_1(z,\beta)$, $\phi_2(z,\beta)$ and $\overline{\phi}_1(z,\beta)$ and $\overline{\phi}_2(z,\beta)$ [3], as well as causality constraints, the expressions (4.26) and (4.27) of the GLM coupled integral equations previously found in CHAPTER 4 can be again obtained [2], [3]:

$$A_1(z,\tau) = -\int_{-\infty}^{z} A_2^*(z,y)\cdot F(y+\tau)\cdot dy \qquad ,|z|>\tau \tag{6.1}$$

$$A_2(z,\tau) = -F(z+\tau) - \int_{-\infty}^{z} A_1^*(z,y)\cdot F(y+\tau)\cdot dy = 0\,,|z|>\tau \tag{6.2}$$

where $A_1(z,\tau)$ and $A_2(z,\tau)$ are the kernel functions that satisfy the GLM coupled integral equations.

It is interesting to note that the integration range in the system (6.1), (6.2) has a lower limit of $-\infty$, different from the restricted lower limit taken in (4.26) and (4.27) as in [2], [4]. The reason is that the causality restriction $F(\tau) = 0$ for $\tau < 0$ is not applied in our case due to considerations explained later.

Solving the GLM coupled integral equations (6.1), (6.2), the kernel functions $A_1(z,\tau)$, $A_2(z,\tau)$ can be calculated for a target frequency response, $S_{11}(\beta)$, expressed through $F(\tau)$, see

(4.11). By neglecting the integral terms of (6.1) and (6.2), the zero-order approximate solution of the GLM equation will be obtained as [1], [2], [4]:

$$A_1(z,\tau) = 0 \qquad ,|z| > \tau \tag{6.3}$$

$$A_2(z,\tau) = -F(z+\tau) \quad ,|z| > \tau \tag{6.4}$$

This zero-order approximation ignores the multiple reflections occurred at intermediate points of the structure, and only the case of a single scattering event is taken into account. The approximation is valid for devices with low reflectivity, or at the beginning (close to the input port) of general devices with high reflectivity. When multiple reflections within the structure (cases of multiple scattering events) cannot be neglected, higher-order approximations of the iterative solution of the GLM equations can be employed [1], [2].

Moreover, it must be reminded that due to causality considerations, the condition shown in (4.14), which is provided conveniently below, must be satisfied [3]:

$$\begin{bmatrix} A_1(z,\tau) \\ A_2(z,\tau) \end{bmatrix} = 0 \;\forall\; z < |\tau| \tag{4.14}$$

In order to solve the synthesis problem, the structure will be divided into several layers that will have a nonuniform profile. The iterative solution of the GLM equations will be employed to solve each of the layers. If the length of the layers is short enough, then the very simple zero-order approximation of (6.3) and (6.4) will be enough to solve the problem. Each of the layers will be solved consecutively, from the input to the output port of the device, following the same principle as the technique originally proposed in [1] for reconstructing fiber Bragg gratings with high reflectivity in the optical field.

Recalling the solution previously obtained with the output port matched of (4.4), and substituting (4.6) and (4.7), expressions for the forward travelling wave, $a^+(z,\beta) = u_1(z,\beta)$, and backward travelling wave, $a^-(z,\beta) = u_2(z,\beta)$, can be obtained as a function of $A_1(z,\tau)$, $A_2(z,\tau)$ [1]. If the zero-order approximation of (6.3), (6.4) is employed to calculate the kernel functions $A_1(z,\tau)$, $A_2(z,\tau)$ in the range $z > \tau$ (fully included within the region of validity of the GLM equations), and the causality restrictions of (4.14) are applied to limit the integration range, then the forward and backward travelling waves will have the following expressions along the structure:

$$a^{+}(z,\beta) = e^{-j\cdot\beta\cdot z} - S_{11}(\beta)\cdot\int_{-\infty}^{z} F^{*}(z+\tau)\cdot e^{j\cdot\beta\cdot\tau}\cdot d\tau \tag{6.5}$$

$$a^{-}(z,\beta) = S_{11}(\beta)\cdot e^{j\cdot\beta\cdot z} - \int_{-\infty}^{z} F(z+\tau)\cdot e^{-j\cdot\beta\cdot\tau}\cdot d\tau \tag{6.6}$$

where the solution has been obtained with the boundary conditions $a^{+}(z=0,\beta)=1$ and $a^{-}(z=L,\beta)=0$ (i.e., output port matched), and is valid for low reflectivity, or in general at the beginning of the structure (the zero-order approximation of the iterative solution of the GLM equations has been employed). Now, the local reflection coefficient along the structure, $\rho(z,\beta)$, can be obtained from (6.5) and (6.6) as:

$$\rho(z,\beta) = \frac{a^{-}(z,\beta)}{a^{+}(z,\beta)} = e^{j\cdot 2\cdot\beta\cdot z}\frac{S_{11}(\beta)-\bar{\rho}(\beta)}{1-S_{11}(\beta)\cdot\bar{\rho}^{*}(\beta)} \tag{6.7}$$

where $\bar{\rho}(\beta)$ is:

$$\bar{\rho}(\beta) = \int_{-\infty}^{2z} F(\tau)\cdot e^{-j\cdot\beta\cdot\tau}\cdot d\tau \tag{6.8}$$

and the expression achieved for $\rho(z,\beta)$ in (6.7), is valid for the same conditions as (6.5) and (6.6). In order to apply the ILP synthesis method, the structure will be divided into layers which have non-uniform profile and the same length, Δz. Since the coupled-mode equations are linear, the local reflection coefficient, $\rho(z,\beta)$, is identical to the reflection coefficient at the input of the section located at the region $[z,L]$. Thus, the reflection coefficient at the input of the m-th layer (S_{11} parameter of the section located at $[m\cdot\Delta z, L]$) can be defined as:

$$S_{11,m}(\beta) = \rho(m\cdot\Delta z,\beta) \tag{6.9}$$

and $S_{11,m}(\beta)$ can be propagated along the device, through a layer of length Δz, by using (6.7) as:

$$S_{11,m+1}(\beta) = e^{j\cdot 2\cdot\beta\cdot\Delta z}\cdot\frac{S_{11,m}(\beta)-\bar{\rho}_{m}(\beta)}{1-S_{11,m}(\beta)\cdot\bar{\rho}_{m}^{*}(\beta)} \tag{6.10}$$

where $\bar{\rho}_{m}(\beta)$ will correspond to:

$$\bar{\rho}_m(\beta) = \int_{-\infty}^{2\cdot\Delta z} F_m(\tau)\cdot e^{-j\cdot\beta\cdot\tau}\cdot d\tau \tag{6.11}$$

while $F_m(\tau)$ will be the inverse Fourier transform of $S_{11,m}(\beta)$ that is defined as:

$$F_m(\tau) = \frac{1}{2\pi}\int_{-\infty}^{\infty} S_{11,m}(\beta)\cdot e^{j\beta\tau}\cdot d\beta \tag{6.12}$$

When the length of the layers Δz is short enough, (6.10) will be accurate, since it is applied at the beginning of the corresponding structure section. If the use of longer layers is required, then higher order approximations of the iterative solution of the GLM equations could be employed to obtain (6.5) and (6.6), and from them (6.7) and (6.10).

Inspecting (6.11), it can be noted that since $F_m(\tau)$ is a causal function (it is the inverse Fourier transform of $S_{11,m}(\beta)$, i.e., the impulse response in reflection of the device section at $[m\cdot\Delta z, L]$), the lower limit of the integral in (6.11) could be theoretically replaced by 0. However, in practice, $F_m(\tau)$ is numerically calculated from $S_{11,m}(\beta)$ using the iFFT, and due to the limited bandwidth and spectral resolution employed, $F_m(\tau)$ becomes slightly inaccurate and noncausal. The use of the lower integration limit of $-\infty$ in (6.11) significantly reduces the error caused by numerical inaccuracies, in the propagation of the reflection coefficient along the layers of the structure [1].

In order to calculate the coupling coefficient profile of a layer, the solution previously found in CHAPTER 4, equation (4.24), for the GLM method can be employed. If the length of the layer, Δz, is short enough, then the zero-order approximation of the iterative solution of the GLM equations of (6.3) and (6.4) can be used, resulting in [1], [2]:

$$K(z) = -2\cdot F(2z) \tag{6.13}$$

If the use of longer layers is required, higher order approximations of the series solution of (4.31) could be employed.

Thus, the coupling coefficient required for the target $S_{11}(\beta)$ can be calculated in a layer by layer procedure, where the contribution of the *m*-th layer is (assuming that its length Δz is short enough), [1]:

$$K(m\cdot\Delta z + z') = -2\cdot F_m(2z'), \qquad 0 \le z' \le \Delta z \tag{6.14}$$

with $F_m(\tau)$ given by (6.12).

Therefore, in order to synthesize a microwave device with a target frequency response given by its $S_{11}(\beta)$ parameter, the structure is divided into layers of a short enough length, Δz, that have nonuniform profile. The input port will be placed at $z = 0$. That point corresponds to the input of the $m = 0$ layer. Then $S_{11,m=0}(\beta) = S_{11}(\beta)$ is taken and the coupling coefficient profile required for the $m = 0$ layer is calculated using (6.14). Next, applying (6.10), the propagation of $S_{11,m=0}(\beta)$ along the structure is performed, obtaining $S_{11,m=1}(\beta)$ and effectively "peeling off" the $m = 0$ layer. Proceeding iteratively, i.e. calculating the coupling coefficient profile of the m layer with (6.14), and propagating $S_{11,m}(\beta)$ along the device with (6.10), obtaining $S_{11,m+1}(\beta)$ and "peeling off" the m layer, we can continue until the end of the structure is reached at $z = L$. In this way, the coupling coefficient of the whole structure is calculated layer by layer, from the input to the output port.

It is interesting to note that in this synthesis method, the coupling coefficient profile calculated for each layer is not used to propagate the $S_{11,m}(\beta)$-parameter along the structure, see (6.10). Therefore, the error produced when calculating $K(z)$ does not accumulate along the device through the layer peeling procedure [1]. As it has been already mentioned, this is an important advantage of the ILP method with respect to the CLP method.

6.1. Relevant Numerical Aspects for the Practical Implementation of the ILP Method

As in the case of section 5.1, where topics concerning the sampling theorem and discrete signal processing were addressed for the practical implementation of the CLP method, several details must be considered so as to properly implement the numerical version of the ILP technique. Indeed, this section will cover specific features of the ILP implementation, such as the choice of the thickness of the layer or the determination of the amplitude of the coupling coefficient based on the particular method employed for the propagation of the reflection coefficient. Several aspects will be common with the ones that were analyzed for the CLP technique in section 5.1, and a comparison between the later and ILP will be possible.

In order to deal with the introduced issues, the first part of this section will be devoted to the determination of the necessary sampling period of the propagation axis for ILP, by taking advantage of the background already developed in section 5.1 for CLP. As it will be shown, the selection of the desired thickness of the layer, Δz, for ILP will need to be coherent with this sampling period in z. Finally, a discussion comparing the computational efficiency of the CLP and ILP methods will be provided.

On the second part of this section, it will be shown how the method employed for the propagation of the reflection coefficient at each layer, will eventually have an influence on how the amplitude for the coupling coefficient must be taken.

6.1.1. Relationship between the Target Response, the Propagation Axis, and the Layer Thickness in Practical Discretized-Data Calculations

In order to implement the ILP synthesis technique in practice, it is obvious that sampled and finite data must be employed for the definition of the target impulse response in reflection,

$F(\tau)$, as well as for its corresponding Fourier transform, i.e. the target frequency response in reflection, $S_{11}(\beta)$. Therefore, it will be necessary to maintain the coherence between the different sampling parameters of the reflection distance, τ, the propagation axis, z, and the phase constant, β. Several useful relationships were found during the study of this issue for the CLP method in section 5.1. It is advisable to perform a thorough reading of that section since just a brief summary of the discrete time aspects gathered in that section will be done in the present one.

As it was stated in section 5.1, if N samples are considered for the $F(\tau)$ definition, then the discretized version of $F(\tau)$, $F_D[n]$, will be expressed as:

$$F_D[n] = \sum_{i=0}^{N-1} F\left(\tau = i \cdot T_{D,\tau}\right) \cdot \delta[n-i] \tag{5.13}$$

where the τ points where $F(\tau)$ is sampled are given from the sampling period of τ, $T_{D,\tau}$, as:

$$\tau_{D,n} = n \cdot T_{D,\tau} = 0 \cdot \ T_{D,\tau}, 1 \cdot T_{D,\tau}, 2 \cdot T_{D,\tau}, \dots, (N-1) \cdot T_{D,\tau} \tag{5.14}$$

The associated sampled version of the $S_{11}(\beta)$-parameter, $S_{11,D}[k]$, will be related with $F_D[n]$ by the FFT algorithm through:

$$S_{11,D}[k] = T_{D,\tau} \cdot FFT\{F_D[n]\} = \sum_{i=0}^{N-1} S_{11}(\beta = i \cdot \Delta\beta_D) \cdot \delta[k-i] \tag{5.16}$$

where $\Delta\beta_D$ is the sampling ratio of the β axis, that is in turn related with the maximum duration of the impulse response in reflection, $\tau_{D,max} = N \cdot T_{D,\tau}$, through (5.22) as:

$$\Delta\beta_D = \frac{2 \cdot \pi}{\tau_{D,max}} \tag{5.22}$$

Moreover, since half of the N samples of $S_{11,D}[k]$ are redundant [5] (see section 5.1), the maximum phase constant sample that has non-redundant information is $\beta_{D,max}$, where:

$$\beta_{D,max} = \Delta\beta_D \cdot \frac{N}{2} \tag{5.27}$$

As it was found in (5.29), the sampling periods of τ and z, $T_{D,\tau}$ and $T_{D,z}$, respectively, are related with $\beta_{D,max}$ as:

$$\beta_{D,max} = \frac{\pi}{T_{D,\tau}} = \frac{\pi}{2 \cdot T_{D,z}} \tag{5.29}$$

Now, considering that a structure with length L must be divided into N_z optimum points when discretized data are considered, it can be directly deduced that:

$$T_{D,z} = \frac{L}{N_z} \tag{5.11}$$

The optimum number of points for the z-axis, N_z, is (see section 5.1):

$$N_z = N \tag{5.31}$$

and the z axis gets discretized accordingly as:

$$z_{D,n} = 0 \cdot \ T_{D,z}, 1 \cdot T_{D,z}, 2 \cdot T_{D,z}, \dots, (N-1) \cdot T_{D,z} \tag{5.25}$$

Thus, if $F_D[n]$ is defined with N samples from $\tau = 0$ to $\tau = \tau_{D,max}$ every $T_{D,\tau}$ then, the z axis should be optimally defined with $N_z = N$ points. This condition implies that the $S_{11,D}[k]$ must be defined with a total of N samples, where only the first $\frac{N}{2}$ provide original information [5]. It is possible to relate the optimum sampling period of z, $T_{D,z}$, with the $\beta_{D,max}$ where the last non-redundant sample of $S_{11,D}$ is defined, i.e. $S_{11,D}\left[\frac{N}{2}\right]$, by means of (5.30) and (5.33) as:

$$T_{D,z} = \frac{T_{D,\tau}}{2} = \frac{\pi}{2 \cdot \beta_{D,max}} = \frac{\lambda_{g,D,min}}{4} \tag{6.15}$$

where $\lambda_{g,D,min}$ is the wavelength that corresponds to $\beta_{D,max}$, see (5.33).

At this point, it must be reminded that it was necessary to consider a special sampling period of the z axis for the CLP method, $T_{D,z,CLP} = 2 \cdot T_{D,z} = \frac{\lambda_{g,D,min}}{8}$, so as to obtain a convergent $K(z)$, due to the inherent limitations of the numerical solution of the Riccati equation of (5.10). Therefore, the number of points needed for the z axis in the CLP method was $N_{z,CLP} = 2 \cdot N_z = 2 \cdot N$. In order to propagate the reflection coefficient at each point, it was necessary to solve the Riccati equation at $N_{z,CLP}$ points.

Unlike the CLP technique, the ILP synthesis method does not require to solve numerically the Riccati equation for the propagation, since the procedure is performed by means of (6.10) and (6.11), which are deduced from the zero-order approximation of the GLM equations. Therefore, when using the ILP synthesis technique, the z axis can be divided into the optimum number of points $N_{z,ILP} = N_z = \frac{N_{z,CLP}}{2}$. Accordingly, the sampling period of z that is necessary to employ for ILP, $T_{D,z,ILP}$, will be the optimum $T_{D,z}$, and it will be related with $\beta_{D,max}$ by (6.15). The relationship between $T_{D,z,ILP}$ and $\lambda_{g,D,min}$ is graphically depicted in Fig. 6.1.

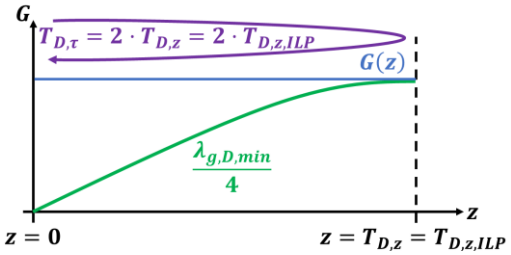

Fig. 6.1. The practical ILP implementation requires a sampling period of the z axis, $T_{D,z,ILP}$, that matches the optimum $T_{D,z}$. The optimum $T_{D,z}$ is related with the minimum wavelength $\lambda_{g,D,min}$ associated with the maximum defined phase constant, $\beta_{D,max}$, of the the S_{11}-parameter. The structure features physical dimensions G along the propagation axis, z.

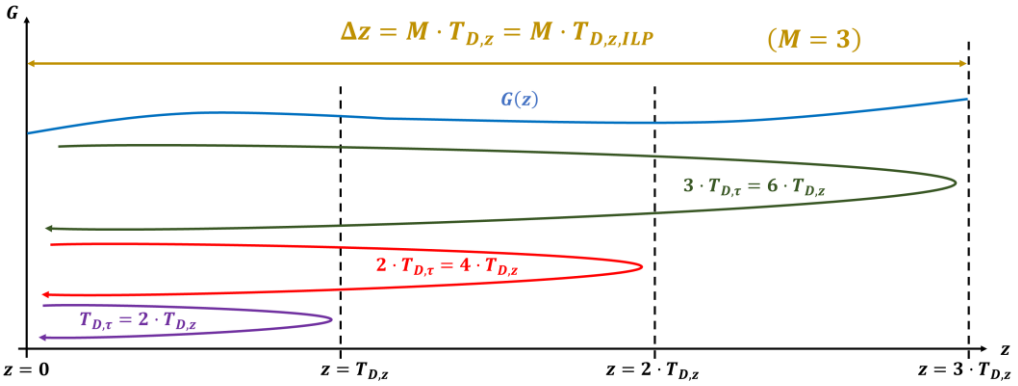

Fig. 6.2. Sketch of the relationship between the sampling periods of the z, $T_{D,z,ILP} = T_{D,z}$, and τ, $T_{D,\tau}$, axes with the finite layer thickness, Δz, for the case $M = 3$, i.e. $\Delta z = 3 \cdot T_{D,z} = 6 \cdot T_{D,\tau}$. The structure features physical dimensions G along the propagation axis, z.

Moreover, it must be stressed that in contrast to CLP, in ILP the layer features a finite thickness, Δz, see Fig. 6.2. Accordingly, Δz should be chosen as an integer number of samples in z, i.e.:

$$\Delta z = M \cdot T_{D,z} \tag{6.16}$$

being M a positive integer number.

Therefore, the number of layers, N_L, in which a structure of length L is divided will be calculated taking into account (5.11) as:

$$N_L = \frac{L}{\Delta z} = \frac{N_{z,ILP}}{M} = \frac{N_{z,CLP}}{2 \cdot M} \tag{6.17}$$

The propagation of the reflection coefficient will be performed in ILP at each layer, so the distance between two consecutive propagations will be $\Delta z = M \cdot T_{D,z,ILP}$. As a consequence, the shortest selectable distance will be given by $M = 1$, yielding to $\Delta z = T_{D,z,ILP}$.

It is worth noting that for CLP, the propagation must be carried out every $T_{D,z,CLP}$ in z, or in other words, $N_{z,CLP}$ times. However, the number of propagations needed for ILP will coincide with the number of layers, $N_L = \frac{N_{z,ILP}}{M} = \frac{N_{z,CLP}}{2 \cdot M}$. Therefore, in the worst case where $M = 1$, the number of propagations that are needed in ILP is half of the propagations that would be necessary with CLP for the same pair $F_D[n]$, $S_{11,D}[k]$. Indeed, this is the most important improvement that ILP offers when compared to CLP. As it has been already mentioned, the propagation of the reflection spectrum is the source of a great part of the numerical error that is added to $K(z)$. Therefore, the reduction of the number of propagation steps from $N_{z,CLP}$ to $N_L = \frac{N_{z,CLP}}{2 \cdot M}$ results in a reduction of the error that is accumulated during the iterative process of layer-peeling, leading to a more accurate propagation of the reflection coefficient, as well as to a better result for $K(z)$.

Furthermore, it must be pointed out that the propagation method used for ILP is not based on the numerical solution of the Riccati equation of (5.10) and it is more accurate as long as the zero-order approximation between two adjacent layers remains sufficiently accurate (see the development of the ILP method at the beginning of this chapter). Moreover, taking into account that ILP employs a non-infinitesimal layer in contrast to the infinitesimal layer of CLP, the discretization of the z axis should be better assimilated by ILP. It is also worth noting that the addition of negative values of τ in (6.11) tends to minimize the numerical error that is added to the propagation process.

On the other hand, it must be also noted that unlike the CLP case (see (5.10)), the value of $K(z)$ at the m-th layer is not employed in ILP for the calculation of the reflection coefficient at the next $m + 1$ layer, $S_{11,m+1}(\beta)$, see (6.10) and (6.11). Thus, the calculation of $S_{11,m+1}(\beta)$ does not include the error committed in the $K(m \cdot \Delta z')$ calculation.

The combination of these improvements for the propagation procedure drives to a target reflection coefficient at each layer that features better numerical quality than the one that would be obtained in each discretized point of z for CLP. As a consequence, the numerical accuracy and the computational efficiency of the whole synthesis process with ILP exceeds the performance that can be achieved with CLP.

6.1.2. Relationship between the Propagation Method and the Amplitude of the Coupling Coefficient

One of the most important aspects of the ILP method is the specific procedure that is employed for the deduction of the reflection coefficient that must be satisfied at the $m+1$ layer, $S_{11,m+1}(\beta)$. Taking under consideration the theoretical development of the ILP technique done at the beginning of this chapter, the $S_{11,m+1}(\beta)$ must be calculated using (6.10), that in turn depends on the previous determination of $\bar{\rho}_m(\beta)$ by means of (6.11), which is conveniently rewritten below:

$$\bar{\rho}_m(\beta) = \int_{-\infty}^{2\cdot\Delta z} F_m(\tau)\cdot e^{-j\cdot\beta\cdot\tau}\cdot d\tau \tag{6.11}$$

It is obvious that the integral of (6.11) can be implemented in practice by means of numerical integration methods such as the trapezoidal one, which is implemented in the Matlab "*trapz.m*" function.

However, a deeper observation reveals that (6.11) is a simple Fourier transform, where the upper limit $+\infty$ of the formal definition of (4.12) has been substituted by $2\cdot\Delta z$. Taking advantage of this fact, the FFT algorithm can be employed to perform a fast and accurate calculation of $\bar{\rho}_m(\beta)$, and of $S_{11,m+1}(\beta)$ as a consequence. Nevertheless, in order to maintain the coherence between the sampling parameters of $S_{11,m}(\beta)$ and $F_m(\tau)$, the FFT of the discretized version of $F_m(\tau)$, $F_{D,m}[n]$, (see section 6.1.1) must be performed over the N samples that compose $F_{D,m}[n]$, but some of them correspond to samples of τ, $\tau_{D,n}$, that will satisfy $\tau_{D,n} > 2\cdot\Delta z$, with $n = 0, 1, 2, \ldots, N-1$. In order to address the calculation of (6.11) with the FFT, a modified version of $F_m(\tau)$, $F'_m(\tau)$, must be defined in the following manner:

$$F'_m(\tau) = \begin{cases} F_m(\tau) & \text{, for } \tau < 2\cdot\Delta z \\ 0 & \text{, otherwise} \end{cases} \tag{6.18}$$

Therefore, the integral (6.11) can be rapidly calculated with the FFT algorithm by also taking into account the necessary scaling factor (see (5.16)) as:

$$\bar{\rho}_m(\beta = k \cdot \Delta\beta_D) = \bar{\rho}_{D,m}[k] = T_{D,\tau} \cdot FFT\{F'_{D,m}[n]\} \tag{6.19}$$

where $\Delta\beta_D$ is the sampling ratio of the β axis, $T_{D,\tau}$ is the discretization period of the τ axis and n is the ordinal number that corresponds to each of the N discretized samples of $F'_m(\tau)$, i.e. $n = 0, 1, 2, \ldots, N-1$.

In fact, when dealing with long impulse responses, the largest negative values (in modulus) of τ are progressively less relevant for the calculation of $\bar{\rho}_m(\beta)$, and can be accordingly neglected by assuming that they are null in the definition of (6.18). However, it is very important to keep $F'_m(\tau) = F_m(\tau)$ for those samples that are not much lower than $\tau_{D,n} = 2 \cdot \Delta z$ in order to finally obtain an accurate $K(z)$. It is important to recall that the samples corresponding to negative values of τ will appear at the end of the discretized version of $F_m(\tau)$, $F_{D,m}[n]$, due to the time domain aliasing [5].

However, it must be highlighted that the propagated impulse response in reflection $F_{m+1}(\tau) = FT^{-1}\{S_{11,m+1}(\beta)\}$ (calculated with (6.10), (6.11) and (6.12)) attained for the layer $m+1$ as a result of the application of both procedures to calculate (6.11) (trapezoidal integration and FFT algorithm) is not exactly the same at $\tau_{D,n} = 0$, as it can be observed in the example provided in Fig. 6.3. The example given in that figure corresponds to the actual calculation of $F_{m+1}(\tau)$, with $m = 4003$, for the design example that will be thoroughly detailed in section 6.2.1.

In view of Fig. 6.3a, the sampled version of $F_{m+1}(\tau)$ that results from the numerical integration of $\bar{\rho}_m(\beta)$ in (6.11), $F_{m+1,int}(\tau_{D,n})$, carries the effects predicted for the theoretical Fourier transform of a signal that presents a discontinuity at $\tau_{D,n} = 0$ [6]. The value of $F_{m+1,int}(\tau_{D,n} = 0)$ corresponds to the mean value of $F_{m+1}(\tau = 0^-)$ and $F_{m+1}(\tau = 0^+)$, i.e. $F_{m+1,int}(\tau_{D,n} = 0) = \frac{F_{m+1}(\tau=0^-)+F_{m+1}(\tau=0^+)}{2}$, see the grey trace of Fig. 6.3b.

However, in the case of the $F_{m+1}(\tau)$ obtained by employing the FFT to calculate $\bar{\rho}_m(\beta)$ in (6.11), $F_{m+1,FFT}(\tau_{D,n})$, the value provided at $\tau_{D,n} = 0$ is directly $F_{m+1}(\tau = 0^+)$, see the black line of Fig. 6.3b. Since the coupling coefficient at $z = 0$ must be strictly taken at $\tau = 0^+$ (see (5.1)), the coupling coefficient at $z_{D,n} = m \cdot \Delta z$ to be deduced from $F_{m,FFT}(\tau_{D,n} = 0)$, that will be annotated as $K_{FFT}(z_{D,n} = m \cdot \Delta z)$, will be:

$$K_{FFT}(z_{D,n} = m \cdot \Delta z) = -2 \cdot F_m(\tau = 0^+) = -2 \cdot F_{m,FFT}(\tau_{D,n} = 0) \tag{6.20}$$

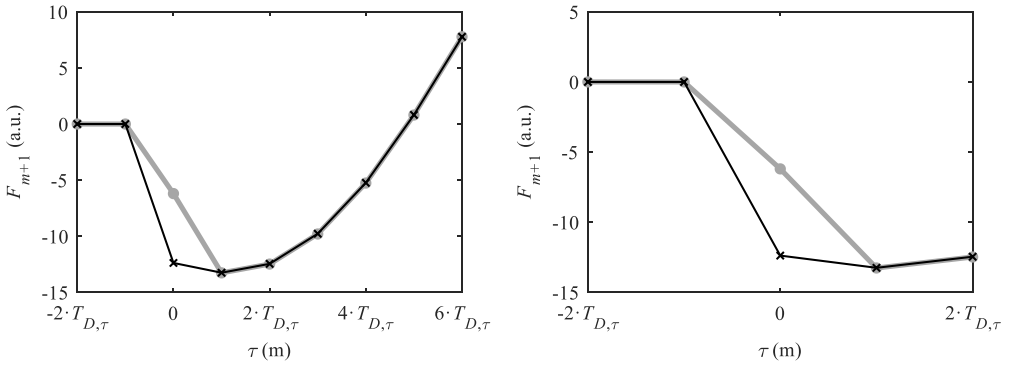

Fig. 6.3. (a) Overview and (b) detail of $F_{m+1}(\tau)$ with $m = 4003$, calculated with (6.10), (6.11) and (6.12), when the result of (6.11) is computed by performing the numerical integral (grey line) and the FFT (black line).

On the other hand, if the same coupling coefficient is calculated by means of a numerical integration method, $K_{int}(z_{D,n} = m \cdot \Delta z)$, it will be necessary to consider that $F(\tau = 0^+) = 2 \cdot F(\tau = 0)$, since $F(\tau = 0^-) = 0$ due to causality considerations (see (4.13)), and then:

$$K_{int}(z_{D,n} = m \cdot \Delta z) = -2 \cdot F_m(\tau = 0^+) = -4 \cdot F_{m,int}(\tau_{D,n} = 0) \tag{6.21}$$

It is worth noting that the sample of $F_{m+1}(\tau)$ at $\tau_{D,n} = 0$ is the only one that becomes troublesome, since $F_{m+1,FFT}(\tau_{D,n} \neq 0) = F_{m+1,int}(\tau_{D,n} \neq 0)$ as it can be observed in Fig. 6.3a. This is something that may be expected due to the fact that $F_m(\tau)$ will be continuous for $\tau \neq 0$. Thus, for $m \cdot \Delta z < z_{D,n} < (m+1) \cdot \Delta z$ in (6.14), it will be satisfied that:

$$\begin{aligned} &K_{int}(m \cdot \Delta z < z_{D,n} < (m+1) \cdot \Delta z) = -2 \cdot F_{m,int}(m \cdot \Delta z < z_{D,n} < (m+1) \cdot \Delta z) = \\ &K_{FFT}(m \cdot \Delta z < z_{D,n} < (m+1) \cdot \Delta z) = -2 \cdot F_{m,FFT}(m \cdot \Delta z < z_{D,n} < (m+1) \cdot \Delta z) \end{aligned} \tag{6.22}$$

In order to conclude this subsection devoted to explore the numerical implementation of the integral of (6.11) for the calculation of $\bar{\rho}_m(\beta)$ and its implications in the amplitude of the resulting coupling coefficient at $z_{D,n} = m \cdot \Delta z$, it must be highlighted that the choice between a numerical integration method and the FFT must be coherent with the expressions given in (6.20)-(6.22) in order to obtain an accurate $K(z)$. It is obvious that if the presented amplitude criterion is not followed, the frequency response featured by the obtained $K(z)$ will not match the target frequency response.

Moreover, a final remark must be done regarding the great computational efficiency of the implementation of the ILP method that is achieved with the use of the FFT algorithm in the

calculation of (6.11), resulting much faster than the method based on numerical integration. Indeed, if the CLP propagation procedure, that consists in solving the Riccati equation, is compared with the FFT implementation of (6.11) that is used for ILP, the computation time required for the propagation in ILP will represent a small fraction of that of CLP. Therefore, the ILP synthesis method is much faster than CLP when the target frequency responses are defined with the same parameters in terms of $\beta_{D,max}$, $\Delta\beta_D$ (in β domain) or $T_{D,\tau}$ and $\tau_{D,max}$ (in τ domain). The exact improvement in terms of computational time-saving achieved by performing a synthesis with ILP instead of CLP depends on the definition parameters of the target frequency response, $\beta_{D,max}$ and $\Delta\beta_D$ (or their counterparts in τ-domain, $T_{D,\tau}$ and $\tau_{D,max}$), as well as on the layer thickness selected for the case of ILP, Δz (see (6.16)). However, by way of example, when the synthesis of the planar low-pass filter of section 5.2.3 (that was originally carried out with CLP) is repeated using ILP for the same target frequency response and choosing $\Delta z = T_{D,z}$, i.e. $M = 1$, the synthesis process gets approximately completed 300 times faster.

6.2. DESIGN OF RECTANGULAR WAVEGUIDE LOW-PASS FILTERS WITH HIGH REJECTION LEVELS

Once the theoretical basis of the ILP synthesis method has been thoroughly described, the improvement in terms of synthesis accuracy that is expected from the use of this method will be tested in practical design examples. For doing so, the design of several rectangular waveguide filters, with target frequency responses that feature high rejection levels, will be addressed by following the filter design procedure explained in section 5.2.

Indeed, the first aim of this section will be to complete the whole design process of the 25-th order Chebyshev low-pass filter that was firstly considered in section 5.2.4. In that section, the design workflow was interrupted since the CLP synthesis method was not able to achieve an accurate enough coupling coefficient for the target frequency response, due to its challenging requirements in terms of rejection level. However, in the present section, the target response will be directly obtained in the τ-domain by using the method detailed in section 5.2.2.1, and it will be subsequently synthetized with the ILP method. Moreover, as it was explained in section 2.2.3, the simulation results will show a degradation with respect to the single-mode expected response due to the parasitic couplings to cut-off modes. In order to compensate for these effects, the uniform scaling method that was presented in section 2.2.3.1 will be employed. The designed filter will be fabricated using the DMLS Additive Manufacturing technique and a later silver coating will be applied, being the filter measured at both stages.

Then, a 21-st order modified Zolotarev response will be considered to design a rectangular waveguide filter with a length shorter than that of the previous 25-th order Chebyshev filter. The values of the starting Zolotarev commensurate-line UE prototype will be modified in order to find a commensurate-line UE prototype that will allow us to synthetize a smooth profile filter with suitable dimensions for a subsequent fabrication using the DMLS technique. The parasitic effects of cut-off modes will be compensated by means of the uniform scaling method of section 2.2.3.1.

Finally, a pure 21-st order Zolotarev response will be employed to synthetize a low-pass filter. In this case, it will be shown how the cut-off modes can dramatically degrade the frequency response that can be expected with the single-mode approximation. In order to avoid these effects, a recursive correction based on the distributed scaling method of section 2.2.3.2 will be

applied. As it will be shown, the accurate compensation performed leads to a final structure that practically features the intended single-mode frequency response.

6.2.1. Rectangular Waveguide Low-Pass Filters Suitable for Direct Metal Laser Sintering Fabrication (II)

In this practical example, the design process of the 25-th order Chebyshev low-pass filter that was firstly addressed in section 5.2.4 will be resumed. However, the ILP synthesis technique will be employed for the current synthesis attempt, since the CLP method did not provide the necessary accuracy for the coupling coefficient calculation and the obtained structure did not achieve the desired requirements for the frequency response as a result (see section 5.2.4). Despite the difference in the synthesis technique employed, the design workflow that will be employed in this case will follow the general procedure thoroughly detailed in section 5.2.

Firstly, it is convenient to remind the requirements for the filter: the passband defined from 10.65 to 11.65 GHz must satisfy a Return Loss (RL) level greater than 20 dB. Moreover, a minimum rejection level of 80 dB must be guaranteed for the stopband located between 14 GHz and 15 GHz.

In order to achieve this final performance in measurements, several design margins will be included in the Chebyshev low-pass frequency response of the starting UE prototype. Thus, a minimum RL of 25 dB must be satisfied for an expanded passband defined from 10.6 GHz to 11.95 GHz, and a minimum rejection level of 80 dB must be achieved from 13.95 GHz up to 15 GHz. Accordingly, the cut-off frequency of the low-pass filter response was selected as $f_c = 11.95$ GHz, whereas the maximum rejection frequency was fixed as $f_0 = 16.045$ GHz.

Furthermore, the filter must be implemented in the WR75 standard, which is characterized by a waveguide width, $a = 19.05$ mm, and height, $b = 9.525$ mm, that will be employed at its ports.

The procedure for the calculation of the UEs of the 25-th order Chebyshev low-pass prototype is fully detailed in section 5.2.4. A summary of the different frequency translations applied for f_c and f_0 in section 5.2.4 is provided Table 6.1.

Frequency, f (GHz)	Phase constant, β (rad/m)	Electrical length, θ (rad)	Normalized frequency, ω (rad/s)
$f_c = 11.95$	$\beta_c = 188.496$	$\theta_c = 1.01$	$\omega_c = 1$
$f_0 = 16.045$	$\beta_0 = 293.058$	$\theta_0 = \pi/2$	$\alpha = 1.181$

Table 6.1. Summary of the different translations for the frequencies f_c and f_0 that define the starting 25-th order Chebyshev UE prototype and their associated frequency transformations.

Unit Element	Height (mm)
$b_S = b_L$	9.525
$b_1 = b_{25}$	7.808
$b_2 = b_{24}$	11.794
$b_3 = b_{23}$	6.148
$b_4 = b_{22}$	14.235
$b_5 = b_{21}$	5.439
$b_6 = b_{20}$	15.305
$b_7 = b_{19}$	5.215
$b_8 = b_{18}$	15.688
$b_9 = b_{17}$	5.138
$b_{10} = b_{16}$	15.837
$b_{11} = b_{15}$	5.107
$b_{12} = b_{14}$	15.892
b_{13}	5.099

Table 6.2. Height values of the starting 25-th order Chebyshev UE low-pass filter prototype for $b_S = b_L = 9.525$ mm.

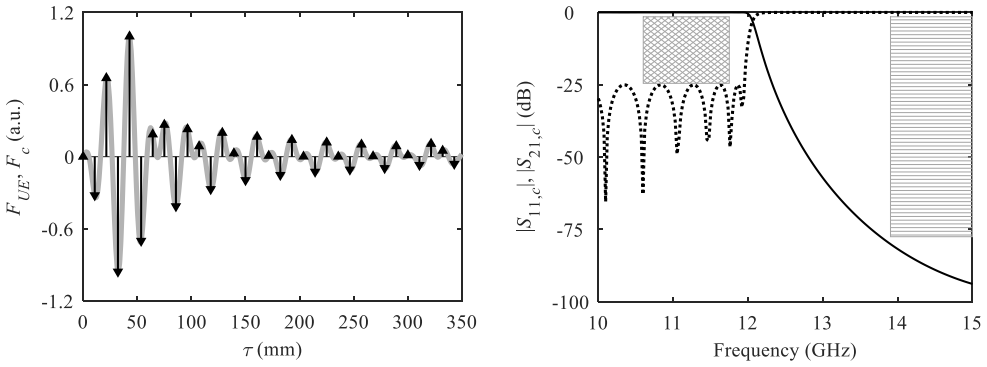

Fig. 6.4. (a) Impulse response in reflection of the 25-th order Chebyshev UE prototype, $F_{UE}(\tau)$, (black line) and its corresponding continuous underlying version (grey line) that will be the target for the ILP method, $F_c(\tau)$, obtained applying the interpolation method with $m = 2$. (b) Magnitude of the $S_{11,c}$ (dashed line) and $S_{21,c}$ (solid line) for the target 25-th order Chebyshev low-pass response. The specification masks for the frequency response in terms of return loss (grey diamond pattern) and the rejection level (grey rectangle pattern) are also provided.

In the same way, for the sake of convenience, the height values of the UEs of the commensurate-line starting prototype that was calculated in section 5.2.4, are again given here in Table 6.2.

It is important to stress that up to this point, the design workflow is exactly the same that was carried out in section 5.2.4. However, the ILP synthesis method needs a target impulse response in reflection in the τ domain, $F(\tau)$, as input parameter. Therefore, the procedure detailed in section 5.2.2.1.3 to calculate the coefficients a_n of the Dirac delta train of the impulse response in reflection of the commensurate-line UE prototype, $F_{UE}(\tau)$, will be employed. Taking into account that the length of each commensurate line was determined in section 5.2.4 as $l = 5.36$ mm, then $T_\tau = 2 \cdot l = 10.72$ mm. Since the interpolation is going to be applied for a low-pass response design, the interpolation parameter $m = 2$ must be used, and accordingly, $\beta_{max} = 2 \cdot \beta_0 = 586.116$ rad/m from (5.81). Thus, the target continuous underlying impulse response, $F_c(\tau)$, can be determined by performing the bandlimited interpolation of (5.80). Both impulse responses in reflection, $F_{UE}(\tau)$ and $F_c(\tau)$, are depicted in Fig. 6.4a and the corresponding frequency response for $F_c(\tau)$ is provided in Fig. 6.4b. It must be noticed that the frequency response in reflection of the UE prototype, $S_{11,UE}(\beta)$, and the target one, $S_{11,c}(\beta)$, will coincide in the bandwidth of interest considered for this design case, due to the relationship of (5.85) and thus, the frequency response given in Fig. 6.4b may correspond to both $S_{11,UE}(\beta)$ and $S_{11,c}(\beta)$. Moreover, it is worth noting that the frequency response obtained by following the bandlimited interpolation method in the τ domain is the same that was obtained in section 5.2.4, where the direct β-domain modification of (5.100) is employed to calculate $S_{11,c}(\beta)$.

It is obvious that discretized and non-infinite values of $F_c(\tau)$ are needed to compute the ILP synthesis method and accordingly, the τ axis has been discretized every $T_{D,\tau} = \frac{T_\tau}{40}$ and the duration has been limited to $\tau_{D,max} = 160000 \cdot T_{D,\tau}$. Thus, the resulting z axis will be sampled with a ratio $T_{D,z} = \frac{T_{D,\tau}}{2} = \frac{T_\tau}{80}$ because of (6.15). The length selected for each layer, Δz, will be two times $(M = 2)$ the sampling period of z, i.e. $\Delta z = M \cdot T_{D,z} = 2 \cdot T_{D,z}$ by (6.16). Consequently, $K(z)$ will be defined every $T_{D,z} = \frac{\Delta z}{2}$ but the reflection coefficient will be propagated once per layer, so the propagation will be performed every Δz. Finally, it must be stressed that the length of the synthesized structure, L, will be half of $\tau_{D,max}$, and then $L = \frac{\tau_{D,max}}{2} = 80000 \cdot T_{D,\tau} = 160000 \cdot T_{D,z}$. Taking into account that $\Delta z = 2 \cdot T_{D,z}$, the structure will be divided into $N_L = \frac{L}{\Delta z} = 80000$ layers in z, according to (6.17).

Using these parameters for the definition of the target $F_c(\tau)$, the coupling coefficient is calculated with the ILP method at each m layer by means of (6.14). The reflection coefficient is propagated with (6.10), (6.11) and (6.12). Proceeding in an iterative manner, the coupling coefficient, $K(z)$, that is shown in Fig. 6.5a is obtained.

The corresponding dimensions of the rectangular waveguide device with exclusive variations in its height is obtained by considering $K_b(z) = K(z)$ in (2.130), which is provided below:

$$b(z) = b(0) \cdot e^{-2 \cdot \int_0^z K_b(r) \cdot dr} \tag{2.130}$$

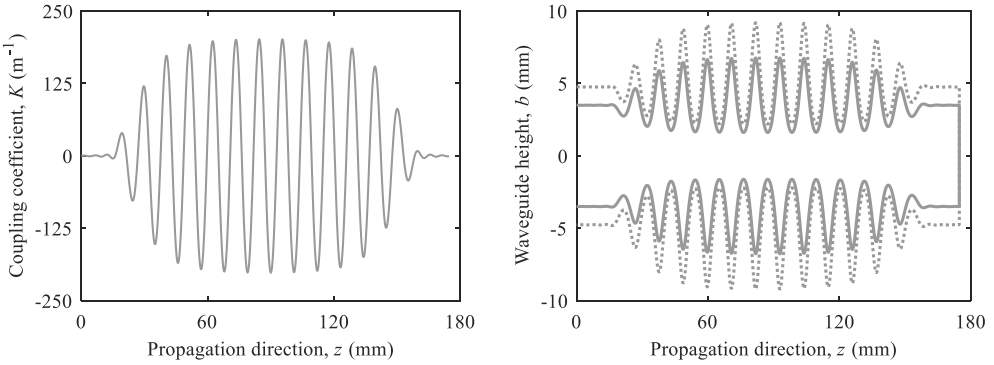

Fig. 6.5. (a) Coupling coefficient, K, along the propagation axis, z, calculated by means of the Integral Layer Peeling method for the target impulse response in reflection, $F_c(\tau)$, of Fig. 6.4. (b) Waveguide height profile, $b(z)$, along the propagation axis, z, calculated from $K(z)$ with $b(0) = 9.525$ mm (grey dotted line) and $b(0) = 7$ mm (grey solid line).

where the height of the WR75 standard was initially selected for the input port, i.e. $b(0) = 9.525$ mm. The waveguide height profile of the structure is shown in Fig. 6.5b. The length of the synthetized structure is L =174.59 mm.

Once the required $K(z)$ has been determined from the target $F_c(\tau) = FT^{-1}\{S_{11,c}(\beta)\}$ with the ILP synthesis method, it is advisable to check if that synthesis technique provided an accurate result or not. For doing so, the target frequency response will be compared with the single-mode analysis that results from the numerical solution of (2.91), (2.92) for the synthetized $K(z)$. The result of this analysis is given in Fig. 6.6, where a remarkable agreement between the target and the analyzed response can be observed, something that confirms the improvement of the accuracy that can be achieved with the use of ILP instead of CLP. In fact, it is suggested to compare the result of ILP of Fig. 6.6 with the one that was shown for CLP in Fig. 5.30.

However, the resulting device features a maximum height of $\max\{b(z)\} = 18.41$ mm, that may be troublesome for the application of the uniform scaling technique detailed in section 2.2.3.1 for the compensation of the reactive effects of cut-off modes. As it was stated in that section, it is very important to ensure that all the relevant higher-order modes are far from the propagation regime along the whole structure. In this case, the first modes that can couple energy with the fundamental TE_{10} are the degenerated TE_{12} and TM_{12} (see section 2.1.2.1). The cut-off frequency of those modes for $\max\{b(z)\}$ can be calculated using the expression (2.50) that results in 18.08 GHz, being a value that is dangerously close to the operational bandwidth, which reaches 15 GHz in our rejection band specifications. In this situation, the performance of the uniform scaling method may not be good enough and thus, the height profile is recalculated for

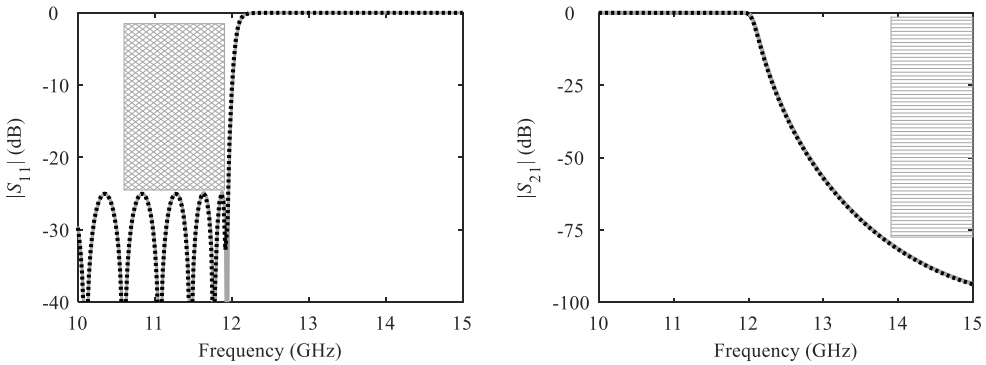

Fig. 6.6. Magnitude of the (a) S_{11} and (b) S_{21}-parameter that correspond to the target frequency response (grey solid lines) and results of the single-mode analysis of $K(z)$ (black dotted lines). The specification masks for the frequency response in terms of return loss (grey diamond pattern) and the rejection level (grey rectangle pattern) are also provided.

$b(0) = 7$ mm (see Fig. 6.5b). With the selected $b(0) = 7$ mm, the resulting $\max\{b(z)\} = 13.52$ mm, and the cut-off frequency of the TE_{12} and TM_{12} modes is increased up to 23.53 GHz, being a value that is sufficiently far from our bandwidth of interest.

However, the use of input ports different from the specified dimensions of the WR75 standard obliges to the employment of tapers in height in order to match the height of the WR75 standard, $b = 9.525$ mm, with the input height of the synthetized filter, $b(0) = 7$ mm. Fortunately, the section 4.2.3.1 is devoted to the synthesis of rectangular waveguide tapers in height. Using the procedure explained in that section, the coupling coefficient of a Hecken taper, $K_{taper}(z)$, is calculated so as to match this difference in height with $RL \geq 40$ dB for a minimum matched frequency of 10.35 GHz, that is far enough from the lowest frequency (10.6 GHz) required for the filter passband (including the design margin). The resulting coupling coefficient for the taper features a length of $L_{taper} = 28$ mm. In order not to increase the length of the filter, L, the tapers will be fully included at both extremes of the filtering structure. For doing so, it can be demonstrated that $K_{taper}(z)$ must be added to the $K(z)$ of the filter at these extremes, in the following manner:

$$K'(z) = \begin{cases} K_{taper}(z) + K(z) & \text{, for } 0 \leq z \leq L_{taper} \\ K(z) & \text{, for } L_{taper} < z < L - L_{taper} \\ -K_{taper}\big(z - (L - L_{taper})\big) + K(z) & \text{, for } L - L_{taper} \leq z \leq L \end{cases} \tag{6.23}$$

where $K'(z)$ is the coupling coefficient for the filter that includes the tapered matching sections at its both extremes. The modified coupling coefficient $K'(z)$ does not notably alter the original $K(z)$ of the filter as it can be observed in their comparison, which is provided in Fig. 6.7a, and hence, the frequency response of the whole structure is expected to be very similar to that of the original filter.

Now, if $K'(z)$ is employed to calculate $b(z)$ using $b(0) = 9.525$ mm in (2.130), the extremes of the structure will implement a combination of the taper profile with the beginning and the end of the filter, while the central part of the structure will be exactly the same as the one that was obtained for the filter with $b(0) = 7$ mm. The comparison between the height profile obtained with $K(z)$ and $b(0) = 7$ mm, and the one resulting from $K'(z)$ and $b(0) = 9.525$ mm, is given in Fig. 6.7b.

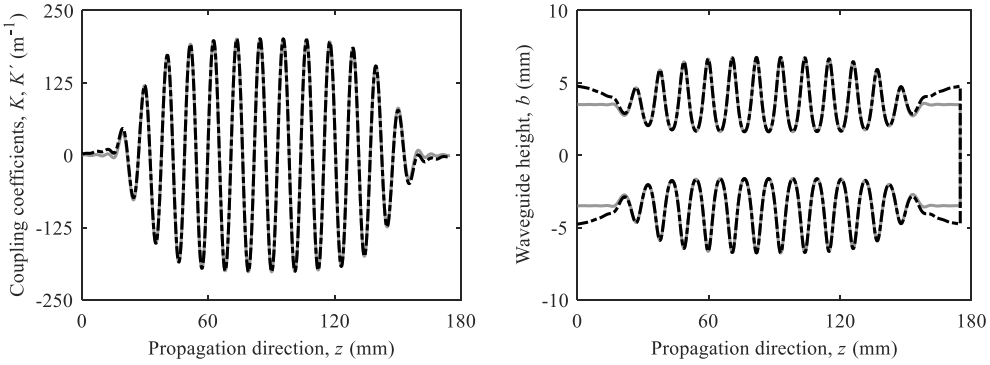

Fig. 6.7. (a) Coupling coefficients $K(z)$ (grey solid line) and $K'(z)$ (black dash-dotted line) along the propagation axis, z. (b) Waveguide height profile, $b(z)$, along the propagation axis, z, calculated from $K(z)$ with $b(0) = 7$ mm (grey solid line) and from $K'(z)$ with $b(0) = 9.525$ mm (black dash-dotted line).

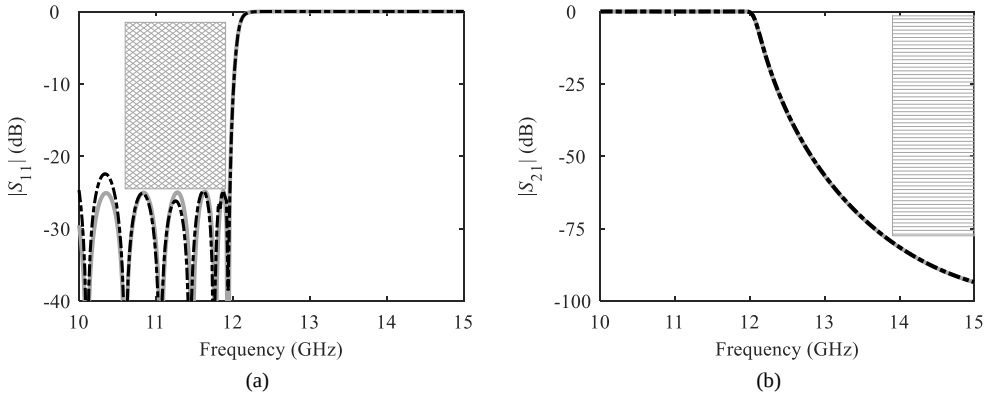

Fig. 6.8. Magnitude of the (a) S_{11} and (b) S_{21}-parameter that correspond to the single-mode analysis performed to $K(z)$ (grey solid lines) and to $K'(z)$ (black dash-dotted lines). The specification masks for the frequency response in terms of return loss (grey diamond pattern) and the rejection level (grey rectangle pattern) are also provided.

As it was expected, the solution of the single-mode coupled-mode equations of (2.91), (2.92) for $K'(z)$ confirms that the addition of the tapers does not degrade the frequency response that was obtained by performing the same analysis but for $K(z)$. The comparison between both single-mode coupled-mode analyses is shown in Fig. 6.8.

It must be highlighted that up to this point, the frequency responses that have been shown resulted from the solution of the coupled-mode equation system of (2.91), (2.92) that assumes single-mode operation. However, if a full-wave CST Microwave Studio simulation is performed for the last tapered structure, see Fig. 6.7b, the result will be quite different from that obtained with the single-mode analysis, as it is clear in view of their comparison of Fig. 6.9. A clear shift

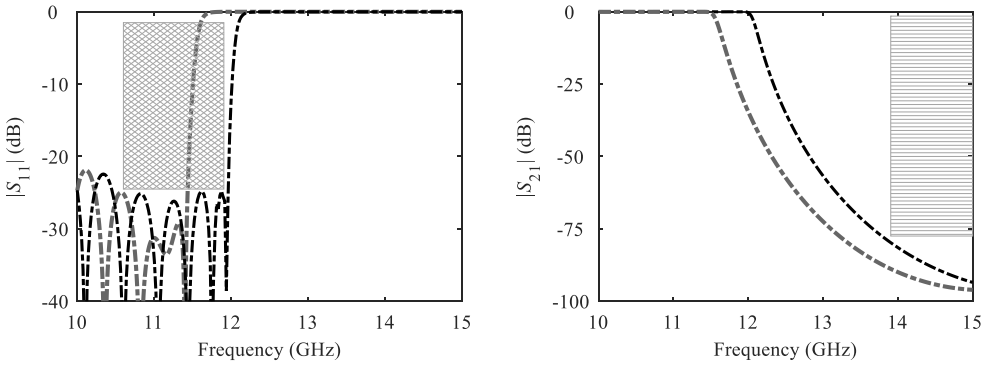

Fig. 6.9. Magnitude of the (a) S_{11} and (b) S_{21}-parameter that correspond to the single-mode analysis performed to $K'(z)$ (black dash-dotted lines) and results of the CST simulation of the same structure (grey dash-dotted lines). The specification masks for the frequency response in terms of return loss (grey diamond pattern) and the rejection level (grey rectangle pattern) are also provided.

of the expected frequency response is registered when the effects of higher-order modes are taken into account in the full-wave CST Microwave Studio simulation.

In order to compensate for the reactive impact of the cut-off modes, the uniform scaling method of section 2.2.3.1 will be employed. For doing so, all the coupling coefficients of the form $C_{m,i} = C_{1,i}$ for all the relevant modes for which the coupling is not null need to be firstly calculated (see section 2.1.2.1) using (2.74), (2.75), and (2.76). In this case, where symmetrical variations in height are performed, the modes that interact between each other are the TE_{pq} with $p = 1$ and $q = 0, 2, 4, \ldots, \infty$ and the TM_{pq} with $p = 1$ and $q = 2, 4, 6, \ldots, \infty$. Since $m = 1$ in $C_{m,i}$, the $m = 1$ index refers to the forward travelling wave of the fundamental TE_{10} mode, while the i index corresponds to the rest of the listed TE_{pq} and TM_{pq} modes (including their forward $(i > 0)$ and backward $(i < 0)$ travelling waves). Due to the fact that a finite number of modes must be employed for the numerical calculations, the subindex q has been limited in both TE and TM modes up to $q = 128$ for the solution of the general coupled-mode equation system of (2.44), where one equation of this form is included for each considered mode:

$$\frac{da_m}{dz} + j \cdot \beta_m \cdot a_m = \sum_i a_i \cdot C_{mi} \tag{2.44}$$

By solving the equation system of (2.44) for $f_t = f_c = 11.95$ GHz (see section 2.2.3), the complex amplitudes of all the considered modes, a_1 and a_i, along the propagation axis will be determined, and thus, the average effective phase constant, $\bar{\beta}_{eff}(f_t)$, can be calculated using the expression (2.227), although applied just to the core of the filter where the coupling is high:

$$\bar{\beta}_{eff}(f_t) = \frac{\int_{z_0}^{z_1} \beta_{eff}(f_t) \cdot dz}{z_1 - z_0} \tag{6.24}$$

where β_{eff} is the effective phase constant at each z-point that encompasses the phase constant of the fundamental mode, β_1, and the reactive contributions of the cut-off modes, as it can be seen in the expression (2.222) that is rewritten again here for the sake of clarity:

$$\beta_{eff}(f_t) = \beta_1(f_t) - Im\left\{\sum_{|i|>1} \frac{C_{1,i}(f_t) \cdot a_i(f_t)}{a_1(f_t)}\right\} \tag{2.222}$$

Applying the calculation of (2.222) and (6.24) from $z_0 = 50$ mm to $z_1 = 125$ mm in order to take into account the core of the filter where the coupling is high (see Fig. 6.7a), an average effective phase constant, $\bar{\beta}_{eff} = 206.66$ rad/m is calculated. Therefore, the scaling factor, ψ, that must be applied to the z axis will be determined from (2.230) that is given again here:

$$\psi(f_t) = \frac{\bar{\beta}_{eff}(f_t)}{\beta_1(f_t)} \tag{2.230}$$

Taking into account that $\bar{\beta}_{eff} = 206.66$ rad/m and $\beta_1(f_t) = \beta_c = 188.496$ rad/m (see Table 6.1), the scaling factor will be obtained from (2.230) as $\psi(f_t) = \frac{206.66\ rad/m}{188.496\ rad/m} = 1.098$. Then, the necessary scaling $\frac{z}{\psi}$ is performed for the final z-axis, while the initial amplitude of $K'(z)$ must be multiplied by ψ, according to the scaling property of (2.229) that is being applied. The result of the compensated coupling coefficient is depicted in Fig. 6.10a, while its associated $b(z)$ profile is calculated using $b(0) = 9.525$ mm (WR75 standard) in (2.130). In these figures, the original $K'(z)$ (Fig. 6.10a) and $b(z)$ (Fig. 6.10b) without the compensation of cut-off modes are also provided for the sake of completeness. The length of the final structure is 159.3 mm.

A new CST Microwave studio simulation is performed for the compensated structure and its results are shown in Fig. 6.11, together with the single-mode simulation of $K'(z)$ and the CST simulation of the non-compensated structure that was previously provided in Fig. 6.9. As it can be observed, the uniform scaling method has compensated the parasitic reactive effects of cut-off modes that prevented the fulfillment of the passband requirements prescribed by the mask of Fig. 6.9. As a consequence, the results of the CST simulation for the compensated filter almost fit the behavior predicted by the single-mode analysis of $K'(z)$, and the requirements for RL and rejection level of the frequency response are fulfilled.

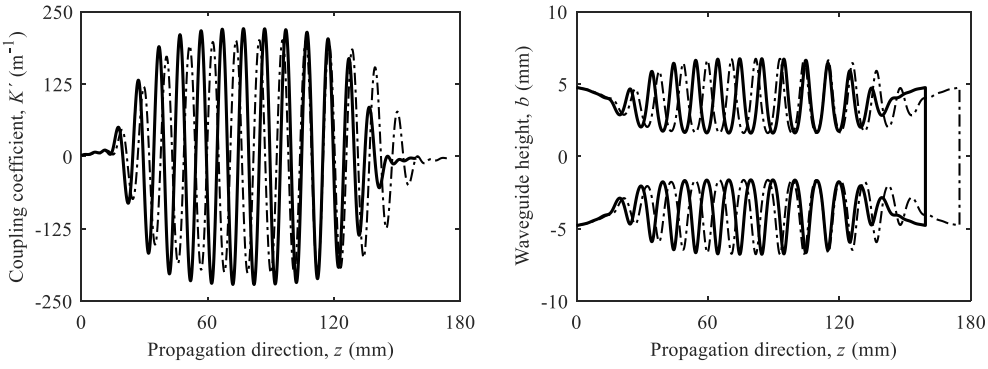

Fig. 6.10. (a) Coupling coefficient, K', and (b) associated waveguide height profile, b, along the propagation axis, z, before (black dash-dotted line) and after (black solid line) performing the compensation of cut-off modes.

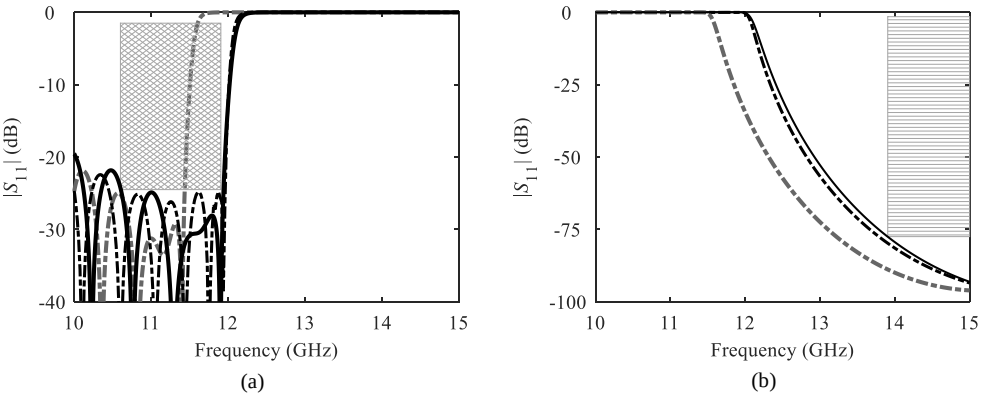

Fig. 6.11. Magnitude of the (a) S_{11} and (b) S_{21}-parameter that correspond to the single-mode analysis performed to $K'(z)$ (black dash-dotted lines), results of the CST simulation of the same structure (grey dash-dotted lines) and results of the CST simulation of the structure obtained after applying the cut-off mode compensation (black solid lines). The specification masks for the frequency response in terms of return loss (grey diamond pattern) and the rejection level (grey rectangle pattern) are also provided.

The designed structure was fabricated in a single piece, by means of the DMLS Additive Manufacturing technique, by growing it following the propagation direction, z. The sintering system was the EOS EOSint M 280 [7] and the printing powder was the AlSi10Mg aluminum alloy, which was sintered in layers of nominal thickness of 100 μm. Once the sintering process finished, the excessive roughness of both port flanges was corrected by performing a polishing procedure. A photograph of the prototype is shown in Fig. 6.12.

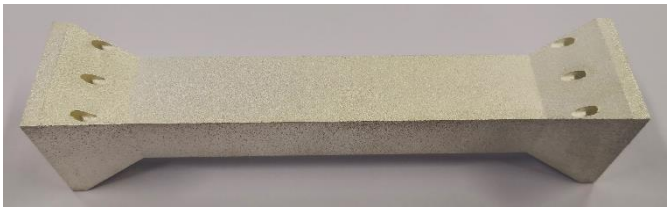

Fig. 6.12. Photograph of the WR75 Chebyshev filter fabricated with DMLS in AlSi10Mg and subsequently coated with a 40 µm silver layer.

At this point, it must be highlighted that one of the most troublesome aspects from the point of view of Additive Manufacturing in metals is the existence of overhanging surfaces perpendicular to the growing direction, because they would eventually warp or even fall off. Unfortunately, if we try to print a device designed by classical techniques in the propagation direction, we will find plenty of problematic overhanging walls. Since it is commonly impossible to use inner auxiliary supports in a waveguide structure, the remaining option is to print the piece in a different orientation with the help of external auxiliary supports that must be designed ad-hoc for each different structure.

On the other hand, the ILP method automatically produces smooth profiles that avoid large overhanging layers and hence, the parts are directly suitable for a DMLS fabrication, unlike other approaches where the geometry of a classical filter is modified so as to allow a DMLS fabrication [8]. Moreover, these smooth profiles can be grown by following the propagation direction without using additional inner and/or outer auxiliary supports, something that clearly eases the printing process while reducing the costs as well as the insertion losses, since the staircase effect [8] is minimized.

Finally, the fabricated filter was measured using an Agilent E8364B PNA vector network analyzer, proper waveguide-to-coaxial transitions and a calibration kit. A good agreement is achieved between simulation and measurement results, as it can be seen in Fig. 6.13. Moreover, the required frequency specifications are completely met. The small discrepancies found, like the slight frequency shift, can be explained by the fabrication tolerances and the high loss level introduced by the AlSi10Mg aluminum alloy. In fact, the insertion loss, IL, reaches a worst value of $IL = 0.87$ dB at the upper limit of the passband (11.65 GHz). In order to reduce the losses, the filter was coated with a 40 µm silver layer and a new set of measurements were done. In the inset of Fig. 6.13 it can be appreciated that the IL turn to 0.15 dB as a consequence of the silver coating and the performance of the filter gets notably improved.

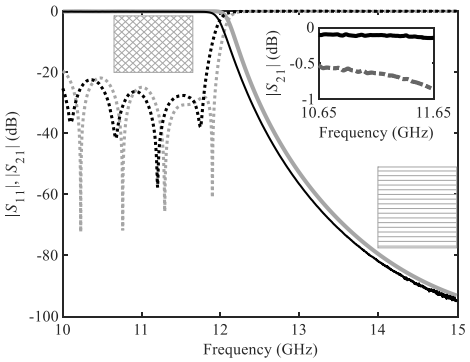

Fig. 6.13. Magnitude of the S_{11} (dotted lines) and S_{21}-parameter (solid lines) that correspond to the CST simulation of the filter obtained after applying the cut-off mode compensation (grey lines), and to the measurements (black lines). In the inset, a detail of the $|S_{21}|$-parameter is provided, where the grey dash-dotted line corresponds to the measurements made before silver plating. The specification masks for the filter performances in terms of return loss (grey diamond pattern) and the minimum rejection level (grey rectangle pattern) are also provided.

The results obtained confirm the accuracy of the ILP synthesis technique as well as the effectiveness of the compensation procedure for the effects of cut-off modes.

On the other hand, the inherent benefits of a smooth-profiled filter for a final DMLS fabrication have been proved, since the manufactured prototype complied with all the required specifications with a remarkable agreement with the results obtained in simulation.

6.2.2. High Performance Modified Zolotarev Low-Pass Filter in Rectangular Waveguide

In this section, the design procedure developed in section 5.2 for the design of rectangular waveguide low-pass filters will be further exploited in order to obtain a high performance device in terms of length and rejection level. As it has been seen in the previous section 6.2.1, the 25-th order Chebyshev response achieved the desired frequency specifications with a filter length of 159.3 mm. In the design process that will be carried out in this section, several criterions will be followed so as to minimize the length of the filter while ensuring the compliance of the same requirements that were demanded for the 25-th order Chebyshev low-pass filter. Specifically, the design security margins will be trimmed and a frequency response more selective than the canonical low-pass Chebyshev will be used. Moreover, the values of the starting UE prototype

will be properly optimized so as to generate a filter response adequate to subsequently synthetize a smooth-profiled structure that will feature safe dimensions for a final DMLS fabrication.

Firstly, it is necessary to recall the requirements that must be satisfied by the final filter: the passband will be defined from 10.65 to 11.65 GHz with $RL \geq 20$ dB, while a minimum rejection level of 80 dB must be guaranteed for the stopband located between 14 GHz and 15 GHz. However, as it was previously explained, it is necessary to include security margins for the target frequency response of the initial UE prototype so as to prevent the possible effects caused by the nominal deviations of ±100 μm of the DMLS fabrication technique. However, in order to achieve a shorter filter in the current design, the passband of the target frequency response will be fixed from 10.6 GHz to 11.75 GHz, with a minimum RL of 25 dB. Regarding the required rejection level in the stopband, a minimum of 80 dB must be achieved from 13.8 GHz up to 15 GHz. The waveguide standard to be employed for the implementation will be WR75, which features a width, $a = 19.05$ mm and a height $b = 9.525$ mm.

In order to synthetize a rectangular waveguide filter intended to meet the aforementioned requirements in terms of frequency response and fabrication aspects, the first task is to select a starting commensurate-line UE prototype that also satisfies those specifications. It must be highlighted that this choice represents a critical design step, since the smooth-profiled structure that will be synthetized using ILP with an interpolated version of the impulse response of that initial UE prototype, will feature similar physical dimensions (length and heights) to the ones of the initial UE prototype. Thus, the transitions between adjacent UEs exhibited by the initial commensurate-line UE prototype will provide an intuitive knowledge of the angles that will be eventually found in the synthetized smooth structure. In fact, the transitions of the starting UE prototype can be controlled by means of two design parameters of the filter: its order, N, and the frequency of the highest rejection level, f_0 (or its corresponding phase constant, β_0). If the order of the filter is increased while the rejection level is kept constant (at a certain frequency), the difference in characteristic impedance (or equivalently in height for rectangular waveguide technology) between any consecutive UEs will be reduced, and the resulting angle in the synthetized smooth filter will be smaller as a result. On the other hand, when the value of f_0 is reduced while maintaining the filter order constant, the length of the commensurate-line sections, l, is increased, since that length has an inverse proportional relationship with β_0, see (5.96). Thus, the distance between the midpoints of two consecutive line sections becomes longer in the UE prototype, and the corresponding transition between a maximum and a minimum in the height of the synthetized smooth structure will feature less abrupt angles. It is worth noting that increasing the order and reducing the value of f_0 make the initial commensurate-line UE prototype longer, so the synthetized smooth filter will be longer as well. Therefore, a trade-off

solution must be reached between the largest angle that can be fabricated and the maximum affordable length for the filter, in terms of insertion losses, longest footprint allowed and maximum building volume of the sintering system.

Regarding the specific case of this design example, an initial all-pole N = 21-st order Zolotarev low-pass response was selected, since it will provide less abrupt transitions between adjacent UEs than a Chebyshev response of the same order and cut-off frequency (while being slightly more selective) [9], something that is desirable for an eventual DMLS fabrication because of the reasons previously commented. The frequency selected to exhibit the highest rejection level was f_0 = 17.568 GHz, which corresponds to a phase constant of β_0 = 329.201 rad/m, that can be calculated employing (2.117):

$$\beta(f) = \frac{2 \cdot \pi \cdot f}{c} \cdot \sqrt{1 - \left[\frac{f_c^{TE_{10}}}{f}\right]^2} \tag{2.117}$$

where $f_c^{TE_{10}}$ is calculated for the width of the WR75 standard ($a = 19.05$ mm), according to (2.118).

The upper value of the passband (including security margin) was taken as the cut-off frequency of the filter, i.e., f_c = 11.75 GHz, leading to a cut-off phase constant of β_c = 182.889 rad/m. Furthermore, the value selected for the minimum frequency of the passband was f_{Zolo} = 8.298 GHz, yielding to an associated phase constant β_{Zolo} = 55.199 rad/m. Since β_0, β_c and β_{Zolo} are known, and taking into account that all the line sections of the UE prototype have identical electrical length at β_0 of $\theta_0 = \frac{\pi}{2}$ rad, the electrical length of the lines for β_c and β_{Zolo} can be also determined by (5.42), being θ_c = 0.873 rad and θ_{Zolo}= 0.263 rad.

Finally, the frequency parameters of the 21-st order all-pole normalized Zolotarev response can be calculated by means of (5.49), i.e., the normalized cut-off frequency has the typical value of ω_c = 1 rad/s, the normalized minimum frequency of the passband is ω_{Zolo} = 0.34 rad/s, while the normalized frequency that specifies the highest rejection level that will be achieved with the commensurate-line UE prototype is $\omega = \alpha =$ 1.305 rad/s, see Fig. 5.8.

Unit Element	Zolotarev heights (mm)	Modified heights (mm)
$b_S = b_L$	9.525	9.525
$b_1 = b_{21}$	5.914	5.510
$b_2 = b_{20}$	10.838	9.284
$b_3 = b_{19}$	2.933	2.446
$b_4 = b_{18}$	7.946	7.646
$b_5 = b_{17}$	1.412	2.057
$b_6 = b_{16}$	4.100	9.185
$b_7 = b_{15}$	0.646	2.253
$b_8 = b_{14}$	1.989	9.525
$b_9 = b_{13}$	0.337	2.153
$b_{10} = b_{12}$	1.217	8.882
b_{11}	0.259	1.984

Table 6.3. Values of the Unit Elements for the pure and the modified Zolotarev prototypes.

Once the normalized frequency values, ω_c, ω_{Zolo} and α, have been defined, the normalized all-pole low-pass Zolotarev response is completely determined. Then, using (5.51), the normalized response can be translated to the Richards transform domain, see section 5.2.1. Finally, the values of the Unit Elements of the commensurate-line UE prototype that satisfies the intended frequency response can be calculated as explained in section 5.2.1. The results are given in Table 6.3.

It must be highlighted that the minimum height of the commensurate-line UE prototype of the Zolotarev filter is $b_{11} = 0.259$ mm, which is a value that may become problematic for the DMLS manufacturing tolerances (±100 μm), even more if it is recalled that the final smooth filter will feature similar physical dimensions to those of the initial UE prototype. In order to find more suitable dimensions for the initial commensurate-line UE prototype, an optimization procedure was performed using *Keysight Genesys* by requiring a minimum UE value (height in

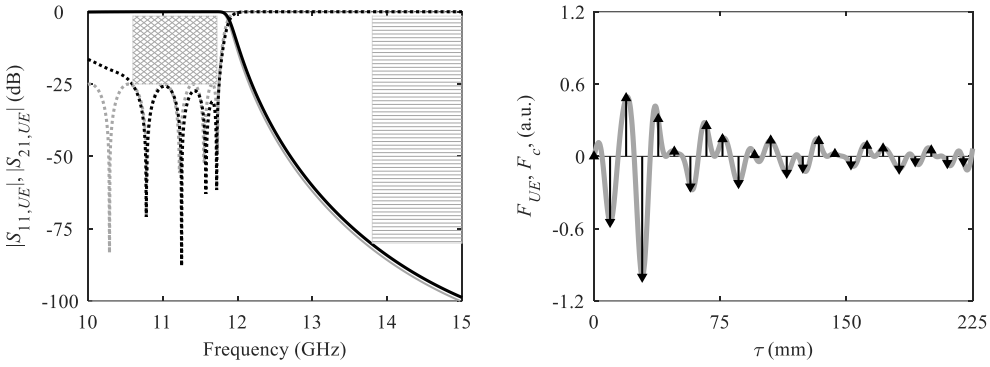

Fig. 6.14. (a) Comparison between the frequency responses of the Zolotarev (grey lines) and the modified-Zolotarev (black lines) commensurate-line UE prototypes: magnitude of S_{11} (dotted lines) and S_{21} (solid lines) parameters. The specifications for the frequency response (including security margins) for the return loss (rhombus-based pattern mask) and for the rejection level (rectangle–based pattern mask) are also included for a sake of clarity. (b) Impulse response in reflection of the modified-Zolotarev UE prototype (black line),F_{UE}, along the τ axis, and its corresponding underlying continuous version (grey line), F_c, obtained after applying the interpolation method with $m = 2$.

our case of rectangular waveguide) of 1.750 mm and a maximum UE value (height) of 9.525 mm for the commensurate-line prototype, while still demanding the fulfillment of the requirements made for the frequency response. This optimization procedure gave rise to a modified Zolotarev commensurate-line prototype that features the UE dimensions gathered in Table 6.3. A comparison between the frequency responses of the canonical and modified Zolotarev UE prototypes is shown in Fig. 6.14a, where the masks required for the return loss and rejection level are also included for the sake of completeness.

Once a valid commensurate-line UE prototype was found, its impulse response in reflection was calculated by means of the procedure detailed in section 5.2.2.1.3. Then, the interpolation method explained in sections 5.2.2.1.1 and 5.2.2.1.2 was applied in order to obtain the underlying continuous impulse response in reflection. An interpolation parameter m = 2 was selected in (5.81) since a low-pass filter response was desired, leading to $\beta_{max} = 2 \cdot \beta_0$ in (5.80). A discretization period of $T_{D,\tau} = T_\tau/40$ was employed for an impulse response defined between $\tau_{D,n=0} = 0$ m and $\tau_{D,max} = 8000 \cdot T_\tau$, leading to a corresponding frequency response in reflection that was defined from $\beta_{D,n=0} = 0$ rad/m up to $\beta_{D,max} = 40 \cdot \beta_0$, every $\Delta\beta = \beta_0/2000$. Actually, the "interpft.m" *Matlab* function can be employed to efficiently implement (5.80), leading to the interpolated impulse response in reflection, $F_c(\tau)$, that is shown in Fig. 6.14b. Nevertheless, it must be pointed out that $m - 1$ samples with zero value must be inserted between each pair of samples of $F_{UE}(\tau)$ in order to properly compute (5.80) with "interpft.m".

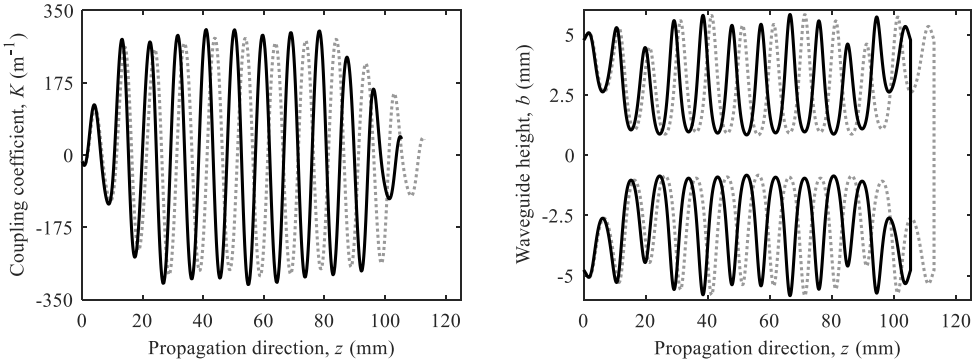

Fig. 6.15. (a) Coupling coefficient, K, along the propagation axis, z, calculated using the Integral Layer Peeling method for the interpolated impulse response in reflection of the modified-Zolotarev UE prototype: original synthesis (grey dotted line) and final coupling coefficient (black solid line) that was calculated after the cut-off modes compensation. (b) Waveguide height profile, $b(z)$, associated with both versions of $K(z)$: before (grey dotted line) and after cut-off mode compensation (black solid line).

Once the target interpolated impulse response in reflection, $F_c(\tau)$, was determined, the ILP synthesis technique was applied, using a layer thickness of $\Delta z = 3 \cdot T_{D,z} = 3 \cdot \frac{T_{D,\tau}}{2} = \frac{3 \cdot T_\tau}{80}$ (i.e. three times the discretization period that was chosen for the propagation axis, $T_{D,z}$), to calculate the required $K(z)$ that is shown in Fig. 6.15a, in grey dotted line. The length of the synthetized structure is L= 113 mm. It is interesting to note that the Fast Fourier Transform (FFT) algorithm was employed to efficiently compute the integral of (6.11). As it has been explained in section 6.1.2, when using the FFT to compute (6.11) in the calculation of the frequency response propagation, the coupling coefficient must be computed using equations (6.20) and (6.22).

Once $K(z)$ has been calculated, the waveguide height profile along the propagation direction, $b(z)$, is immediately known by applying (2.130) with an input port height of the WR75 standard, i.e., $b(0) = 9.525$ mm. The attained height profile is depicted in Fig. 6.15b, in grey dotted line. The maximum height obtained for the synthetized structure is $\max\{b(z)\} = 11.67$ mm. The cut-off frequency of the closest higher-order modes (TE_{12} and TM_{12}) for that $\max\{b(z)\}$ is 26.87 GHz by (2.50), being a value higher than that obtained for the 25-th order Chebyshev filter synthetized in the previous section 6.2.1, even when $b(0) = 7$ mm was chosen. Therefore, the profile obtained by means of $b(0) = 9.525$ mm can be maintained for the subsequent stage of cut-off modes compensation. It is worth noting that the direct use of the required WR75 standard port avoids the need of additional tapers, as well as their extra design stage. Furthermore, it must be stressed that the minimum mechanical gap of the synthetized structure is 1.67 mm, being a gap high enough to be safely fabricated with the DMLS technique.

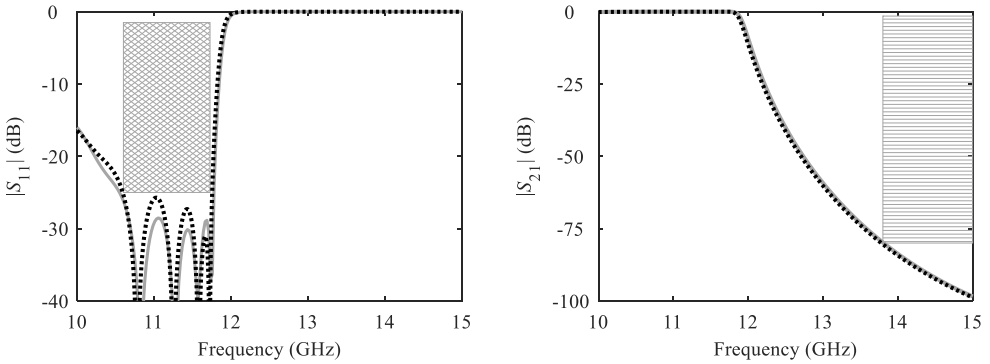

Fig. 6.16. Comparison between the (a) S_{11} and (b) S_{21}-parameter of the target frequency response (black dotted line) and of the single-mode simulation (grey solid line) of the modified-Zolotarev filter. The specifications required (including security margins) for the return loss (rhombus-based pattern mask) in (a) and for the rejection level (rectangle –based pattern mask) in (b) are also included for a sake of clarity.

In order to verify the accuracy of the ILP synthesis, the single-mode coupled-mode equation system of (2.91), (2.92) was solved, leading to the frequency responses that are shown in Fig. 6.16. As it can be seen in these graphs, the synthesis has been accurate enough to provide $|S_{11}|$ and $|S_{21}|$-parameters that fulfil the return loss and rejection level requirements, respectively.

In order to determine the scaling factor, $\psi(f_t)$, which is needed to compensate for the reactive coupling to cut-off modes, the first step is to analyze the synthetized structure using the coupled-mode equation system of (2.44) for a frequency, f_t. The value selected for this frequency was $f_t = f_c = 11.75$ GHz in order to adjust the cut-off frequency of the filter with the highest accuracy. As it has been previously calculated, the corresponding phase constant for $f_t = f_c$ in the case of the fundamental TE_{10} mode is $\beta_1(f_t = f_c) = 182.889$ rad/m. For the correction of the effects of cut-off modes in a rectangular waveguide structure that only features symmetrical variations in its height (see section 2.1.2.1), the relevant higher-order modes are the TE_{pq} as well as the TM_{pq} with $p = 1$ and $q = 2, 4, 6, ...$ The coupling coefficients between all these modes and the fundamental TE_{10} ($m = 1$), $C_{m,i} = C_{1,i}$, can be calculated using (2.74), (2.75), and (2.76). Once all the necessary coupling coefficients were calculated, the equation system of (2.44) was solved numerically using the *Matlab* function "bvp4c.m". Due to the fact that a finite number of modes must be selected in order to compute (2.44), a maximum $q = 128$ was chosen for both TE and TM modes, leading to an effective phase constant, β_{eff}, that was calculated by means of (2.222), ensuring that the number of cut-off modes that were taken was enough to obtain an average effective phase constant that converged to a fixed value of $\bar{\beta}_{eff}$= 196.65 rad/m, using

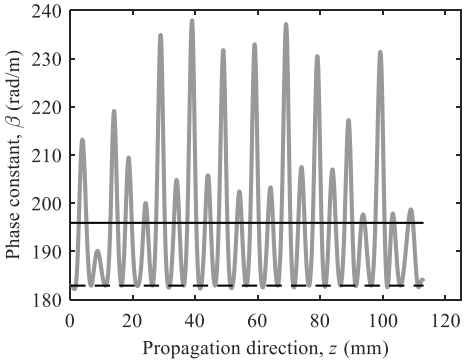

Fig. 6.17. Phase constant of the fundamental TE_{10} mode for a frequency $f_t = 11.75$ GHz (black dashed line), effective phase constant caused by cut-off modes, β_{eff}, along the propagation direction, z, for the same frequency (grey line), and its average value, $\bar{\beta}_{eff}$, (black solid line).

(6.24) for the whole structure (from $z_0 = 0$ to $z_1 = L$). The effective phase constant at f_t = 11.75 GHz, β_{eff}, as well as its average value, $\bar{\beta}_{eff}$, and the phase constant at that frequency for the TE_{10} fundamental mode, β_1, are shown in Fig. 6.17.

Thus, a value of the scaling factor, $\psi(f_t) = 1.075$, is obtained by means of (2.230). Finally, the scaling factor is applied to z yielding to a new propagation axis and a new coupling coefficient, $K \cdot \psi(f_t)$, along the $z/\psi(f_t)$ propagation axis, according to (2.229). The resulting coupling coefficient is depicted in Fig. 6.15a, where it is also compared with the one that was originally obtained from the ILP synthesis. The final waveguide height dimensions of the filter are calculated again using (2.130) with $b(0) = 9.525$ mm (WR75 standard port). The height profile of the structure along the scaled propagation axis is shown in Fig. 6.15b, in black solid line. The designed waveguide filter features a final length of 105 mm, which implies the 65.9% of the length of the 25-th order Chebyshev filter of section 6.2.1. It must be highlighted that this reduction in size becomes more remarkable if it is taken into account that both structures have been designed to satisfy the same final specifications.

The final filter was simulated with CST Microwave Studio and the results, shown in Fig. 6.18, confirm the fulfilment of all the required specifications for the frequency response, as it can be seen from their corresponding masks also included in the graph. The modified-Zolotarev filter was fabricated in a single piece, by means of the Additive Manufacturing DMLS technique, employing an EOS EOSint M280 system [7] and using AlSi10Mg alloy as the material for the sintering powder. The structure was grown in vertical direction, i.e., following the propagation axis, z. As it has been previously stated, the choice of this direction has two clear advantages:

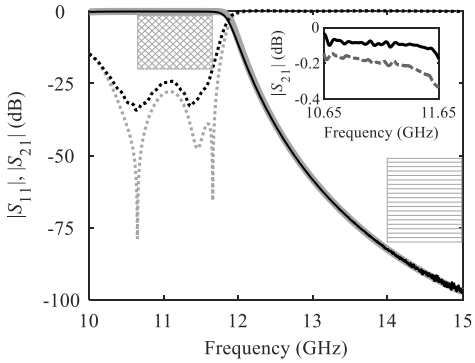

Fig. 6.18. Comparison of the S_{11} (dotted lines) and S_{21} (solid lines)-parameters obtained from the CST simulation (grey lines) and from the measurement (black lines). The specifications required for the return loss level (rhombus-based pattern mask) and for the rejection level (rectangle –based pattern mask) are also included for a sake of clarity. In the inset a detail of the S_{21} measurement before (dashed line) and after silver plating (black line) is given.

Fig. 6.19. Photograph of the final WR75 modified-Zolotarev low-pass filter fabricated by means of Additive Manufacturing DMLS technique.

the first one is that additional supporting structures were not needed since the filter neither features overhanging walls nor critical angles greater than 45º, and consequently, we can consider the synthetized filter as a self-supporting structure in that direction. Moreover, the staircase effect [8] is minimized leading to a reduction of the insertion loss caused by this effect. Once the filter was fabricated, a mechanical post-processing procedure that consisted in polishing both port flanges was performed, looking for an improvement of their flatness as well as a significant reduction of their roughness, since the surface finish quality of these zones may become critical in a subsequent characterization stage.

At this point, the filter was measured using an Agilent E8364B PNA vector network analyzer and the obtained results are depicted in Fig. 6.18. A very good agreement between the simulation and measurement results can be observed and the compliance of the frequency specifications is guaranteed. The slight differences that can be found may be attributed to the DMLS fabrication tolerances. In order to minimize the insertion losses, an additional post-processing step was applied by performing a silver coating of 20 µm of thickness over the whole surface of the structure. A photograph of the final filter is provided in Fig. 6.19. The filter was again measured after the aforementioned silver-plating process by also using the same set-up as

in the first characterization, see the inset of Fig. 6.18. As it was expected, a remarkable reduction of the insertion loss is achieved, and a final worst value of these losses is obtained at the upper limit of the passband with a value of 0.17 dB.

The high quality of the obtained results confirms the reliability of the design method for high-performance rectangular waveguide filters. Moreover, the suitability of the smooth-profiled waveguide structures that result from ILP for a subsequent direct DMLS fabrication was again proved, as it can be concluded in view of the level of agreement reached between the simulation and measurement results.

6.2.3. Zolotarev Low-Pass Filter with Accurate Compensation of Parasitic Effects of Cut-Off Modes

Up to this point, the design processes that have been previously presented within this section 6.2 (25-th order Chebyshev and 21-st order modified-Zolotarev) were successfully completed by using the uniform scaling method for the compensation of the reactive effects caused by the cut-off modes in the frequency response. In both examples, the addition of higher-order modes to the single-mode simulation mainly resulted in a slight frequency shift, without further degradation in the shape of the frequency response. Thus, the uniform scaling method obtained a good performance by compensating the undesired frequency shift with a uniform compression of the propagation axis. The compression ratio is obtained as a function of the fundamental mode and the average effective phase constants. However, it must be noted that the addition of higher-order modes may involve more noticeable effects than a simple frequency displacement, being also typical the deterioration of the S_{11}-parameter along the passband that leads to the infringement of the RL specifications. Thus, in the following design procedure of a genuine 21-st order Zolotarev low-pass filter, it will be shown a strongly degraded passband case, and the performance of the uniform scaling compensation method will be compared with the application of the recursive distributed scaling technique that was thoroughly explained in section 2.2.3.2.

Unlike the low-pass filter design cases of the 25-th order Chebyshev of section 6.2.1 and the high-performance modified-Zolotarev of section 6.2.2, the specifications that will be required for this filter are a passband defined from 10 GHz to 11.75 GHz with $RL \geq 20$ dB, and a

stopband from 14 GHz to 15 GHz with a minimum rejection level of 60 dB. Thereby, following the design security criterion, the demanded requirements for the frequency response of the Zolotarev commensurate-line UE prototype will be a safety margin of 5 dB, i.e. $RL \geq 25$ dB, for a passband that will be extended up to 11.95 GHz, while the minimum rejection level of 60 dB must be guaranteed beyond 13.9 GHz. The waveguide standard for the physical implementation of the filter will be WR75, with $a = 19.05$ mm and $b = 9.525$ mm.

As in the previous design examples, the first step is to find a suitable commensurate-line UE starting prototype. The lower passband frequency for the Zolotarev response was fixed to $f_{Zolo} = 8.08$ GHz, whereas the cut-off frequency of the filter was selected as the upper limit of the passband, $f_c = 11.95$ GHz. The maximum rejection frequency was fixed to $f_0 = 15.80$ GHz. The different frequency translations needed to achieve the normalized response and the UE prototype are summarized in Table 6.4: from f to β (2.117), from β to θ (5.42), and from θ to ω (5.49).

A minimum order $N = 21$ was estimated in order to comply with the specifications for the frequency response, and the length of each commensurate line, $l = 5.47$ mm, was determined from (5.98). Once the normalized all-pole Zolotarev frequency response was achieved, it was translated to the Richards transform domain by means of (5.51) and the UEs provided in Table 6.5 were determined following the procedure explained in section 5.2.1.

Frequency, f (GHz)	Phase constant, β (rad/m)	Electrical length, θ (rad)	Normalized frequency, ω (rad/s)
$f_{Zolo} = 8.08$	$\beta_{Zolo} = 384.86$	$\theta_{Zolo} = 0.21$	$\omega_{Zolo} = 0.243$
$f_c = 11.95$	$\beta_c = 188.496$	$\theta_c = 1.03$	$\omega_c = 1$
$f_0 = 15.80$	$\beta_0 = 287.158$	$\theta_0 = \pi/2$	$\alpha = 1.166$

Table 6.4. Summary of the different translations for the frequencies f_{Zolo}, f_c and f_0 that define the starting 21-st order Zolotarev commensurate-line UE prototype and their associated frequency transformations.

Unit Element	Zolotarev heights (mm)
$b_S = b_L$	9.525
$b_1 = b_{21}$	7.336
$b_2 = b_{20}$	10.528
$b_3 = b_{19}$	5.182
$b_4 = b_{18}$	10.664
$b_5 = b_{17}$	3.887
$b_6 = b_{16}$	9.450
$b_7 = b_{15}$	3.104
$b_8 = b_{14}$	8.142
$b_9 = b_{13}$	2.655
$b_{10} = b_{12}$	7.397
b_{11}	2.508

Table 6.5. Values of the Unit Elements for the 21-st order Zolotarev commensurate-line prototype.

In this case, the target $S_{11,c}(\beta)$ for the smooth-profiled filter has been obtained following the direct β-domain approach of section 5.2.2.2. Firstly, the transmission matrix of the starting UE prototype is calculated by cascading the corresponding N matrices of each commensurate-line section. Then, the $S_{11,UE}(\beta)$-parameter of the starting UE prototype is calculated from its transmission matrix through (5.94) and (5.95). The obtained $S_{11,UE}(\beta)$, and its associated $S_{21,UE}(\beta)$, for the case under study are depicted in Fig. 6.20a and Fig. 6.20b, respectively. Finally, the target $S_{11,c}(\beta)$ that is also shown in Fig. 6.20a is achieved by applying (5.100) for the low-pass filter case of $m = 2$. The magnitude of $S_{21,c}(\beta)$ is also provided in Fig. 6.20b.

The target $S_{11,c}(\beta)$ was numerically defined up to $\beta_{D,max} = 50 \cdot \beta_0$ with a sample every $\Delta\beta_D = \frac{\beta_0}{1000}$. The $S_{11,c}(f)$ is provided, with the specification masks, in Fig. 6.21a for the sake of clarity.

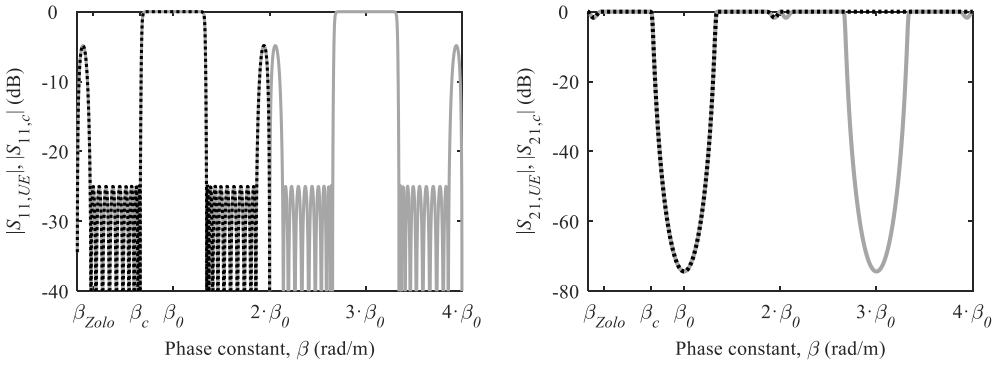

Fig. 6.20. Frequency response of the Zolotarev UE prototype (grey solid lines) and subsequent target response for the ILP synthesis (black dotted lines) with their most relevant parameters in β domain: (a) $|S_{11}|$ and (b) $|S_{21}|$-parameters.

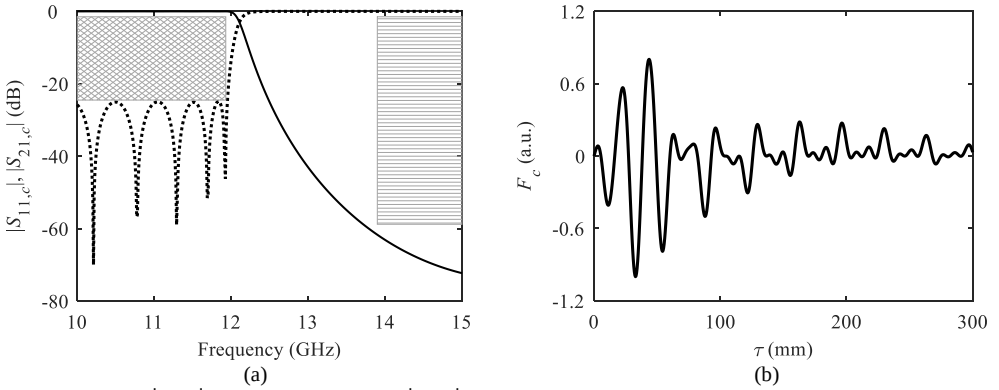

Fig. 6.21. (a) $|S_{11,c}|$ (black dotted line) and $|S_{21,c}|$ (black solid line) of the target frequency response for the ILP synthesis, obtained from the bandlimited response of the starting Zolotarev UE prototype, $|S_{11,UE}|$. The specification masks for the frequency response in terms of return loss (grey diamond pattern) and rejection level (grey rectangle pattern) are also provided. (b) Target continuous response in reflection in τ, $F_c(\tau)$, obtained as the inverse Fourier transform of $|S_{11,c}|$.

Once the target $S_{11,c}(\beta)$ has been determined, its corresponding $F_c(\tau)$ (shown in Fig. 6.21b) is directly obtained by means of the inverse Fourier transform of (4.11), i.e. $F_c(\tau) = FT^{-1}\{S_{11,c}(\beta)\}$. As a consequence of the numerical sampling parameters used for $S_{11,c}(\beta)$, the resulting $F_c(\tau)$ is defined from $\tau_{D,n=0} = 0$ to $\tau_{D,max} = 2000 \cdot T_\tau$ with a discretization period of $T_{D,\tau} = T_\tau/25$ (see section 6.1.1). Regarding the synthesis process with ILP, a layer thickness equal to the discretization period of the z axis has been chosen, i.e. $\Delta z = T_{D,z}$. The $K(z)$ obtained with the ILP synthesis is depicted in Fig. 6.22a. The corresponding waveguide height profile, $b(z)$, shown in Fig. 6.22b, was obtained by identifying $K_b(z)$ with the synthetized $K(z)$ and selecting the height of the WR75 standard for the input port, $b(0) = 9.525$ mm, in (2.130).

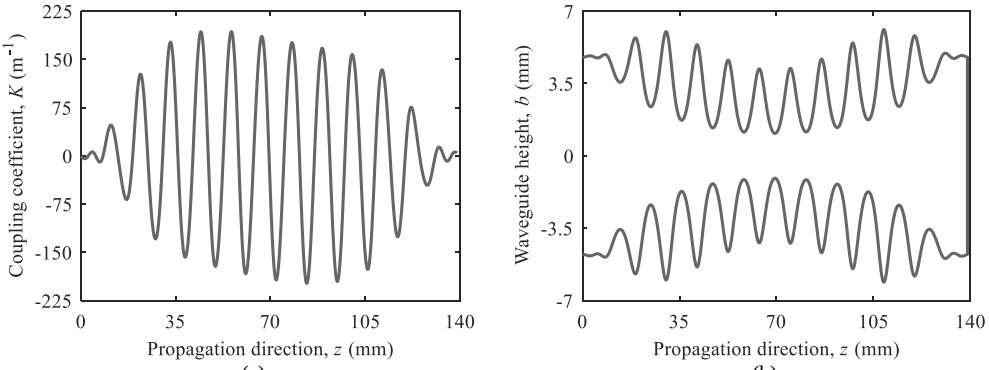

Fig. 6.22. (a) Coupling coefficient, K, along the propagation axis, z, calculated by means of the Integral Layer Peeling method for the target impulse response in reflection, $F_c(\tau)$. (b) Waveguide height profile, $b(z)$, along the propagation axis, z, calculated from $K(z)$ with $b(0) = 9.525$ mm.

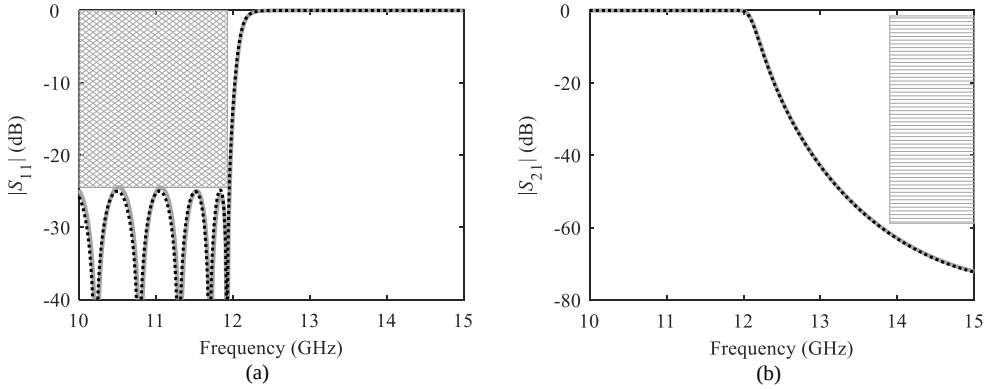

Fig. 6.23. Magnitude of the (a) S_{11} and (b) S_{21}-parameter that correspond to the target frequency response (grey solid lines) and result of the single-mode analysis of $K(z)$ (black dotted lines). The specification masks for the frequency response in terms of return loss (grey diamond pattern) and the rejection level (grey rectangle pattern) are also provided.

In order to verify the accuracy of the $K(z)$ calculated by means of the ILP synthesis method, the single-mode simulation based on solving the single-mode coupled-mode equation system of (2.91), (2.92) was performed. The results depicted in Fig. 6.23 confirm the accuracy of the solution attained for $K(z)$.

However, when higher-order modes are taken into account in the solution of the coupled-mode theory, the behavior of the passband gets critically degraded as it can be seen in the results provided by the full-wave CST Microwave simulation of Fig. 6.25 (black dash-dotted lines).

The first approach for the compensation of the reactive effects of cut-off modes will be the use of the uniform scaling method, see section 2.2.3.1. For doing so, the first task is to ensure that all the relevant higher-order modes (see section 2.1.2.1) are in cut-off regime along the

whole structure. Since the maximum height of the $b(z)$ profile shown in Fig. 6.22b is $\max\{b(z)\} = 12.22$ mm, the corresponding cut-off frequency for the closest relevant parasitic modes (TE_{12} and TM_{12}) will be 25.75 GHz by (2.50). Thus, the cut-off regime is automatically ensured for all the relevant higher-order modes. Next, the effective phase constant, $\beta_{eff}(z)$, is calculated from the solution of the coupled-mode equation system of (2.44) for a frequency $f_t = f_c = 11.95$ GHz by taking into account, in addition to the fundamental TE_{10}, all the modes (TE_{pq} or TM_{pq}) that satisfy $p = 1$ and $q = 2, 4, 6, ...$, see section 2.1.2.1. Due to computational limitations, a maximum $q = 128$ was chosen in both TE and TM cases for solving (2.44). The

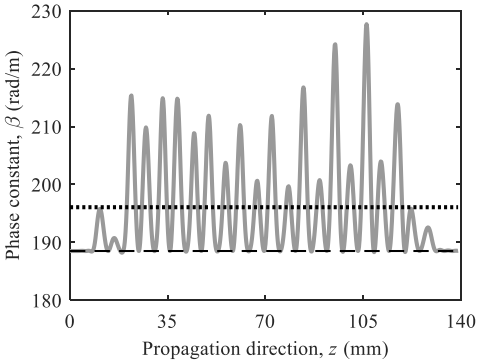

Fig. 6.24. Phase constant of the fundamental TE_{10} mode for a frequency $f_t = 11.95$ GHz (black dashed line), effective phase constant caused by cut-off modes, β_{eff}, along the propagation direction, z, (grey line), and its average value, $\bar{\beta}_{eff}$ (black dotted line).

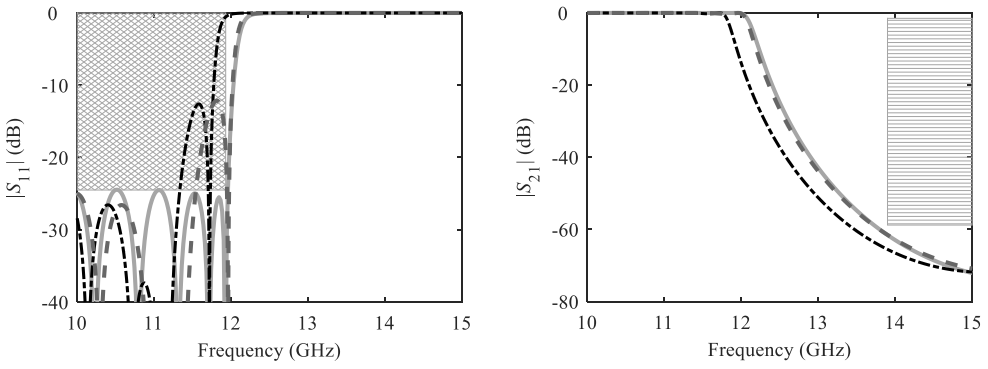

Fig. 6.25. Magnitude of the (a) S_{11} and (b) S_{21}-parameter that correspond to the single-mode analysis performed to $K(z)$ (light grey solid traces), the result of the CST simulation of the same structure (black dashed-dotted line) and the CST simulation of the structure obtained after applying the cut-off modes uniform scaling compensation (dark grey dashed line). The specification masks for the frequency response in terms of return losses (grey diamond pattern) and the rejection level (grey rectangle pattern) are also provided.

coupling coefficients necessary for the calculations can be determined by (2.74), (2.75), and (2.76). Then $\beta_{eff}(z)$ is calculated from (2.222) and the result is shown in Fig. 6.24, where the phase constant of the fundamental TE_{10} mode and the average value of $\beta_{eff}(z)$, $\bar{\beta}_{eff} = 190.91$ rad/m, obtained by (2.227), are also provided. Since the phase constant of the fundamental TE_{10} mode is $\beta_1(f_t) = \beta(f_t = f_c) = 188.496$ rad/m, as it was given in Table 6.4, the necessary scaling factor to achieve the compensated propagation axis $\frac{z}{\psi(f_t)}$ will be $\psi(f_t) = 1.04$, as it is deduced from (2.230). If the scaling is properly applied to the propagation axis of the structure of Fig. 6.22b (with the amplitude of the coupling coefficient automatically scaled as $\psi \cdot K(z)$, as required) and the resulting structure is simulated with CST Studio Suite, the frequency response shown in Fig. 6.25, in grey dotted lines, is obtained.

As it can be observed in the CST simulation results of Fig. 6.25a, the uniform scaling method (grey dashed line) has corrected the frequency shift featured by the original synthetized structure (black dash-dotted line). However, the parasitic effects of cut-off modes also increased the level of the S_{11} lobe centered approximately at 11.5 GHz (black dash-dotted line) with respect to the lobe level obtained with the single-mode analysis (grey solid line). In view of the CST simulation results of the structure obtained with the application of the uniform scaling method (dashed grey line), the troublesome lobe was just shifted to 11.75 GHz. As a consequence, the obtained S_{11} does not satisfy the RL specification mask.

Once the uniform scaling method for the compensation of the effects of cut-off modes has shown to be not completely efficient for this case, the iterative distributed scaling procedure that was fully described in section 2.2.3.2 will be employed. For doing so, the original propagation axis, z, will be now denoted by z_1 for the sake of clarity. Thus, the first iteration step of the procedure, $l = 1$, will need the corresponding effective phase constant $\beta_{eff,1}(f_t, z_1)$ that has been previously calculated as $\beta_{eff}(f_t, z)$ when applying the uniform scaling method, i.e. $\beta_{eff,1}(f_t, z_1) = \beta_{eff}(f_t, z)$. Moreover, as it was explained in section 2.2.3.2, the expected phase constant for the structure, $\beta_{eff,0}(f_t, z_1(z_0))$, is also needed for the calculation. It is obvious that in this initial step, $\beta_{eff,0}(f_t, z_1(z_0))$ corresponds to the phase constant of the fundamental TE_{10} mode, $\beta_1(f_t)$, which is fixed along z_1. Actually, the position parameter of this initial step, $z_1(z_0)$, simply implies that the initially expected $\beta_{eff,0}$ will be constant along the z_1 axis. Both, $\beta_{eff,1}(f_t, z_1)$ and $\beta_{eff,0}(f_t, z_1(z_0)) = \beta_1(f_t)$ are shown in Fig. 6.26a. Therefore, the new propagation axis z_2 that is a distributed version of z_1 can be obtained as a function of $\beta_{eff,1}(f_t, z_1) = \beta_{eff}(f_t, z)$ and $\beta_{eff,0}(f_t, z_1(z_0)) = \beta_1(f_t)$ using the expression (2.233) evaluated for $l = 1$, i.e.:

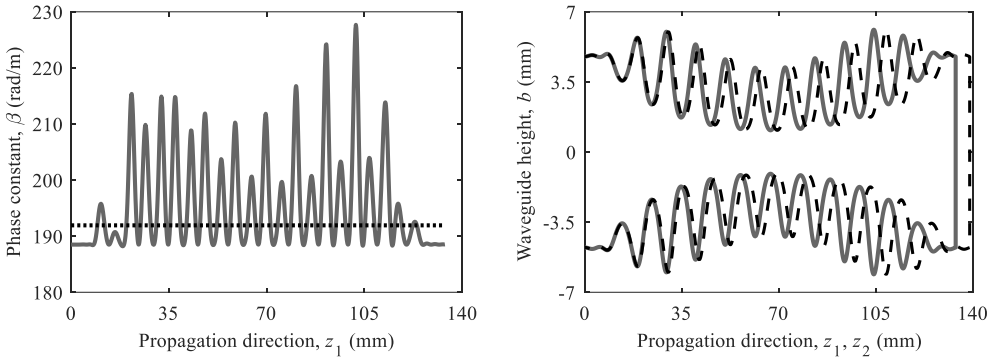

(a) (b)

Fig. 6.26. First iteration ($l = 1$) of the distributed scaling method: (a) Phase constant of the fundamental TE_{10} mode, $\beta_{eff,0}(f_t, z_1(z_0)) = \beta_1(f_t)$ (black dotted line) and effective phase constant, $\beta_{eff,1}(f_t, z_1)$ (grey solid line) and (b) original height profile, $b(z_1)$ (black dotted line) and redistributed height profile, $b(z_2)$ (grey solid line).

$$z_2(f_t, z_1) = \int_0^{z_1} \frac{\beta_{eff,0}(f_t, r(z_0))}{\beta_{eff,1}(f_t, r)} \cdot dr = \int_0^{z_1} \frac{\beta_1(f_t)}{\beta_{eff}(f_t, r)} \cdot dr \tag{6.25}$$

The waveguide height profile, $b(z_1) = b(z)$, was redistributed to $b(z_2)$ as it is depicted in Fig. 6.26b, and it was subsequently simulated with CST Microwave Studio. The resulting S_{11}-parameter in the filter passband is shown in Fig. 6.29, in grey dotted line. It is clear that the new structure with height profile $b(z_2)$ has improved the S_{11}-parameter featured by the original device with $b(z_1) = b(z)$, which is also shown in Fig. 6.29 in black dash-dotted line. Nevertheless, the $S_{11}(f)$ achieved by $b(z_2)$ in the passband does not satisfy the specification mask for the *RL* level. Accordingly, a new iteration step of the recursive distributed scaling method will be required.

For the new compensation step with $l = 2$, the expected effective phase constant in z_2 will be $\beta_{eff,1}(f_t, z_2(z_1))$, i.e. the effective phase constant calculated for $b(z_1)$ but redistributed in z_2 with the function $z_2(f_t, z_1)$ that was calculated with (6.25). However, in order to calculate the actual effective phase constant featured by $b(z_2)$, $\beta_{eff,2}(f_t, z_2)$, it will be necessary to solve the coupled-mode equation system (2.44) again for $f_t = 11.95$ GHz by calculating the corresponding coupling coefficients of $b(z_2)$ with (2.74), (2.75) and (2.76), for all the modes (TE_{pq} or TM_{pq}) that satisfy $p = 1$ and $q = 0$ (not for the TM_{pq} case), $2, 4, \ldots$, employing a maximum modal index q, $q = 128$, for both TE_{pq} and TM_{pq}. modes, so as to perform numerical calculations using a finite number of modes. The actual $\beta_{eff,2}(f_t, z_2)$ is calculated by (2.222) and compared with the expected $\beta_{eff,1}(f_t, z_2(z_1))$ in Fig. 6.27a. It is worth noting that in this

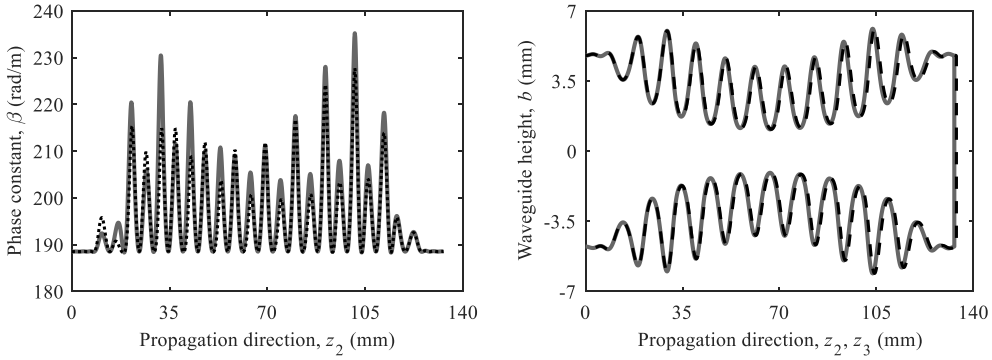

(a) (b)

Fig. 6.27. Second iteration ($l = 2$) of the distributed scaling method: (a) expected effective phase constant, $\beta_{eff,1}(f_t, z_2(z_1))$ (black dotted line) and actual value obtained from the simulation of $b(z_2)$ for the effective phase constant, $\beta_{eff,2}(f_t, z_2)$ (grey solid line) and (b) height profile of the original $b(z_2)$ (black dotted line) and of the redistributed $b(z_3)$ (grey solid line).

case the expected and the actual effective phase constants are much closer to each other than in the first compensation step of Fig. 6.26a and thus, the new redistributed propagation axis, z_3, should be quite similar to z_2. The propagation axis z_3 will be attained by setting $l = 2$ in (2.233), yielding to:

$$z_3(f_t, z_2) = \int_0^{z_2} \frac{\beta_{eff,1}(f_t, r(z_1))}{\beta_{eff,2}(f_t, r)} \cdot dr \tag{6.26}$$

As it was expected, the height profile $b(z_3)$ is very similar to $b(z_2)$, but the CST simulation performed for the former (grey dashed line of Fig. 6.29) improves the $S_{11}(f)$ of the later (grey dotted line of Fig. 6.29) and almost satisfies the Return Loss level required.

If a third step is considered, i.e. $l = 3$, the expected effective phase constant for z_3 will be the $\beta_{eff,2}(f_t, z_3(z_2))$, while the actual $\beta_{eff,3}(f_t, z_3)$ must be obtained from (2.222) after solving (2.44) for the coupling coefficients of $b(z_3)$, that will be calculated for the same modes of the previous steps. The obtained $\beta_{eff,3}(f_t, z_3)$ is compared with the expected $\beta_{eff,2}(f_t, z_3(z_2))$ in Fig. 6.28a, showing a slight difference between them. If $l = 3$ is selected in (2.233), the redistributed propagation axis z_4 arises as:

$$z_4(f_t, z_3) = \int_0^{z_3} \frac{\beta_{eff,2}(f_t, r(z_2))}{\beta_{eff,3}(f_t, r)} \cdot dr \tag{6.27}$$

The waveguide structure with height profile defined by $b(z_4)$ is simulated with CST Microwave Studio and the resulting $S_{11}(f)$ finally fulfills the Return Loss specification required for the filter, as it can be seen in the black solid line of Fig. 6.29.

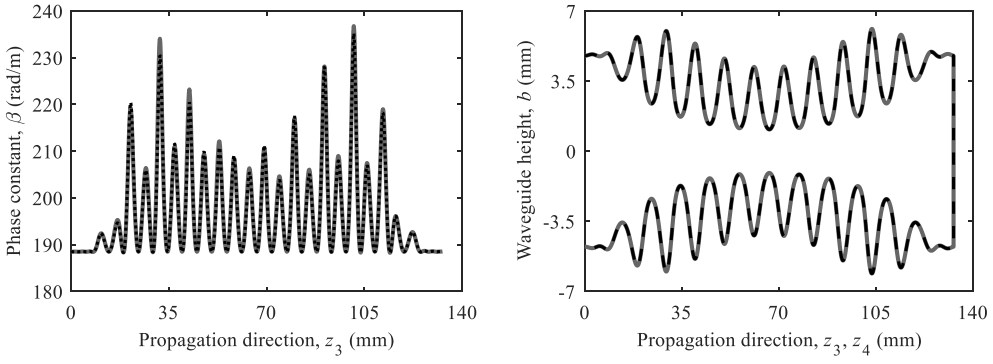

(a) (b)

Fig. 6.28. Last iteration ($l = 3$) of the distributed scaling method: (a) expected effective phase constant, $\beta_{eff,2}(f_t, z_3(z_2))$ (black dotted line) and actual value obtained from the simulation of $b(z_3)$ for the effective phase constant, $\beta_{eff,3}(f_t, z_3)$ (grey solid line) and (b) height profile of the original $b(z_3)$ (black dotted line) and of the final redistributed $b(z_4)$ (grey solid line).

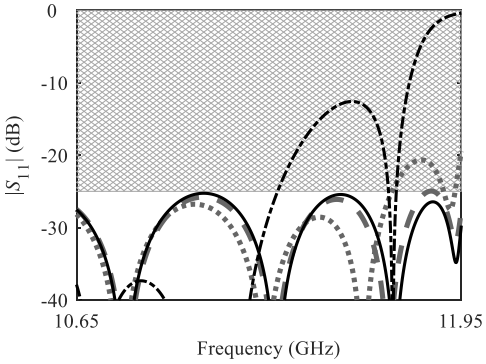

Fig. 6.29. Evolution of the simulated $|S_{11}|$-parameter in the filter passband, during the three performed steps of the iterative distributed scaling technique for the compensation of the reactive effects of cut-off modes: (a) original structure obtained from the ILP synthesis in the initial z_1 axis, $b(z_1)$ (black dash-dotted line), structure redistributed according to the z_2 achieved in the first step ($l = 1$), $b(z_2)$ (grey dotted line), $b(z_3)$ achieved in the second step ($l = 2$) (grey dashed line), and the last $b(z_4)$ achieved in the third step ($l = 3$) (black solid line). The specification mask for the $RL \geq 25$ dB is also included (diamond-based pattern).

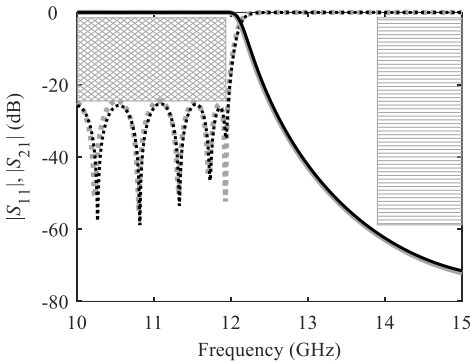

Fig. 6.30. Frequency responses, $|S_{11}|$ (dotted lines) and $|S_{21}|$ (solid lines), calculated from the single-mode analysis of the $K(z)$ obtained form the ILP synthesis (grey lines) and from the full-wave CST simulation of the structure achieved at the final step ($l = 3$) of the iterative distributed scaling method for the compensation of the cut-off mode effects, $b(z_4)$ (black lines).

The full-wave CST simulation results of the final structure with height profile $b(z_4)$ ($S_{11}(f)$ and $S_{21}(f)$-parameters) are compared with the single-mode analysis performed to the $K(z)$ originally synthesized with ILP, see Fig. 6.30.

A very good agreement can be observed between the simulation results provided in Fig. 6.30 and thus, it can be concluded that the parasitic effects of cut-off modes have been fully compensated by means of a third-order iterative distributed scaling procedure. As a consequence, the degradation exhibited by the multimode frequency response with respect to the response expected from the single-mode simulation, has been successfully overcome.

In order to conclude this section, it must be highlighted that a practical example of strong degradation of the frequency response caused by higher-order modes has been shown. Although the application of the uniform scaling compensation method has not provided an appropriate correction for this case, a very satisfactory compensation has been achieved with the use of the iterative distributed scaling method. This distributed scaling technique has exhibited a very powerful performance by achieving a frequency response very close to that predicted by the single-mode operation model that is employed for the ILP synthesis procedure.

6.3. ASSESSMENT OF CRITICAL PARAMETERS FOR THE QUALITY OF THE SYNTHESIS

Due to the inherent limitations that arise in the practical numerical implementation of the ILP synthesis method, it is necessary to perform an appropriate definition of the target frequency response as well as of the degrees of freedom that can be arbitrarily selected for a synthesis process. Thorough and interesting studies regarding the importance of the choices of these parameters were previously performed for the GLM and CLP synthesis techniques in [10], [11].

In this section, an assessment of the influence of the discretization features selected for the definition of the target response, as well as the own parameters of ILP will be carried out. This study will be performed by imposing different initial configurations for the synthesis of the 25-th order Chebyshev low-pass filter response of section 6.2.1. This synthesis example was chosen since the difference in the quality of the synthesis should become more apparent by requiring challenging responses with high maximum rejection levels. The resulting coupling coefficient, $K(z)$, for each configuration will be shown. The quality of the synthesis will be evaluated by considering the level of agreement between the target and the analyzed frequency responses, where the latter is obtained from the numerical solution of the single-mode coupled-mode equation system of (2.91), (2.92), for each $K(z)$ attained.

$$\frac{da^+}{dz} = -j \cdot \beta \cdot a^+ + K \cdot a^- \tag{2.91}$$

$$\frac{da^-}{dz} = j \cdot \beta \cdot a^- + K \cdot a^+ \tag{2.92}$$

It is worth noting that the solution of (2.91), (2.92) is the most suitable method in order to determine if the $K(z)$ obtained has been accurately calculated. All the synthesis techniques that have been presented within this thesis (including ILP) are devoted to solve the inverse scattering problem of determining $K(z)$ from a target response (given by the Fourier transform pair $S_{11}(\beta) = FT\{F(\tau)\}$) under the single-mode operation assumption, which is mathematically formulated by means of (2.91), (2.92). Thus, by solving (2.91) and (2.92) with a given $K(z)$, the complex amplitudes of the forward, a^+, and backward, a^-, traveling waves are obtained and then, the corresponding S-parameters can be deduced from (2.105)-(2.110). Accordingly, if the S-parameters that result from this analysis fit the target ones, the $K(z)$ achieved from the synthesis process can be rated as accurate and vice-versa.

The characteristics of the discretized data of the target transform pair, $S_{11,c}(\beta) = FT\{F_c(\tau)\}$, that are provided for the numerical implementation of the ILP method should constitute an important influence for the final quality of the synthesized $K(z)$, as they actually are for the GLM and CLP methods [10], [11]. Thus, different values of the maximum phase constant, $\beta_{D,max}$, and of the sampling ratio between two samples of the $S_{11,c}(\beta)$, $\Delta\beta_D$, will be selected for the definition of the target response. As it was stated in section 6.1.1, $\beta_{D,max}$ is related to the sampling period of the τ and z axes, $T_{D,\tau}$ and $T_{D,z}$, respectively by (6.15). Furthermore, $\Delta\beta_D$ is linked with the maximum duration of $\tau_{n,D}$, $\tau_{D,max}$, due to (5.22). Apart from the pure discretization parameters of the target response, several values of linear delay, τ_{del}, will be imposed to the target $S_{11,c}(\beta)$ in order to clarify its effect in the obtained $K(z)$. Finally, different layer thicknesses, Δz, will be employed to synthetize the same frequency response, and the impact of this choice in the final result will be evaluated.

6.3.1. Variation of the $\beta_{D,max}$, $T_{D,\tau}$ Pair in the Target Response Definition

In order to determine the effect of the modification of the pair conformed by the maximum phase constant, $\beta_{D,max}$, and the sampling period in τ, $T_{D,\tau}$, (that are related to each other by (6.15)), four different synthesis processes of the filter of section 6.2.1 have been carried out. For each of them, different values of the $\beta_{D,max}$, $T_{D,\tau}$ pair have been employed, also adapting the layer thickness, Δz, so as to keep it constant. As it was stated in section 6.1.1, when dealing with discretized data, the thickness of the layer, Δz, must be chosen so as to be an entire number, M, of sampling periods in z, $T_{D,z}$, see (6.16). Since $T_{D,z}$ is going to be modified due to the $\beta_{D,max}$ variation (see (6.15)), the value of M must be reconsidered for each synthesis.

The different values that have been determined to carry out this study of the choice of $\beta_{D,max}$, $T_{D,\tau}$, are provided in Table 6.6 as a function of the phase constant β_0 that features the maximum rejection level of the filter response, see section 6.2.1. Moreover, the layer thicknesses that must be selected for each case so as to maintain it constant are given in Table 6.6 in terms of $T_{D,z} = \frac{T_{D,\tau}}{2}$. Finally, the rest of the relevant parameters for the synthesis that are kept unaltered are also provided in Table 6.6 for the sake of completeness.

$\beta_{D,max} \leftrightarrow T_{D,\tau}$	$\Delta\beta_D \leftrightarrow \tau_{D,max}$	τ_{del}	Δz
$5 \cdot \beta_0 \leftrightarrow \frac{\pi}{5 \cdot \beta_0}$	$\frac{\beta_0}{2000} \leftrightarrow \frac{4000 \cdot \pi}{\beta_0}$	$\frac{\tau_{D,max}}{2}$	$T_{D,z} = \frac{T_{D,\tau}}{2}$
$10 \cdot \beta_0 \leftrightarrow \frac{\pi}{10 \cdot \beta_0}$	$\frac{\beta_0}{2000} \leftrightarrow \frac{4000 \cdot \pi}{\beta_0}$	$\frac{\tau_{D,max}}{2}$	$2 \cdot T_{D,z} = T_{D,\tau}$
$20 \cdot \beta_0 \leftrightarrow \frac{\pi}{20 \cdot \beta_0}$	$\frac{\beta_0}{2000} \leftrightarrow \frac{4000 \cdot \pi}{\beta_0}$	$\frac{\tau_{D,max}}{2}$	$4 \cdot T_{D,z} = 2 \cdot T_{D,\tau}$
$40 \cdot \beta_0 \leftrightarrow \frac{\pi}{40 \cdot \beta_0}$	$\frac{\beta_0}{2000} \leftrightarrow \frac{4000 \cdot \pi}{\beta_0}$	$\frac{\tau_{D,max}}{2}$	$8 \cdot T_{D,z} = 4 \cdot T_{D,\tau}$

Table 6.6. Frequency response and ILP parameters for the four synthesis procedures performed to determine the impact of the variation of the $\beta_{D,max}$, $T_{D,\tau}$ pair on the synthesis result. The thickness of the layer Δz has been adapted in each case so as to remain constant in the four synthesis procedures.

The coupling coefficients that result from the choice of $\beta_{D,max} = 5 \cdot \beta_0, 10 \cdot \beta_0, 20 \cdot \beta_0,$ and $40 \cdot \beta_0$ (with their associated $T_{D,\tau}$ and Δz, see Table 6.6) are depicted in Fig. 6.31a, Fig. 6.32a, Fig. 6.33a, and Fig. 6.34a, respectively. The resulting S_{11} and S_{21} from the single-mode analyses performed to each $K(z)$ are also shown in Fig. 6.31b-Fig. 6.31c, Fig. 6.32b-Fig. 6.32c, Fig. 6.33b-Fig. 6.33c, and Fig. 6.34b-Fig. 6.34c, respectively.

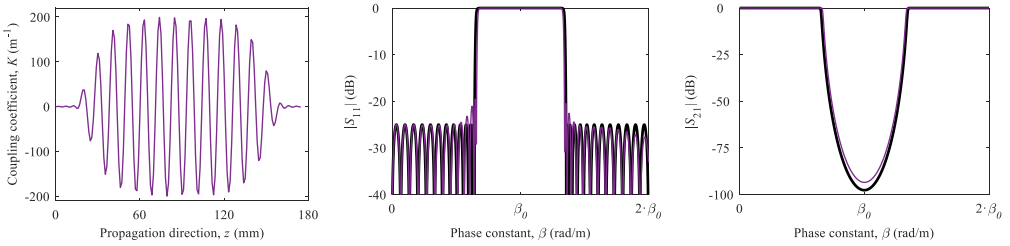

(a) (b) (c)

Fig. 6.31. (a) Coupling coefficient synthetized with a target response defined with $\beta_{D,max} = 5 \cdot \beta_0$ and $\Delta z = T_{D,z}$. The comparisons between the target (black lines) and the resulting (purple lines) (b) $S_{11}(\beta)$- and (c) $S_{21}(\beta)$-parameters from the single-mode analysis of $K(z)$ are provided.

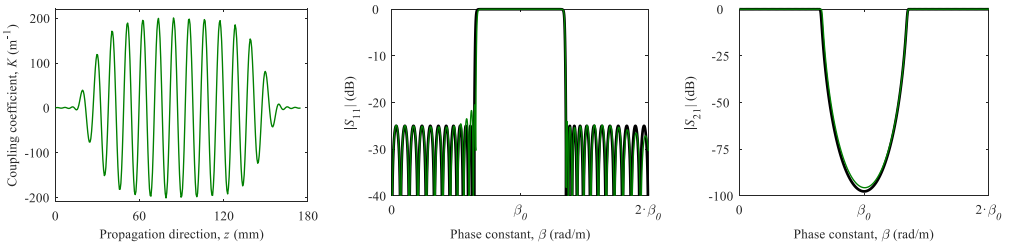

(a) (b) (c)

Fig. 6.32. (a) Coupling coefficient synthetized with a target response defined with $\beta_{D,max} = 10 \cdot \beta_0$ and $\Delta z = 2 \cdot T_{D,z}$. The comparisons between the target (black lines) and the resulting (green lines) (b) $S_{11}(\beta)$- and (c) $S_{21}(\beta)$-parameters from the single-mode analysis of $K(z)$ are provided.

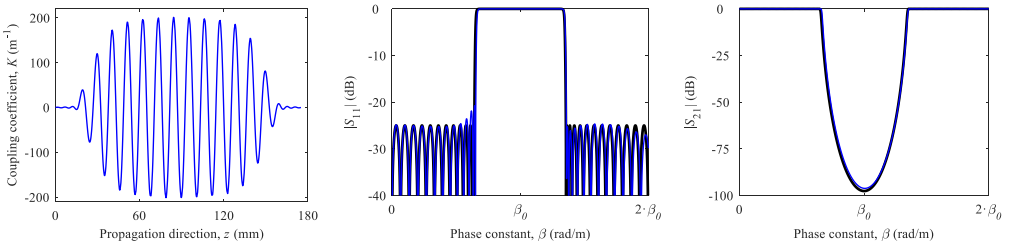

(a) (b) (c)

Fig. 6.33. (a) Coupling coefficient synthetized with a target response defined with $\beta_{D,max} = 20 \cdot \beta_0$ and $\Delta z = 4 \cdot T_{D,z}$. The comparisons between the target (black lines) and the resulting (blue lines) (b) $S_{11}(\beta)$- and (c) $S_{21}(\beta)$-parameters from the single-mode analysis of $K(z)$ are provided.

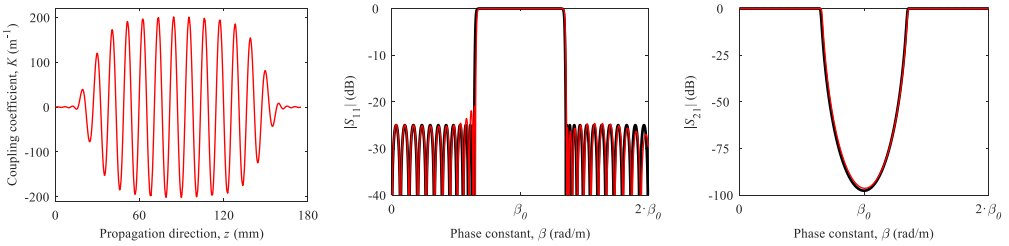

(a) (b) (c)

Fig. 6.34. (a) Coupling coefficient synthetized with a target response defined with $\beta_{D,max} = 40 \cdot \beta_0$ and $\Delta z = 8 \cdot T_{D,z}$. The comparisons between the target (black lines) and the resulting (red lines) (b) $S_{11}(\beta)$- and (c) $S_{21}(\beta)$-parameters from the single-mode analysis of $K(z)$ are provided.

As it can be observed in the results of Fig. 6.31-Fig. 6.34, the modification of the pair $\beta_{D,max}, T_{D,\tau}$ does not seem to notably affect the quality of the synthesis, even in the case where $\beta_{D,max} = 5 \cdot \beta_0$, which represents just a slight increase in the definition of the frequency

response (as well as in $T_{D,\tau}$) with respect to the initial commensurate-line UE prototype, see section 5.2. However, if the comparison between the different $K(z)$ of Fig. 6.35a is carefully examined, it will be clear that the synthesis that employs the lowest value of $\beta_{D,max}$ drives to a $K(z)$ that is clearly undersampled in the z axis. A good example of this aspect can be observed in the purple trace of Fig. 6.35a, which corresponds to the synthesis of a frequency response defined up to $\beta_{D,max} = 5 \cdot \beta_0$. Since the sampling period in the z axis, $T_{D,z}$, is related to $T_{D,\tau}$ as $T_{D,z} = \frac{T_{D,\tau}}{2}$, a low value of $\beta_{D,max}$ leads to an excessively large $T_{D,z}$, due to (6.15). This deficiency in the resolution of the z axis leads to a coupling coefficient that does not sample the highest peaks of $K(z)$, which are actually trapped with a synthesis using $\beta_{D,max} = 40 \cdot \beta_0$ (red line in Fig. 6.35a). As a consequence of this effect, the undersampled structure shows a slight loss of rejection level when compared to the analyses performed to the coupling coefficients that have been obtained from responses calculated with higher values of $\beta_{D,max}$, as it can be seen in Fig. 6.35b. Indeed, this tendency is completely monotonic as it can be seen in the results of Fig. 6.35, i.e. the smaller the sampling period $T_{D,z}$ chosen (the higher $\beta_{D,max}$ employed), the higher the amplitudes of $K(z)$ reached and hence, the closer the maximum rejection level approaches to the target.

However, despite of this slight difference in the obtained S_{21}-parameter, the incidence of the choice of β_{max} in the obtained $K(z)$ is quite weak, since the coupling coefficient as well as the obtained responses are rather similar to each other, according to the results provided between Fig. 6.32-Fig. 6.35.

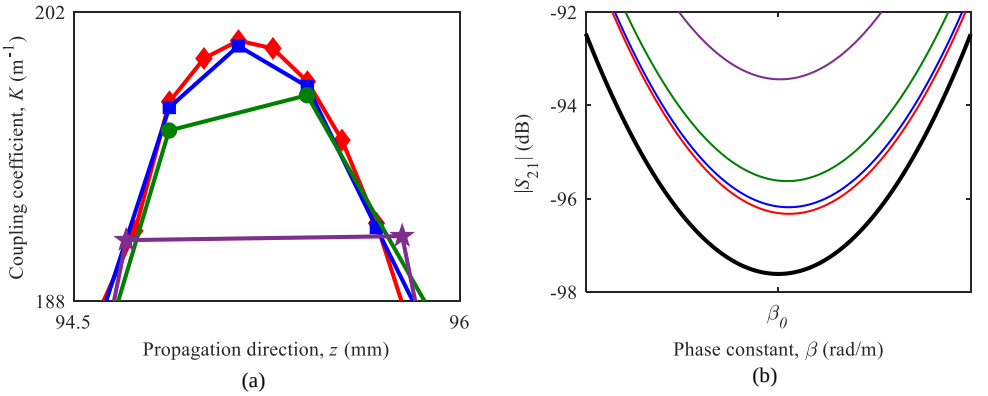

Fig. 6.35. (a) Detail of the coupling coefficients synthetized with a target response defined with $\beta_{D,max} = 5 \cdot \beta_0$ (purple line), $\beta_{D,max} = 10 \cdot \beta_0$ (green line), $\beta_{D,max} = 20 \cdot \beta_0$ (blue line), and $\beta_{D,max} = 40 \cdot \beta_0$ (red line) while maintaining the layer thickness fixed. (b) Comparison between the target (black line) and the resulting $S_{21}(\beta)$-parameters from the single-mode analysis of the different coupling coefficients synthetized, following the same color code as in (a).

Therefore, it can be concluded that the choice of the pair $\beta_{D,max}$, $T_{D,\tau}$ does not have a critical impact on the quality of the synthesis. However, it is advisable to employ a high enough value of $\beta_{D,max}$ (or short enough $T_{D,\tau}$) so as to consider a suitable spatial resolution, $T_{D,z} = \frac{T_{D,\tau}}{2}$, for reaching the extreme values of $K(z)$. By doing so, the frequency response associated to $K(z)$ will be better fitted to the target.

6.3.2. Variation of the $\Delta\beta_D$, $\tau_{D,max}$ Pair in the Target Response Definition

As in the case of the pair $\beta_{D,max}$, $T_{D,\tau}$, the impact of the selection of the pair $\Delta\beta_D$, $\tau_{D,max}$ in the result of the synthesis has been studied by imposing four different values of that pair in the discretized versions of the target responses for the realization of their corresponding syntheses, while leaving the rest of the parameters constant. The specific values of $\Delta\beta_D$, $\tau_{D,max}$ as well as the other necessary definition parameters for the synthesis are provided in Table 6.7.

The different $K(z)$ attained as a result of the syntheses with $\Delta\beta_D = \frac{\beta_0}{125}, \frac{\beta_0}{250}, \frac{\beta_0}{500}$, and $\frac{\beta_0}{1000}$, or equivalently with $\tau_{D,max} = \tau_{D,max1} = \frac{250\cdot\pi}{\beta_0}$, $\tau_{D,max2} = \frac{500\cdot\pi}{\beta_0}$, $\tau_{D,max3} = \frac{1000\cdot\pi}{\beta_0}$, and $\tau_{D,max4} = \frac{2000\cdot\pi}{\beta_0}$, are depicted in Fig. 6.36a, Fig. 6.37a, Fig. 6.38a, and Fig. 6.39a, respectively.

$\beta_{D,max} \leftrightarrow T_{D,\tau}$	$\Delta\beta_D \leftrightarrow \tau_{D,max}$	τ_{del}	Δz
$40 \cdot \beta_0 \leftrightarrow \frac{\pi}{40 \cdot \beta_0}$	$\frac{\beta_0}{125} \leftrightarrow \frac{250 \cdot \pi}{\beta_0}$	$\frac{\tau_{D,max}}{2}$	$2 \cdot T_{D,z} = T_{D,\tau}$
$40 \cdot \beta_0 \leftrightarrow \frac{\pi}{40 \cdot \beta_0}$	$\frac{\beta_0}{250} \leftrightarrow \frac{500 \cdot \pi}{\beta_0}$	$\frac{\tau_{D,max}}{2}$	$2 \cdot T_{D,z} = T_{D,\tau}$
$40 \cdot \beta_0 \leftrightarrow \frac{\pi}{40 \cdot \beta_0}$	$\frac{\beta_0}{500} \leftrightarrow \frac{1000 \cdot \pi}{\beta_0}$	$\frac{\tau_{D,max}}{2}$	$2 \cdot T_{D,z} = T_{D,\tau}$
$40 \cdot \beta_0 \leftrightarrow \frac{\pi}{40 \cdot \beta_0}$	$\frac{\beta_0}{1000} \leftrightarrow \frac{2000 \cdot \pi}{\beta_0}$	$\frac{\tau_{D,max}}{2}$	$2 \cdot T_{D,z} = T_{D,\tau}$

Table 6.7. Frequency response and ILP parameters for the four synthesis procedures performed to determine the impact of the variation of the $\Delta\beta_D$, $\tau_{D,max}$ pair on the synthesis result.

The S_{11}- and S_{21}-parameters that are obtained from the solution of the single-mode coupled-mode equation system of (2.91) and (2.92) for each $K(z)$ are provided in Fig. 6.36b-Fig. 6.36c, Fig. 6.37b-Fig. 6.37c, Fig. 6.38b-Fig. 6.38c, and Fig. 6.39b-Fig. 6.39c.

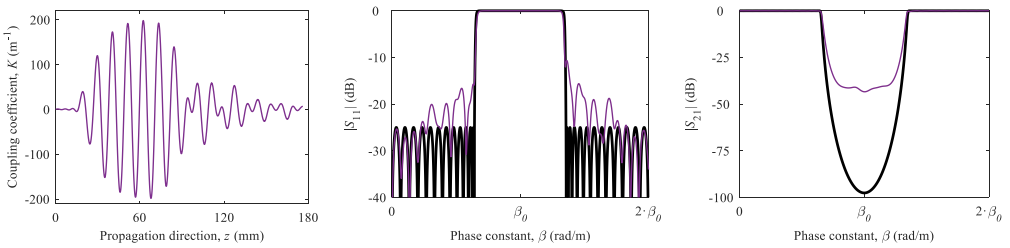

(a) (b) (c)

Fig. 6.36. a) Coupling coefficient synthetized with a target response defined with $\Delta\beta_D = \frac{\beta_0}{125}$. The comparisons between the target (black lines) and the resulting (purple lines) (b) $S_{11}(\beta)$- and (c) $S_{21}(\beta)$-parameters from the single-mode analysis of $K(z)$ are provided.

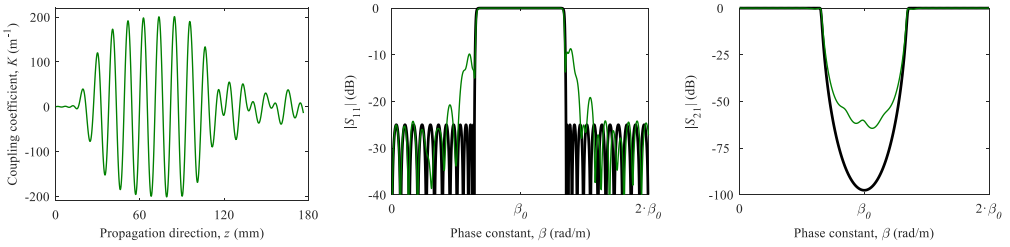

(a) (b) (c)

Fig. 6.37. (a) Coupling coefficient synthetized with a target response defined with $\Delta\beta_D = \frac{\beta_0}{250}$. The comparisons between the target (black lines) and the resulting (green lines) (b) $S_{11}(\beta)$- and (c) $S_{21}(\beta)$-parameters from the single-mode analysis of $K(z)$ are provided.

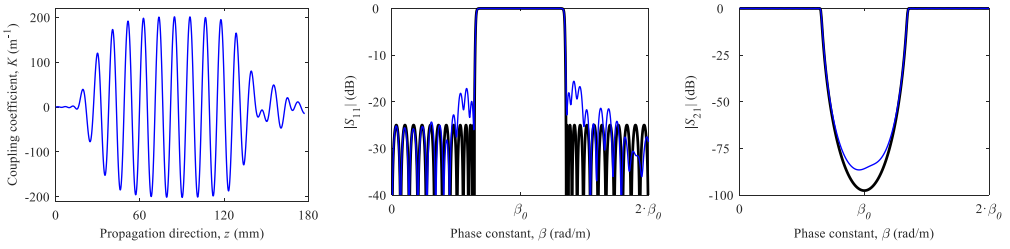

(a) (b) (c)

Fig. 6.38. (a) Coupling coefficient synthetized with a target response defined with $\Delta\beta_D = \frac{\beta_0}{500}$. The comparisons between the target (black lines) and the resulting (blue lines) (b) $S_{11}(\beta)$- and (c) $S_{21}(\beta)$-parameters from the single-mode analysis of $K(z)$ are provided.

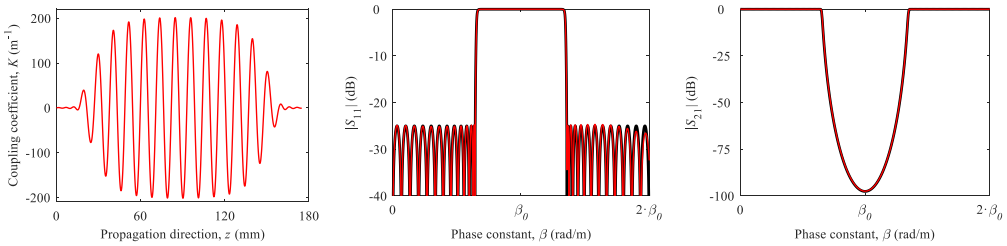

(a) (b) (c)

Fig. 6.39. (a) Coupling coefficient synthetized with a target response defined with $\Delta\beta_D = \frac{\beta_0}{1000}$. The comparisons between the target (black lines) and the resulting (red lines) (b) $S_{11}(\beta)$- and (c) $S_{21}(\beta)$-parameters from the single-mode analysis of $K(z)$ are provided.

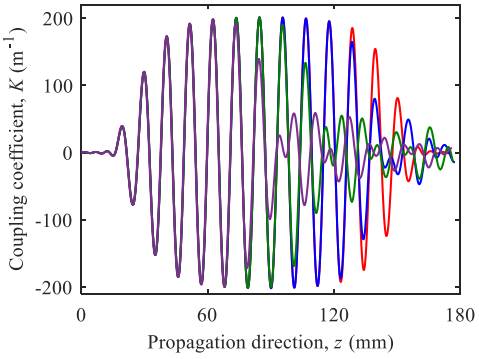

(a)

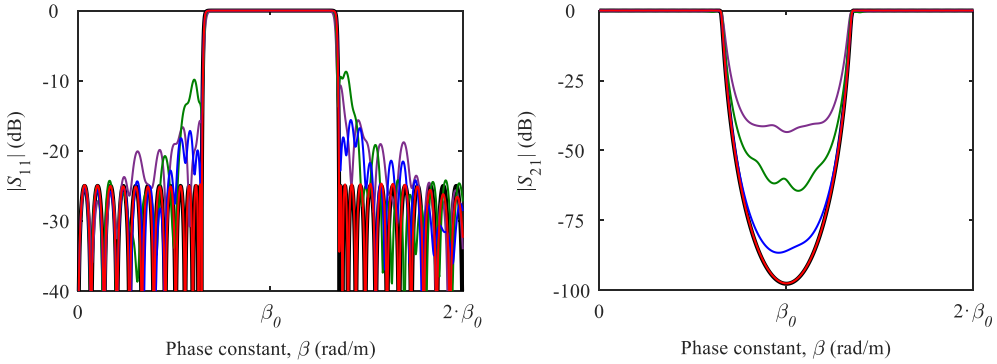

(b) (c)

Fig. 6.40. (a) Comparison between the coupling coefficients synthetized with a target response defined with $\Delta\beta_D = \frac{\beta_0}{125}$ (purple line), $\Delta\beta_D = \frac{\beta_0}{250}$ (green line), $\Delta\beta_D = \frac{\beta_0}{500}$ (blue line), and $\Delta\beta_D = \frac{\beta_0}{1000}$ (red line). Comparisons between the target (black lines) and the resulting (b) $S_{11}(\beta)$- and (c) $S_{21}(\beta)$-parameters from the single-mode analyses of the different coupling coefficients synthetized are provided following the same color code as in (a).

In view of the results provided in Fig. 6.36-Fig. 6.39, the selection of the $\Delta\beta_D$ parameter for the frequency response has a direct impact in the coupling coefficient obtained as well as in the achieved frequency response. As it can be seen in the comparative graph of Fig. 6.40a, a low frequency resolution (large $\Delta\beta_D$), results in a synthesis process that accumulates numerical error too fast, leading to an inaccurate determination of $K(z)$. In fact, the larger the $\Delta\beta_D$ employed (i.e. the lower the frequency resolution), the faster the numerical error is added to $K(z)$. As a consequence, the corresponding S-parameters get more degraded with the largest values of $\Delta\beta_D$ when compared to the target responses (see S-parameter comparative graphs of Fig. 6.40b and Fig. 6.40c). The only synthesis that has obtained accurate results is the one that employed the most refined resolution, $\Delta\beta_D = \frac{\beta_0}{1000}$ (red traces in Fig. 6.40).

The maximum $\Delta\beta_D$ that can be employed for an accurate calculation of $K(z)$ may be understood as the minimum sampled information of the $S_{11}(\beta)$ that must be supplied to the ILP method in order to avoid an excessive accumulation of error due to numerical uncertainty.

However, a dual explanation from the point of view of the τ domain can be provided. As it has been stated before, the duration of the impulse response $F_c(\tau)$, $\tau_{D,max}$, depends on $\Delta\beta_D$ by (5.22). Thus, each target $F_c(\tau)$ that was employed for the syntheses features a different duration $\tau_{D,max1} = \frac{250\cdot\pi}{\beta_0}$, $\tau_{D,max2} = \frac{500\cdot\pi}{\beta_0}$, $\tau_{D,max3} = \frac{1000\cdot\pi}{\beta_0}$, and $\tau_{D,max4} = \frac{2000\cdot\pi}{\beta_0}$, as it can be seen in Fig. 6.41.

If the Fourier Transform [6] and the theory of signals and systems are considered [12], it will be clear that the inverse Fourier Transform of a bandlimited $S_{11}(\beta)$ leads to an infinite $F(\tau)$. Moreover, if the properties of the FFT are also taken into account, it will be clear that the inverse

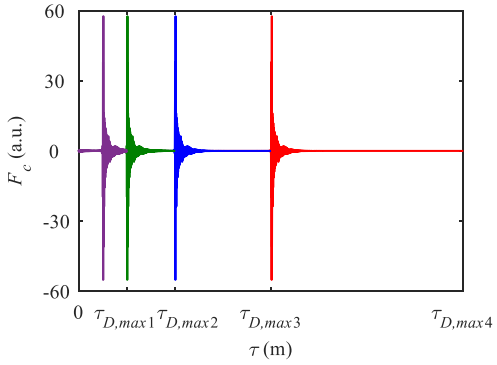

Fig. 6.41. Comparison between the different target impulse responses in reflection, $F_c(\tau)$, defined with $\tau_{D,max1} = \frac{250\cdot\pi}{\beta_0}$ (purple line), $\tau_{D,max2} = \frac{500\cdot\pi}{\beta_0}$ (green line), $\tau_{D,max3} = \frac{1000\cdot\pi}{\beta_0}$ (blue line), and $\tau_{D,max4} = \frac{2000\cdot\pi}{\beta_0}$ (red line).

FFT of a bandlimited $S_{11}(\beta)$ leads to a $F(\tau)$ that is affected by the aliasing phenomenon [5]. This parasitic effect cannot be avoided in practical implementations, being more obvious with lower values of τ_{max} since the overlapping of the underlying periodic replicas of $F(\tau)$ associated with the FFT gets increased [5] and hence, the resulting discretized version of $F(\tau)$ gets degraded. Since the conversion between the τ and β domain is performed at each layer in the ILP technique due to the propagation of the reflection coefficient of (6.10)-(6.12), it will be advisable to extend the τ axis to the longest possible $\tau_{D,max}$ so as to reduce the effect of aliasing and the numerical error that it carries.

6.3.3. Definition of the Target Response by Imposing Different Linear Delays

Regarding the determination of the impact of the linear delay of the target response on the calculation of $K(z)$ by means of ILP, four different syntheses were executed by imposing different linear delays, τ_{del}, to the target responses by following the criterion summarized in Table 6.8, where the values of the rest of the relevant parameters for the synthesis are also provided.

$\beta_{D,max} \leftrightarrow T_{D,\tau}$	$\Delta\beta_D \leftrightarrow \tau_{D,max}$	τ_{del}	Δz
$40 \cdot \beta_0 \leftrightarrow \frac{\pi}{40 \cdot \beta_0}$	$\frac{\beta_0}{2000} \leftrightarrow \frac{4000 \cdot \pi}{\beta_0}$	$0.1 \cdot \tau_{D,max}$	$T_{D,z} = \frac{T_{D,\tau}}{2}$
$40 \cdot \beta_0 \leftrightarrow \frac{\pi}{40 \cdot \beta_0}$	$\frac{\beta_0}{2000} \leftrightarrow \frac{4000 \cdot \pi}{\beta_0}$	$0.2 \cdot \tau_{D,max}$	$T_{D,z} = \frac{T_{D,\tau}}{2}$
$40 \cdot \beta_0 \leftrightarrow \frac{\pi}{40 \cdot \beta_0}$	$\frac{\beta_0}{2000} \leftrightarrow \frac{4000 \cdot \pi}{\beta_0}$	$0.3 \cdot \tau_{D,max}$	$T_{D,z} = \frac{T_{D,\tau}}{2}$
$40 \cdot \beta_0 \leftrightarrow \frac{\pi}{40 \cdot \beta_0}$	$\frac{\beta_0}{2000} \leftrightarrow \frac{4000 \cdot \pi}{\beta_0}$	$0.4 \cdot \tau_{D,max}$	$T_{D,z} = \frac{T_{D,\tau}}{2}$

Table 6.8. Frequency response and ILP parameters for the four synthesis procedures performed to determine the impact of the variation of τ_{del} on the synthesis result.

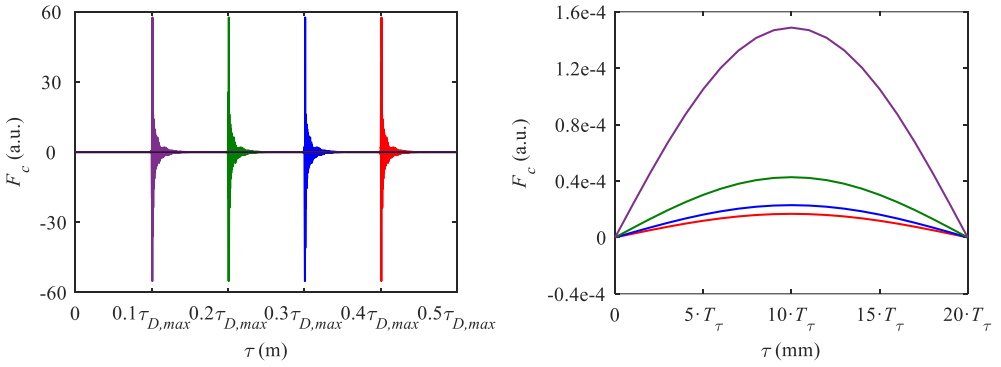

Fig. 6.42. (a) Comparison between the different target impulse responses in reflection, $F_c(\tau)$, defined with $\tau_{del} = 0.1 \cdot \tau_{D,max}$ (purple line), $\tau_{del} = 0.2 \cdot \tau_{D,max}$ (green line), $\tau_{del} = 0.3 \cdot \tau_{D,max}$ (blue line), and $\tau_{del} = 0.4 \cdot \tau_{D,max}$ (red line). (b) Detail of the comparison for the first $20 \cdot T_{D,\tau}$ of these impulse responses where the effect of aliasing can be observed.

Since the four target responses were defined with the same $\Delta\beta_D$, their $\tau_{D,max}$ are also identical. However, by modifying the τ_{del}, the most relevant part (the one that features the maximum amplitude) is not placed at the same point of the τ axis, as it can be seen in Fig. 6.42a, where the different $F_c(\tau)$ are depicted. Indeed, the relevant part of each $F_c(\tau)$ is placed approximately at $0.1 \cdot \tau_{D,max}$ (purple line), $0.2 \cdot \tau_{D,max}$ (green line), $0.3 \cdot \tau_{D,max}$ (blue line), and $0.4 \cdot \tau_{D,max}$ (red line), something that becomes noticeable by taking into account the properties of the Fourier transform [6], since the target responses will be described by the Fourier pair:

$$S_{11}(\beta) \cdot e^{-j\cdot\beta\cdot\tau_{del}} = FT\{F(\tau) * \delta(\tau - \tau_{del})\} \tag{6.28}$$

It is worth noting that the amplitude of $F_c(\tau)$ at the early instants of τ depends on the delay τ_{del} introduced, as it is clear in view of Fig. 6.42b. Thus, as it was partially introduced in section 6.3.2, the effect of the aliasing [5] at $\tau = 0$ will depend on the amplitude of $F_c(\tau)$ at the early instants of τ, due to the fact that the overlapping between the adjacent underlying replicas of $F_c(\tau)$ gets increased when high amplitudes of the original $F_c(\tau)$ are found at these first values of the τ axis [5]. Since the coupling coefficient calculation of (6.14) and the propagation of the reflection spectrum that depends on (6.11) rely on the FFT for their efficient numerical implementation, it will be necessary to ensure the minimum amplitude of the initial $F_c(\tau = 0)$ so as to minimize the error contribution added by aliasing. Since the high values of τ_{del} reduce the initial amplitudes of $F_c(\tau)$ (see Fig. 6.42b), the error caused by the aliasing should be reduced in the accumulative layer-by-layer procedure when high values of τ_{del} are employed.

Moreover, if a high value of τ_{del} is imposed, the impulse response in reflection, $F_c(\tau)$, tends to be more strictly causal, because its amplitude at the negative instants of τ decreases (it is important to recall that the negative instants of τ appear at the end of $F_c(\tau)$ due to the time domain aliasing). Thus, the causality principle assumed in the ILP and CLP methods for the target response in reflection gets closer to be fulfilled, even though it will never be strictly achieved if the duration of $F_c(\tau)$ is infinite.

The resulting $K(z)$ for the four synthesis processes with $\tau_{del} = 0.1 \cdot \tau_{D,max}$, $\tau_{del} = 0.2 \cdot \tau_{D,max}$, $\tau_{del} = 0.3 \cdot \tau_{D,max}$, and $\tau_{del} = 0.4 \cdot \tau_{D,max}$, are provided in Fig. 6.43a, Fig. 6.44a, Fig. 6.45a, and Fig. 6.46a, respectively. The results of their corresponding single-mode analyses are given in Fig. 6.43b-Fig. 6.43c, Fig. 6.44b-Fig. 6.44c, Fig. 6.45b-Fig. 6.45c, and Fig. 6.46b-Fig. 6.46c.

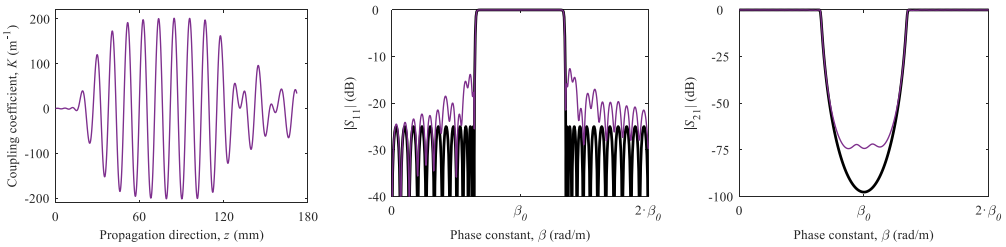

(a) (b) (c)

Fig. 6.43. (a) Coupling coefficient synthetized with a target response defined with $\tau_{del} = 0.1 \cdot \tau_{D,max}$. The comparisons between the target (black lines) and the resulting (purple lines) (b) $S_{11}(\beta)$- and (c) $S_{21}(\beta)$-parameters from the single-mode analysis of $K(z)$ are provided.

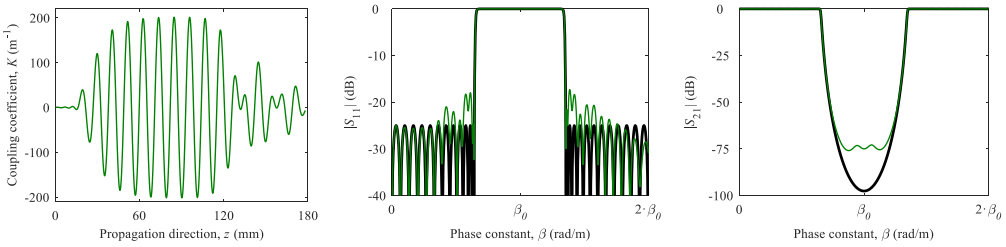

(a) (b) (c)

Fig. 6.44. (a) Coupling coefficient synthetized with a target response defined with $\tau_{del} = 0.2 \cdot \tau_{D,max}$. The comparisons between the target (black lines) and the resulting (green lines) (b) $S_{11}(\beta)$- and (c) $S_{21}(\beta)$-parameters from the single-mode analysis of $K(z)$ are provided.

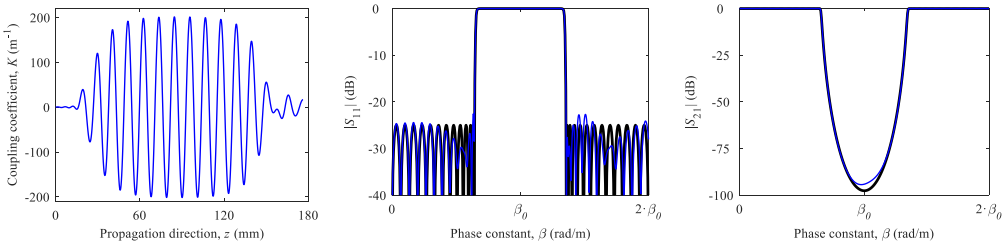

(a) (b) (c)

Fig. 6.45. (a) Coupling coefficient synthetized with a target response defined with $\tau_{del} = 0.3 \cdot \tau_{D,max}$. The comparisons between the target (black lines) and the resulting (blue lines) (b) $S_{11}(\beta)$- and (c) $S_{21}(\beta)$-parameters from the single-mode analysis of $K(z)$ are provided.

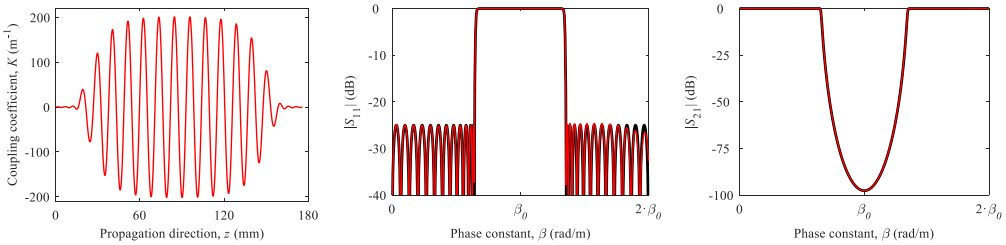

(a) (b) (c)

Fig. 6.46. (a) Coupling coefficient synthetized with a target response defined with $\tau_{del} = 0.4 \cdot \tau_{D,max}$. The comparisons between the target (black lines) and the resulting (red lines) (b) $S_{11}(\beta)$- and (c) $S_{21}(\beta)$-parameters from the single-mode analysis of $K(z)$ are provided.

In view of the results shown in Fig. 6.43-Fig. 6.46, the synthesis procedures that employ the lowest linear delays achieve a poorer quality for the $K(z)$ obtained, and their corresponding analyses do not fit the target response as perfectly as the syntheses realized with the response that features the highest delay, see Fig. 6.46. Therefore, as it was expected, the numerical error introduced by the aliasing effect becomes more important when lower delays are introduced in the target responses and hence, it will be highly recommended to perform an additional linear delay of at least $\tau_{del} = 0.4 \cdot \tau_{D,max}$ for the ILP syntheses. Nonetheless, higher values of τ_{del} may be employed for the synthesis of the most challenging responses.

6.3.4. Definition of Different Layer Thicknesses, Δz

In order to finalize the assessment of the critical parameters that affect an ILP synthesis process, the choice of the thickness of the layer, Δz, will be studied. It is worth noting that the

selection of this parameter is independent from the definition of the target frequency response and it conforms an exclusive degree of freedom of the ILP technique.

In this case, the definition of the layer thickness will be done in terms of an integer number of samples of the z axis, $T_{D,z}$, according to (6.16). Thus, the initial synthesis will be performed by employing the longest layer. For the rest of the synthesis procedures, Δz will be progressively thinner. The specific values selected for Δz, as well as for the rest of the frequency response parameters, are given in Table 6.9. The coupling coefficients, $K(z)$, obtained and their corresponding single-mode analysis results are provided in Fig. 6.47, Fig. 6.48, Fig. 6.49, and Fig. 6.50.

$\beta_{D,max} \leftrightarrow T_{D,\tau}$	$\Delta\beta_D \leftrightarrow \tau_{D,max}$	τ_{del}	Δz
$10 \cdot \beta_0 \leftrightarrow \frac{\pi}{10 \cdot \beta_0}$	$\frac{\beta_0}{1000} \leftrightarrow \frac{2000 \cdot \pi}{\beta_0}$	$\frac{\tau_{D,max}}{2}$	$18 \cdot T_{D,z} = 9 \cdot T_{D,\tau}$
$10 \cdot \beta_0 \leftrightarrow \frac{\pi}{10 \cdot \beta_0}$	$\frac{\beta_0}{1000} \leftrightarrow \frac{2000 \cdot \pi}{\beta_0}$	$\frac{\tau_{D,max}}{2}$	$12 \cdot T_{D,z} = 6 \cdot T_{D,\tau}$
$10 \cdot \beta_0 \leftrightarrow \frac{\pi}{10 \cdot \beta_0}$	$\frac{\beta_0}{1000} \leftrightarrow \frac{2000 \cdot \pi}{\beta_0}$	$\frac{\tau_{D,max}}{2}$	$6 \cdot T_{D,z} = 3 \cdot T_{D,\tau}$
$10 \cdot \beta_0 \leftrightarrow \frac{\pi}{10 \cdot \beta_0}$	$\frac{\beta_0}{1000} \leftrightarrow \frac{2000 \cdot \pi}{\beta_0}$	$\frac{\tau_{D,max}}{2}$	$T_{D,z} = \frac{T_{D,\tau}}{2}$

Table 6.9. Frequency response and ILP parameters for the four synthesis procedures performed to determine the impact of the variation of Δz on the synthesis result.

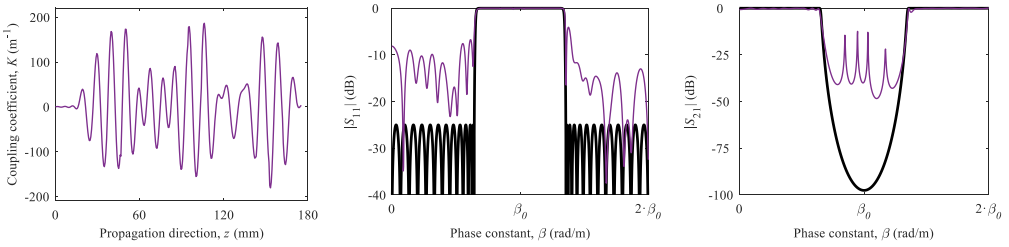

(a) (b) (c)

Fig. 6.47. (a) Coupling coefficient synthetized with a target response defined with $\Delta z = 18 \cdot T_{D,z}$. The comparisons between the target (black lines) and the resulting (purple lines) (b) $S_{11}(\beta)$- and (c) $S_{21}(\beta)$-parameters from the single-mode analysis of $K(z)$ are provided.

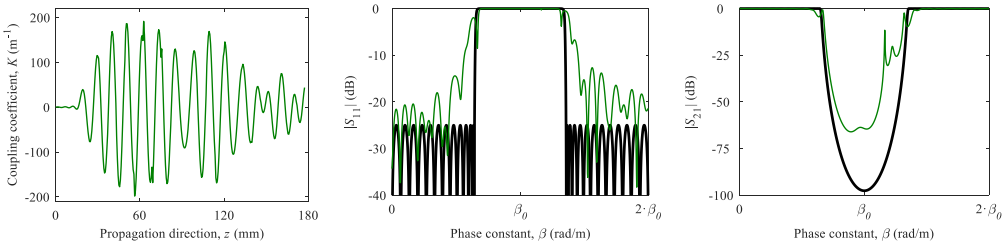

(a) (b) (c)

Fig. 6.48. (a) Coupling coefficient synthetized with a target response defined with $\Delta z = 12 \cdot T_{D,z}$. The comparisons between the target (black lines) and the resulting (green lines) (b) $S_{11}(\beta)$- and (c) $S_{21}(\beta)$-parameters from the single-mode analysis of $K(z)$ are provided.

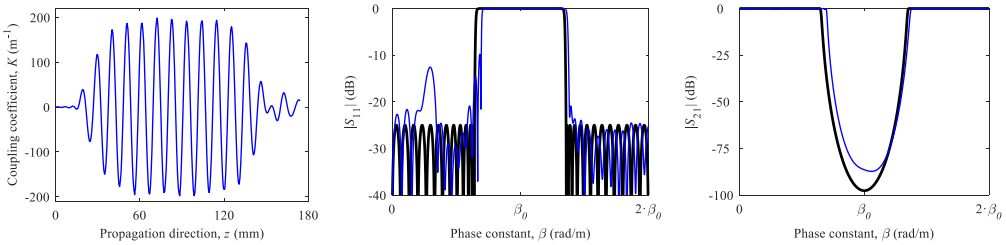

(a) (b) (c)

Fig. 6.49. (a) Coupling coefficient synthetized with a target response defined with $\Delta z = 6 \cdot T_{D,z}$. The comparisons between the target (black lines) and the resulting (blue lines) (b) $S_{11}(\beta)$- and (c) $S_{21}(\beta)$-parameters from the single-mode analysis of $K(z)$ are provided.

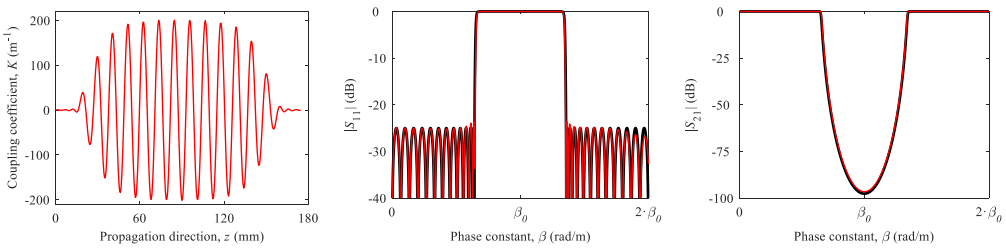

(a) (b) (c)

Fig. 6.50. (a) Coupling coefficient synthetized with a target response defined with $\Delta z = T_{D,z}$. The comparisons between the target (black lines) and the resulting (red lines) (b) $S_{11}(\beta)$- and (c) $S_{21}(\beta)$-parameters from the single-mode analysis of $K(z)$ are provided.

As it can be seen, the most accurate result is obtained by selecting the thinnest layer possible, $\Delta z = T_{D,z} = \frac{T_{D,\tau}}{2}$ (see Fig. 6.50). This conclusion is in full agreement with the philosophy of the ILP method, since the calculation of the coupling coefficient at each m-th layer, $K(m \cdot \Delta z + z')$, see (6.14), is based on the accuracy of the zero-order approximation of the GLM solution for that layer. As it has been previously commented in the theoretical

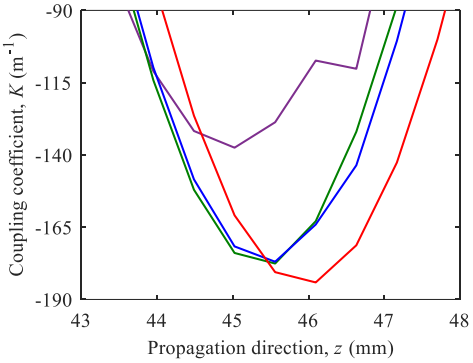

Fig. 6.51. Detail of the coupling coefficients synthetized with a target response defined with $\Delta z = 18 \cdot T_{D,z}$ (purple line), $\Delta z = 12 \cdot T_{D,z}$ (green line), $\Delta z = 6 \cdot T_{D,z}$ (blue line), and $\Delta z = T_{D,z}$ (red line).

development of the ILP method, this approximation is suitable for low reflectivity cases. If the layer under study does not feature a large thickness, the response of that layer and the coupling coefficient can be reasonably characterized by considering a single reflection, i.e. the zero-order approximation of the GLM equations of (6.3) and (6.4). However, when a thicker layer is considered, like in the cases of the synthesis of Fig. 6.47-Fig. 6.49, the response of that layer cannot be correctly characterized using a single scattering event (zero-order GLM approximation) as it is actually a function of multiple events and hence, the calculation of $K(z)$ becomes inaccurate. In order to illustrate this reasoning, a comparative detail of the different coupling coefficients that have been synthetized is provided in Fig. 6.51. As it can be observed, when the thickness of the layer is short enough (red trace), the coupling coefficient is calculated with higher accuracy. However, when an excessive thickness is employed for the layer as in the case of the purple trace, $K(z)$ gets underestimated with the zero-order GLM solution and hence, the performance of its associated frequency response is very poor.

It must be highlighted that Δz is not only important for the $K(z)$ calculation, but also for the propagation of the reflection coefficient. Since the reflection coefficient of the next layer, $S_{11,m+1}(\beta)$, is determined from Δz and from the previous $F_m(\tau)$ by means of (6.10) and (6.11) that in turn rely on the zero-order approximation of the solution of the GLM equations, the use of a thin layer will result in a better propagation of the reflection coefficient.

Nevertheless, it is worth noting that in some practical cases where an excessive number of propagations is needed, the numerical error accumulated at each propagation overcomes the accuracy provided by taking a thin Δz, leading to a degraded final result. In those situations, a thicker layer (with $M > 1$, see (6.16)) could help to obtain more accurate results, since the zero-

order GLM approximation may still be suitable, and the number of propagations as well as their associated numerical error will be reduced.

Therefore, it can be concluded that in a general situation the length of each layer must be selected as short as possible. However, in those cases where the numerical error caused by an excessive number of propagations of the reflection coefficient becomes troublesome, a trade-off must be found between the selection of Δz and the number of propagations, so as to obtain an accurate result for the coupling coefficient.

REFERENCES

[1] A. Rosenthal and M. Horowitz, "Inverse scattering algorithm for reconstructing strongly reflecting fiber Bragg gratings," *IEEE J. Quantum Electron.*, vol. 39, no. 8, pp. 1018-1026, Aug. 2003.

[2] I. Arnedo, M. A. G. Laso, F. Falcone, D. Benito, T. Lopetegi, "A Series Solution for the Single-Mode Synthesis Problem Based on the Coupled-Mode Theory," *IEEE Trans. Microw. Theory Tech.*, vol. 56, no. 2, pp.457-466, Feb. 2008.

[3] G. H. Song and S. Y. Shin, "Design of Corrugated Waveguide Filters by the Gel'fand-Levitan-Marchenko Inverse-Scattering Method," *J. Opt. Soc. Amer. A*, vol. 2, no. 11, pp. 1905-1915, Nov. 1985.

[4] E. Peral, J. Capmany, and J. Marti, "Iterative Solution to the Geld'Fand-Levitan-Marchenko coupled equations and application to synthesis of fiber gratings," *IEEE J. Quantum Electron.*, vol. 32, no. 12, pp. 2078-2084, Dec. 1996.

[5] A. V. Oppenheim and R. W. Schafer, *Discrete-Time Signal Processing*, 3rd ed. New York, NY, USA: Pearson, 2013.

[6] A. Papoulis, The Fourier Integral and its Applications (Electronic Science Series). New York, NY, USA: McGraw-Hill, 1962.

[7] EOSint M280 Datasheet, EOS. [Online] Available: https://cdn0.scrvt.com/eos/e1dc925774b24d9f/8d4013a5bc26/EOS_System_Data_Sheet_EOSINT_M280_EN_V2_Web.pdf.

[8] O. A. Peverini *et al.*, "Selective Laser Melting Manufacturing of Microwave Waveguide Devices," *Proc. IEEE*, vol. 105, no. 4, pp. 620-631, April 2017.

[9] R. J. Cameron, C. M. Kudsia, R. R. Mansour, "Microwave filters for communication systems: fundamentals, design and applications", Hoboken, NJ: John Wiley & Sons, 2007.

[10] Israel Arnedo, "New Methods for the Synthesis of Microwave Devices Based on the Coupled-Mode Theory," Doctoral Thesis, Universidad Pública de Navarra, España, 2009.

[11] Magdalena Chudzik, "Synthesis Techniques for Novel Devices Based on Smooth Profiles with Application from the Microwave to the Terahertz Regions," Doctoral Thesis, Universidad Pública de Navarra, España, 2013.

[12] A. V. Oppenheim, A. S. Willsky, and S. H. Nawab, *Signals & Systems*, 2nd ed. Upper Saddle River, NJ, USA: Prentice Hall, 1997.

upna

Universidad Pública de Navarra
Nafarroako Unibertsitate Publikoa

CHAPTER 7. CONCLUSIONS

The main objectives proposed for this thesis have been successfully achieved. The electromagnetic behavior of general nonuniform waveguide structures has been modelled using the Coupled-Mode Theory and taking advantage on this formulation, a thorough study of some of the most widely employed waveguide technologies in the microwave and millimeter wave range was performed. The single-mode operation assumption allowed to satisfy the necessary conditions for dealing with the synthesis problem by using different theoretical models devoted to allow the synthesis in technologies where the phase constant can vary along the propagation axis, and the compensation of the parasitic effects of higher-order modes. As a result, different synthesis methods that were proposed in the past have been investigated and a novel synthesis technique has been fully developed and demonstrated, showing a great improvement in the rejection levels of the frequency responses that can be properly synthetized. The synthesis techniques allowed us to propose novel design methods for some of the most frequently employed passive devices in microwave engineering, such as multiplexers, tapers and filters. The feasibility of these methods was confirmed through several practical design examples where realistic target specifications were required. In all cases, a good agreement was achieved between the target, simulated and measured results.

The analysis of the electromagnetic behavior of general nonuniform waveguide structures has been carried out using the Coupled-Mode Theory that in turn rests on the cross-section method. The set of coupled-mode equations shows that the coupling coefficient is a key parameter, since it is related with the physical dimensions of the waveguide and at the same time it determines the frequency response.

One of the most widely employed technologies for the implementation of microwave devices, the rectangular waveguide, was studied with the formulation of the Coupled-Mode Theory. By doing so, closed-form expressions were obtained for the coupling coefficients between all TE and TM modes of the rectangular waveguide. Moreover, the relevant couplings that must be studied in order to characterize the behavior of a rectangular waveguide device when it is excited with the fundamental mode were determined as a function of the geometrical variations featured by the cross-section of the structure along the propagation direction.

In order to address the synthesis problem, i.e. to deduce the required coupling coefficient from the target response in reflection, the single-mode assumption was introduced. The reformulation of the Coupled-Mode Theory by considering this approximation yields to a univocal relationship between the coupling coefficient and the physical dimensions of the rectangular waveguide. This link is also obtained for the case of TEM and QTEM transmission lines through the characteristic impedance. The relationship between the physical dimensions and the characteristic impedance was given explicitly for the cases of single microstrip line and symmetrical edge coupled microstrip lines.

In addition, a model for waveguides that can exhibit a phase constant variable along the propagation direction has been provided for the first time. This approximation is exact for a single frequency and it rests on the definition of a reference phase constant that is assumed to remain fixed along a normalized propagation axis. The synthesis can be performed according to both variables and the final device is obtained by applying a denormalization procedure that redistributes the normalized propagation axis as a function of the reference phase constant selected for the synthesis, as well as of the actual phase constant featured at each point of that axis.

On the other hand, novel compensation procedures for the possible degradation in the frequency response that can be caused by parasitic couplings to higher-order modes in closed-boundary waveguides, have been proposed. These effects can be assimilated as a continuous variation of the phase constant of the fundamental mode along the propagation axis, and the uniform and distributed scaling compensation methods were developed as a result. Both techniques have been tested in practical design examples where a remarkable performance has been attained, especially for the case of the recursive distributed scaling method.

Using the equation system attained for the single-mode approximation of the Coupled-Mode Theory, the most straightforward synthesis approach for electromagnetic bandgap (EBG) structures was presented. The analytical spurious-free EBG solution that does not feature parasitic stopbands was described in detail, and different solutions to control its length and extreme dimensions were achieved.

A method for the design of multiplexers by exploiting the EBG concept, as well as the simultaneous backward and forward coupling of the microstrip coupled-line technology, was described and a practical example was successfully developed. This technique allows us to select the backward coupling band with the period of the EBG, while the length of the structure controls the forward-coupled band. Since the input port is matched for all the frequencies, the remaining frequency components that have not been backward or forwardly coupled are driven to the direct port.

Next, the exact series solution of the one-dimensional Inverse Scattering synthesis problem was thoroughly developed by means of the Gel'fand, Levitan, Marchenko (GLM) equations. It allows us to directly synthetize the coupling coefficient that is needed to achieve any stable, passive and causal target response in reflection. Since the terms of the series of the GLM solution must be truncated in practical implementations, the associated restrictions in the rejection levels that can be achieved make it attractive to synthetize low reflectivity responses.

Linked to the GLM synthesis technique and to several solutions of the single-mode approximation of the Coupled-Mode Theory, a new design procedure arose for tapered matching sections in general waveguide technology for single-mode operation, that was described in detail. This method allows the generalization of the Klopfenstein and Hecken taper solutions for general waveguide technology. Moreover, the use of novel taper solutions that are obtained from a modified version of the frequency response of the multisection Chebyshev transformers, leads to final synthetized devices that are shorter than the Klopfenstein taper, which was considered as the shortest solution up to the date. Many practical design examples were successfully synthesized and fabricated in rectangular waveguide technology, where the matching of waveguides with different height, width, as well as different simultaneous height and width, was required. The excellent performance of the ideal modelling of technologies where the phase constant can vary along the propagation direction was demonstrated in some of these examples.

The Continuous Layer Peeling (CLP) synthesis technique was the second Inverse Scattering method that was covered in depth in the thesis. It was initially intended for the synthesis of highly reflective responses. The method is based on the principle of causality and allows us to determine the coupling coefficient by assuming that it is divided into infinitesimal layers. Several relevant aspects for the numerical implementation of the method were also addressed.

In order to exploit the high-rejection capabilities of the CLP technique, a method for the design of novel low-pass and band-pass filters without spurious rejection bands was fully described. The method starts from the determination of the Unit Elements of a commensurate-line prototype that complies with the frequency response requirements. Then, the response in

reflection of the prototype can be extracted and properly modified in either phase constant or reflection distance domains, giving rise to the target response for the synthesis. The resulting synthesized structure retains similar dimensions to the starting commensurate-line prototype but featuring a profile that varies in a smooth fashion. Following this procedure, a spurious-free microstrip low-pass filter was designed, which showed a great level of agreement between the target response and the simulation and measurement results, where the absence of spurious rejection bands was ensured at least up to the 15th harmonic of the maximum rejection frequency in measurement. The method was also employed to synthetize a rectangular waveguide low-pass filter intended to be fabricated with metal Additive Manufacturing (AM) techniques. However, it was not possible to achieve an accurate enough solution for the coupling coefficient due to the extreme challenging rejection requirements of the target response.

The so-called Integral Layer Peeling (ILP) synthesis technique constitutes the last synthesis method described in the thesis. Like CLP, ILP is based on the layer peeling approach, but in contrast to the former, the later incorporates important differences in its implementation, such as the finite layer thickness and a different propagation method for the reflection spectrum, that drives to a great improvement in the accuracy that can be achieved for the coupling coefficient, even when the target response features very high rejection levels. Several aspects of the numerical implementation were addressed and some of them were compared with the corresponding from CLP, showing a better behavior of ILP in terms of accuracy and computational efficiency.

The accuracy of the ILP method was successfully tested, surpassing the accuracy issues that were found during the initial synthesis attempt of rectangular waveguide filters with CLP. The length of this initial filter was improved in a subsequent design example by requiring a more suitable response for the starting prototype. In both cases, the uniform scaling method for the compensation of the parasitic effects of cut-off modes was successfully applied and a very good agreement was obtained between the target response and the final simulation results.

These two filter designs were fabricated in a single piece using a metal AM procedure: the Direct Metal Laser Sintering (DMLS) technique. The structures were printed following the propagation direction, without needing auxiliary supports, something that represents a clear advantage with respect to other approaches that are followed in the literature to fabricate rectangular waveguide filters with these AM techniques. The good quality of the measurement results confirmed the suitability of the smooth profiled filters for a fabrication with metal AM techniques.

The last design example of a rectangular waveguide low-pass filter exposed the dramatic degradation in the frequency response that can be caused by the cut-off modes in certain cases.

In order to overcome these effects, the recursive distributed scaling method was employed. The result of this technique exhibited a remarkable fitting with the frequency response that was expected from the single-mode assumption. Accordingly, the recursive distributed scaling method can be considered as a powerful technique to compensate for the spurious effects of cut-off modes.

Finally, a complete assessment was performed in order to identify the critical parameters of the numerical definition of the target response, as well as the layer thickness, that may affect the quality of the results that are obtained with the ILP synthesis method. The insight gathered in this study will be very useful for future synthesis processes that will be carried out by means of the ILP technique.

CONCLUSIONES

Los objetivos principales que se propusieron al comienzo de esta tesis han sido logrados de forma satisfactoria. El comportamiento electromagnético de las estructuras generales de guía de onda no uniformes ha sido modelado utilizando la Teoría de Acoplo de Modos, y aprovechando su formulación, se ha realizado un estudio exhaustivo de algunas de las tecnologías de guía de onda más ampliamente utilizadas en el rango de microondas y milimétricas. La suposición de operación de modo único permitió cumplir con los principios necesarios para abordar el problema de síntesis al usar también diferentes aproximaciones teóricas dedicadas a tratar con tecnologías en las que los cambios de dimensiones conllevan una modificación de la constante de fase y con los efectos parásitos de los modos de orden superior en guías de contorno cerrado. Como resultado, se han investigado diferentes métodos de síntesis que se propusieron en el pasado y se ha descrito y probado una nueva técnica, que muestra una gran mejora con respecto a la precisión que se podía lograr. Las técnicas de síntesis presentadas permitieron proponer diferentes métodos de diseño para algunos de los dispositivos más frecuentemente utilizados en ingeniería de microondas, como multiplexores, tapers y filtros. La viabilidad de los métodos de diseño se confirmó a través de varios ejemplos prácticos de diseño en los que se requerían especificaciones realistas, logrando un alto grado de similitud entre los resultados esperados y medidos en todos los casos.

El análisis del comportamiento electromagnético de una estructura de guía de onda general se ha llevado a cabo de forma exacta y sin tomar una aproximación mediante la Teoría de Acoplo de Modos, que a su vez se basa en el método de la sección transversal. El conjunto de ecuaciones de acoplo de modos que se han obtenido ha demostrado que el coeficiente de

acoplamiento es un parámetro clave, ya que está relacionado con las dimensiones físicas de la estructura de guía de onda, y a su vez, determina su respuesta de frecuencia.

El estudio de una de las tecnologías más utilizadas en microondas, la guía de onda rectangular, se realizó aplicando la formulación de la Teoría de Acoplo de Modos. Como resultado, se obtuvieron expresiones analíticas para los coeficientes de acoplo que pueden darse entre los diferentes tipos de modos que pueden propagarse en una guía de onda rectangular. Estos coeficientes de acoplo únicamente dependen de las dimensiones físicas de la guía de onda. Además, se determinaron los acoplamientos relevantes que deben estudiarse para caracterizar el comportamiento de la estructura cuando esta se excita con el modo fundamental, considerando para ello las variaciones geométricas que presenta la sección transversal de la estructura de guía de onda rectangular a lo largo de la dirección de propagación.

Con el objetivo de abordar el problema de la síntesis, es decir, para deducir el coeficiente de acoplamiento a partir de una respuesta en reflexión, se introdujo el supuesto de operación monomodo. La reformulación de la Teoría de Acoplo de Modos al considerar esta aproximación produce una relación unívoca entre el coeficiente de acoplamiento y las dimensiones físicas de la guía de onda rectangular. Esta relación es extensiva para el caso de líneas de transmisión TEM y QTEM, pero con la impedancia característica como variable intermedia y, en consecuencia, se estudió detalladamente la relación entre las dimensiones físicas y la impedancia característica para los casos de línea de microstrip exclusiva y de líneas de microstrip acopladas.

Además, se ha proporcionado un modelo para guías de onda que exhiben una constante de fase que puede variar a lo largo de la dirección de propagación. Esta aproximación es exacta para una frecuencia única y se basa en la definición de una constante de fase de referencia que se asume que permanece constante a lo largo de un eje de propagación normalizado. La síntesis se puede realizar de acuerdo con ambas variables y el dispositivo final se obtiene aplicando un proceso de desnormalización que redistribuye el eje de propagación normalizado en función de la constante de fase de referencia seleccionada, así como de la constante de fase real presentada en cada punto de ese eje.

Por otro lado, se ha propuesto un procedimiento de compensación de los posibles efectos espurios que pueden ser causados por los acoplamientos parásitos a modos de orden superior en guías de onda de contorno cerrado. Estos efectos pueden asimilarse como una variación continua de la constante de fase, y como resultado se desarrollaron los métodos de compensación de escalado uniforme y distribuido. Ambas técnicas han sido probadas en ejemplos prácticos de diseño, en los que se ha logrado un rendimiento notable, especialmente para el caso del método de escalado distribuido recursivo.

Por medio del sistema de ecuaciones de la aproximación monomodo de la Teoría de Acoplo de Modos, se ha presentado el enfoque de síntesis más directo, que consiste en la síntesis de estructuras periódicas y cuasi periódicas unidimensionales, también conocidas como EBGs. Se desarrolló el método para sintetizar estructuras EBG óptimas que no exhiben bandas espurias y se proporcionaron diferentes soluciones para controlar su longitud y dimensiones físicas extremas.

Un método basado en el concepto de EBGs y que emplea el acoplamiento simultáneo *backward* y *forward* propio de la tecnología de líneas acopladas microstrip ha sido aplicado para el diseño de multiplexores, describiéndose así mismo un ejemplo de diseño práctico. Esta técnica permite seleccionar la banda de acoplamiento *backward* con el período de la EBG, mientras que la longitud de la estructura controla la banda de acoplamiento *forward*. Dado que el puerto de entrada está idealmente adaptado a todas las frecuencias, las componentes frecuenciales que no se han escogido para acoplarse *backward* o *forward* se dirigen al puerto directo.

A continuación, se desarrolló la solución en serie exacta del problema de síntesis mediante las ecuaciones de Gel'fand, Levitan, Marchenko (GLM). Esta técnica permite sintetizar directamente el coeficiente de acoplamiento necesario para lograr cualquier respuesta objetivo estable, pasiva y causal en reflexión. Dado que los términos de la serie de la solución GLM deben truncarse en implementaciones prácticas, las restricciones asociadas en el nivel de rechazo que se puede lograr hacen que sea un método atractivo para sintetizar respuestas de baja reflectividad.

Vinculado a la técnica de síntesis GLM y a varias soluciones de la aproximación de modo único de la Teoría de Acoplo de Modos, se ha propuesto y descrito en detalle un procedimiento de diseño para tapers en tecnología de guía de onda general para operación monomodo. Este método permite la síntesis de las soluciones clásicas de Klopfenstein y Hecken para tapers en línea de transmisión en tecnología de guía de onda general. Además, el uso de nuevas funciones que se obtienen de una versión modificada de la respuesta en frecuencia de los transformadores Chebyshev multisección conduce a la síntesis de tapers finales que son más cortos que el taper Klopfenstein, considerado hasta la fecha como la solución para taper más corta. Muchos ejemplos prácticos de diseño de tapers en guía rectangular han sido exitosamente realizados y fabricados, requiriendo la adaptación de guías de onda de diferente altura, anchura, y altura y anchura simultáneamente. En algunos de estos ejemplos de diseño, se demostró el excelente rendimiento del modelado de guías de onda no uniformes en las que cambia la constante de fase a lo largo del eje de propagación mediante una constante de fase fija de referencia que no varía en un eje de propagación normalizado.

El tercer método de síntesis que se desarrolla en esta tesis es la técnica de CLP, que inicialmente estaba dirigida a la síntesis de respuestas con altos niveles de rechazo. El método

se basa en el principio de causalidad y permite determinar el coeficiente de acoplamiento del dispositivo que presenta una respuesta causal, estable y pasiva objetivo, al suponer que está dividido en capas infinitesimales. Varios aspectos numéricos que resultan esenciales para la implementación práctica de este método también fueron tratados.

Con objeto de explotar las capacidades de rechazo de la técnica CLP, se ha descrito de forma precisa un método de diseño de filtros paso bajo y paso banda que no presentan bandas de rechazo espurias. Este método parte de la determinación de los *Unit Elements* de un prototipo de línea comensurada que cumpla con los requisitos necesarios en frecuencia. Luego, la respuesta en la reflexión del prototipo puede ser deducida y adecuadamente modificada tanto en el dominio de fase constante como de distancia de reflexión, dando lugar a la respuesta objetivo para la síntesis. La estructura resultante conserva dimensiones similares al filtro de línea comensurada inicial, pero con la diferencia de que presenta un perfil que varía de manera suave. Siguiendo este procedimiento, se diseñó un filtro de paso bajo de microstrip libre de bandas espurias, en el que se logró un gran nivel de ajuste entre la respuesta objetivo y los resultados de simulación y medida, en los que la ausencia de bandas de rechazo espurias quedó patente al menos hasta el decimoquinto armónico de la frecuencia de máximo rechazo. Este método también se empleó para sintetizar un filtro de guía de onda rectangular de paso bajo destinado a ser fabricado con técnicas de fabricación aditiva en metal. Sin embargo, los requisitos de rechazo extremadamente exigentes de la respuesta objetivo causaron una acumulación excesiva de error numérico durante el proceso de síntesis que condujo a un coeficiente de acoplamiento poco preciso.

La llamada técnica de síntesis de ILP es el último método de síntesis incluido en la tesis. Como CLP, ILP se basa en el enfoque de *layer-peeling*, pero en contraste con CLP, ILP incorpora diferencias importantes en su implementación, como el grosor de capa finita y un método de propagación diferente para el coeficiente de reflexión, que conducen a una gran mejora en la precisión que se puede lograr para el coeficiente de acoplo, incluso cuando la respuesta objetivo presenta niveles de rechazo muy elevados. Varios aspectos de la implementación numérica de ILP fueron tratados, y algunos de ellos se compararon con los propios de CLP, mostrando un mejor comportamiento de ILP en términos de precisión y eficiencia computacional.

La precisión del método ILP se probó con éxito al finalizar la síntesis del filtro en guía rectangular que no fue posible sintetizar con la técnica CLP. De hecho, la longitud final excesiva de este filtro inicial se mejoró en un ejemplo de diseño posterior al requerir una respuesta más adecuada para el prototipo inicial. En ambos casos, se aplicó el método de escalado uniforme para la compensación de los efectos parásitos de los modos de corte obteniendo un muy buen ajuste entre la respuesta objetivo y las simulaciones finales.

Los dos filtros diseñados fueron fabricaron en una sola pieza utilizando un procedimiento AM en metales: la técnica DMLS. Las estructuras se imprimieron siguiendo la dirección de propagación sin necesidad de soportes auxiliares, algo que representa una clara ventaja con respecto a otros enfoques que se han seguido en la literatura para fabricar filtros de guía de ondas rectangulares con estas mismas técnicas. La buena calidad de los resultados de medición confirmó la idoneidad de los filtros de perfil suave para ser fabricados mediante estas técnicas de AM en metales.

El último ejemplo de diseño de un filtro de paso bajo de guía de onda rectangular puso de manifiesto la importante degradación que en ciertos casos sufre la respuesta en frecuencia a causa de los modos en corte. Para superar estos efectos, se empleó el método de escala distribuida recursiva. El resultado de la aplicación de esta técnica mostró un ajuste de gran calidad respecto a la respuesta de frecuencia esperada bajo el supuesto de operación monomodo. En consecuencia, el método de escalado distribuido recursivo puede considerarse como una técnica poderosa para compensar los efectos espurios de los modos de corte.

Finalmente, se realizó un estudio completo para identificar los parámetros críticos de la respuesta objetivo y el grosor de la capa que pueden afectar la calidad de los resultados que se obtienen con ILP. La información obtenida será muy útil para futuros procedimientos de síntesis que se llevarán a cabo mediante dicha técnica.

upna

Universidad Pública de Navarra
Nafarroako Unibertsitate Publikoa

CHAPTER 8. FUTURE RESEARCH LINES

During the research process of this thesis, several interesting ideas have been proposed for the future improvement and further development of the benefits that can be currently achieved with the synthesis techniques and their resulting nonuniform waveguide structures. Some of these promising research lines belong to the purely theoretical realm with potential applications, while others are related to attractive designs of microwave and millimeter wave components. A summary of the most remarkable topics that would be worth addressing in the future is listed below:

- Overcoming the limitations imposed by the all-pole responses in transmission that can be currently targeted for the synthesis. It would be very interesting to develop a method to calculate general passive, stable and causal responses for satisfying arbitrarily required specifications with a device length controlled “a priori” by the designer, without featuring the constraint of belonging to the all-pole category in transmission. The potential applications that would be covered by the synthesis methods would benefit from this expansion of the responses.

- Linked with the previous point, one of the most promising improvements would come from a hypothetic technique to determine the target response that would lead to the most optimum structure in terms of its extreme dimensions (profile excursion and length). This advance would provide a complete control over the most important characteristics of the final device prior to starting the synthesis process. By doing so, the frequency response specifications

and the requirements for the physical dimensions of the final structure would be jointly considered in the determination of the target response.

- The performance of the ILP synthesis method could be improved by taking thicker layers and a solution of the GLM equations of an order higher than zero. The accuracy of the ILP method could be increased as a result, leading to filters that could achieve higher steepness in the transition between the passband and the stopband.

- It is necessary to perform an assessment of the capabilities of the cut-off mode compensation methods developed in this thesis, but for the case where simultaneous width and height variations are performed in the rectangular waveguide. As a result, the variety of the geometries that can be applied to satisfy a certain coupling coefficient would be expanded.

- Moreover, the method proposed for the synthesis of rectangular waveguide band-pass filters may benefit from the introduction of variations in the width of the waveguide so as to achieve higher rejection levels for the lower stopband. The improvement of these filters will require a previous study of the cut-off mode compensation methods for simultaneous height and width variations, which has been proposed in the previous point.

- The power handling capabilities of the proposed low-pass and band-pass filters should be studied since their smooth profiles probably feature higher power thresholds than their starting commensurate-line prototypes.

- It would be interesting to explore the development of couplers and power splitters with different frequency-selective features in their outputs based on some of the filtering structures presented in this thesis.

- The selectivity of the proposed smooth-profiled filters could be even improved with the use of multipath structures with transversal interference characteristics that may allow the introduction of transmission zeros in the frequency response.

- The synthesis techniques could be immediately applied and exploited for higher frequency bands or ranges, such as the THz. Indeed, the length limitations that are typically found at low frequencies vanish at those ranges, due to the inherent reduction in wavelength that those much higher frequencies involve.

- Finally, the novel possibilities offered by the Additive Manufacturing (AM) techniques can be applied to expand the performance of the nonuniform waveguide devices. Indeed, the dimensional limitations proper from planar transmission line technologies could be also improved with the use of the latest advances carried out in the AM field.

MOST RELEVANT RESEARCH MERITS OF THE AUTHOR

JOURNAL PAPERS: 8 (+1)

1. **J.M. Percaz**, J. Hussain, I. Arregui, F. Teberio, D. Benito, P. Martin-Iglesias, M.A.G. Laso, I. Arnedo, and T. Lopetegi, "Synthesis of Rectangular Waveguide Filters with Smooth Profile Oriented to Direct Metal Additive Manufacturing," *IEEE Transactions on Microwave Theory and Techniques*, submitted 2020.

2. I. Arregui, F. Teberio, I. Arnedo, **J. M. Percaz**, P. Martin-Iglesias, T. Lopetegi, and M. A. G. Laso, "High-Power Filter Design in Waveguide Technology: Future Generation of Waveguide Satellite Filters in Payloads Handling Increasing Bit Rates and Numbers of Channels," *IEEE Microwave Magazine*, vol. 21, no. 6, pp. 46-57, June 2020.

3. **J. M. Percaz**, I. Arnedo, I. Arregui, F. Teberio, P. Martin-Iglesias, M. A. G. Laso, and T. Lopetegi, "General Synthesis of Tapered Matching Sections for Single-Mode Operation Using the Coupled-Mode Theory", *IEEE Transactions on Microwave Theory and Techniques*, vol. 67, no. 9, pp. 3511-3526, Sept. 2019.

4. F. Teberio, **J. M. Percaz**, I. Arregui, P. Martin-Iglesias, T. Lopetegi, M. A. G. Laso, and I. Arnedo , "Design Procedure for New Compact Waffle-Iron Filters With Transmission Zeros", *IEEE Transactions on Microwave Theory and Techniques*, vol. 66, no. 12, pp. 5614-5624, Dec. 2018.

5. F. Teberio, **J. M. Percaz**, I. Arregui, P. Martin-Iglesias, T. Lopetegi, M. A. G. Laso, and I. Arnedo , "Rectangular Waveguide Filters With Meandered Topology," *IEEE Transactions on Microwave Theory and Techniques*, vol. 66, no. 8, pp. 3632-3643, Aug. 2018.

6. F. Teberio, **J. M. Percaz**, I. Arregui, P. Martin-Iglesias, T. Lopetegi, M. A. G. Laso, and I. Arnedo, "Routing with Classical Corrugated Waveguide Low-Pass Filters with Embedded Bends," *Progress In Electromagnetics Research Letters*, Vol. 75, pp. 1-6, 2018.

7. I. Arnedo, M. Chudzik, **J. M. Percaz**, I. Arregui, F. Teberio, Benito, D., T. Lopetegi, and M. A. G. Laso, "Synthesis of One Dimensional Electromagnetic Bandgap Structures with Fully Controlled Parameters," *IEEE Transactions on Microwave Theory and Techniques*, vol. 65, no. 9, pp. 3123-3134, Sept. 2017.

8. **J. M. Percaz**, M. Chudzik, I. Arnedo, I. Arregui, F. Teberio, M. A. G. Laso, and T. Lopetegi, "Producing and Exploiting Simultaneously the Forward and Backward Coupling in EBG-Assisted Microstrip Coupled Lines," *IEEE Antennas and Wireless Propagation Letters*, vol. 15, pp. 873-876, 2016.

9. Arregui, F. Teberio, I. Arnedo, **J. M. Percaz**, A. Gomez-Torrent, M. Chudzik A. G. Laso, and T. Lopetegi, "Resonant Quasi-Periodic Structure for Rectangular Waveguide Technology with Wide Stopband and Band-Pass Behavior," *Progress In Electromagnetics Research C*, Vol. 69, pp. 97-104, 2016.

INTERNATIONAL CONFERENCES: 15

1. P. Martin-Iglesias, T. Raadik, F. Teberio, **J. M. Percaz**, S. Martin-Iglesias, L. Pambaguian, I. Arregui, I. Arnedo, Lopetegi, and M. A. G. Laso, "Multiphysic Analysis of High Power Microwave Filter Using High Performance Aluminium Alloy," *2019 IEEE MTT-S International Microwave Workshop Series on Advanced Materials and Processes for RF and THz Applications (IMWS-AMP)*, Bochum, Germany, 2019, pp. 58-60.

2. L. Miranda, F. Teberio, P. Martin-Iglesias, I. I. Calero Arregui, I. Arnedo, **J. M. Percaz**, David Santiago, T. Lopetegi, and Miguel A. G. Laso, "Stepped-Impedance Band-Pass Filters with Improved Selectivity," *2019 IEEE MTT-S International Microwave Symposium (IMS)*, Boston, MA, USA, 2019, pp. 1198-1200.

3. P. Martin-Iglesias, T. Raadik, F. Teberio, **J. M. Percaz**, Martin-Iglesias, S., L. Pambaguian, I. Arregui, I. Arnedo, T. Lopetegi, and M. A. G. Laso, "Evaluation of High Performance Aluminum for Microwave Filters," *2019 IEEE MTT-S International Microwave Symposium (IMS)*, Boston, MA, USA, 2019, pp. 1183-1186.

4. **J. M. Percaz**, I. Arnedo, I. Arregui, L. Miranda, I. Calero, D. Santiago, M. Chudzik, F. Teberio, P. Martin-Iglesias, T. Lopetegi, and M. A. G. Laso, "Synthesis of Tapers Using the Coupled-Mode Theory," *2018 IEEE MTT-S Latin America Microwave Conference (LAMC 2018)*, Arequipa, Peru, 2018, pp. 1-4.

5. F. Teberio, **J. M. Percaz**, I. Arregui, P. Martin-Iglesias, T. Lopetegi, M. A. G. Laso, and I. Arnedo, "Novel Compact Bent Transformers Embedding Routing Capability in Waveguide Structures," *2018 48th European Microwave Conference (EuMC)*, Madrid, 2018, pp. 121-124.

6. **J. M. Percaz**, M. Chudzik, I. Calero, F. Teberio, I. Arregui, T. Lopetegi, I. Arnedo, and M. A. G. Laso, "Analog Signal Processing: A Time-Domain Demonstration of Microwave Differentiation," *2018 48th European Microwave Conference (EuMC)*, Madrid, 2018, pp. 870-873.

7. F. Teberio, P. Martin-Iglesias, I. Arregui, **J. M. Percaz**, T. Lopetegi, M. A. G. Laso, and I. Arnedo, "Quasi-Analytical Design of Commensurate-Line Waveguide Band-Pass Filters," *2018 IEEE MTT-S International Conference on Numerical Electromagnetic and Multiphysics Modeling and Optimization (NEMO)*, Reykjavik, 2018, pp. 1-4.

8. F. Teberio, I. Arnedo, **J. M. Percaz**, I. Arregui, P. Martin-Iglesias, T. Lopetegi, and M. A. G. Laso, "Accurate Design Procedure for Waffle-Iron Low-Pass Filter," *2018 IEEE/MTT-S International Microwave Symposium - IMS*, Philadelphia, PA, 2018, pp. 1238-1241.

9. P. Martin-Iglesias, Montero, I., F. Teberio, I. Arregui, **J. M. Percaz**, T. Lopetegi, I. Arnedo, L. Olano, and M. A. G. Laso, "Enhanced multipactor performance in 3D printed microwave parts," *2017 IEEE MTT-S International Microwave Workshop Series on Advanced Materials and Processes for RF and THz Applications (IMWS-AMP)*, Pavia, 2017, pp. 1-3.

10. F. Teberio, I. Arnedo, **J. M. Percaz**, I. Arregui, T. Lopetegi, and M. A. G. Laso, "Meandered corrugated waveguide low-pass filter," *2017 IEEE MTT-S International Microwave Workshop Series on Advanced Materials and Processes for RF and THz Applications (IMWS-AMP)*, Pavia, 2017, pp. 1-3.

11. F. Teberio, I. Arnedo, **J. M. Percaz**, I. Arregui, T. Lopetegi and M. A. G. Laso, "Accurate design of corrugated waveguide low-pass filters using exclusively closed-form expressions," *2017 47th European Microwave Conference (EuMC)*, Nuremberg, 2017, pp. 632-635.

12. **J. M. Percaz**, I. Arnedo, M. Chudzik, I. Arregui, F. Teberio, C. Briso-Rodríguez, J. Moreno, T. Lopetegi, and M, A. G. Laso, “Synthesis and Applications of Smooth-Profiled Planar Coupled-Lines,” *2017 Microwave Theory and Techniques Workshop*, ESA – ESTEC, Noordwijk, 2017.

13. Gomez-Torrent, F. Teberio, A. Martinez, **J. M. Percaz**, I. Arnedo, I. Maestrojuan, I. Arregui, G. Crespo, T. Lopetegi, M. A. G. Laso, and J. Teniente, "A study of the additive manufacturing technology for RF/microwave components," *2017 11th European Conference on Antennas and Propagation (EUCAP)*, Paris, 2017, pp. 567-571.

14. Arnedo, I. Arregui, F. Teberio, M. Chudzik, A. Lujambio, D. Benito, **J. M. Percaz**, A. Gomez-Torrent, T. Lopetegi, and M. A. G. Laso, "Microwave periodic structures and synthesized structures with smooth profiles and their applications," *2016 IEEE MTT-S Latin America Microwave Conference (LAMC)*, Puerto Vallarta, 2016, pp. 1-3.

15. F. Teberio, A. Gomez-Torrent, I. Arregui, **J. M. Percaz**, I. Arnedo, M. Chudzik, T. Lopetegi, and M. A. G. Laso, "Sensitivity analysis of a 3-D printed low-cost compact waveguide low-pass filter," *2016 46th European Microwave Conference (EuMC)*, London, 2016, pp. 249-252.

NATIONAL CONFERENCES: 3

1. Calero, F. Teberio, P. Martin-Iglesias, L. Miranda, I. Arregui, I. Arnedo, **J. M. Percaz**, D. Santiago, T. Lopetegi, D. Benito, and M. A. G. Laso, "Filtros paso banda basados en saltos de impedancia con alta selectividad", *XXXIV Simposium Nacional de la Unión Científica Internacional de Radio (URSI 2019)*, Sevilla, Spain, 2019.

2. F. Teberio, I. Arregui, A. Gomez-Torrent, E. Menargues, I. Arnedo, M. Chudzik, **J. M. Percaz**, M. Zedler, F. Görtz, R. Jost, T. Lopetegi, and M. A. G. Laso, "Multipactor Analysis of a High-Power Low-Loss Compact Waveguide Low-Pass Filter", *XXX Simposium Nacional de la Unión Científica Internacional de Radio (URSI 2015)*, Pamplona, Spain, 2015.

3. **J. M. Percaz**, M. Chudzik, I. Arnedo, I. Arregui, F. Teberio, A. Gómez-Torrent, E. Menargues, M. A. G. Laso, and T. Lopetegi, "Diseño de multiplexores basados en EBG explotando el acoplamiento forward y backward en líneas microstrip acopladas", *XXX Simposium Nacional de la Unión Científica Internacional de Radio (URSI 2015)*, Pamplona, Spain, 2015.

upna

Universidad Pública de Navarra
Nafarroako Unibertsitate Publikoa

upna

Universidad Pública de Navarra
Nafarroako Unibertsitate Publikoa

upna

Universidad Pública de Navarra
Nafarroako Unibertsitate Publikoa

upna

Universidad Pública de Navarra
Nafarroako Unibertsitate Publikoa